Ocean tides of ancient oceans and the evolution of the Earth-Moon system

Dissertation

zur Erlangung des akademischen Grades
Dr. rer. nat.
an der Fakultät für Mathematik, Informatik und Naturwissenschaften
der Universität Hamburg

eingereicht beim Fachbereich Informatik

vorgelegt von

Petra Nerge
aus Hamburg

Hamburg, September 2025

Reviewers

Prof. Dr. Thomas Ludwig
Prof. Dr. Maik Thomas

Date of disputation

31.03.2026

Dem gefallenen Blatt und dem austreibenden Blatt.

O Mensch! Gib acht!
Was spricht die tiefe Mitternacht?
„Ich schlief, ich schlief –,
Aus tiefen Traum bin ich erwacht: –
Die Welt ist tief,
Und tiefer als der Tag gedacht.
Tief ist ihr Weh –,
Lust – tiefer noch als Herzeleid:
Weh spricht: Vergeh!
Doch alle Lust will Ewigkeit –,
– will tiefe, tiefe Ewigkeit!“

in Nietzsche (1885)

Abstract

Ocean tides cause an exchange of angular momentum between the Earth and the Moon, resulting in the lengthening of the day and the Moon moving away from the Earth. This process essentially governs the evolution of the Earth-Moon system. The extent of the ocean tides is largely subject to the prevailing resonance conditions. These depend on the tide-generating force, the Earth rotation rate, and the geometry of the oceans. During the history of the Earth, these quantities have changed significantly. However, there is a considerable research deficit regarding a differentiated reconstruction of the Earth's history and especially the tides of earlier oceans and their impact on the Earth's rotation.

For the period ~620 million years (Myr) ago, the ocean tides are reconstructed in their spatial and temporal characteristics by a time step model. At the same time, the associated angular momentum transfer between Earth and Moon is computed. Geological proxy data provide information about the tidal spectrum of the Australian continental plate during this period. This data also document a shortened lunar distance and a shorter day of 21.9 hours. The simulations include the lunar and solar principal constituents of the tide-generating force (M_2, S_2, K_1, O_1). In the early history of the Earth, a supercontinent known as Rodinia dominated the topography. This continent was located about ~620 Myr ago in the Southern Hemisphere, across the South Pole.

The simulated ocean tides are qualitatively and quantitatively validated by observational data for current conditions. The tidal exchange of angular momentum between the Earth and the Moon is found to accelerate the Moon's orbit. As a result, the Moon moves away from the Earth and the day length increases. This result aligns with observational data. Within reasonable limits, the spectral distribution of tides for the period ~620 Myr ago is supported by the geological data and our prior knowledge. The interpretation of the regional distribution of angular momentum transfer as a function of the land-water distribution and the associated oceanic tidal systems allows the complex influence of the land-water distribution on angular momentum transfer to be estimated. A reliable example is obtained by the effect of the single supercontinent Rodinia, which existed during most of the *Neoproterozoic* (~1000 to 539 Myr ago), on angular momentum exchange between Earth and Moon resulting from ocean tides. The results of the present study are considered a significant advance in the interdisciplinary geoscientific and astronomical research on the deep-time evolution of the Earth and the Earth-Moon system.

Kurzfassung

Die Gezeiten der Ozeane verursachen einen Austausch von Drehimpuls zwischen der Erde und dem Mond. Dieser Austausch hat zur Folge, dass der Tag sich verlängert und der Mond sich von der Erde entfernt. Die Entwicklung des Erde-Mond-Systems wird im Wesentlichen durch diesen Prozess bestimmt. Das Ausmaß der Gezeiten hängt weitgehend von den vorherrschenden Resonanzbedingungen ab. Diese hängen wiederum von der Gezeitenkraft, der Rotationsgeschwindigkeit der Erde sowie der Geometrie der Ozeane ab. Im Laufe der Erdgeschichte haben sich diese Größen erheblich verändert. Es besteht jedoch erheblicher Forschungsbedarf hinsichtlich einer differenzierten Rekonstruktion der Erdgeschichte, insbesondere der Gezeiten früherer Ozeane und deren Einfluss auf die Erdrotation.

Anhand eines Zeitschrittmodells werden die räumlichen und zeitlichen Eigenschaften der Gezeiten für den Ozean vor ~620 Myr rekonstruiert. Gleichzeitig wird die damit verbundene Drehimpulsübertragung zwischen Erde und Mond berechnet. Geologische Proxydaten liefern Informationen über das Gezeitenspektrum der australischen Kontinentalplatte in diesem Zeitraum. Diese Daten belegen eine kürzere Mondentfernung und einen kürzeren Tag von etwa 21.9 Stunden. In den Simulationen werden die halbtäglichen und täglichen Hauptbeiträge des Mondes und der Sonne zur Gezeitenkraft, die M_2, S_2, K_1 und O_1 Partialtiden, berücksichtigt. In der Frühgeschichte der Erde dominierte ein einziger Superkontinent namens Rodinia die Topographie. Dieser befand sich vor ~620 Myr in der südlichen Hemisphere um den Südpol gelegen.

Die simulierten Gezeiten des Ozeans werden anhand von Beobachtungsdaten für die gegenwärtigen Bedingungen qualitativ und quantitativ validiert. Dabei beschleunigt der Drehimpulstransfer durch die Gezeiten den Mond auf seiner Umlaufbahn. Infolgedessen entfernt sich der Mond von der Erde und die Tageslänge nimmt zu. Dieses Ergebnis steht im Einklang mit den Beobachtungsdaten. Innerhalb angemessener Grenzen werden die spektrale Verteilung der Gezeiten für den Zeitraum vor ~620 Myr durch die geologischen Daten und unser Vorwissen gestützt. Die Analyse der regionalen Verteilung des Drehimpulsaustauschs als Funktion der Land-Wasser-Verteilung und der damit verbundenen Gezeitensysteme ermöglicht eine Abschätzung des komplexen Einflusses der Land-Wasser-Verteilung auf den Drehimpulstransfer. Es konnte ein aussagekräftiges Beispiel für der Einfluss des Superkontinenten Rodinia, der während des größten Teils des Neoproterozoikums (vor etwa 1000 bis 539 Myr) existierte, auf den Drehimpulstransfer zwischen Erde und Mond gewonnen werden. Die Ergebnisse der vorliegenden Studie werden als bedeutender Fortschritt in der interdisziplinären geowissenschaftlichen und astronomischen Forschung zur Entwicklung der Erde und des Erde-Mond-Systems in der weit zurückliegenden Erdgeschichte angesehen.

Acknowledgements

I would like to express my profound thanks to my supervisors, Prof. Dr. Thomas Ludwig and Prof. Dr. Jürgen Sündermann, for their invaluable guidance, unwavering trust, and continuous, unfailing support of my work.

I would like to thank Prof. Dr. Maik Thomas for his support throughout my studies and for reviewing this thesis.

My appreciation is extended to Dr. Philipp Weis for his provision of unrestricted access to the TiME tidal model and for his assistance.

Special thanks go to Prof. Dr. Thomas Ludwig and the Scientific Computing Group at the Department of Informatics at the University of Hamburg for the excellent working environment and atmosphere. I would particularly like to thank Prof. Dr. Michael Kuhn and Dr. Jannek Squar for their unceasing assistance and support with infrastructure and all other related aspects.

I would like to thank Dr. Roman Sulzbach for his insightful commentary on the TiME21 tidal atlas version.

My sincere thanks go out to André Hufschmidt for his assistance with the proofreading of my dissertation, for the constructive discussions we had, for his encouragement, and for his patience.

Special acknowledgment is due to Dr. Hermann Lenhart, who facilitated my initiation into the field of oceanography.

I am so thankful for Ms. Lindau-Langlois for providing trusting guidance, support, and commitment to me.

Lastly, my deepest thanks are extended to Gudrun and Aino for being friends I can always count on.

Contents

Acronyms

AMOC	Atlantic Meridional Overturning Circulation.
AusTides	Electronic product that is equivalent to paper Australian National Tide Tables.
CMB	Core-mantle boundary.
CryoSat-2	Satellite for monitoring the cryosphere system.
cy	Century.
d	Mean solar day.
$\mathbf{d}_{\text{☾}}$	Mean lunar day.
EGM	Joint NASA Goddard Space Flight Center and the National Imagery and Mapping Agency Earth geopotential model (Lemoine et al., 1998).
ENSO	El Niño Southern Oscillation.
Envisat	Environmental Satellite.
EOT	Empirical Ocean Tide models.
FES	Finite Element Solution global tide model.
GDP	Global Drifter Program.
GEBCO	General Bathymetric Chart of the Oceans.
GEOSAT	GEOdetic SATellite.
GESLA	Global Extreme Sea Level Analysis project.
GFDL	Geophysical Fluid Dynamics Laboratory.
GOT	Goddard/Grenoble Ocean Tide model.
GPS	Global Positioning System.
HAMTIDE	Hamburg direct data Assimilation Methods for TIDEs models.
HIM	Hallberg Isopycnal model.
HYCOM	HYbrid Coordinate Ocean Model.
IODP	International Ocean Discovery Program.
LEGOS	Laboratoire d'Etudes en Géophysique et Océanographie Spatiales.

LGM Last glacial maximum 22 000 to 18 000 BC.
LLR Lunar Laser Ranging.

MPIOM Max Planck Institute Ocean Model.
Myr Million years.

NOAA National Oceanic and Atmospheric Administration.

OTIS Oregon State University Tidal Inversion Software.

RMS Root-mean-square residual.

SAL Self-attraction and loading effect.
SLR Satellite laser ranging.
SpEnOI Spectral Ensemble Optimal Interpolation data assimilation code.

TICON Tide gauge dataset of TIdal CONstants.
TiME Tidal Model forced by Ephemerides.
T-UGO Toulouse-Unstructured Grid Ocean model.
TOPEX Ocean Topography Experiment.
TPXO TOPEX (Ocean Topography Experiment)/Poseidon global tide models.

VLBI Very Long Base Interferometry.

yr Tropical year.

Nomenclature

Greek Constants

Symbol	Description	Unit
$\mathbf{\Theta}_{♁}$	Earth's moment of inertia.	$8.23 \times 10^{37}\,\mathrm{kg\,m^2}$
ϱ	Density of seawater.	$1024\,\mathrm{kg\,m^3}$
$\Omega_{♁}$	Earth's mean angular velocity.(Gross, 2007).	$7.292 \times 10^{-5}\,\mathrm{rad\,s^{-1}}$

Latin Constants

Symbol	Description	Unit
$a_{☾}$	Lunar mean semi-major axis.	$3.834 \times 10^{8}\,\mathrm{m}$
$a_{\odot}$	Solar mean semi-major axis.	$1.496 \times 10^{11}\,\mathrm{m}$
C	Earth's principal moment of inertia referring to the polar axis of rotation.	$8.04 \times 10^{37}\,\mathrm{kg\,m^2}$
$e_{☾}$	Lunar eccentricity.	0.0555
$e_{\odot}$	Solar eccentricity.	0.0167
$\vec{\boldsymbol{g}}$	Earth's mean gravity acceleration.	$9.806\,\mathrm{m\,s^{-2}}$
G	Gravitational constant.	$6.6743 \times 10^{-11}\,\mathrm{m^3\,kg^{-1}\,s^{-2}}$
$i_{☾}$	Lunar inclination.	5.157°
$i_{\odot}$	Solar inclination.	23.5°
$m_{♁}$	Earth's mass.	$5.972 \times 10^{24}\,\mathrm{kg}$
$m_{\odot}$	Sun's mass.	$1.989 \times 10^{30}\,\mathrm{kg}$
$m_{☾}$	Moon's mass.	$7.348 \times 10^{22}\,\mathrm{kg}$
R	Earth's mean radius.	$6.371 \times 10^{3}\,\mathrm{m}$

Greek Symbols

Symbol	Description	Unit
α	Right ascension.	rad, °
δ	Declination.	rad, °
$\Delta l.o.d$	Change in length of day.	ms/cy (century)
ϵ	Frictional angle.	rad, °
ϵ	Obliquity of the ecliptic.	rad, °
ζ	Sea surface elevation.	m
ζ_{σ}^{0}	Amplitude of sea surface elevation due to the partial tide with frequency σ.	m
$\mathbf{\Theta}$	Moment of inertia.	$\mathrm{kg\,m^2}$

ϑ	Zenith distance.	rad, °
θ	Mean sidereal time.	s
λ	Geographical longitude.	rad, °
ν	True anomaly.	rad, °
σ_σ	Tidal angular frequency.	$\mathrm{rad\,s^{-1}}$, $\mathrm{^\circ\,s^{-1}}$
τ	Hour angle.	rad, °
Φ	Potential.	$\mathrm{m^2\,s^{-2}}$
Φ^c	Centrifugal potential.	$\mathrm{m^2\,s^{-2}}$
$\Phi^{gravity}$	Gravity potential.	$\mathrm{m^2\,s^{-2}}$
Φ^g	Gravitational potential.	$\mathrm{m^2\,s^{-2}}$
Φ^t	Astronomical tidal potential.	$\mathrm{m^2\,s^{-2}}$
Φ^t_σ	Partial tide with frequency σ.	$\mathrm{m^2\,s^{-2}}$
ϕ^0_σ	Phase of sea surface elevation due to the partial tide with frequency σ.	rad, °
φ	Geographical latitude.	rad, °
Ω	Longitude of the ascending node.	rad, °
Ω	Mean angular velocity.	$\mathrm{rad\,s^{-1}}$, $\mathrm{^\circ\,s^{-1}}$
ω	Argument of periapsis.	rad, °
ω_{cw}	Angular velocity of Chandler wobble.	$\mathrm{rad\,s^{-1}}$, $\mathrm{^\circ\,s^{-1}}$
$\vec{\boldsymbol{\omega}}$	Angular velocity vector (rotation vector).	$\mathrm{rad\,s^{-1}}$, $\mathrm{^\circ\,s^{-1}}$

Latin Symbols

Symbol	Description	Unit
a	Semi-major axis.	km, au
$a_{\leftmoon}$	Semi-major axis of the lunar orbit.	km, au
$\vec{\boldsymbol{a}}$	Acceleration.	$\mathrm{m\,s^{-2}}$
$\vec{\boldsymbol{a}}_c$	Orbital acceleration.	$\mathrm{m\,s^{-2}}$
$\vec{\boldsymbol{a}}_g$	Gravitational acceleration.	$\mathrm{m\,s^{-2}}$
$\vec{\boldsymbol{a}}_t$	Tidal acceleration.	$\mathrm{m\,s^{-2}}$
CB	Celestial body.	
c	Mean distance.	m
c_σ	Amplitude coefficient of the partial tide with frequency σ.	
D	Doodson's tidal constant.	$\mathrm{m^2\,s^{-2}}$
$\vec{\boldsymbol{d}}$	Directional vector.	m
e	Eccentricity.	
f	Latitude-dependent Coriolis parameter.	$\mathrm{rad\,s^{-1}}$, $\mathrm{^\circ\,s^{-1}}$
F	Tidal form factor.	
G_A	Geodetic function.	$\mathrm{m^2\,s^{-2}}$
h	Longitude of mean Sun.	rad, °
h, k, l	Tidal Love numbers of Earth.	
h', k', l'	Loading Love numbers of Earth.	
i	Inclination.	rad, °

L	Magnitude of angular momentum.	$\mathrm{kg\,m^2\,s^{-1}}$
$L_{♁}^{rot}$	Magnitude of Earth's rotational angular momentum.	$\mathrm{kg\,m^2\,s^{-1}}$
$\vec{\boldsymbol{L}}$	Angular momentum.	$\mathrm{kg\,m^2\,s^{-1}}$
l	Degree of Legendre polynomials.	
M	Magnitude of torque.	$\mathrm{N\,m}$
$\vec{\boldsymbol{M}}$	Torque.	$\mathrm{N\,m}$
m	Mass.	kg
m	Order of Legendre functions.	
N	Longitude of mean Moon's ascending node.	$\mathrm{rad\,s^{-1}}$, $^\circ\,\mathrm{s^{-1}}$
N	Number of time steps per tidal period.	
$\vec{\boldsymbol{n}}$	Mean revolution.	$\mathrm{rad\,s^{-1}}$, $^\circ\,\mathrm{s^{-1}}$
O	Origin of coordinate system.	
o	Related to origin of coordinate system.	
$P_l(x)$	Legendre polynomials.	
P	Period of tidal constituent/partial tide.	s
$P_l^m(x)$	Associated Legendre functions.	
p	Longitude of mean perigee.	rad, $^\circ$
p_s	Longitude of mean perihelion.	rad, $^\circ$
r^{ab}	Correlation coefficient.	
r	Radial distance (distance to origin).	m
$\vec{\boldsymbol{r}}$	Position vector.	m
rms	Root mean square residual of tidal sea surface elevations.	m
s	Longitude of mean Moon.	rad, $^\circ$
t	Time.	s
V	Volume.	$\mathrm{m^3}$

Symbols

Symbol	Description	Unit
♁	Earth.	
☾	Moon.	
☉	Sun.	
♈	Vernal equinox.	

1. Introduction

Observations of the Earth's rotation show a long-term trend of a *secular* decreasing rotation rate. The length of the day has increased and the number of days per year has decreased throughout Earth's history to the present. This effect is also known as tidal friction. Its detailed effects over long periods of Earth's history are an open question. However, the issue of tides is closely related to the Earth's rotation.

Below is an introduction to the study's research question, its elaboration, and the fundamental terminology. Beginning with an outline of the change in day length in modern times in Section 1.1 and in Earth's history in Section 1.2, its relationship to tides is discussed in Section 1.3. An introduction to tides in Section 1.4 is followed by an overview of approaches to modeling tidal friction in Section 1.5. This is complemented by the specification of the research question and the methodology of the study in Section 1.6. Finally, an outline of the thesis is given in Section 1.7.

1.1. Current change in day length

Present geodetic and astronomical observations confirm a secular increase in day length of about 1.8 ms/cy and a lunar recession rate of about 3.8 cm/yr (year) (Stephenson et al., 2016; J. G. Williams & Boggs, 2016). Insufficient evidence has been obtained for a secular change in the distance of the Earth from the Sun (Simon et al., 1994) and thus for a secular change in the year length. By comparing ancient solar eclipses with those of his own time, Halley (1695) is the first to point to a secular increase in the day length (Morrison & Stephenson, 2001). At this time, the Earth was still considered an ideal clock, and the differences he thought were changes in the Moon's orbit actually were due to changes in the Earth's rotation. More recent observations using Lunar Laser Ranging (LLR), Very Long Base Interferometry (VLBI), and geostationary satellites have revealed variations on the short-term scale of decades to hours in particular.

1.2. Distant past day lengths

Geochemical and geochronological evidence places the age of the Earth-Moon system at 4400 Myr to 4540 Myr (e. g. Barboni et al., 2017; Borg et al., 2011; Maurice et al., 2020). The Geological Time Scale in Table 1.1 shows the subdivision of the Earth's history.

From the final results of various available paleontological reports based on single or multiple specimens, the history of Earth's rotation rate by days per year, shown in Figure 1.1, was compiled by Deines and Williams (2016, Table 1). The number of days per year for most of the time has been decreasing throughout Earth's history to modern times. If the length of the year is assumed to have been constant throughout Earth's history (Section 1.1),

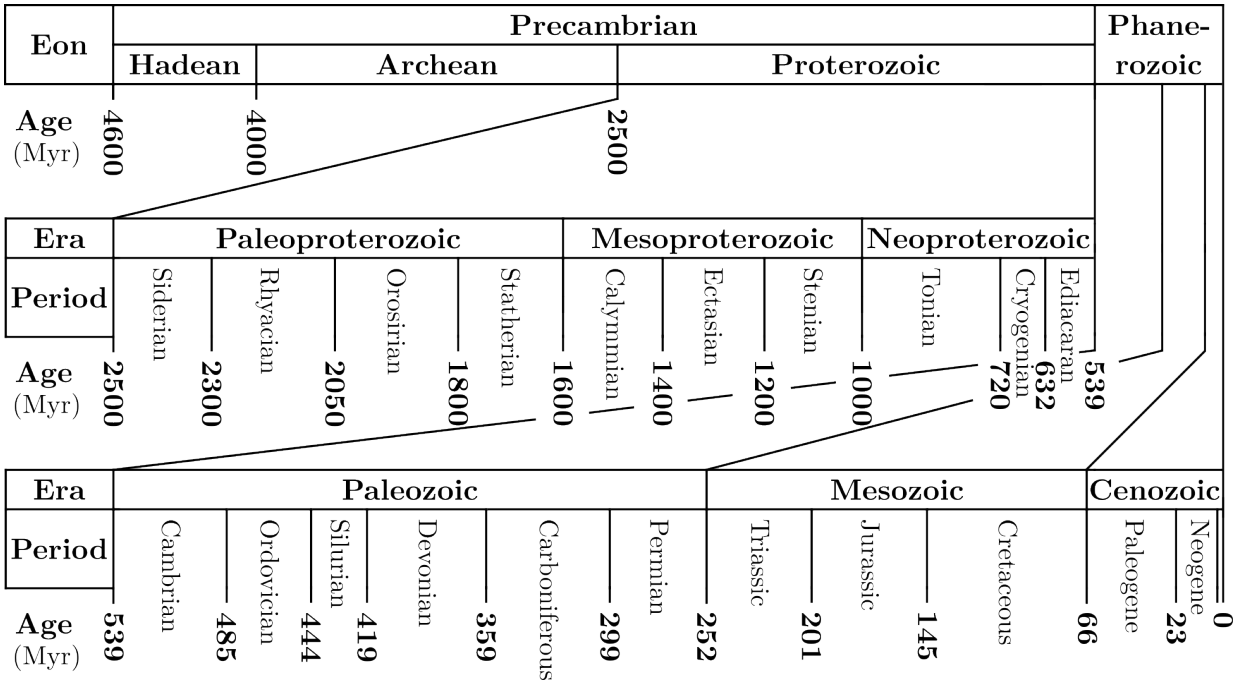

Table 1.1.: The Geological Time Scale (GTS) as a hierarchical classification of Earth history in the descending rank order of Eon, Era, Period according to the nomenclature of geochronology. The age is given in millions of years (Myr). Rock records of the Earth form the basis for the classification of geological time. The data are based on the International Chronostratigraphic Chart (ICC) latest version v2022/10 of the International Commission on Stratigraphy (ICS).

the length of the day has been increasing. As shown by the paleontological evidence, secular retardation is a phenomenon that has existed for more than a billion years. In general, the data show a pattern of non-linear decreasing days per year throughout geologic history. Some of the data are likely to be contradictory. For example, tidal sedimentation data indicate 400 days (d)/yr at ~620 Myr ago and fossil data indicate 400 d/yr to 420 d/yr between 350 Myr to 520 Myr ago. However, Lambeck (1980b) and Scrutton (1978) have cast doubt on the reliability of much of the paleontological fossil record from Paleozoic. Furthermore, the seven available Earth-Moon distances derived from tidal sedimentation throughout Earth's history show a pattern of non-linear, progressively increasing distances and thus lunar cycles (Coughenour et al., 2013; De Azarevich & Azarevich, 2017; K. A. Eriksson & Simpson, 2000; Kvale & Archer, 1990; Sonett & Chan, 1998; G. E. Williams, 2000).

Since the late 1980s, knowledge of the Earth's paleo-rotation rate and the lunar paleo-orbit has been inferred from sediments via ocean tides by means of tidal theory as the only unambiguous observational data (Kvale et al., 1999; Rosenberg, 1997; Sonett et al., 1996; G. E. Williams, 1989a, 1989b, 2000). Sedimentary growth rings of sediments can record the rhythmic, periodic rise and fall of ocean tides with their periods, forming so-called tidal rhythmites, which are preserved under favorable conditions throughout Earth's history. The difference in height between low and high tide, the range of the tides, and the resulting velocity of the currents directly control sediment transport and deposition (Boothroyd, 1985; FitzGerald & Nummedal, 1983; Mazumder & Arima, 2005; G. E. Williams, 2000). Relatively

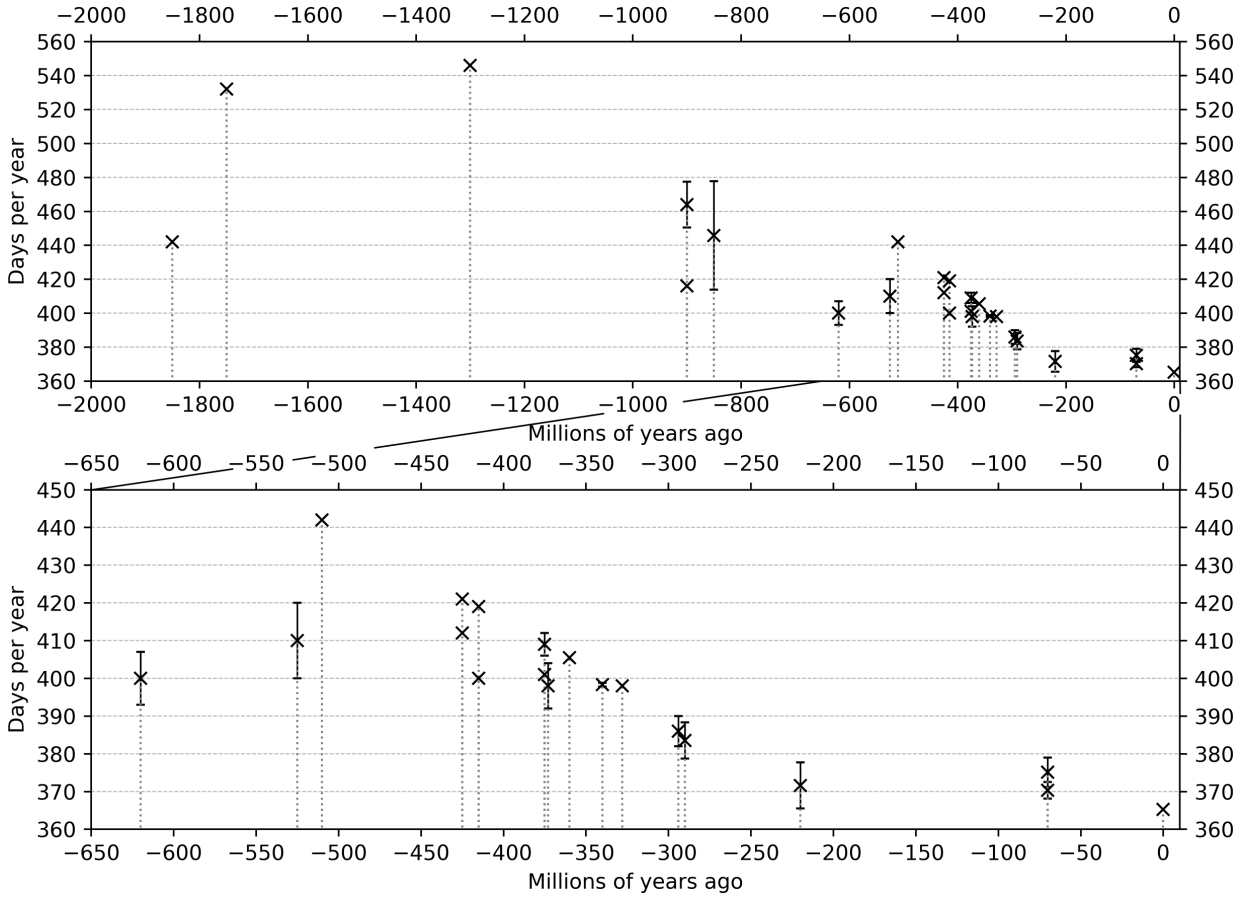

Figure 1.1.: Earth's paleo-rotation rate by the number of days per year (constant length throughout Earth's history), as compiled in Deines and Williams (2016, Table 1) from the final results of various available paleontological reports based on single or multiple specimens. Available error estimates were taken from the reports, otherwise the standard deviation was given.

thick sediment layers, the *laminae*, result from large tidal ranges. Thinner laminae result from smaller tidal ranges.

G. E. Williams (1989a, 1989b, 2000) and G. E. Williams (1989c, 1997, 1998b) have provided the unique internally self-consistent data on ocean tides, Earth rotation, and lunar orbital quantities from the analysis of tidal rhythmites from the Elatina Formation in South Australia for the Late Neoproterozoic about ~620 Myr ago. The number of days per year were derived to be (400 ± 7) d/yr and the length of day was derived to be (21.9 ± 0.4) h and an Earth-Moon distance of 0.965 ± 0.005 of the present distance. This yields a mean lunar recession rate of (2.2 ± 0.3) cm/yr since ~620 Myr ago, which is slightly over half of the present recession rate of (3.82 ± 0.07) cm/yr.

1.3. Changes in day length and tides

Kant (1754) provided the first theoretical considerations of the secular lengthening of the day. A force that gradually slows the Earth's rotation is exerted on the continental margins

and the ocean floor by the east-west motion of the ocean tides. Meanwhile, the theoretical relationship between the deceleration of the Earth's rotation rate and the expansion of the Moon's orbit with the tides can be established through the conservation of energy and angular momentum. The tides induce a torque that transfers energy and angular momentum from the Earth rotation to the Moon's orbit. First, the Earth's rotation slows, lengthening the day, and second, the Moon moves into a higher elliptical orbit with a greater distance from the Earth, lengthening the month as orbital period. Munk and McDonald (1960) first showed that the ocean is the main dissipator of tidal energy. It has been confirmed many times since then. However, while Kant's remarkable insight into the mechanism of tidal friction is widely accepted today, the precise effect of tidal friction over long periods of time remains uncertain. This includes the geological time scale.

The Earth must have rotated faster and the Moon must have been much closer in the past. Gerstenkorn (1955) pointed out that about 1500 Myr ago the Moon would have been so critically close to the Earth that devastating tidal waves would have passed around the Earth in a schematic backtracking of the Moon's orbit with constant current values. The Gerstenkorn Event is what geologists call the time when the Moon was only a few Earth radii away. However, there is no evidence of such a catastrophe at that time in geological records or in the surface features of the Earth nor of the Moon. Instead, the presence of oceans with lunar tides prior to 3000 Myr ago is indicated by growth patterns, mat-like structures formed by algal growth known as stromatolites, found in *Archean* rocks (Pannella, 1976). In addition, lunar tides prior to 3200 Myr to 3000 Myr are indicated by Archean sedimentary structures indicative of tidal deposits (K. A. Eriksson, 1977; K. A. Eriksson & Simpson, 2000; von Brunn & Mason, 1977; Watchorn, 1980). On the Geological Time Scale (Table 1.1), consistent with Section 1.2, there must have been epochs when Earth's rotation slowed and the Moon receded from Earth much more slowly than today.

1.4. Tides outline

The tide-generating force of the Moon and the Sun can be decomposed into strictly periodic constituents related to their orbital cycles (Darwin, 1883–1886; Doodson, 1921). These tidal constituents are also referred to as partial tides or simply as the tides. The periods of the tides range from semi-diurnal to multiannual. Each tidal constituent is generally represented by an alphanumeric term: e. g. M_2 (semi-diurnal principal lunar tide), S_2 (semi-diurnal principal solar tide), K_1 (diurnal declinational lunisolar tide), and O_1 (diurnal declinational lunar tide). The subscripts denote the diurnal tides (1) and the semi-diurnal (2) tides. Thus, the tidal pattern at any location on Earth can be described by the sum of a series of these tidal constituents.

Ocean dynamics and the depth and the shape of ocean basins and coastlines prevent the undisturbed motion of tides as *equilibrium tide*s. The spatial and temporal characteristics of the tides are essentially determined by the given resonance conditions. Whether ocean tides can be excited by the individual tidal constituents depends on the geometry of the ocean basins and the Earth's rotational velocity, as these attenuate or amplify certain tidal constituents. An overview of the global tidal ranges is given in Figure 1.2, and an overview of the global type of the tidal regime is given in Figure 1.3. Tides for different

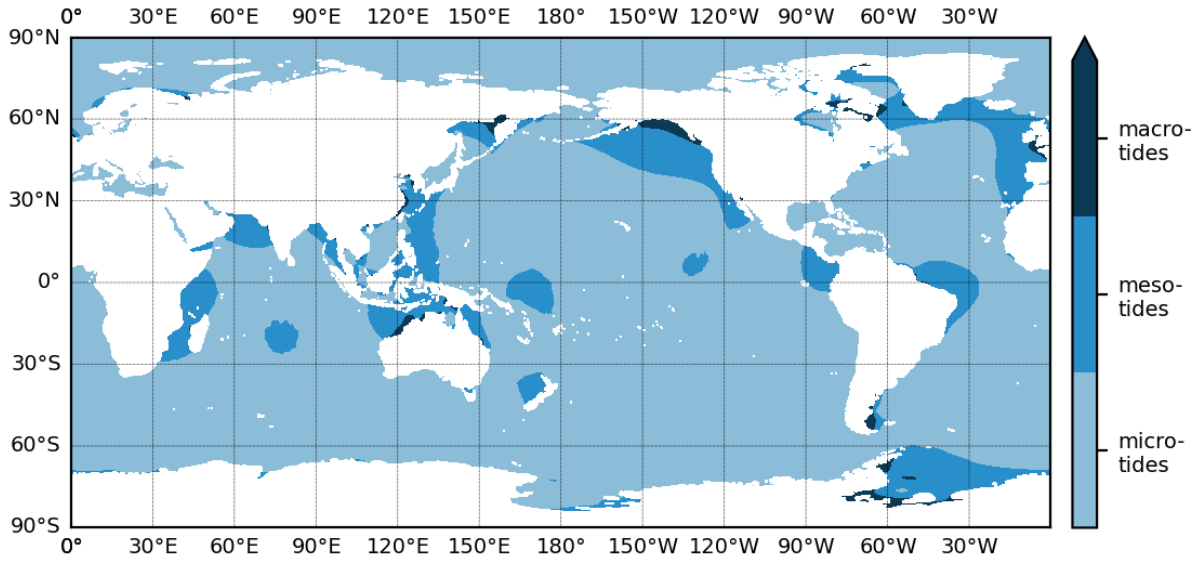

Figure 1.2.: Global map of the tidal range of the superimposed ocean tides M_2, S_2, K_1 and O_1. Tidal ranges greater than 4 m are called macrotides, those between 2 and 4 m are called mesotides, and those less than 2 m are called microtides. The data used are from Hart-Davis et al. (2021a) and Hart-Davis et al. (2021b).

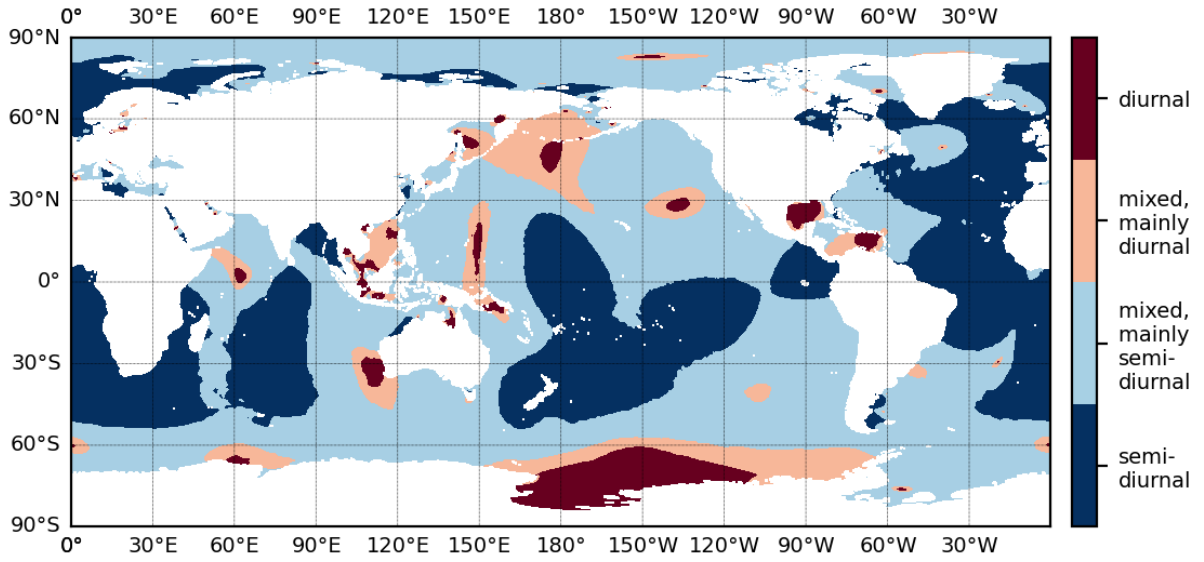

Figure 1.3.: Global map of tidal regime types: semi-diurnal; mixed, mainly semi-diurnal; mixed, mainly diurnal; diurnal. The type is based on the form factor F, the amplitude ratio of the diurnal declinational tides K_1 and O_1 to the semi-diurnal principal tides M_2 and S_2. The data used are from Hart-Davis et al. (2021a) and Hart-Davis et al. (2021b).

local resonance conditions are shown in Figures 1.4 to 1.6. The different tidal ranges show the influence of the given resonance conditions on the intensity of the tides. As well as the different tidal patterns such as mainly semi-diurnal (Figure 1.4), mainly diurnal (Figure 1.5), and mixed tides (Figure 1.6). In addition, the tides show an approximately semi-monthly

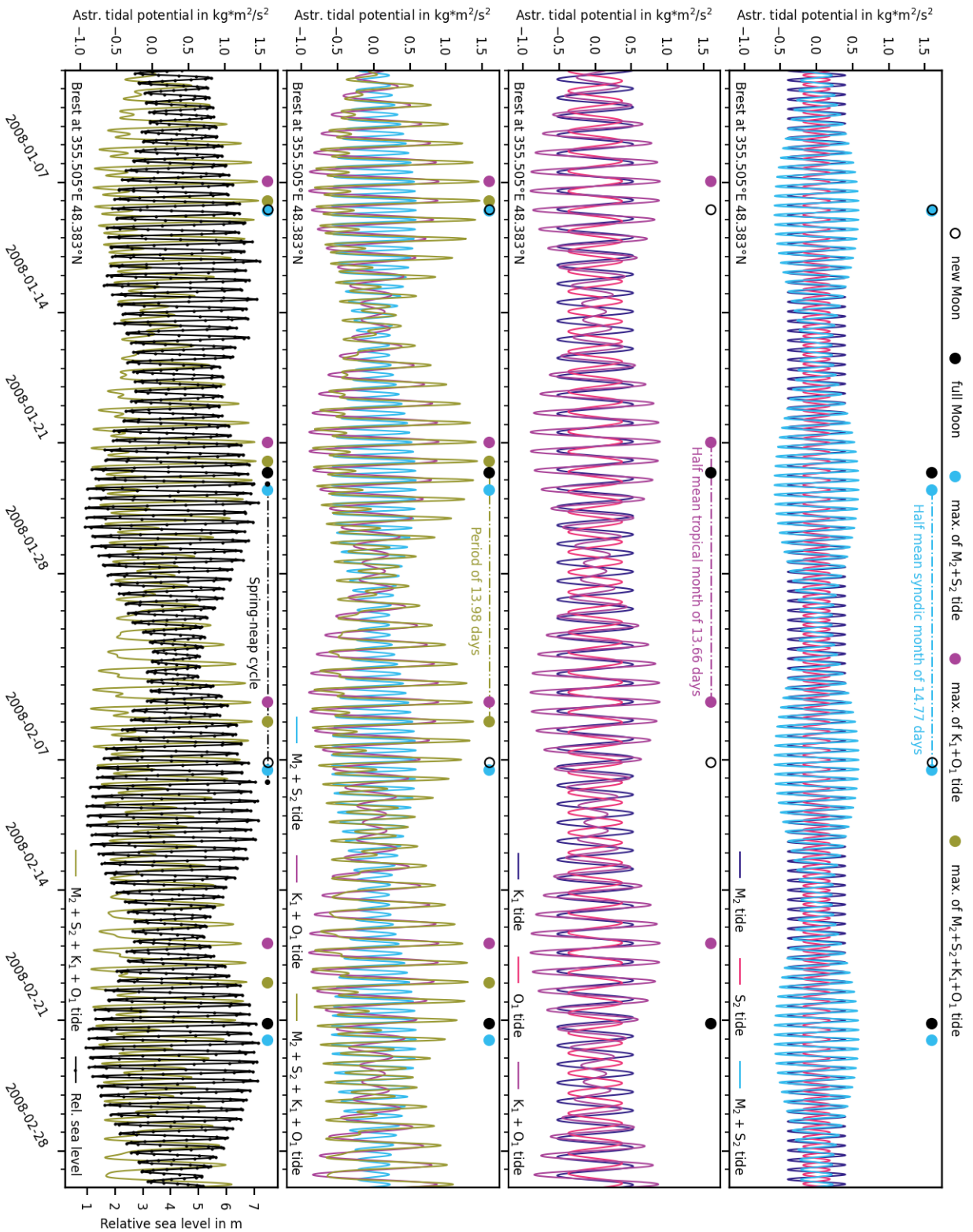

Figure 1.4.: Relative sea level measured hourly at the tide gauge at Brest, France, for the period January to February 2008 (Caldwell et al., 2015). This is contrasted with the astronomical tidal potential (normalized to one) with the two semi-diurnal principal tides M_2 and S_2 and the two diurnal declinational tides K_1 and O_1, and their superpositions, as the main excitation for the rise and fall of sea level. The sea level data show a semi-diurnal pattern, with the neap and spring tides occurring phase-shifted with the interference pattern in the astronomical tidal potential.

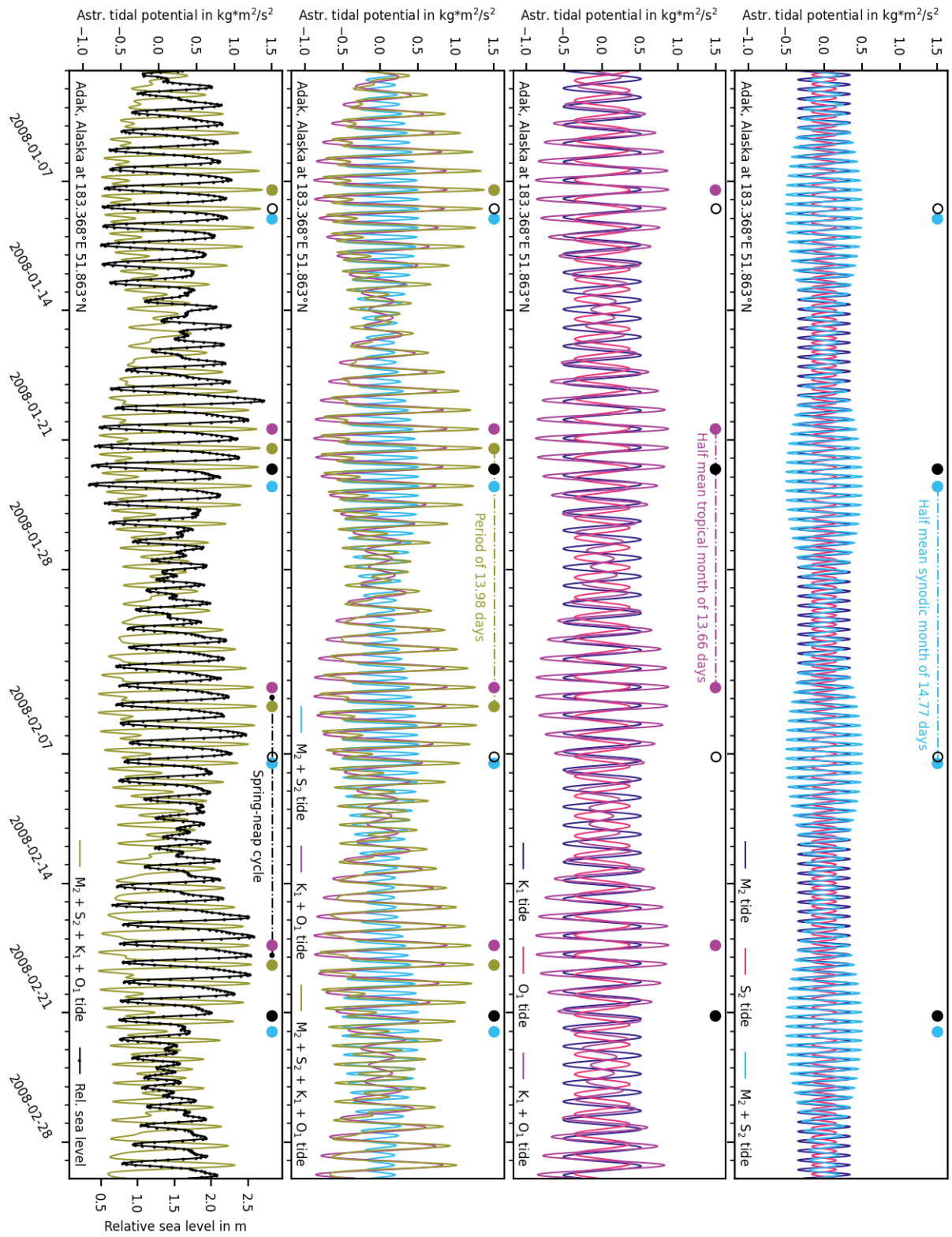

Figure 1.5.: Relative sea level measured hourly at the tide gauge at Adak Island, Alaska, for the period January to February 2008 (Caldwell et al., 2015). This is contrasted with the astronomical tidal potential (normalized to one) with the two semi-diurnal principal tides M_2 and S_2 and the two diurnal declinational tides K_1 and O_1, and their superpositions, as the main excitation for the rise and fall of sea level. The sea level data show a mainly diurnal pattern, with the neap and spring tides occurring phase-shifted with the interference pattern in the astronomical tidal potential.

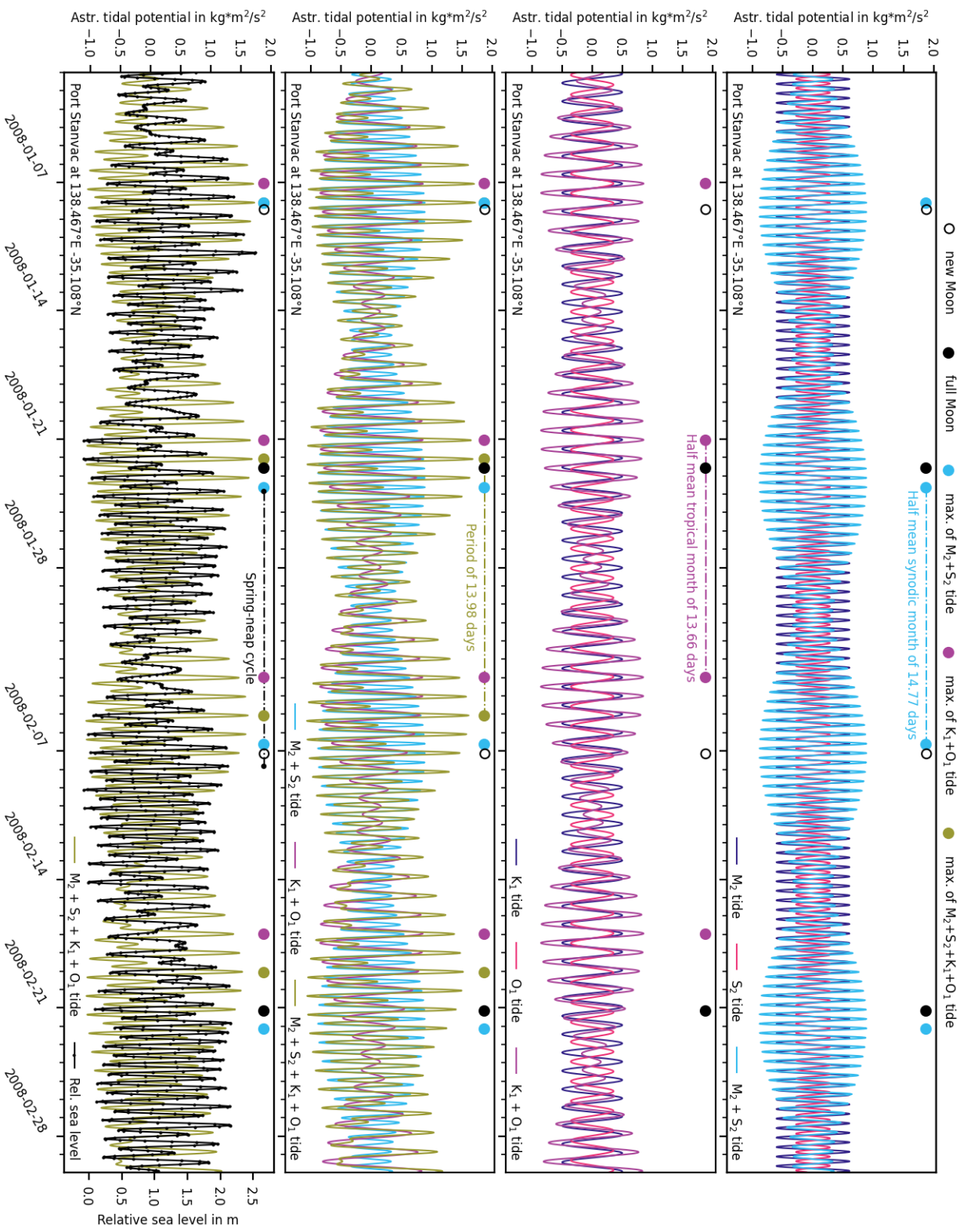

Figure 1.6.: Relative sea level measured hourly at the tide gauge at Port Stanvac, south of Adelaide, South Australia, for the period January to February 2008 (Caldwell et al., 2015). This is contrasted with the astronomical tidal potential (normalized to one) with the two semi-diurnal principal tides M_2 and S_2 and the two diurnal declinational K_1 and O_1, and their superpositions, as the main excitation for the rise and fall of sea level. The sea level data show a mixed, mainly semi-diurnal pattern, with the neap and spring tides occurring phase-shifted with the interference pattern in the astronomical tidal potential.

inequality with the so-called spring tides (high tides) and neap tides (low tides). Due to good resonance conditions in the oceans, the lunar M_2 tide, which is the dominant contributor to the tide-generating force on Earth, is currently associated with anomalously high tidal friction.

1.5. Approaches to modeling oceanic tidal friction

Measuring the physical state of the oceans remains limited by the cost and technology required. With the advent of high-performance computing, the physical state and dynamics of the oceans could be simulated using hydrodynamic numerical methods and become increasingly accessible. This applies in particular to calculating the tidal friction acting on the Earth's rotation, since the global scale must be considered. However, simulating ocean tides requires detailed knowledge of land-water distribution and bathymetry. But plate tectonics keeps ocean basins opening and closing, and keeps the continental plates moving against each other (e. g. Torge, 2001). For example the Permian and much of the Neoproterozoic were characterized by a single supercontinent (Li et al., 2008; Scotese, 2009, 2017). The further back in Earth's history we go, however, the more sparse the information becomes.

Global numerical simulations of ocean tides show, consistent with analyses of observational data, the significant effect of ocean tides on the secular decrease of the Earth's rotation rate and tidal friction in the Earth-Moon system for modern times. One of the first model simulations of the M_2 tide for the Permian ocean 250 Myr to 230 Myr ago showed that the angular momentum transfer in the Earth-Moon system was smaller by a factor 2 than at modern times—with comparable tidal amplitudes (Sündermann & Brosche, 1978). In the permanently evolving ocean basins, the resonance properties of the ocean and thus also the characteristics and energetics of the ocean tides must have altered. The modeling of global ocean tides for different periods of Earth's history and the results of solving the spectral problem confirm this (e. g. Blackledge et al., 2020; Brosche & Sündermann, 1978, 1982, 1990; Hansen, 1982; Kagan & Maslova, 1994; Webb, 1982a).

Uncertainty about the relative importance of dissipation in the shallow shelf seas compared to that in the open ocean further hampers simulations of ocean tides in Earth's history. Also, the secular increase in day length due to ocean tides is superimposed on, for example, longer-term effects on the Earth's moment of inertia due to glacial rebound. Overall, tidal friction is a complex function of shallow and open ocean regions and continental configuration. These have changed significantly over Earth's history and are poorly understood (Hansen, 1982; Sündermann & Brosche, 1978; Tyler, 2021).

1.6. Research objectives

A significant research deficit remains regarding the differentiated reconstruction of the Earth's history, in particular the tides of the early oceans and the associated tidal friction (Brosche & Sündermann, 2011). So far, the very limited availability of high quality geological data has prevented a detailed data-based quantification of the angular momentum transfer in the Earth-Moon system for times in the distant past. The present study aims to

address these shortcomings by incorporating the geological data on the evolution of the Earth-Moon system provided by G. E. Williams (1989a, 1989b, 2000) and G. E. Williams (1989c, 1997, 1998b). In parallel, a synthesis of the formation (1300 Myr to 900 Myr) and breakup (< 600 Myr) of the supercontinent Rodinia with Neoproterozoic paleogeographic data has been provided by Li et al. (2008). Paleogeographic maps for the period 750 Myr to 540 Myr ago in the Late Neoproterozoic have been compiled by Scotese (2009). It would be unreasonable not to use these data in the absence of better data.

For a time slice of the Late Neoproterozoic, ~620 Myr ago, hydrodynamic numerical simulations are performed to reconstruct the oceanic tides in their spatial and temporal characteristics. The semi-diurnal major tides M_2 and S_2 and the diurnal major tides K_1 and O_1 are considered according to G. E. Williams (1989a, 1989b, 2000) and G. E. Williams (1989c). At the same time, the associated angular momentum transfer between the Earth and the Moon is determined. The geological data provided by G. E. Williams (1989a, 1989b, 2000) and G. E. Williams (1989c) offer a valuable opportunity to evaluate the numerical results, as they provide observational data on the tidal spectrum of the Australian continental plate. The land-water distribution and the bathymetry are based on Scotese (2017) and Scotese and Wright (2018). The unknown ocean depths are mapped using two representative depths for the shelf and the open ocean. The ocean model employed is an extension of Weis (2006). A reliable example of the effect of the supercontinent Rodinia, which existed during most of the Neoproterozoic, on the tidal friction is obtained. The purpose of this study is to perform a first-order estimation in order to provide an approximation for an evaluation of the simulation results in conjunction with independent geological data on the tidal spectrum and the evolution of the lunar orbit.

1.7. Outline

Chapter 2 provides the theoretical embedding of the Earth's rotation, tides, tidal friction, and tidal sedimentation. In Chapter 3, the current state of art on secular changes in the Earth's rotation rate in modern times and throughout the Earth's history is discussed, with a focus on the Late Neoproterozoic ~620 Myr ago. A further point of discussion is the modeling of ocean tides in modern times and throughout the Earth's history in the context of tidal friction and angular momentum transfer between the Earth and Moon. The research approach and methodology of the study, as well as initial results for modern times, are discussed in Chapter 4. The data utilized as well as the resources employed, such as the tidal model and the analysis methods, are presented. The chapter concludes with the implementation and evaluation of the resources for simulating ocean tides with regard to tidal friction in modern times. Chapter 5 presents the final results of this study. In this chapter, the simulated ocean tides and the resulting angular momentum transfer between Earth and Moon under the conditions in modern times and under the conditions ~620 Myr ago are shown. In the context of angular momentum transfer, the investigations encompass the examination of the impact of land-water distribution on tidal dynamics. A summary follows each chapter. Chapter 6 provides a condensed summary, conclusions, and an outline of future research.

2. Theoretical embedding

The theoretical foundations of the various aspects of the present study, such as the Earth's rotation in Section 2.1, the tides in Section 2.2 with their effect on the Earth's rotation rate in Section 2.3, followed by tidal sediments as a record of the Earth's rotation rate in the Earth's history in Section 2.4, are brought together in this chapter. The interrelationship of these aspects serves as the framework for the elaboration and the methodology of the study.

2.1. Rotation of the Earth

The intrinsic rotation of the Earth fluctuates around a temporal mean motion for a variety of exogenous and endogenous causes and origins. In Section 2.1.1, a classification of the Earth's rotational fluctuations is given based on the definition of the Earth's rotation. Subsequently, the basic quantities of Earth's rotation are outlined. In Section 2.1.2, the causes of the Earth rotation fluctuations are shown by describing the behavior and properties of the individual components of the Earth and their interactions. It is also shown which components have to be taken into account for a secular increase of the length of the day. Finally, a mathematical description of the rotation of the Earth is given in Section 2.1.3.

2.1.1. Description

In general, the Earth's rotation is understood as the temporal change of a terrestrially fixed coordinate system relative to a spatially fixed coordinate system. The time-dependent rotation vector results as the time derivative of the rotation matrix between the terrestrially and spatially fixed coordinate system. *Precession* and *nutation* are the changes in orientation of the Earth's rotation vector with respect to the spatially fixed coordinate system; polar motion is the change in orientation with respect to the terrestrially fixed coordinate system. Fluctuations in the length of day are changes in the amount of the Earth rotation vector. The Earth's angular momentum vector is characterized by the fact that it is an integral variable of the Earth system directly accessible from the measurements. In contrast, the individual angular momenta and torques of the Earth's components relating to the Earth's rotational changes cannot generally be measured directly. First of all, the individual excitation processes can be investigated separately. Then, an integral calculation and modeling of the Earth's rotational changes based on the interactions and coupling mechanisms between the components can be addressed.

For many purposes, the shape and size of the Earth can be represented geometrically with a sphere for which only the radius of the sphere needs to be specified. The more accurate reference of an ellipsoid with an *equatorial bulge* and a flattening at the poles incorporates the effect of the intrinsic Earth rotation on its shape and size. Between the equatorial

radius and the polar radius the difference is 21 km and the flattening is about 1/300 where the mean radius of the Earth is 6371 km (Moritz, 2000). Furthermore, the *Earth axis* of rotation, which passes through the North and South Poles, is inclined by about 23.5° and the Moon's orbit is inclined about 5.1° to the plane of the Earth's orbit around the Sun, known as the *ecliptic*. The Sun and the Moon initially exert a noticeable gravitational force on the equatorial bulge of the Earth, resulting in a torque that tries to upright the Earth axis. Further with the Earth's moment of inertia, which tries to evade the gravitational pull perpendicularly, this results in the precession of the Earth axis around the *ecliptic pole*s opposite to the Earth's rotation, with a period of currently about 25 800 yr (Figure 2.1). The displacement of the Earth axis is only about 50″ per year, but can add up to considerable size over longer periods of time. Hence, the *Earth's lunisolar precession* was already known in ancient times (Guthmann, 2000), as evidenced by the work of the Greek astronomer *Hipparchus* (190 to 120 BC).

The *nutation* with its short-period oscillations with small amplitudes up to 15″ superimposes the Earth's lunisolar precession (Figure 2.1). It was discovered in 1748 by the third Astronomer Royal *James Bradley* (Guthmann, 2000). The largest contribution to nutation is caused by the *lunar orbital precession* or the lunar *ascending node* and *descending node* precession (Figure A.1) with a period of about 18.6 years (Guthmann, 2000). Thus, the *declination* of the lunar orbit changes constantly, because once the *inclination* of the lunar orbit is added to the *obliquity* of the ecliptic and then subtracted, when the lunar nodes have further moved by half the period.

Euler first pointed out in 1765 that the axis of rotation of the Earth could move. This movement should be reflected in fluctuations of the pole height with a period of about 10 months for an ellipsoidal rigid Earth. *Küstner* succeeded in proving this in 1888. Based on an analysis of *Chandler's 1891* latitude determination, the period of the so called *Chandler wobble* is approximately 14 months. Just one year later, *Newcomb* was able to show that together with the mobility of the water masses of the oceans, an elastic yielding of the solid body of Earth causes such an increase in the period from 10 months to 14 months. With the more accurate geodetic space observation techniques a vast range of polar motion could be determined since the beginning of the 1980s (Gross, 2007; Seitz & Schuh, 2010):

- the Chandler wobble having a period of about 432 days and a variable amplitude ranging from 0.1″ to 0.2″[a],
- a forced annual wobble having a nearly constant amplitude of about 0.1″,
- quasi-periodic variations on decadal time scales having amplitudes of about 0.03″,
- a linear trend having a rate of about 0.003″ per year and a direction towards 76° to 78°W; since about the year 2005 however, an abrupt change of movement towards east is observed.

The length of day as the period of the Earth's rotation was determined by observations of successive meridian transits of the *mean Sun*. One *mean solar day* is thus equivalent to one day. Since the Earth's rotation itself served as the basis for time measurement, fluctuations in the rotation period could only be detected with clocks whose rate remained constant for at least several days. With the atomic clock it is now possible to achieve a

[a] 0.1″ is approximately 3 m at the Earth's surface.

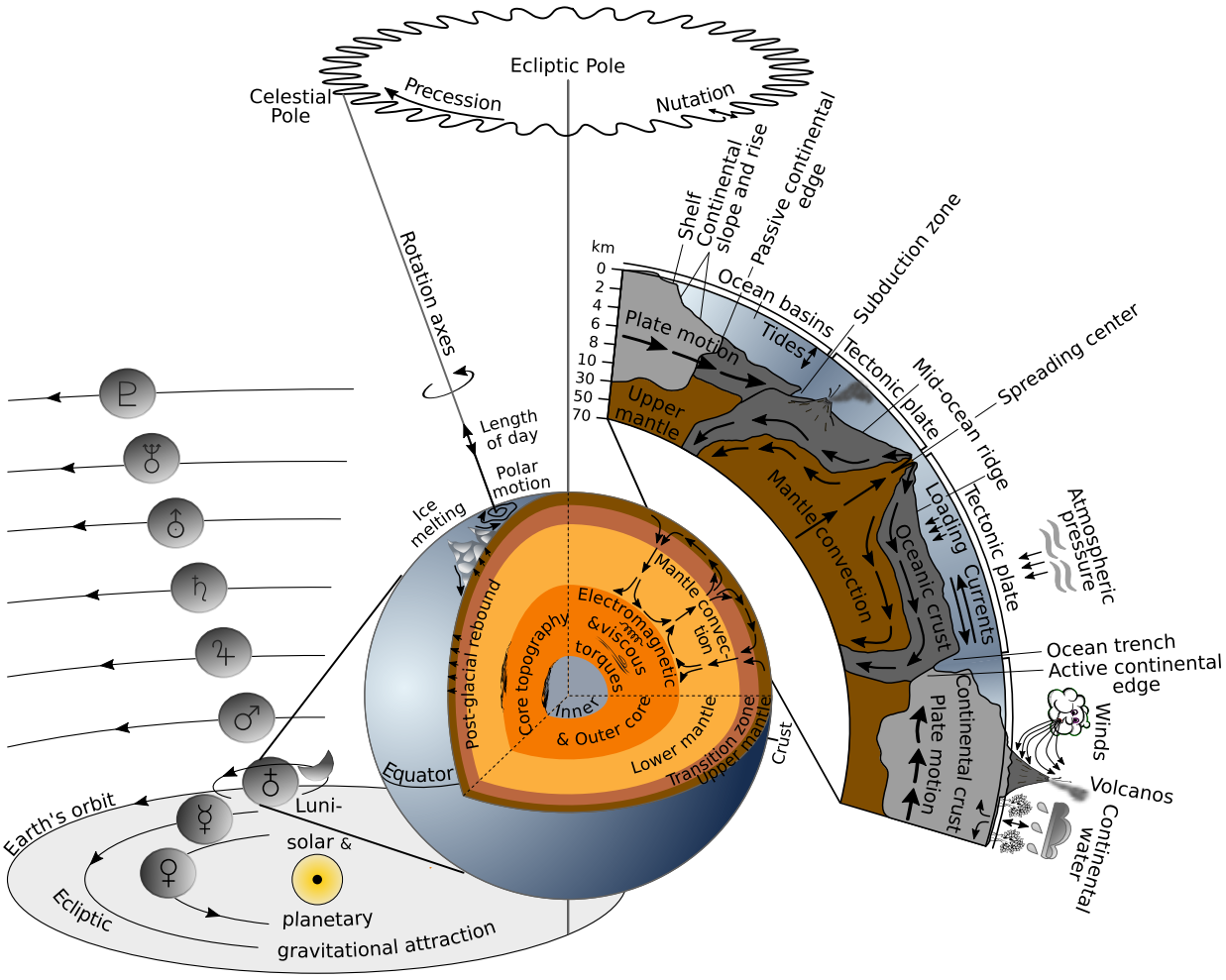

Figure 2.1.: Earth system and its components and its embedding in the planetary system as well as their influences on the Earth rotation (based on Lambeck (1980a)).

strictly uniform time consequence independent of the Earth's rotation, according to which the nominal length of mean solar day is 24 h. A broad spectrum of day length variations could be detected (Seitz & Schuh, 2010):

- a decadal oscillation with deviations of up to several milliseconds,
- a quasi-two-years oscillation with varying amplitude usually less than 0.1 ms,
- annual and semi-annual oscillations with almost the same amplitude of 0.36 ms,
- oscillations with periods of about 13 d to 28 d with amplitudes of up to 0.35 ms,
- a secular perturbation that leads to an increase, currently about 1.8 ms per century (Stephenson et al., 2016).

The Earth adapts to the new conditions by deformations, which in turn are associated with changes in the Earth's inertial tensor. The associated motions are related to the respective angular momentum of the layer (e. g. atmosphere, oceans, mantle). Thus the conservation of angular momentum requires a corresponding changes of the rotational vector, the measurement of which, however, reflects the mutual impact. Anyhow, gravity field

measurements can detect the integral effect of mass redistributions. Only some of the many sources of rotational changes could be definitely assigned (Torge, 2001).

2.1.2. Earth structure

In addition to the components of the Earth, the study of the Earth rotation encompasses their interactions and couplings. The physical environment of the Earth is first classified according to its state such as minerals (earth body, solid earth), air (atmosphere), and water (hydrosphere). This is appropriate because of the different dynamic properties.

Table 2.1 provides the ratios of masses and moments of inertia of the whole Earth, the solid Earth body, the world ocean (as the predominant part of the hydrosphere), and the atmosphere. The solid Earth body provides almost entirely the mass and the moment of inertia of the Earth and establishes mainly the rotational vector of the whole Earth. Of particular importance to Earth rotation research are the interactions between the atmosphere, oceans, and solid Earth body, and within the solid Earth body between core and mantle. An exchange of angular momentum between the system components is made possible by torques caused by

- gravitational effects on density anomalies ("gravitational torque"), e. g. due to Sun and Moon exerting a gravitational force on the equatorial bulge or on the tides,
- the pressure exerted on the topography ("pressure torque", "mountain torque"), e. g. due to atmospheric and oceanic pressure gradients at land and sea surface,
- friction at the interfaces of the system components ("friction torque"), e. g. due to wind shear stresses at land and sea surface or ocean currents close to the bottom,
- electromagnetic effects in the core/mantle area ("*Lorentz* torque").

The geodynamical components of the Earth with their changes and interactions in regard to the Earth's rotation are sketched at Figure 2.1 (Strahler & Strahler, 1999). A series of interconnected paths, along which matter and/or energy move more or less continuously, connect the individual components and their subcomponents. Among the mass cycles, the water cycle and carbon cycle are to be mentioned above all. On the whole, the Earth system can be regarded as a closed system; all of the matter and all of the processes that move materials and energy from one part of the planet to another make up the Earth system.

2.1.2.1. Earth body

The solid earth encompasses the core, mantle and crust: continents, ocean floor, rocks, sand, dust, metal, etc. The propagation behavior of seismic waves in the Earth's interior provides information about the structure of the Earth. The discontinuities in the distribution of the seismic velocities serve as a basis for a fundamental division of the earth's body into cupped areas. This shell model of the Earth is generally accepted today and is sketched in Figure 2.1 (Götze et al., 2015).

The outermost thin shell is the crust. An upper layer of felsic and a lower continuous layer of mafic or igneous rocks form the continental crust. The crust of the ocean basins consists of basalt (Strahler & Strahler, 1999). Then follows the mantle of solid mineral substances, which is partitioned into upper mantle, transition zone, and lower mantle. Of

Table 2.1.: Ratios of masses and moments of inertia of the whole Earth, the solid Earth body, the world ocean, and the atmosphere (Carlson, 2005; Strahler & Strahler, 1999)

		Solid Earth			
	Whole Earth	**Mantle**	**Core**	**World ocean**	**Atmosphere**
Mass	100 % (5.97×10^{24} kg)	68 %	32 %	$<10^{-1}$ %	$<10^{-4}$ %
Inertia	100 % (8.23×10^{37} kg m^2)	89 %	11 %	<1 %	n. s.

all other components, the mantle is the largest contributor to the Earth's total mass at 68 % and to the Earth's moment of inertia at 89 % (Table 2.1). A part of the upper mantle together with the crust forms the lithosphere, the outer part of the Earth consisting of solid rock, which "floats" in the form of more or less rigid plates on the asthenosphere, the shell of tough plastic material. The lower mantle is followed first by the outer core, which reveals a liquid state, and then by the solid inner core to the center of the Earth at a depth of about 6371 km. The core contributes 32 % to the total mass of the Earth and comprises 11 % of the total moment of inertia of the Earth (Table 2.1). The Earth's crust, mantle and core as components of the solid earth are not completely rigid bodies, but posses certain elastic and plastic properties that can be deformed by internal and external forces.

As endogenous processes, post-glacial elevations, earthquakes, volcanic eruptions, plate tectonics, and mantle convection trigger mass deformations and motions. For example, in terms of the secular decrease in day length, the decrease in the flattening of the Earth since the last ice age is consistent with measurements and counteracts the current secular increase in day length due to the tides of the earth body and the oceans by about 22 % (Morrison & Stephenson, 2001). Moreover, a dynamo process with enormous currents in the liquid outer core is indicated by the Earth's magnetic field. Secular variations of the geomagnetic field are correlated with the decadal Earth's rotation variations. The mechanism by which this correlation can be explained is the core-mantle coupling, which in the electromagnetic case is via *Lorentz* torques, in the topographical case via pressure torques (e. g. Holme, 1998).

As an exogenous interaction, the Sun, the Moon, and the planets cause deformations of the solid earth by their tide-generating potentials, the so-called earth body tides, which can also cause oscillations in the length of day. Besides, the tides are subject to friction that causes an adjustment of their equilibrium position, which is associated with a secular decreases in Earth's rotation. However, oceanic tides are currently the dominant contributor to the secular decrease (Kagan & Sündermann, 1996; Morrison & Stephenson, 2001; Munk & McDonald, 1960). In contrast to the seismic oscillations, no natural frequencies of the solid earth are in the frequency band of the essential tides (semi-diurnal, diurnal, long-periodic). Furthermore, the tides in the oceans and atmosphere change the oceanic and atmospheric loads on the solid earth. In addition, there are load deformations due to variable air, water, snow and ice loads over different time periods (Seitz & Schuh, 2010).

2.1.2.2. Atmosphere

The atmosphere is the gaseous part of the Earth: nitrogen (78 %), oxygen (21 %), argon, carbon dioxid, neon, helium, xenon, hydrogen, methane, and nitrogen oxide. Its lower boundary is given by the earth body, modified by vegetation, as well as by ocean surface. Their density is highest at sea level with $1.2041\,\mathrm{kg\,m^{-3}}$ and decreases rapidly with increasing altitude. From the ground to an altitude of about 80 km, the composition of the atmosphere is very similar in terms of the proportion of the gases involved (Strahler & Strahler, 1999).

Of the endogenous triggers of the Earth's rotational fluctuations within the earth body (Section 2.1.2.1), the atmosphere, and the hydrosphere (Section 2.1.2.3), those of the atmosphere are among the largest (Gross, 2007; Schuh et al., 2003; Seitz & Schuh, 2010). Interannual, seasonal, and interseasonal variations in the length of day are mainly caused by the motion term of the zonal winds (e. g. Eubanks, 2013; Hide & Dickey, 1991; Rosen, 1993). An impressive example on the interannual scale is the El Niño phenomenon, which is striking due to strong disturbances in atmospheric and oceanic conditions in the tropical Pacific with impacts far beyond. It recurs with varying strength every two to seven years and is called El Niño Southern Oscillation (ENSO). Irregular changes in polar motion and increases in day length of several 0.1 to 1 ms were clearly attributed to El Niño's impacts (Salstein et al., 1999). Even for durations of a few days, the zonal winds have an influence on the day length (Dickey et al., 1992; Rosen et al., 1990). Investigations of atmospheric models show that in the short-period range especially the mountain torque shows large fluctuations, matching the fluctuations of synoptic weather processes. Salstein and Rosen (1994) could prove a sudden acceleration of the atmosphere for the passage of a high pressure area over the Andes.

The atmospheric tides have a small but measurable influence on the Earth's rotation. Like the tides of the earth body and the oceans, they are on the one hand generated by lunisolar gravitation, and on the other hand thermally excited by solar radiation (Lambeck, 1980b). With regard to secular changes of the Earth's rotation, atmospheric tides can be considered negligible.

2.1.2.3. Oceanosphere

The hydrosphere is the area of water consisting of free water in gaseous, liquid, and solid state; it includes the water of the oceans and seas, lakes, rivers, glaciers, ice polar caps, the water in the lithosphere such as groundwater and soil moisture, and the water in the atmosphere such as water vapor, droplets, and ice crystals. On the one hand, the hydrosphere can be subdivided according to aggregate states into water ice (cryosphere), liquid water, and water vapor and on the other hand according to whereabouts in water of the oceans (oceanosphere), water of the continents, and atmospheric water. The remarks here are based on Götze et al. (2015) and Strahler and Strahler (1999).

The term "world ocean" describes the interconnected oceans and smaller seas. The marginal seas, such as Mediterranean seas (e. g. European Mediterranean Sea) and inland seas (e. g. Baltic Sea), connect the oceans to the surrounding land masses. After all, the marginal seas also include the numerous gulfs and open bays as well as straits, sounds, and canals. The water volume of the world ocean is $1.38 \times 10^{18}\,\mathrm{m^3}$, which is a little more than 97 % of the total free water on Earth, and its surface $3.6 \times 10^{14}\,\mathrm{m^2}$ covers 71 % of the

Earth's surface. Seawater is a solution of salts—a 30 ‰ to 40 ‰ brine—whose constituents have remained at approximately the same ratio over long geological periods. With an average seawater density of 1037 kg m^{-3}, the total mass of the ocean is 1.4×10^{21} kg, which corresponds to 0.02 % of the Earth's mass (Table 2.1). The mean depth of the Atlantic, Pacific, and Indian Ocean is about 4000 m. If, on the other hand, the world ocean including the shallow seas is considered, the mean depth is about 3730 m. The seafloor has an important relief from the coast to the deep sea and can therefore be divided into different depths and areas (Figure 2.1). A bathymetric map of the world's oceans is provided in Figure 2.2.

The land and the sea meet along the coast. In the area influenced by the tides, the coastal area is flooded by the sea at high tide and becomes dry at low tide. Today the continents have coastlines with a length of about 400 000 km. The adjacent continental shelf is constantly covered by water and is the area of shallow seas (Figures 2.1 and 2.2). Its topography is characterized by a flat slope along with slight elevations and depressions. The lower limit is generally defined at 200 m, with data varying between 130 m to 500 m. The average width of the shelf is 65 km, but it can vary considerable. The subsequent continental slope usually begins abruptly with a steep relief. It extends to water depths of around 2000 m to 4000 m and to widths between 20 km to 100 km. Plate tectonics, however, keeps the ocean basins continuously opening and closing, and the lithospheric plates moving against each other on the asthenosphere. Upwelling basaltic magma at the mid-ocean ridge axes forms new oceanic crust (Figure 2.1). On both sides of the trench system, magma spreads to the continental margins where oceanic crust is subducted into the Earth's mantle, moving the lithospheric plates against each other. At passive continental margins (Figure 2.1), where continental lithosphere meets oceanic lithosphere without the plate tectonic processes, the continental rise leads with a flattened relief from the continental slope to the deep-sea plain. The width of the continental rise can be up to 600 km. Its lower limit is generally defined at about 5000 m. At active continental margins (Figure 2.1), the transition between continental lithosphere and oceanic lithosphere coincides with plate tectonic boundaries and processes. The transition is constituted by oceanic (abyssal) trenches, which are elongated, narrow depressions in the sea floor with typical depths from 3000 m to 4000 m below the level of the surrounding seabed. With a maximum depth of 11 034 m, the Mariana Trench in the Pacific Ocean is the deepest of all trenches.

The mid-ocean ridges pass through the world ocean as broad mountain systems with typical depths of 2600 m (Figures 2.1 and 2.2). They are characterized by high seismic activity, high heat flux and active volcanism. In their central part, a longitudinal trench has sunk deeply. This is where new oceanic crust material is formed. The mid-oceanic ridges form a global continuous mountain range, the so-called Ocean Ridge, which is the longest mountain range in the world with a length of 65 000 km[b]. In contrast, the seamounts are irregularly distributed and consist of high towering, conically shaped, active or inactive individual volcanoes or chains of volcanoes. Some rise above sea level, others are hidden. Oceanic plateaus can stretched over hundreds of square kilometers. They are elevated up to 3000 m above the adjacent oceanic floor.

The oceans have a layered structure with regard to temperature and oxygen content. In

[b]NOAA. What is the longest mountain range on earth? National Ocean Service website, http://oceanservice.noaa.gov/facts/midoceanridge.html, 09/03/25.

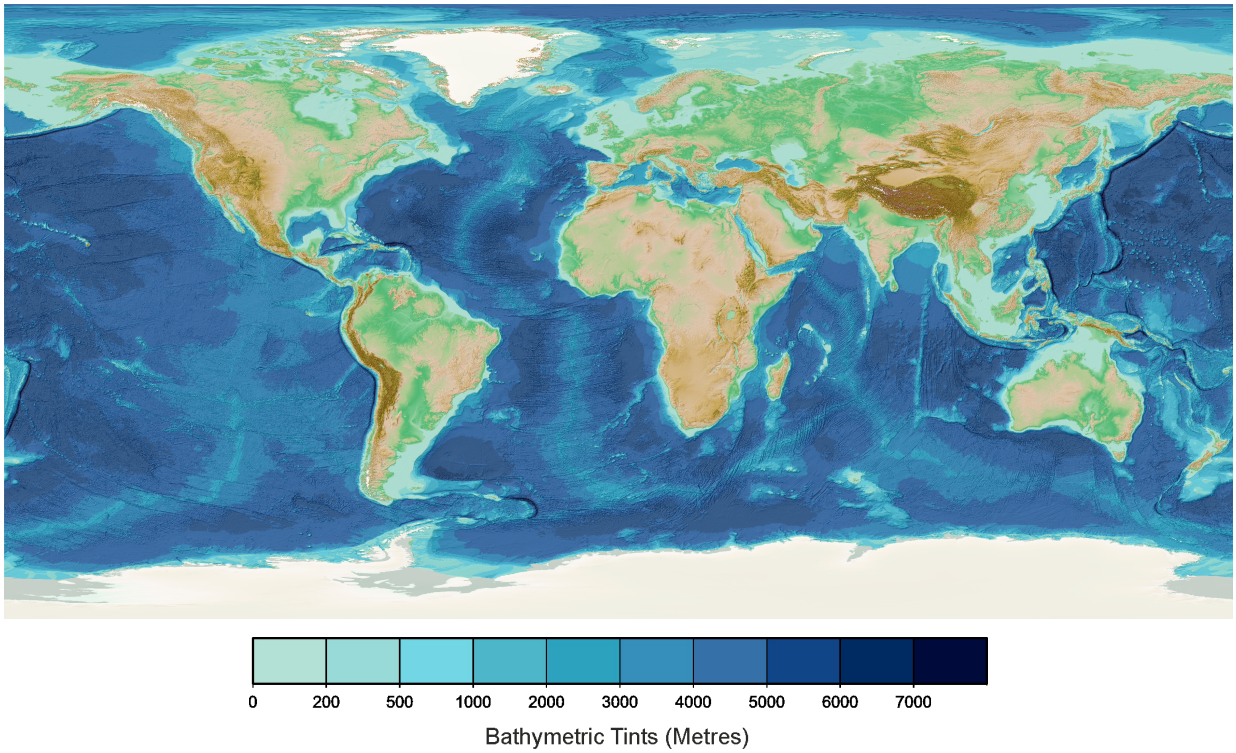

Figure 2.2.: Bathymetric chart of the world's oceans[c].

terms of temperature, the ocean water has a three-layer vertical structure. At the top, a warm layer of water is present in the mid-latitudes during the summer and throughout the year in the low latitudes; in the equatorial belt, the temperature is 20 °C to 25 °C. The surface water heated by the Sun mixes with the water below to a depth of about 500 m via the wave motion and its temperature varies mainly with latitude. The temperature rapidly drops below the warm layer and mark a second layer, the so-called thermocline, below which is the third layer of very cold water whose temperature can drop to 0 °C to 5 °C with increasing depth. In Arctic and Antarctic regions there is a uniform layer of cold water instead of a three-layer structure.

Wind, changes in atmospheric pressure at sea level, heat exchange with the atmosphere, precipitation and evaporation, and river runoff together excite a three-dimensional circulation in the oceans. In addition to this general circulation, the motion field also contains the tides. Furthermore, changes in the distribution of the oceanic water masses must manifest themselves in a variable bottom pressure field, which in turn is linked to deformations of the earth body and variations in the oceanic gravitational field. This is referred to as a secondary effect of the superimposed self-attraction and loading (SAL) of the water masses. In addition, the tides of the boundary surface between the earth body and the ocean modified by the SAL effect can also alter the resonance conditions of the ocean basins and thus the ocean dynamics. Both numerical and analytical studies of the motion field of the global ocean show that many of the natural frequencies of the world ocean are also

[c]Imagery reproduced from the GEBCO_2020 Grid, GEBCO Compilation Group (2020) GEBCO 2020 Grid (doi:10.5285/a29c5465-b138-234d-e053-6c86abc040b9).

located in the frequency band of the semi-diurnal and diurnal tides (e. g. Gaviño, 1984; M. Müller, 2009; Platzman et al., 1981). The thermal expansions of the water and the non-linear interactions between circulation and tides are superimposed on this (Gross, 2007; Schuh et al., 2003; Seitz & Schuh, 2010).

Measurements of the physical state of the ocean are limited in both large-scale and depth due to the associated costs. By means of data collected by satellites, state variables at the ocean surface have been able to be determined almost completely with increasing accuracy for several decades. The altimeter missions, TOPEX/Poseidon and its successor JASON are of particular interest for determining the time-varying sea surface topography with respect to the Earth's rotation. At depths greater than a few centimeter, state variables can so far only be derived from data collected by satellites using simplified assumptions. With the advent of high performance computing, the physical state and dynamic of the ocean can be simulated and increasingly accessed based on the hydrodynamic numerical method, especially on a large scale and to depth.

Analogous to the atmosphere, the spectrum of Earth rotational fluctuations due to the circulation as endogenous processes is largely continuous. Particular periods stand out on the daily and seasonal time scales as well as in the interannual range, such as near the ENSO.

According to the tide-generating potential, oceanic tides, as exogenous processes, influence the Earth's rotation and gravity field on timescales ranging from a few hours to decades to millennia and even on a secular scale (Gross, 2007; Schuh et al., 2003; Seitz & Schuh, 2010). In addition, oceanic tides are currently the dominant contributor to the secular increase in the length of the day. The tides of the Earth's body alone are currently responsible for only a small fraction of the increase (Kagan & Sündermann, 1996; Morrison & Stephenson, 2001; Munk & McDonald, 1960). The effect of oceanic loading on the continental regions of the solid Earth is of great interest for geodesy and station determination. However, it has a relatively small influence on Earth's rotation. Especially near the coast, tidal oceanic loads cause deformations of the Earth's surface of up to several centimeters. These deformations result in measurable shifts of the station coordinates.

2.1.3. Physical principles

Three equivalent quantities represent the secular deceleration of the Earth's rotation: the angular acceleration of the Earth's rotation or the change in the length of the day with time, the torque exerted on the Earth's rotation axis, and the change in the Earth's rotational energy with time (Munk & McDonald, 1960). The relationship between these quantities is described in the mechanics of rotating bodies. Furthermore, the equations of motion for the Earth's rotation follow from the conservation of angular momentum.

2.1.3.1. Angular momentum of the Earth's rotation

The Earth's rotation with its fluctuations can be described mathematically by the equations of motion for the rotation of a body by the law of conversation of angular momentum

$$\frac{\mathrm{d}\vec{\boldsymbol{L}}}{\mathrm{d}t} = \vec{\boldsymbol{M}} \tag{2.1}$$

and also known as Euler's dynamical equations. According to this, the change in the total angular momentum $\vec{\boldsymbol{L}}$ of a rotating body in the inertial system is equal to the sum of the externally applied torques $\vec{\boldsymbol{M}}$. The transformation to the body-fixed frame rotating at the angular velocity $\vec{\boldsymbol{\omega}}$ yields

$$\frac{\mathrm{d}\vec{\boldsymbol{L}}}{\mathrm{d}t} + \vec{\boldsymbol{\omega}} \times \vec{\boldsymbol{L}} = \vec{\boldsymbol{M}}. \tag{2.2}$$

For a deformable body, the total angular momentum

$$\vec{\boldsymbol{L}}(t) = \boldsymbol{\Theta}(t)\vec{\boldsymbol{\omega}}(t) + \vec{\boldsymbol{L}}^{rel}(t) \tag{2.3}$$

along with

$$\vec{\boldsymbol{L}}^{rot}(t) = \boldsymbol{\Theta}(t)\vec{\boldsymbol{\omega}}(t)$$

is composed of two parts:

$$\vec{\boldsymbol{L}}(t) = \vec{\boldsymbol{L}}^{rot}(t) + \vec{\boldsymbol{L}}^{rel}(t).$$

The first term with the time-dependent inertia tensor $\boldsymbol{\Theta}(t)$ representing the mass distribution corresponds to the rotational angular momentum $\vec{\boldsymbol{L}}^{rot}(t)$. The relative angular momentum $\vec{\boldsymbol{L}}^{rel}(t)$ derives from the non-rigidity of the body, i. e. from the motion relative to the body-fixed reference system.

Immediately, the insertion of Equation (2.3) in Equation (2.2) leads to the *Liouville* dynamic differential equations (e. g. Munk & McDonald, 1960)

$$\frac{\mathrm{d}}{\mathrm{d}t}[\boldsymbol{\Theta}(t) \cdot \vec{\boldsymbol{\omega}}(t) + \vec{\boldsymbol{L}}^{rel}(t)] + \vec{\boldsymbol{\omega}}(t) \times [\boldsymbol{\Theta}(t) \cdot \vec{\boldsymbol{\omega}}(t) + \vec{\boldsymbol{L}}^{rel}(t)] = \vec{\boldsymbol{M}}(t), \tag{2.4}$$

which describe the change of the rotation vector $\vec{\boldsymbol{\omega}}(t)$ of a terrestrial fixed coordinate system relative to this system. In the case of a deformable body, the rotation vector $\vec{\boldsymbol{\omega}}$ is not unique and is understood as the rotation of a reference system which is unambiguously related to the deformable body.

In a right-handed Cartesian coordinate system, which is defined by the equatorial axes x, y and the polar axis z of the body, the axis of rotation coincides with the polar axis in the case of uniform rotation and rotates constantly. If the coordinate axes coincide with the principal inertia axes, the inertia tensor of the rotating body can be represented in diagonal form $\boldsymbol{\Theta}_0 = \mathrm{diag}(A, B, C)$ with the principal moments of inertia A, B, C, where A and B refer to the equatorial axes and C refers to the polar axis of rotation. The Earth is nearly axially symmetric because of $A < B < C$ and $(B - A)/A = 2.2 \times 10^{-5}$ (Gross, 2007). The inertia tensor for uniform rotation $\boldsymbol{\Theta}_0 = \mathrm{diag}(A', A', C)$ is obtained with $A' = (A + B)/2$.

Thus the uniform rotation of the Earth can be expressed by

$$\boldsymbol{\Theta}_0 = \begin{pmatrix} A' & 0 & 0 \\ 0 & A' & 0 \\ 0 & 0 & C \end{pmatrix}, \qquad \vec{\boldsymbol{\omega}}_0 = \begin{pmatrix} 0 \\ 0 \\ \Omega_{\mathfrak{F}} \end{pmatrix}, \qquad \vec{\boldsymbol{L}}_0^{rel} = 0,$$

with $\Omega_{\mathfrak{F}} = 7.292 \times 10^{-5}\,\mathrm{rad\,s^{-1}}$ (Gross, 2007). Apart from this, the Earth rotates around an axis close to the mean position of the greatest principal axis, and the deviations from the uniform rotation are small (Lambeck, 1980b). For the uniform rotation of the Earth, Euler was able to anticipate the fluctuations of the pole height by means of Equation (2.2) (Section 2.1.1, p. 12). This occurs for a rigid Earth with an angular velocity of ${}^{(C-A)\Omega_{\mathfrak{F}}}/_{A}$, corresponding to a period of about 305 days.

An inertia tensor $\boldsymbol{\Theta}(t) = \boldsymbol{\Theta}_0 + \Delta\boldsymbol{\Theta}(t)$ caused by mass displacement $\Delta\boldsymbol{\Theta}(t)$ or any relative motion $\Delta\vec{\boldsymbol{L}}^{rel}(t)$ with $\vec{\boldsymbol{L}}^{rel}(t) = \vec{\boldsymbol{L}}_0^{rel} + \Delta\vec{\boldsymbol{L}}^{rel}(t)$, e. g. related to geophysical processes, causes the uniform rotation with $\vec{\boldsymbol{\omega}}_0$ to change into the rotation vector

$$\vec{\boldsymbol{\omega}}(t) = \vec{\boldsymbol{\omega}}_0 + \Delta\vec{\boldsymbol{\omega}}(t) \quad \text{with} \quad \Delta\vec{\boldsymbol{\omega}}(t) = \Omega_{\mathfrak{F}} \cdot \begin{pmatrix} m_x(t) \\ m_y(t) \\ m_z(t) \end{pmatrix}$$

according to the conservation of angular momentum Equation (2.2). Whereby the dimensionless quantities $m_x(t)$ and $m_y(t)$ mean the pole coordinates of the rotation and $m_z(t)$ the variation in rotation speed. For small perturbations of the forms

$$|\Delta\boldsymbol{\Theta}_{\imath\jmath}| \ll C, \quad |\Delta\vec{\boldsymbol{L}}_{\imath}^{rel}| \ll C\Omega_{\mathfrak{F}}, \quad |m_{\imath}| \ll 1 \quad \text{with} \quad \imath, \jmath = x, y, z,$$

the equatorial and axial components of the Liouville Equation (2.4) can be linearized in first perturbation order as follows

$$\begin{aligned} m_y + \frac{1}{\omega_{cw}} \frac{\partial m_x}{\partial t} &= \chi_y - \frac{1}{\Omega_{\mathfrak{F}}} \frac{\partial \chi_x}{\partial t} \\ m_x - \frac{1}{\omega_{cw}} \frac{\partial m_y}{\partial t} &= \chi_x + \frac{1}{\Omega_{\mathfrak{F}}} \frac{\partial \chi_y}{\partial t} \\ \frac{\partial m_z}{\partial t} &= \frac{\partial \chi_z}{\partial t} \end{aligned}$$

and the equatorial components are independent from the axial component. The ω_{cw} is the angular velocity of the Chandler wobble and the $\chi_{\imath}$ are known as excitation functions also referred to as effective angular momentum functions, which may be expressed in general terms by

$$\begin{aligned} \chi_x(t) &= \chi_x(\Delta\Theta_{xz}(t), \Delta L_x^{rel}(t), M_x(t)), \\ \chi_y(t) &= \chi_y(\Delta\Theta_{yz}(t), \Delta L_y^{rel}(t), M_y(t)), \\ \chi_z(t) &= \chi_z(\Delta\Theta_{zz}(t), \Delta L_z^{rel}(t), M_z(t)). \end{aligned}$$

Thus the mass redistribution (matter term), the relative motion of matter (motion term),

and the external torques are entered into the excitation functions. In Gross (2007) explicit specifications of excitation functions for miscellaneous assumptions about the Earth structure can be found. The m_i are in the order of 10^{-6} or less (Lambeck, 1980b).

An external torque $\vec{\boldsymbol{M}}$

$$\vec{\boldsymbol{M}} = \int_{V_\oplus} \rho_\oplus \vec{\boldsymbol{r}} \times \vec{\boldsymbol{\nabla}} \Phi \, \mathrm{d}V_\oplus \,, \tag{2.5}$$

which does not vanish integrated over the Earth's volume $V_\oplus$, causes the Earth's rotation to change according to the Euler's equations (Equation (2.1)). $\rho_\oplus$ is the Earth's density, $\vec{\boldsymbol{r}}$ is the geocentric position vector, and Φ is the potential of the external force. The polar component

$$M_z = \int_{V_\oplus} \rho_\oplus \frac{\partial \Phi}{\partial \lambda} \, \mathrm{d}V_\oplus \tag{2.6}$$

acts in the direction of the Earth's rotational axis, in this case in terms of the geocentric coordinates r, φ, λ, with the latitude being φ and the longitude being λ. With the polar rotational angular momentum (Equation (2.3))

$$L^{rot}_\oplus = C(\Omega_\oplus)\, \Omega_\oplus \tag{2.7}$$

and its change over time with an time-invariant polar moment of inertia C, the polar component of the external torque becomes

$$M_z = C \, \frac{\mathrm{d}\Omega_\oplus}{\mathrm{d}t} \tag{2.8}$$

in an inertial system using Equation (2.1).The Earth's shape approaches hydrostatic equilibrium on long time scales. Its inertia tensor depends on a spherical component and a flattened component that is proportional to the square of the mean angular velocity of the Earth. With decreasing angular velocity, the flattening and the radius of the Earth decrease. The small dependence of the moment of inertia on the angular velocity can be accounted for by $d[C(\Omega_\oplus)\Omega_\oplus]/dt = SC(\Omega_\oplus)d\Omega_\oplus/dt$ with the factor $S = 1.005$ (J. G. Williams & Boggs, 2016). Equivalent to the torque M_z in the direction of the Earth's rotational axis is the Earth's rotational energy rate

$$\frac{\mathrm{d}E_{rot}}{\mathrm{d}t} = \Omega_\oplus \, M_z = C \, \Omega_\oplus \frac{\mathrm{d}\Omega_\oplus}{\mathrm{d}t}, \tag{2.9}$$

which relates the Earth's angular acceleration to the transfer of angular momentum.

Another method to determine the acceleration of the Earth's rotation provides the axial component of the angular momentum in the Earth-Moon system.

2.1.3.2. Angular momentum of the Earth-Moon system

The orbits of the celestial bodies are determined by *Newton's* law; they move as if their entire mass were concentrated as a point mass at their center of gravity. It is a multi-body

problem to determine the orbits of the celestial bodies. In addition to the effect of the Sun, the planets are subject to the effect of every other planet. The multi-body problem can be separated into a two-body problem, in which only the mutual attraction between the Sun and the planets is considered, due to the relatively small mass of the planets compared to the mass of the Sun. An elliptical orbit of the planet around the Sun is the solution to the two-body problem. The position of the Sun is one focus of the ellipse. When the gravitational attraction of the planets is added as a perturbation to the two-body problem, the elliptical orbits vary periodically in size, shape, and spatial position, and secularly in the remaining orbital elements. To a good approximation, the orbits can be considered elliptical. The orbital elements are described in Appendix A.1.

The Earth with its satellite the Moon, together with the Sun, form a three-body problem. When separated into two-body problems, the Moon and the Earth describe similar ellipses around the barycenter (center of gravity of the Earth and the Moon). The barycenter itself moves on an ellipse around the Sun. Because the barycenter is within the Earth, the Earth's center oscillates only slightly around the ecliptic plane (Figure A.1). A geocentric lunar orbit and a barycentric solar orbit appear elliptical relative to the Earth. The orbits are superimposed by periodic perturbations in their size, shape, and position, and secular perturbations in the remaining orbital elements, due to the residual mutual gravitational perturbations of the two-body problems. In particular, the Moon is subject to perturbations. Thus, the exact motion of the Moon becomes a complex problem, some parts of which are not yet fully understood.

The angular momentum associated with the lunar orbit around their common center of mass is given by (e. g. Lambeck, 1980b)

$$L_{☾} = \frac{m_{♁} m_{☾}}{m_{♁} + m_{☾}} a_{☾}^2 \left(1 - e_{☾}^2\right)^{1/2} n_{☾}$$

with the masses $m_{♁}$ and $m_{☾}$ of the Earth and the Moon, the semi-major axis and eccentricity $a_{☾}$ and $e_{☾}$ of the lunar orbit, and the mean motion $n_{☾}$ of the Moon (Figure A.1). Since the distance of the Earth and the Moon from the barycenter is approximately $^1/_{81}$ and $^{80}/_{81}$ of the distance between the Earth and the Moon, the orbit of the Earth around their center of mass can be neglected. Unlike the main rotational angular momentum of the Earth $L_{♁}^{rot}$ (Equation (2.7)) the Moon's, which is smaller by a factor of 10^{-5}, is negligible.

In the case of time-invariant quantities C, $m_{♁}$, and $m_{☾}$, the conservation of angular momentum in the Earth-Moon system implies that

$$\frac{m_{♁} m_{☾}}{m_{♁} + m_{☾}} \frac{\mathrm{d}}{\mathrm{d}t} \left[a_{☾}^2 \left(1 - e_{☾}^2\right)^{1/2} n_{☾} \cos i_{☾} \right] + C \frac{\mathrm{d}\Omega_{♁}}{\mathrm{d}t} = 0 \tag{2.10}$$

and

$$L_{☾} \cos i_{☾} + C\,\Omega_{♁} = \text{constant}, \tag{2.11}$$

where $i_{☾}$ is the inclination of the lunar orbit at the Earth's equator and $L_{☾} \cos i_{☾}$ the orbital angular momentum of the Moon parallel to the Earth's rotational axis. The inclination of the Earth on the ecliptic is 23.439° and the inclination of the lunar orbit averages 5.145°. In addition, the lunar orbital precession has a period of about 18.6 yr. This means, that the orbital angular momentum of the Moon, as a vector perpendicular to the lunar orbital

plane, varies between 18.294° and 28.585° relative to the Earth's axis of rotation, with an overall average of 23.439°. In the long term, a cosine projection of 23.439° will be the average contribution of angular momentum transfer from Earth to the lunar orbit.

As a result of the conservation of angular momentum in the Earth-Moon system (Equation (2.10)), the Earth's rotational velocity $\Omega_{♁}$ (length of *mean sidereal day*), the Moon's orbital velocity $n_{☾}$ (length of *sidereal month*), and the Moon's semi-major axis $a_{☾}$, eccentricity $e_{☾}$, and inclination $i_{☾}$ are functionally and quantitatively related. When the Earth's rotational velocity $\Omega_{♁}$ decreases, the transfer of the Earth's rotational angular momentum $L_{♁}^{rot}$ to the Moon's orbital angular momentum $L_{☾}$ causes the Moon to move to a higher elliptical orbit with a longer period. Using Kepler's 3rd law, these changes can be derived from the Lagrangian equations of motion. The rate of the Earth's rotational velocity $^{\mathrm{d}\Omega_{♁}}/_{\mathrm{d}t}$ follows from the transfer between the Earth's rotational angular momentum $L_{♁}^{rot}$ and the lunar orbital angular momentum $L_{☾}$ (Equations (2.6), (2.8) and (2.9)).

2.2. Tides

In order to establish a functional relationship between the tidal mass displacements and the astronomical tidal force, as well as the Earth's rotation, the global material response of the Earth's solid body and the oceans must be known. In addition, the modification of the matter response due to the variable spatial distribution, motions, and interactions of the subsystems must be known. First, Section 2.2.1 outlines the origin of tides and Section 2.2.2 defines the astronomical tidal force. Qualitative and quantitative descriptions of the fundamental quantities of the astronomical tidal force are also given. Section 2.2.3 presents the functional relationship between the solid Earth body tides and the astronomical tidal force. Ocean tides with their energy and angular momentum balance for the study of tidal friction follow in Section 2.2.4.

2.2.1. Description

On Earth the gravitational acceleration by the Sun, Moon, and planets is different at different points. According to *Newton's* law, a closed orbital motion of celestial bodies is a motion around their center of gravity. The total mass of each celestial bodies can be considered as being concentrated at its center of mass. The extension of the celestial bodies does not affect the orbital motion, which is associated with a centrifugal acceleration. All mass elements of the attracted, extended Earth move on their own orbits shifted parallel to the orbit of the Earth's center of gravity (revolution without rotation). Thus, the centrifugal acceleration due to the orbital motion is the same at all points in the attracted, extended Earth and acts in a location-independent manner. These acceleration differences are called tidal accelerations and cause deformations of the ocean, the atmosphere, and the earth body—the tides. With regard to equilibrium, gravitation and centrifugal acceleration of the orbital motion must cancel each other out in the center of gravity of the attracted body. Since the centrifugal acceleration from the Earth's rotation on its own axis is already included in the gravity acceleration, it does not contribute to the tidal accelerations. The superposition of the daily rotation of the Earth on its own axis and the motion of the Moon,

Sun, and planets relative to the Earth brings with it secular and periodic parts of the tides. (e. g. Guthmann, 2000).

Determining the orbits of celestial bodies is a multi-body problem. In addition to the gravitational attraction exerted by the Sun, planets are subject to gravitational forces from all other planets. The calculation of multi-body systems through mathematical means is a complex undertaking. Due to the relatively low planetary mass in comparison to the Sun, the problem can be separated into two-body problems, wherein only the mutual gravitational attraction between Sun and planet is taken into account. The two-body problems with respect to the Sun yield elliptical planetary orbits, with the Sun at one of the foci. When the planetary attractions are incorporated into the problem as a perturbation, the elliptical orbits undergo periodic variations in size, shape and spatial orientation, while the other orbital elements exhibit secular changes (Figure A.1). In essence, the orbits can be considered approximately elliptical. (e. g. Guthmann, 2000).

The Earth in conjunction with its satellite Moon and the Sun constitute a three-body problem. Following the decomposition of this system into two-body problems, the Earth and Moon exhibit analogues ellipses around the common center of gravity, situated within the Earth. This center also moves on an ellipse around the Sun. In this configuration, the Moon's orbit around the Earth und the Sun's orbit around the common center of gravity of Earth and Moon appear as ellipses relative to the Earth. The remaining mutual gravitational disturbances of the two-body problems result in periodic disturbances in size, shape, and spatial orientation, as well as secular disturbances in the other orbital elements, which are superimposed on the orbits. Notably, the Moon is subject to these disturbances, which complicates the precise determination of its orbital motion.

On Earth, the Moon and Sun trigger the largest tidal effects, followed by Venus. For an assessment, the maximum tidal accelerations on the surface of the Earth are due to the Moon $1.37 \times 10^{-6}\,\mathrm{m\,s^{-2}}$, due to the Sun $0.50 \times 10^{-6}\,\mathrm{m\,s^{-2}}$, and due to the Venus $5.88 \times 10^{-12}\,\mathrm{m\,s^{-2}}$ (Wenzel, 1997). Through the deformable earth body, the loading and self-attraction of the tides again cause mass shifts—the secondary tides.

2.2.2. Astronomical tidal force

The widely accepted and utilized approach to calculate the astronomical tidal force on Earth is to separate the multi-body system, consisting of the Sun, Earth, Moon, and planets, into two-body systems, namely Sun-Earth, Moon-Earth, and planet-Earth. The effects of the Moon and Sun are additive; the effects of the other planets can be neglected in this context. Since the gravitational force and the centrifugal force constitute a conservative force field, the resulting field can be expressed as a potential.

A coordinate system whose origin O moves with the center of gravity of the Earth and which does not execute a rotation is considered. In the two-body system of the Earth and a celestial body (e. g. Moon or Sun), d_o is the distance of the celestial body from the origin O, d is the distance of the celestial body from any point P on the extended Earth, m_{cb} is the mass of the celestial body, and G the gravitational constant. The gravitational acceleration

of the celestial body on any point P of the extended Earth

$$\vec{\boldsymbol{a}}_g(P) = \frac{Gm_{cb}}{d^2}\frac{\vec{\boldsymbol{d}}}{d} \tag{2.12}$$

acts location-dependently. Its integration over the volume of the Earth yields the acceleration on the Earth as a point mass at the origin O

$$\vec{\boldsymbol{a}}_g(O) = \frac{Gm_{cb}}{d_o^2}\frac{\vec{\boldsymbol{d}}_o}{d_o}. \tag{2.13}$$

Pursuant to the equilibrium condition, the orbital acceleration

$$\vec{\boldsymbol{a}}_c(O) = -\vec{\boldsymbol{a}}_g(O) \tag{2.14}$$

is balanced by the gravitational acceleration $\vec{\boldsymbol{a}}_g$ at the origin. Moreover, all points P of the extended Earth experience the same orbital acceleration, acting parallel to the connecting line d_o and away from the celestial body:

$$\vec{\boldsymbol{a}}_c(P) = \vec{\boldsymbol{a}}_c(O). \tag{2.15}$$

The tidal acceleration

$$\vec{\boldsymbol{a}}_t(P) = \vec{\boldsymbol{a}}_g(P) + \vec{\boldsymbol{a}}_c(P) = \vec{\boldsymbol{a}}_g(P) - \vec{\boldsymbol{a}}_g(0) \tag{2.16}$$

as resultant of gravitational acceleration and orbital acceleration $\vec{\boldsymbol{a}}_g(P) + \vec{\boldsymbol{a}}_c(P)$ or as differential gravitational acceleration $\vec{\boldsymbol{a}}_g(P) - \vec{\boldsymbol{a}}_g(0)$, vanishes at the origin O and is different from zero everywhere else on the extended Earth (Figure 2.3). At the points A and B on the Earth's surface closest to and furthest from the celestial body, tidal acceleration $\vec{\boldsymbol{a}}_t$ is at a maximum. Due to the Earth's rotation on its axis within 24 h, the points A and B experience maximum und minimum tidal acceleration $\vec{\boldsymbol{a}}_t$ twice a day, respectively the points A and B pass through 2 tides per day in this way (semi-diurnal periodicity).

The transition from the tidal acceleration $\vec{\boldsymbol{a}}_t$ to the astronomical tidal potential Φ^t is given by

$$\vec{\boldsymbol{a}}_t = \vec{\boldsymbol{\nabla}}\Phi^t = \vec{\boldsymbol{\nabla}}\left(\Phi^g + \Phi^c\right). \tag{2.17}$$

Equation (2.12) yields for the gravitational potential

$$\Phi^g = \frac{Gm_{cb}}{d}. \tag{2.18}$$

By employing the law of cosines to the distance d

$$d = \left(r^2 + d_o^2 - 2rd_o\cos\vartheta\right)^{1/2}$$

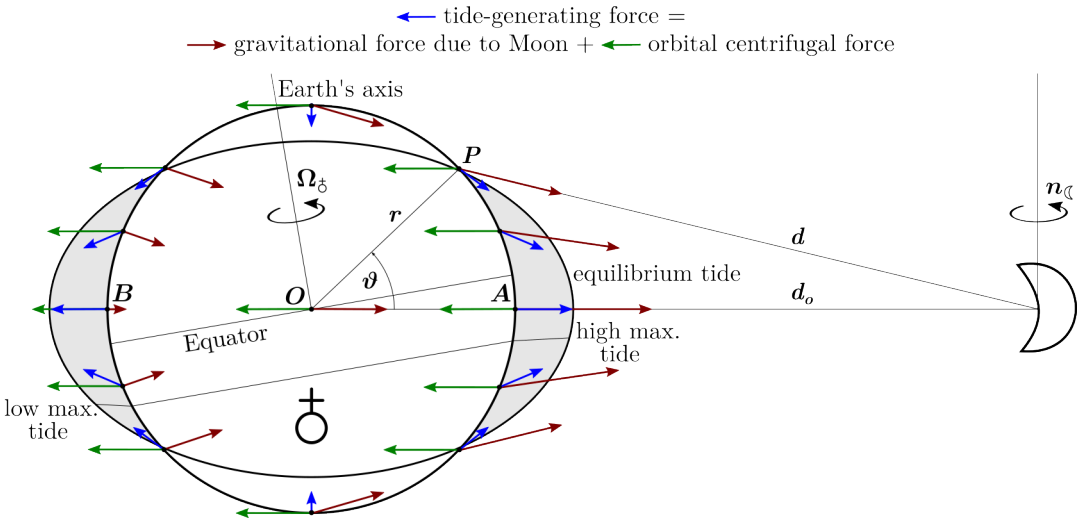

Figure 2.3.: Astronomical tidal force of the Moon on the Earth. Earth and Moon orbit at angular velocity $n_\leftmoon$ on ellipses around their common center of gravity, which lies within the Earth. The superpostion of the gravitational force of the Moon with the orbital centrifugal force gives rise to the astronomical tidal force on the Earth. As a whole, the two forces balance out, and the Earth remains in equilibrium in its orbital motion. An elastic and frictionless Earth could react instantaneously to the astronomical tidal force and form an equilibrium tide in the form of a rotational ellipsoid with the major semi-axis directed toward the Moon. At the points nearest and farthest from the Moon, the astronomical tidal force is greatest. Since the Earth rotates on its own axis with the angular velocity $\Omega_\oplus$, the points pass through the regions with the greatest force twice a day. The figure is schematic not to scale in longitudinal section.

of any point $P(r, \vartheta)$ on the extended Earth with the distance r to the geocentric origin and the zenith distance ϑ from the celestial body, then the reciprocal of the distance

$$\frac{1}{d} = \frac{1}{d_o}\left(1 - 2\frac{r}{d_o}\cos\vartheta + \left(\frac{r}{d_o}\right)^2\right)^{-1/2}$$

is the generating function for the Legendre polynomials (zonal harmonics):

$$\frac{1}{d} = \frac{1}{d_o}\sum_{l=0}^{\infty}\left(\frac{r}{d_o}\right)^l P_l(\cos\vartheta). \tag{2.19}$$

The homogeneous field of the orbital acceleration $\vec{\boldsymbol{a}}_c$ (Equation (2.15)) is equivalent to the potential

$$\Phi^c = -\frac{Gm_{cb}}{d_o^2} r\cos\vartheta \tag{2.20}$$

obtained by multiplying the magnitude of orbital acceleration $|\vec{\boldsymbol{a}}_c| = {}^{Gm_{cb}}/_{d_o^2}$ (Equations (2.13) to (2.15)) by $r\cos\vartheta$. With Equations (2.17), (2.18) and (2.20) the astronomical tidal potential gets

$$\Phi^t = Gm_{cb}\left(\frac{1}{d} - \frac{1}{d_o} - \frac{r\cos\vartheta}{d_o^2}\right). \tag{2.21}$$

The integration constant $^{Gm_{cb}}/_{d_o}$ is subtracted, thus ensuring that the astronomical tidal potential $\Phi^t(O) = 0$ at the Earth's center of gravity is set to zero. This means that only the forces acting relative to the Earth's motion are included in the astronomical tidal potential. Inserting Equation (2.19) into Equation (2.21) yields for the tidal potential

$$\Phi^t = \frac{Gm_{cb}r^2}{d_o^3} \sum_{l=2}^{\infty} \left(\frac{r}{d_o}\right)^{l-2} P_l(\cos\vartheta) \tag{2.22}$$

of the celestial body, since the terms of degree zero $P_0(\cos\vartheta) = 1$ and one $P_1(\cos\vartheta) = \cos\vartheta$ cancel.

The zenith distance is related by the spherical cosine theorem

$$\cos\vartheta = \sin\varphi\sin\delta + \cos\varphi\cos\delta\cos\tau \tag{2.23}$$

to the geocentric coordinates φ and λ (geographic latitude and longitude) of the point P and to the coordinates declination δ and *hour angle* τ (Figure A.1) of the celestial body in the fixed equatorial system. Due to the Earth's rotation the hour angle τ varies by about 2π per 24 h. Along with Equation (2.23) as well as the addition theorem for Legendre polynomials and the fully normalized associated Legendre functions P_l^m of 1st kind of degree l and order m, Equation (2.22) yields the spherical function expansion of the tidal potential

$$\Phi^t = \frac{Gm_{cb}r^2}{d_o^3} \sum_{l=2}^{\infty} \left(\frac{r}{d_o}\right)^{l-2} \sum_{m=-l}^{l} \frac{(l-|m|)!}{(l+|m|)!} P_l^m(\sin\delta) P_l^m(\sin\varphi)\cos(m\tau) \tag{2.24}$$

of the celestial body. The tidal potential of Moon and Sun is calculated from a linear superposition of the potentials caused by each of the two bodies. The series expansion converges rapidly as the relation $^{r}/_{d_o}$ of about 1.6×10^{-2} for the Moon and about 4×10^{-5} for the Sun is obtained for the Earth's surface.

The largest contribution of about 98 % to the lunisolar tidal potential on Earth comes from the 2nd degree potential

$$\Phi_{l=2}^t = \left(\frac{r}{R}\right)^2 D_{cb} \left(\frac{c}{d_o}\right)^3 \begin{cases} & \left(\frac{1}{3} - \sin^2(\varphi)\right)\left(1 - 3\sin^2(\delta)\right) \\ + & \sin(2\varphi)\sin(2\delta)\cos(\tau) \\ + & \cos^2(\varphi)\cos^2(\delta)\cos(2\tau), \end{cases} \tag{2.25}$$

where D_{cb} is the tidal constant of the Moon or Sun and is given by

$$D_{cb} = \frac{3}{4}\frac{Gm_{cb}R^2}{c^3}. \tag{2.26}$$

R is the mean radius of the Earth and c the mean distance of the Moon or Sun. It is $D_{☾} = 2.628\,\mathrm{m^2\,s^{-2}}$ for the Moon and $D_{☉} = 0.460 D_{☾}$ for the Sun (Torge, 2001). Hence, the tidal force on Earth by the Sun amounts to 46 % of that by the Moon. Due to the flattening of the Earth, the Earth's radius varies only by $^1/_{300}$ (Moritz, 2000); thus, except for fractions of 1 %, the tidal accelerations for the radii at the equator and the mean radius of the Earth are the same (Bartels, 1957).

The first summand ($m = 0$) of Equation (2.25) represents the zonal component, which exhibits a maximum at the poles and a zero value at the equator. The second summand ($|m| = 1$) represents the tesseral component, which has a maximum at latitude $\pm 45°$ and vanishes at the equator and at the poles. The third summand ($|m| = 2$) represents the sectoral component, which has a maximum at the equator and vanishes at the poles.

Distance d_o, declination δ, and hour angle τ are non-linear quantities of time. Thus also the amplitude of the summands vary with time. In general, the astronomical tidal potential can be classified in tidal bands by the dependence of the summands on the hour angle τ respectively by the order $|m|$ as follows:

- $|m| = 0$: constant and long-periodic with a period from about 14 days to about 25 800 yr,
- $|m| = 1$: diurnal with a period of about 24 h,
- $|m| = 2$: semi-diurnal with a period of about 12 h.

Each of the three tidal bands in Equation (2.25) varies in a complicated way as they contain products of different time-varying functions.

Harmonic expansion The complex time dependence of the positions of the Moon and the Sun relative to the Earth can be described by means of elaborate harmonic expansions with constant amplitudes and frequencies. According to the lunar theory by E. H. Brown (1905) there are five fundamental quantities: the mean longitudes, measured in the ecliptic from the concurrent *mean vernal equinox*, for the Moon (s), the Sun (h), the *perigee* (p), the ascending node of the Moon's orbit (N), and the *perihelion* (p_s) (Figure A.1, Appendix A.1). Since the lunar orbital nodes are the only ones of all quantities moving clockwise against the orbital direction of the Sun and Moon, occurs $-N$. Whereby the period of mean longitude of the Moon and the Sun is called *tropical month* and *tropical year*, respectively. Table 2.2 provides the periods of the quantities. Except for very small residuals, these mean longitudes change uniformly with time (Bartels, 1957).

Doodson (1921) employed local *mean lunar time* $t_{\leftmoon}$ to apply the elaborate harmonic expansion on the tidal potential

$$\begin{aligned} \Phi^t &= \sum_{ABC,DEF} c_{ABC,DEF}\, G_A(\varphi) \cos\left(A t_{\leftmoon} + Bs + Ch + Dp - EN + Fp_s\right) \\ &= \sum_{ABC,DEF} c_{ABC,DEF}\, G_A(\varphi) \cos(\sigma_{ABC,DEF}\, t) \\ &= \sum_{ABC,DEF} c_{ABC,DEF}\, G_A(\varphi) \cos(\sigma_{ABC,DEF}\, t_0 + A\lambda). \end{aligned} \tag{2.27}$$

Whereby the period of mean lunar time is called *mean lunar day* (Table 2.2). The constituent of cosine terms with constant amplitudes $c_{ABC,DEF}$ and angular frequencies $\sigma_{ABC,DEF}$ are referred to as partial tides. The tidal frequency $\sigma_{ABC,DEF}$ is the change of the cosine argument, usually expressed in degrees per hour, i. e. the *mean solar time* t changes by $^{360°}/_{24\,\mathrm{h}} = 15\,°\,\mathrm{h}^{-1}$. It is composed additively with the integral coefficients A, B, C, D, E, F from the angular frequencies of the fundamental quantities, the local mean lunar time and the Brown variables. Their angular frequencies are easily obtained by dividing 360°

Table 2.2.: Mean longitudes and times with their periods—fundamental tidal periods. The data for ~620 Myr ago are given by G. E. Williams (2000).

			Periods	
Mean times			**Modern**	**~620 Myr ago**
Sidereal	θ	Mean sidereal day	0.997 270 d 23.934 472 h 23 h 56 min 4 s	0.997 506 d[1] 21.845 387 h[1] 21 h 50 min 43 s[1]
Solar	t	Mean solar day	1.000 000 d 24.000 000 h 24 h 0 min 0 s	 (21.9 ± 0.4) h
Lunar	$t_{\mathbb{C}}$	Mean lunar day	1.035 050 d 24.841 200 h 24 h 50 min 28 s	1.033 950 d[2] 22.64 h[2] 22 h 38 min 24 s[2]
Mean longitudes				
Moon	s	Tropical month	27.321 582 d	(28.3 ± 0.5) d[3]
Sun	h	Tropical year	365.242 199 d	(400 ± 7) d
Perigee	p	Perigee period	8.847 yr	(9.7 ± 0.1) yr
Lunar ascending node	N	Lunar nodal period	18.613 yr	(19.5 ± 0.5) yr
Perihelion	p_s	Perihelion period	20 940 yr	
	$s - h$	*Synodic month*	29.530 59 d	(30.5 ± 0.5) d
	$s - p$	*Anomalistic month*	27.554 55 d	
	$h - p_s$	*Anomalistic year*	365.259 64 d	
		Sidereal month	27.32 d	(28.3 ± 0.5) d
		SiderealYear	366.24 d	(401 ± 7) d
		Synodic month per year	12.37	13.1 ± 0.1
		Sidereal month per year	13.37	14.1 ± 0.1
		Lunar semi-major axis	60.27 $R_{\eth}$	(58.16 ± 0.30) $R_{\eth}$
		Lunar recession rate	(3.82 ± 0.07) cm/yr	(2.17 ± 0.31) cm/yr

1 Sidereal day derived form the ratio of tropical year to sidereal year times the mean solar day.
2 Derived from the relationship $t_{\mathbb{C}} = t + h - s$ (Bartels, 1957).
3 Derived that the sidereal month can be used for the tropical month according to Kvale et al. (1999).

by the period (Table 2.2). The local mean solar time $t = t_0 + \lambda$ at a longitude λ (° E) can be obtained from the mean solar time t_0 along the Greenwich meridian ($\lambda = 0°$) at a rate of $15\,° \mathrm{h}^{-1}$. Consequently, the harmonic argument σt_0 for the Greenwich meridian, in conjunction with the tidal band $|m| = A$, implies that $\sigma t_0 + A\lambda$ is along longitude λ. The time dependency expressed by sine and cosine functions is transformed here into solely positive cosine functions through the use of suitable multiplies of 90°. As no real-time calculations are necessary for the purpose of the present study, these terms have been omitted for the sake of convenience. The same applies to the equivalent representation of the harmonic argument in terms of the angular frequencies of the mean times and longitudes. The amplitude $c_{ABC,DEF}\, G_A(\varphi)$ is given for each constituent by the constant amplitude coefficient $c_{ABC,DEF}$ and the geodetic function $G_A(\varphi)$, which is dependent only on the lunar tidal constant (Equation (2.26)), the latitude φ and the tidal band with the order

Table 2.3.: Principal partial tides with the celestial body that causes them and the symbols used. The argument number (Equation (2.28)) specifies the composition of the harmonic argument or constant frequency $\sigma_{ABC,DEF}$ (Equation (2.27)) along with the amplitude coefficient $c_{ABC,DEF}$ (Equation (2.27)) and the geodetic function G_A (Equations (2.26) and (2.27)) for the tide.

Origin	Symbol	Argument number	$c_{ABC,DEF}$	G_A	Harmonic argument	
			semi-diurnal tides			
Moon	M_2	$\{255, 555\}$	0.9081	$D_{\leftmoon} \cos^2(\varphi)$		$2t_{\leftmoon}$
Sun	S_2	$\{273, 555\}$	0.4229	$D_{\leftmoon} \cos^2(\varphi)$	$2t_{\leftmoon} + 2s - 2h$	$2t$
			diurnal tides			
Moon	K_1	$\{165, 555\}$	0.3626	$D_{\leftmoon} \sin(2\varphi)$	$t_{\leftmoon} + s$	$t + h$
Moon	O_1	$\{145, 555\}$	0.3768	$D_{\leftmoon} \sin(2\varphi)$	$t_{\leftmoon} - s$	
Sun	K_1	$\{165, 555\}$	0.1682	$D_{\leftmoon} \sin(2\varphi)$	$t_{\leftmoon} + s$	$t + h$
Sun	P_1	$\{163, 555\}$	0.1755	$D_{\leftmoon} \sin(2\varphi)$	$t_{\leftmoon} + s - 2h$	$t - h$

$|m| = A$ (Table 2.3). In the case of solar constituents the dependence on the solar tidal constant (Equation (2.25)) is expressed as a multiple of the lunar tidal constant (see notes on Equation (2.26)). Consistent with the comments on Equation (2.25), the harmonic analysis in Equation (2.27) assumes a spherical Earth with $r = R$. For $r \neq R$, the constituents must be extended by the factor $(r/R)^2$.

The so-called argument number

$$\{A(B + 5)(C + 5), (D + 5)(E + 5)(F + 5)\} \tag{2.28}$$

represents a specific notation for partial tides, in which a datum of five is set for the last five coefficients in stead of zero, thereby ensuring that the notation remains positive to the greatest extent possible. While Darwin (1883–1886) introduced symbols that represent the individual tidal constituents by an alphanumeric term: e. g. M_2 (semi-diurnal principal lunar tide), S_2 (semi-diurnal principal solar tide), where subscript 1 and 2 denotes the diurnal and semi-diurnal tides, respectively. However, certain symbols such as M_2, S_2, K_1, and O_1 are well established and continue to be used. Nevertheless, Darwin's symbols and Doodson's argument numbers can be regarded as equivalent (Doodson, 1921). In the following, the symbol for the tidal frequency σ is employed as a subscript or superscript to signify the dependency of a variable on a partial tide.

Doodson (1921), superseded the expansion by Darwin (1883–1886), just as the lunar theory by E. H. Brown (1905), which Doodson applied, superseded all earlier theories. Doodson's catalog includes the tidal potential of the Moon and Sun of degree 3 with 378 constituents. The error due to truncation of the astronomical tidal potential was continuously reduced with time and the number of constituents continuously increased with time. New calculations occurred with the revision of astronomical constants, the recalculation of Brown's coefficients, the advent of numerical ephemerides (e. g. Hartmann & Wenzel, 1995).

The principal constituents of the astronomical tidal potential can be represented by the orbital motion of fictitious Moon and Sun, uniformly circular in the equatorial plane. Thus,

the declination δ would always be zero and the diurnal tides would disappear completely (2^{nd} term of Equation (2.25)). The distance would become constantly all the time. As a result, the long-periodic tide would be time-independent and would have a constant effect on the mean sea level. Semi-diurnal tides arise with the period of half a mean lunar day and half a mean solar day. The amplitude coefficients of these tides would be equal to 1.00 for the fictitious Moon and 0.46 for the fictitious Sun. These ideal values are reduced because of the real non-uniform motion of the Moon and Sun on elliptical orbits inclined to the celestial plane. Table 2.3 presents the corresponding semi-diurnal principal lunar and solar tides, designated M_2 tide and S_2 tide, respectively. The argument $2(t_{\mathbb{C}} + s - h)$ of S_2 becomes twice the mean solar time $2t$ through the relation with *mean sidereal time* (measured from lower culmination)

$$\theta = t_{\mathbb{C}} + s = t + h. \tag{2.29}$$

In a linear combination of M_2 and S_2, the tides superimpose both constructively and destructively. Their sinusoids have slightly different periods and their relative phase shifts slowly. A carrier wave is formed with a semi-diurnal period and its envelope reflects the period of successive full Moon occurrences, the synodic month (Table 2.2). The superposition reflects the *neap-spring tidal cycle* arising from the lunar phases (Figure 1.4). At full and new Moon, the Moon and the Sun are aligned with the Earth and their tides are mutually amplified to a *spring tide*—M_2 and S_2 are in phase every half synodic month (Figure 1.4). At crescent Moon, the Moon and the Sun are in quadrature with the Earth and their tides mutually attenuate to a *neap tide*. Hence, the neap-spring tidal cycle correlates to the half synodic month (Figure 1.4).

The diurnal tides have their origin in the inclination of the lunar and solar orbits relative to the *celestial equator* and the related time-dependent declination δ of Moon and Sun (2^{nd} term of Equation (2.25)). Vice versa, the declination δ reduces the semi-diurnal tides (3^{rd} term of Equation (2.25)). A daily inequality in the two successive high tides occurs (Figure 2.3). Whereas, the symmetry of the two sides with tidal depressions is not canceled by the inclination of the lunar and solar orbits; there is no inequality in successive low tides. There are also no diurnal principal tides with inclined orbits, since the declination δ factor annuls the diurnal periods (2^{nd} term of Equation (2.25)); the mean value of $\sin(2\delta)$ becomes zero. It follows that the lunar and solar diurnal declinational tides K_1 and O_1, and K_1 and P_1, as set forth in Table 2.3 are to be regarded as replacing the diurnal principal tides. The frequencies of the lunar and solar K_1 are identical to the mean sidereal time (Equation (2.29)), and therefore the sum of the two is commonly treated as the lunisolar declinational tide K_1.

The diurnal inequality varies with the Moon's motion during a tropical month—from maximum northern declination δ with greatest diurnal inequality, across the equator with a declination δ of zero and ideally no diurnal inequality, to maximum southern declination δ with greatest diurnal inequality, and then return across the equator to maximum of northern declination δ. However, the neap-spring tidal cycle in ocean basins with diurnal tides, since, for example, the semi-diurnal tides M_2 and S_2 are attenuate, goes back not to the synodic month but to the tropical month (K_1 and O_1 are in phase every half tropical month) (Figure 1.5).

An additional consequence arises from the slight elliptical nature of the Moon's orbit around the Earth. The distance between the Earth and the Moon varies between the closest approach, known as the perigee, and its greatest distance, known as the *apogee* (Figure A.1). In this context, a monthly inequality is evident in the spring tides. The amplitude of the spring tides is amplified during perigee and near perigee, whereas it is attenuate during apogee and near apogee. The interval between successive perigean conjunctions is referred to as an anomalistic month. The orbital movement itself is a function of the Moon's elliptical inequality argument $s - p$. The solar analogue is represented by the argument $h - p_s$ (Table 2.2). In addition to the elliptical inequalities in the solar tides, the argument also describes the annual inequality in the motion of the Moon through the Sun in the lunar tides.

The mean period of the monthly spring tide inequality is called the *tidal year*. It has a length of 13.9 synodic months. The tidal year is longer than the solar year of 12.4 synodic months due to the prograde precession of perigee (in the same orbital direction as the orbit of the Earth) with period of 8.9 yr (Table 2.2). There are other multi-year tides. The precession of the lunar orbital nodes (Figure A.1), the lunar orbital precession, with a current period of 18.6 yr changes the inclination of the lunar orbit relative to the Earth's equator from 18° to 28° and reverse every 18.6 yr. Furthermore, as a result of the Earth's lunisolar precession, the *vernal equinox* (Figure A.1) moves westward toward the Earth on its orbit around the Sun with a current period of about 25 800 yr.

However, it is rare that all these cycles coincide and cause exceptionally high and low tides. The maximum tidal range occurs when the Moon is in either new or full phase, at perigee, the Earth is at its perihelion, and the Sun and the Moon have the same declination and are directly over the equator. According to the perturbation calculation, the partial tides associated with the inclination and eccentricity of the mean orbits as well as their periodic perturbations contribute relatively less to the astronomical tidal potential compared to the principal tides M_2 and S_2 (Table 2.3). The major partial tides are described in detail by e. g. Bartels (1957).

2.2.3. Earth body tides

The primary mass redistributions of the solid body of the Earth in response to the astronomical tidal force are shown in functional terms below. This is followed by the functional treatment of secondary mass redistributions in response to ocean mass redistributions caused by the astronomical force.

2.2.3.1. Astronomical tidal potential

The response of the solid Earth to the tidal force field of the Moon and the Sun is virtually static because its main frequencies—the semi-diurnal, diurnal, and long-periodic tidal frequencies—are at least one order of magnitude lower than the natural frequencies of the solid Earth (Section 2.1.2.1). For a spherically symmetric, non-rotating, elastic, isotropic earth model the response is described by the so-called tidal Love's numbers $h_l(r), k_l(r)$, which represent dimensionless proportionality factors between the distortions and the causative potential. The assumption is that there is a linear relationship between the astronomical

tidal potential Φ^t as the causative perturbation potential and the resulting change in the gravitational potential.

Related to the astronomical tidal potential Φ_l^t, Equations (2.22) and (2.24), is a lift of the equipotential surface of gravity, respectively, an equilibrium tide (Appendix B.1 and Figure 2.3) of

$$\overline{\zeta}_l(r,\varphi,\lambda) = \frac{\Phi_l^t(r,\varphi,\lambda)}{g(r)}. \tag{2.30}$$

The resulting mass displacements respectively the tides of the solid Earth are given by

$$\delta_l(r,\varphi,\lambda) = h_l(r) \cdot \overline{\zeta}_l(r,\varphi,\lambda) \tag{2.31}$$

having the additional deformation potential of

$$\Phi_l^{et}(r,\varphi,\lambda) = k_l(r) \cdot \Phi_l^t(r,\varphi,\lambda) \tag{2.32}$$

with a corresponding lift of the equipotential surface of gravity of

$$\overline{\zeta}_l^*(r,\varphi,\lambda) = k_l(r) \cdot \overline{\zeta}_l(r,\varphi,\lambda). \tag{2.33}$$

The total lift of the equipotential surface with respect to an observer is

$$\eta_l(r,\varphi,\lambda) = (1 + k_l(r) - h_l(r)) \cdot \overline{\zeta}_l(r,\varphi,\lambda). \tag{2.34}$$

The tidal Love numbers are functions of the radial distance r from the Earth's center and depend only on the degree l of the astronomical tidal potential Φ_{lm}^t being considered and not on its order m. Their determination relies on density and elastic properties of the Earth's solid body. Seismic reference models, such as PREM and Gutenberg-Bullen, provide these parameters. The Love numbers of low degree l of the different earth models differ by less than 1 % (Zürn & Wilhelm, 1984). For the dominant component of the astronomical tidal potential of the second degree $l = 2$ in the spherical harmonic development (Equation (2.24)), the Love numbers for a consideration of tidal phenomena at the Earth's surface $r = R$ result in (Zürn & Wilhelm, 1984):

$$h_2(R) = 0.61, \quad k_2(R) = 0.30, \quad \gamma_2(R) = 0.69. \tag{2.35}$$

The solid body of the Earth is deformed by about $\pm 0.4\,\mathrm{m}$ into an elongated rotational ellipsoid with its major axis oriented in the direction of the tide-generating body, and the change in gravity is of the order of $1 \times 10^{-6}\,\mathrm{m\,s^{-2}}$ (Zürn & Wilhelm, 1984). The few percent deviation of tides of an elastic solid Earth body from observed Earth tides can be explained by inelasticity, rotation or shape of a rotational ellipsoid, and large-scale mantle inhomogeneities of the Earth body (R. Wang, 1995). This results in complex frequency-dependent Love numbers with phase angles ϵ of a few hundredths of a degree (e. g., Munk & McDonald, 1960). Since its formation at the beginning of the Earth's history about 4500 Myr ago, the Earth's body has hardly changed in its reaction to the astronomical tidal force.

2.2.3.2. Ocean tidal loading

In addition, secondary mass displacements—loading tides—occur due to mass loads on the Earth's surface, which change harmonically with the periods of the astronomical tidal potential (ocean tides, atmospheric tides). On the one hand, the Earth's surface is forced downward for a positive outward load. On the other hand, it is attracted by the load (self-attraction). Both effects of a positive load combined together cause the Earth's surface to sink. Since the load exerts a pressure on the Earth's surface, but the astronomical tidal potential does not, the matter reaction of the solid Earth body to the loading is described by a set of Love numbers h'_s, k'_s different from the tidal ones. The gravitational deformation potential of the load takes the place of the astronomical tidal potential.

The loading of the ocean tides with its gravitational potential Φ^{ot} (Equation (2.47)), resulting from the expansion of the loading in spherical harmonics, causes a lift of the equipotential surface of gravity of

$$\overline{\zeta}'_s(r,\varphi,\lambda) = \frac{\Phi^{ot}_s(r,\varphi,\lambda)}{g(r)} \tag{2.36}$$

by each expansion component Φ^{ot}_s of the gravitational potential. The resulting mass displacements respectively the loading tides of the solid Earth are given by

$$\delta'_s(r,\varphi,\lambda) = h'_s(r) \cdot \overline{\zeta}'_s(r,\varphi,\lambda) \tag{2.37}$$

having the additional deformation potential of

$$\Phi^{lt}_s(r,\varphi,\lambda) = k'_s(r) \cdot \Phi^{ot}_s(r,\varphi,\lambda) \tag{2.38}$$

with a corresponding lift of the equipotential surface of gravity of

$$\overline{\zeta}'^{*}_s(r,\varphi,\lambda) = k'_s(r) \cdot \overline{\zeta}'_s(r,\varphi,\lambda). \tag{2.39}$$

The total lift of the equipotential surface with respect to an observer is

$$\eta'_s(r,\varphi,\lambda) = (1 + k'_s(r) - h'_s(r)) \cdot \overline{\zeta}'_s(r,\varphi,\lambda). \tag{2.40}$$

Love numbers up to a degree of 10 000 are required to describe the load. For the astronomical tidal potential, the degree of 2 is essentially significant. Because the pressure effect is greater than the gravitational attraction effect, the mass load Love numbers h'_s and k'_s are negative (Zürn & Wilhelm, 1984). A lowering of about 4 cm results for an ocean loading of 1 m over a distance of 10° of arc around the observation point. For an ocean loading of 1 m over the entire surface of the Earth, the lowering is about 6 cm (personal communication, A. Hufschmidt, 2023). With tidal loads of several meters, values of more than 10 cm can be reached near the coast. The change in gravity is of the order of $1 \times 10^{-7}\,\mathrm{m\,s^{-2}}$.

2.2.4. Ocean tides

However, due to the dynamics of the oceans, the equilibrium case is not realized for the vast majority of ocean tides. The basic terminologies and representations of the oceanic tidal oscillation system in its spatial and temporal characteristics are introduced in the following description. Then, with regard to their study, the equations of motion, the shallow-water equations valid for long waves, follow. Despite the lack of their analytical solution, certain modified forms of wave shapes are possible. They are used to illustrate the principal tidal processes in the ocean. A classification of the tidal range and the tidal regime by the form factor is then given, followed by an overview of tidal currents in the context of tidal sedimentation. Finally, the energy and angular momentum balance of oceanic tides are discussed in terms of their secular effect on the Earth's rotation rate.

2.2.4.1. Description

The response of the oceans to the tidal force field of the Moon and the Sun, the rise and fall of the sea level as the so-called high and low tides, is usually shown on maps separately for each harmonic constituent of the force (Equation (2.27)). The oceanic tides

$$\zeta_\sigma(\varphi, \lambda, t) = \zeta_\sigma^0(\varphi, \lambda) \cos[\sigma_\sigma t - \phi_\sigma(\varphi, \lambda)], \tag{2.41}$$

like the body tides, occur at the frequencies σ_σ of the partial tides. However, their constant amplitudes ζ_σ^0 and phases ϕ_σ are unknown. Obviously, because of the continents, the oceanic tides cannot propagate endlessly as progressive waves. An unhindered circumpolar movement of the tidal waves from the east to the west is possible around Antarctica, but it is limited by the Drake Passage (between Cape Horn and Graham Land).

On these maps (e. g. Figure 2.4a), the places where the high tide, and thus all other phases of the tide, occur simultaneously are connected by so-called cotidal contours. The high tide times are given with their position within the tidal period in time or radian/degree. Locations where the same *tidal range* or amplitude occurs are connected by what are known as corange or co-amplitude contours. Meanwhile, direct observation by satellite altimetry is the best way to obtain a complete map of ocean tides and their propagation. As an example, Figures 2.4 and 2.5 show the semi-diurnal lunar and solar principal tides M_2 and S_2 and the diurnal lunar and solar declinational tides K_1 and O_1.

As these tide maps show, global ocean tides occur in a geographic and temporal pattern quite different from the double-bulge equilibrium tide shown in Figure 2.3. The time between the Moon's passage through the meridian and the corresponding high tide varies from place to place, and the high tides rarely occur at the same time. Across the surface of the ocean, the tidal range vary greatly. From open oceans, the tides spread to the surrounding shelves (Figures 2.1 and 2.2 and Section 2.1.2.3), where the tidal range tends to increase. In both the open ocean and the shelf seas, the semi-diurnal tides develop large amplitudes (Figures 2.4a and 2.4b). This differs from diurnal tides, whose amplitudes are small in the open ocean and increase only near continents (Figures 2.5a and 2.5b). With considerable variation, tidal amplitudes in the open ocean range from 0 m to 0.6 m. The tidal forces are sufficient for significant tides in the open ocean. However, they are too weak for smaller bodies of water. This includes nearly enclosed seas such as the Baltic Sea and the Mediterranean Sea,

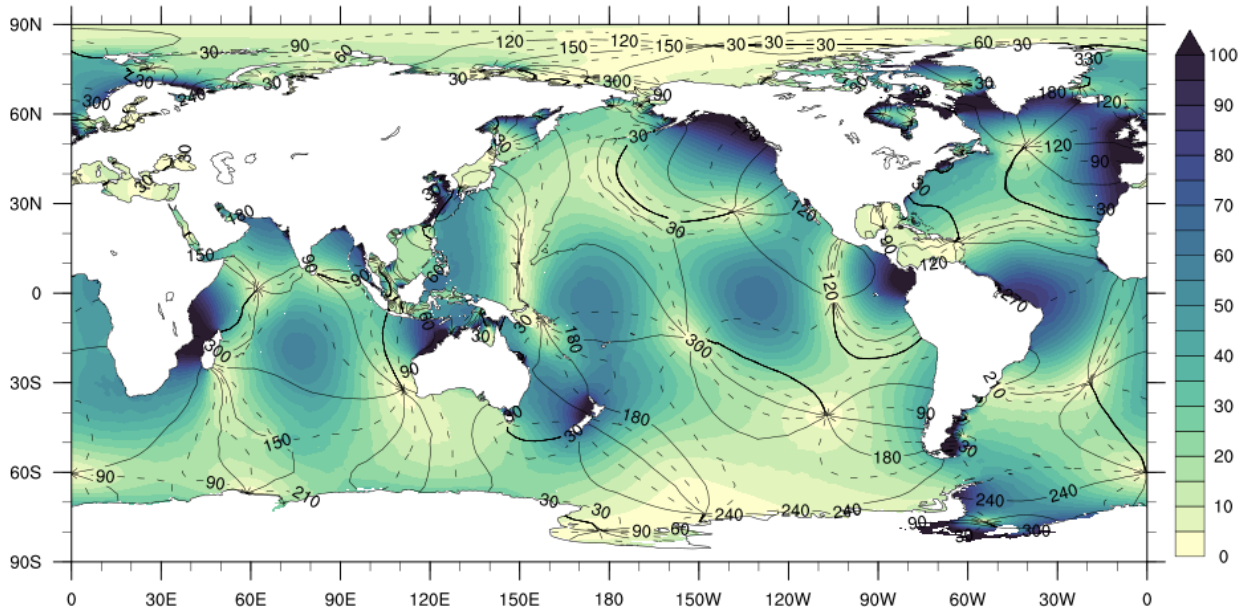

(a) M_2 constituent.

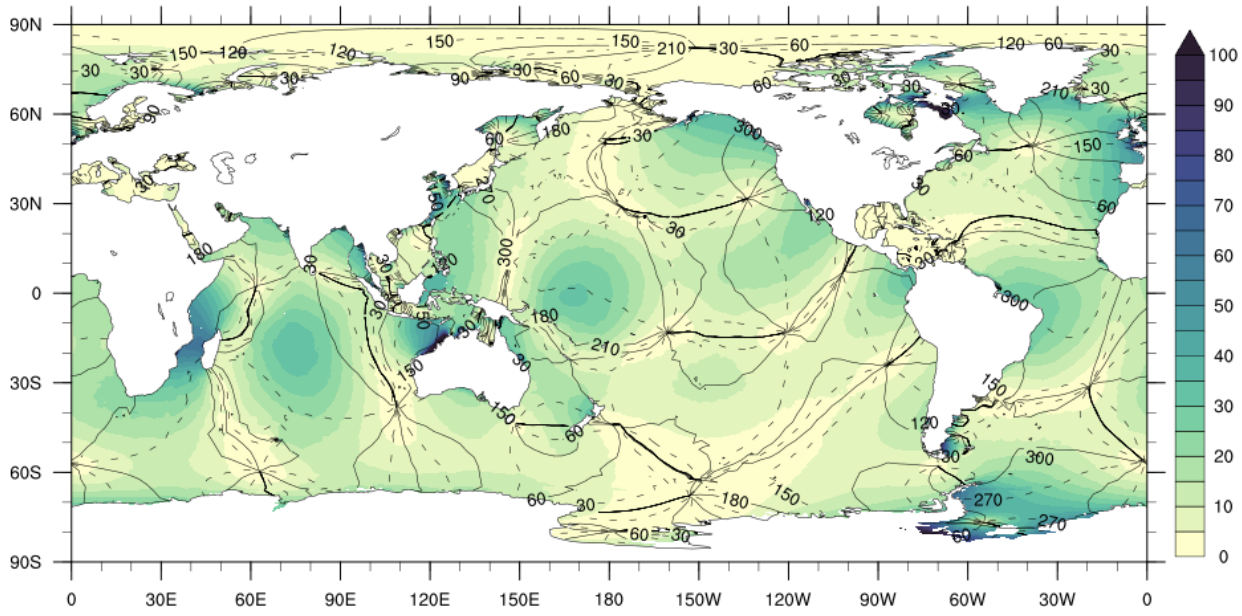

(b) S_2 constituent.

Figure 2.4.: Semi-diurnal tidal maps derived from satellite altimetry (Hart-Davis et al., 2021a; Hart-Davis et al., 2021b). Colors show amplitudes in cm, black lines show contours of the same phase in degrees.

and even shelf seas. There, co-oscillations are stimulated by the tides of the open ocean.

Tides propagate along coastlines along the cotidal lines, which are perpendicular to the coastlines. Along the direction of wave propagation, the coast is to the right in the Northern Hemisphere and to the left in the Southern Hemisphere. The cotidal lines converge at nodes that are designated as amphidromic points, where the amplitude is found to be zero. Once per period, the tidal wave rotate around these points, limiting the size of the

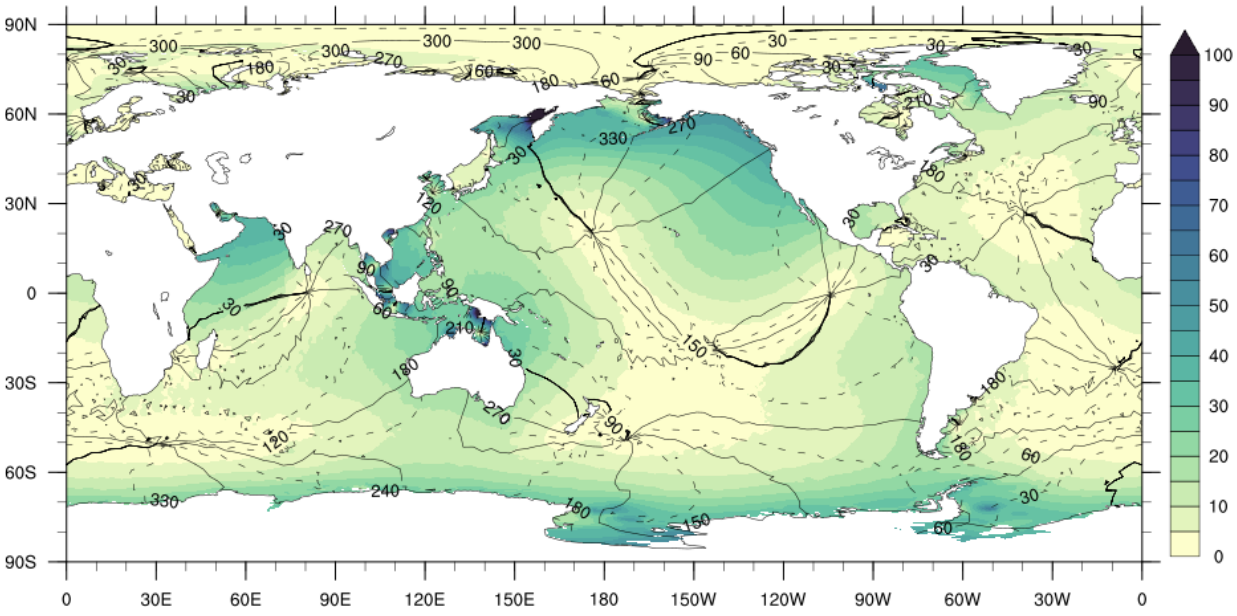

(a) K_1 constituent.

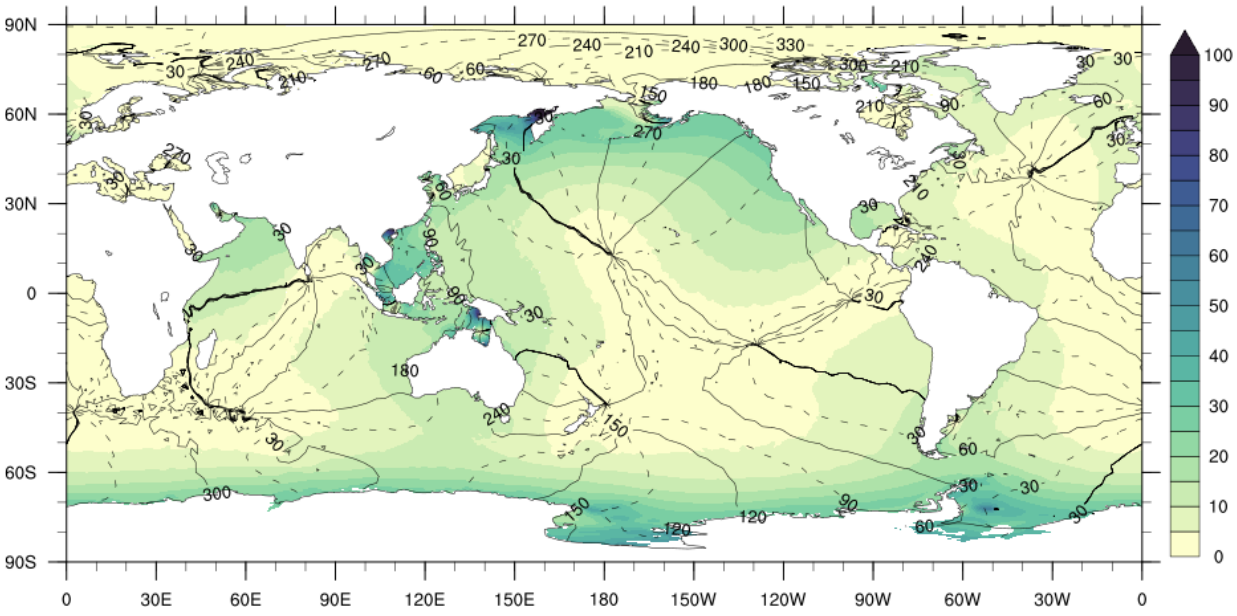

(b) O_1 constituent.

Figure 2.5.: Diurnal tidal maps derived from satellite altimetry (Hart-Davis et al., 2021a; Hart-Davis et al., 2021b). Colors show amplitudes in cm, black lines show contours of the same phase in degrees.

amphidromic system. The direction of rotation is usually counterclockwise in the Northern Hemisphere and clockwise in the Southern Hemisphere. The location of amphidromic points between the semi-diurnal and diurnal tides differs significantly. Within the semi-diurnal and diurnal tides, the pattern of amphidromic systems is maintained with small variations. Extended regions characterized by slow phase changes and high amplitudes simultaneously are designated as anti-amphidromes.

Areas of high semi-diurnal tides occur in all oceans. However, they are most extensive in

the Atlantic Ocean (Figures 2.4a and 2.4b). In the North Atlantic, areas of high semi-diurnal tides extend from the Canary Basin off northwest Africa, through the Iberian Basin, the Western European Basin, and past England, Ireland, and Scotland, east into the North Sea, and west into the Iceland Basin and on into the Irminger and Labrador Basins around southern Greenland. Strongly amplified semi-diurnal tides also occur at the entrance to Hudson Bay and in the Bay of Fundy in the Gulf of Maine, where they dominate the largest tidal range in the world of up to about 17 m. In contrast, semi-diurnal tides do not occur in the Mexican Basin, where diurnal tides dominate. Diurnal tides also occur to a limited extent around southern Greenland into Baffin Bay and at the entrance to Hudson Bay and the Gulf of St. Lawrence. The South Atlantic off South America in the Amazon Basin and on the Argentine shelf also experience high semi-diurnal tides.

In the Indian Ocean, areas of high semi-diurnal tides are found between Africa and Madagascar and off the northwest coast of Australia. An extensive anti-amphidrome is located in the south-central Indian Ocean. Throughout the Indian Ocean off Australia and in the Arabian Sea, there are high diurnal tides.

In the Pacific, high semi-diurnal tides are found in the Guatemala Basin and the Gulf of Alaska. There is also the area around New Zealand and the East China Basin. Anti-amphidromic systems occur in the south-central Pacific. The North Pacific has relatively high diurnal tides, with stronger ones in the Gulf of Alaska and farther east in the southern part of the Bering Sea. However, these tides have much smaller amplitudes than the M_2 semi-diurnal tide. The highest diurnal tides in the world are to be found in the Okhotsk Basin. Together with the poorly developed semi-diurnal tides, the sea there is dominated by the diurnal tides. Tidal variations in sea level can reach up to 13 m. Strong diurnal tides are also found from the South China Basin to the Java Sea, the west coast of New Guinea, and northern Australia. There are strong diurnal tides in the vicinity of Antarctica, with the addition of strong semi-diurnal tides in the Weddell Sea.

It is obvious that the observed semi-diurnal and diurnal tides cannot be treated as equilibrium tides. The conservation laws of momentum, mass and energy define the fundamental dynamical equations of ocean motion.

2.2.4.2. Equations of motion

The hydrodynamic equations of continuity and momentum balance govern the tidal motions of the ocean surface. Tidal waves belong to the class of shallow-water or long waves; with $\lambda > 20H$ their wavelengths λ are everywhere much larger than the ocean depth H. As shown in Figures 2.4a, 2.4b, 2.5a and 2.5b, there are in most cases several hundred kilometers between successive cotidal lines of tidal waves. Thus, the wavelengths are many times larger. The deepest point in the ocean is 13 km, while the average ocean depth is only 3.8 km. In a non-rotating reference system, the speed

$$c = \sqrt{gH} \tag{2.42}$$

of long waves in the ocean, the behavior of which is dominated by gravity forces (gravity waves), is solely defined by the water depth H and the gravity acceleration g. With a speed of about $195\,\mathrm{m\,s^{-1}}$, the long tidal waves propagate at a considerable rate in waters of

average depth. Nevertheless, regardless of the obstacles caused by the land masses, the tides cannot follow the Moon as equilibrium tides. At period T, the wavelength with $\lambda = cT$ is thus about 9000 km for the semi-diurnal tides and twice that for the diurnal tides. The velocity would be sufficient only around Antarctica.

Waves at the sea surface continue to move on circular orbits with a diameter equal to the wavelength in the idealized case of great depth and associated negligible friction. Due to the relatively small amplitudes compared to the wavelength of the tidal wave, the orbits are elliptical. There is hardly any vertical motion, more like a straight back and forth. Due to the long wavelength, the orbits extent almost undisturbed to the seafloor. There they are subject to bottom friction and attenuation. Since the vertical motion is negligible in comparison to the horizontal motion, the pressure distribution can be considered to be hydrostatic. It is only the weight of the water above any given point in the water column that gives the pressure.

Thus, for the vertical momentum equation, hydrostatic equilibrium can be used. In the spherical polar notation, the horizontal momentum equations

$$\frac{\partial u}{\partial t} + \frac{u}{R\cos\varphi}\frac{\partial u}{\partial \lambda} + \frac{v}{R}\frac{\partial u}{\partial \varphi} - fv = -\frac{g}{R\cos\varphi}\frac{\partial \zeta}{\partial \lambda} + \frac{1}{R\cos\varphi}\frac{\partial \Phi^{tg}}{\partial \lambda} + F_{f,\lambda} \tag{2.43}$$

$$\frac{\partial v}{\partial t} + \frac{u}{R\cos\varphi}\frac{\partial v}{\partial \lambda} + \frac{v}{R}\frac{\partial v}{\partial \varphi} + fu = -\frac{g}{R}\frac{\partial \zeta}{\partial \varphi} + \frac{1}{R}\frac{\partial \Phi^{tg}}{\partial \varphi} + F_{f,\varphi} \tag{2.44}$$

establish the dynamic equilibrium between the tide-generating potential Φ^{tg}, Equation (2.46), and the internal forces in the ocean, such as inertia, pressure gradient, and friction. In addition, in the relative frame of reference of an observer on the Earth, the rotation of the Earth acts on the tidal wave with the Coriolis force. The wave must follow a curved path. With respect to the propagation direction, to the right in Northern Hemisphere and to the left in Southern Hemisphere. Where $\vec{\boldsymbol{v}} = (u, v)$ is the vertically integrated velocity with the zonal component u and the meridional component v, $f = 2\Omega_{\delta}\sin(\varphi)$ is the latitude-dependent Coriolis parameter, $H = D + \zeta$ is the height of the water column with the sea level elevation ζ and the undisturbed depth D, and $F_{f,\lambda}$ and $F_{f,\varphi}$ are the zonal and meridional frictional forces, respectively. The unresolved physics of dissipation mechanisms such as bottom friction, turbulent eddy viscosity (horizontal momentum diffusion), and topographic wave drag (excitation of internal tides) are included in a variety of parametrized forms.

There are still two equations that are missing for the other state variables, the pressure and the density. They are result of the conservation of mass and energy. For the fundamental aspects of tides, changes in density can be neglected. Density can be assumed constant and the ocean incompressible, equivalent to barotropic conditions. This reduces the conservation of mass to a divergence-free velocity vector field. The conservation of mass is obtained after vertical integration:

$$\frac{\partial \zeta}{\partial t} = -\frac{1}{R\cos\varphi}\left[\frac{\partial}{\partial \lambda}(Hu) + \frac{\partial}{\partial \varphi}(Hv\cos\varphi)\right]. \tag{2.45}$$

Together, Equations (2.43) to (2.45) are also called the shallow-water equations. In their linearized form, they become *Laplace's* tidal equations.

The astronomical tidal potential (Equations (2.24), (2.25) and (2.27)) must be superimposed by the potentials of the Earth body due to its tides (Equation (2.32)) and the loading by the ocean tides (Equation (2.38)) in the equations of motion (Equations (2.43) and (2.44)). In the pressure gradient of the equations of motion, the deformation of the seafloor due to the astronomical tidal potential (Equation (2.31)) and the oceanic tidal potential (Equation (2.37)) must be taken into account. Equivalent, they are included in the tide-generating potential

$$\Phi^{tg}(R,\varphi,\lambda) = \sum_{l=2}^{\infty}(1+k_l(R)-h_l(R))\Phi_l^t(R,\varphi,\lambda) + \sum_{s=0}^{\infty}(1+k'_s(R)-h'_s(R))\Phi_s^{ot}(R,\varphi,\lambda). \tag{2.46}$$

The ocean tides (Equations (2.43) to (2.45)) are based on a spherical symmetric Earth model, as are the body tides and the loading tides (Section 2.2.3). Furthermore, the treatment is restricted to the Earth's surface $r = R$.

There is a gravitational deformation potential associated with the ocean tides

$$\Phi^{ot}(R,\varphi,\lambda) = 4\pi G\varrho R\sum_{s=0}^{\infty}\frac{1}{2s+1}\zeta_s\begin{cases}(r/R)^s & \text{for } r<R\\ (R/r)^{s+1} & \text{for } r>R\end{cases}, \tag{2.47}$$

where the ocean tide constitutes a thin spherical layer with the surface density of $\varrho\zeta(\vec{r})$ (Munk & McDonald, 1960). ϱ is the seawater density. ζ_s is the expansion of the tidal sea level elevation in spherical surface functions (Appendix C.1). The ocean tide potential (Equation (2.47)) in the system of differential equations of the ocean motion field, (Equations (2.43) and (2.44)), implies for its solution the integration of the tidal oscillation system $\zeta(\varphi,\lambda,t)$ over the perturbed surface topography of the world ocean. The simplifying local parameter approach

$$\Phi^{sal} = g\varepsilon\zeta \tag{2.48}$$

for the joint self-attraction and loading potential $\Phi^{sal} = \sum_s(1+k'_s-h'_s)\Phi_s^{ot}$ in Equation (2.46) comes from Accad and Pekeris (1978), who deduced that the self-attraction and loading potential Φ^{sal} is proportional to the sea surface elevation ζ. The proportionality factor ε is in the range 0.08 to 0.1, i. e. the self-attraction and loading potential is globally assumed to be 8 % to 10 % of the pressure gradient (e. g. Seiler, 1989). Global-scale numerical simulations have shown a 10 % change in the amplitude of the tidal sea surface elevation ζ_σ^0 due to the SAL effect, but a 30 % change in the phase ϕ_σ (Ray, 1998).

In the absence of an analytical solution of the hydrodynamic tidal equations (Equations (2.43) to (2.45)) for real oceans, the first attempts to get an overview of tides in real oceans relied solely on coastal tide measurements. Since the availability of suitable high performance computers, a numerical solution of the equations is possible (Section 3.2).

2.2.4.3. Tidal wave propagation

Analytical studies of the linearized barotropic shallow-water equations for frictionless bodies of water in conjunction with simplified geometries have yielded modified forms of plane wave

propagation in non-rotating reference systems. The geometries encompass water bodies characterized by infinite vertical unilateral boundaries and infinite channels of constant width, as well as enclosed and semi-enclosed rectangular basins, all with constant depth. In general, these are dispersive waves whose frequencies are a non-linear function of their wavenumbers. The propagation of tidal waves is governed by their frequency, the deflection force resulting from Earth's rotation, the gravity acceleration, and the dimensions of the body of water concerned (LeBlond & Mysak, 1978).

The interaction of inertia, Coriolis force, and pressure gradient give rise to the occurrence of *Poincaré* waves, a form of gravity waves. Contrary to the dispersion-free gravity waves in the non-rotating reference system, this type of wave is normal dispersive due to the deflection force of the Earth's rotation, exhibiting a faster propagation speed than indicated in Equation (2.42). In the context of the open ocean with constant depth, a sinusoidal wave is formed along the propagation direction. This wave is characterized by constant amplitude throughout its extent, with transverse crests that do not vary in height. Figure 5.1e provides an example in the North Pacific. In the Northern Hemisphere, the particles exhibit a clockwise movement, whereas in the Southern Hemisphere, they display a counterclockwise trajectory. Wave propagation and real wavenumbers are constrained to wave frequencies that exceed the Coriolis parameter. For frequencies below the Coriolis parameter, the wavenumbers become imaginary, and Poincaré waves become evanescent. The restriction imposes a substantial constraint on the dynamics of tidal waves. The tidal frequencies can be found to be above a given latitude below the Coriolis parameter. This critical latitude φ_c results from the definition of the Coriolis parameter. For semi-diurnal tides, this phenomenon occurs at approximately $\pm 75°$, and for diurnal tides, it occurs at approximately $\pm 30°$.

The restriction imposed by Poincaré waves can be overcome by incorporating a novel wave type characterized by imaginary wavenumbers transverse to the wave propagation. However, only the solution in which the amplitude decays exponentially with distance from a vertical boundary is valid. The other solution involves the exponential growth of amplitude with distance from the boundary. A mass transport or a vertical integrated current perpendicular to the boundary is inherently excluded as a boundary condition. In the *Kelvin* wave solution, characterized by propagation along a straight vertical boundary, an additional boundary condition is applied: the transverse current to the boundary disappears everywhere. In the Northern Hemisphere, the boundary is located to the right of the wave propagation, as shown by the semi-diurnal M_2 and S_2 tides in the North Atlantic (Figure 2.4) and the diurnal K_1 and O_1 tides in the North Pacific (Figure 2.5). In the Southern Hemisphere, the boundary occurs to the left of the wave propagation. For example, this is the case for the M_2 and S_2 tides in the Weddell Sea (Figure 2.4) and for the diurnal K_1 and O_1 tides along the Antarctic coastline (Figure 2.5). Due to their non-dispersive nature, they maintain their shape as they propagate along the boundary at the speed of gravity waves in non-rotating reference frames (Equation (2.42)). The Rossby radius of deformation c/f, which is defined as the ratio of propagation speed c of the Kelvin wave (Equation (2.42)) and the Coriolis parameter f, determines the scale length for the exponential decay of the Kelvin wave transverse to the boundary. At the distance of the Rossby radius, the amplitude is $\exp(-1) \approx 0.37$ of the boundary amplitude. That occurs for Kelvin waves, which propagate in the open ocean at mean depth at speeds of about $195\,\mathrm{m\,s^{-1}}$, at low

latitudes at about 3000 km, at mid-latitudes at about 2000 km, and at high latitudes at about 1500 km. Both the propagation velocity and the decay scale are the same for all tidal constituents.

On the scale of the Rossby radius, a steep continental slope is virtually indistinguishable from a vertical boundary. A barotropic Kelvin wave extends far from the coast and occupies a considerable part of a typical modern ocean (Figures 2.4 and 2.5). The Pacific Ocean is clearly sufficiently spacious for a Kelvin wave to fully develop, while the Atlantic Ocean may be too constricted in this regard. Furthermore, Kelvin waves can propagate in both hemisphere, parallel to the equator in an easterly direction, as a virtual coast. The characteristic meridional width of these waves, given by the equatorial Rossby radius, is about 2000 km at mean ocean depth.

Kelvin waves automatically satisfy the boundary conditions for an infinite channel of constant width. In contrast, Poincaré waves are modified by the boundary conditions, resulting in the occurrence of discrete wavenumbers both longitudinal and transversal to the direction of wave propagation. In the transverse direction, an sinusoidal oscillation develops that is proportional to the channel width. The wave fronts are perpendicular to the channel walls. The nodal lines, for which the amplitude is zero, are parallel to the walls. Across the channel width, the progressive Poincaré wave demonstrates an asymmetric distribution. At the equator, where the Coriolis parameter is zero, the asymmetry would be eliminated. Analogous, Poincaré waves can propagate in the equatorial waveguide given by the equatorial Rossby radius. Furthermore, Poincaré waves can also occur in the presence of a coast if the coastline runs along of the zero lines of the sinusoidal transverse current component.

A pair of Kelvin waves propagating in opposite directions within an infinite channel of constant width may interfere constructively, thereby forming a fixed pattern of rotating waves known as amphidromes. Along the channel axis, at half the channel width, nodal points with an amplitude of zero and anti-nodal points with a maximum amplitude alternate at intervals of a quarter wavelength. The amplitude remains greatest at the channel edges. The cotidal lines extend radially around the nodal points. In the Northern Hemisphere, the amphidromes are counterclockwise; in the Southern Hemisphere, they are clockwise. The constructive interference of two Poincaré waves propagating in opposite direction eliminates the asymmetric transverse wave height distribution. The wave structure emerges as a series of cells along the channel. The dimensions of the cells in the transverse and longitudinal directions are half the wavelength of the corresponding wave component. Nodal points are located in the center of the cells and form clockwise amphidromes in the Norther Hemisphere and counterclockwise amphidromes in the Southern Hemisphere. Additional amphidromic points are located at the corners of the cells.

In the context of a closed end of a channel and a semi-enclosed basin, it is evident that neither the Kelvin wave nor the Poincaré wave as an incident wave can be reflected on its own. The boundary condition that no perpendicular mass transport is possible at the closed end cannot be met due to the interference patterns of the Kelvin wave and the Poincaré wave with nodal points instead of nodal lines. The reflection process can be understood as a result of the contributions of a Kelvin wave and a full spectrum of Poincaré waves (Taylor, 1922). For evanescent Poincaré waves, the interference pattern becomes that of two counter-propagating Kelvin waves as the distance from the closed

end of the channel increases. For propagating Poincaré waves, the amphidromic pattern of two counter-propagating Kelvin waves undergoes a distortion due to the presence of the Poincaré waves, resulting in a pronounce lateral structure along the channel.

In the real ocean, the reflected wave proves to be weaker than the incident wave. This is due to energy dissipation occurring at the boundary and the complex reflection processes. As a result, for a Kelvin wave, the nodal points of the amphidromic system shift to the left in the direction of the incident wave. The displacement is greater in proportion to the weakness of the reflected Kelvin wave (Pugh, 1981; Taylor, 1919). Depending on the degree of displacement and the width of the channel, the amphidromic points may lie on land, while the cotidal lines continue to be concentrated on them. This phenomenon is referred to as degenerate amphidromes.

In the shelf seas with an average depth of about 40 m, the shallow-water waves decelerate to a speed of about $20\,\mathrm{m\,s^{-1}}$, thereby reducing the Rossby radius in mid-latitudes to about 200 km. For semi-diurnal tides, the wavelength decreases from about 9000 km to about 900 km, and for diurnal tides, it reduces from 18 000 km to 1800 km. The tidal waves undergo a degree of deformation at the shelf edges, subsequently accumulating in the shelf seas. The wave amplitude increases as a result of the energy flux, a phenomenon that also occurs on the shelves towards the coast. Moreover, the waves are decelerated more in the trough than in the crest. The wave front becomes steeper. In addition to the shortening and deceleration of the classical Kelvin wave along the continental slope, a realistic current over the continental slope and shelf (e. g. Bay of Biscay) is generated. The current runs continuously across the slope, where it peaks. Consequently, vertical current velocity must be generated in combination with depth variation. The shelf can act as a waveguide, trapping waves along the shelf.

2.2.4.4. Tidal elevations

Tidal ranges can be broadly classified in the following way (Figure 1.2):

$$\begin{aligned} &\text{Microtides}: && 2\zeta^0 &&< 2\,\mathrm{m} \\ &\text{Mesotides}: && 2\,\mathrm{m} < 2\zeta^0 &&< 4\,\mathrm{m} \\ &\text{Macrotides}: && 4\,\mathrm{m} < 2\zeta^0. \end{aligned} \tag{2.49}$$

The four different patterns found in ocean tides in different parts of the world are semi-diurnal, diurnal, mixed mainly semi-diurnal, and mixed mainly diurnal (Figure 1.3). In a semi-diurnal tidal pattern, there are two high tides and two low tides on each lunar day. The heights of successive high tides and low tides are approximately equal. This is due the suppression of the diurnal constituents of the tides. In the Atlantic (Figures 2.4a, 2.4b, 2.5a and 2.5b), semi-diurnal tides with a period around the half lunar day of 12 h 25 min dominate. In a diurnal tidal pattern, each lunar day has a high tide and a low tide. In this case, the semi-diurnal tidal constituents are filtered out. In shallow inland seas such as the Gulf of Mexico and along the coast of Southeast Asia, diurnal tides with a period around the lunar day of 24 h 50 min are common (Figures 2.4a, 2.4b, 2.5a and 2.5b). All intermediate tidal regimes are classified as mixed tidal systems with 1 to 2 tides per lunar day, depending on the relative importance of the diurnal and semi-diurnal constituents

(Russell & MacMillan, 1970). Mixed or semi-diurnal tidal regimes make up the majority (about 90 %) of modern tidal systems. Purely diurnal tidal regimes account for only 10 % of observations (Lisitzin, 1974).

The nature and type of a tidal regime is determined by the form factor

$$F = \frac{\zeta^0_{K_1} + \zeta^0_{O_1}}{\zeta^0_{M_2} + \zeta^0_{S_2}}, \tag{2.50}$$

defined as the amplitude ratio of the diurnal declinational tides K_1 and O_1 to the semi-diurnal principal tides M_2 and S_2. Where the type is semi-diurnal at $F < 0.25$ $(= 0)$, mixed mainly semi-diurnal at $0.25 \geq F < 1.5$ $(= 1)$, mixed mainly diurnal at $1.5_, \geq F < 3.0$ $(= 2)$, and diurnal at $F \geq 3.0$ $(= 3)$.

2.2.4.5. Tidal currents

Tidal waves increase in height and become asymmetrical in profile as they enter shallow water. Accompanying this are ebb and flood currents of varying strength. Flood currents are stronger and shorter in duration than ebb currents. In addition, vertical convergence of the current is associated with the transformation of the tidal wave in shallow water. In straits and estuaries, the horizontal convergence of the current is added to this. Both convergences also increase the tidal range.

Maps for tidal currents are difficult to produce. This is due to their strong spatial variability. For all shallow-water waves, including tides, the maximum current velocities u_{max} near the seafloor increase with tidal range and shoaling (Bridge & Demicco, 2008):

$$u_{max} = \frac{2\zeta^0_\sigma c}{2D} = \frac{\zeta^0_\sigma \sqrt{gD}}{D}. \tag{2.51}$$

Near the seafloor, a maximum current velocity of $0.3\,\mathrm{m\,s^{-1}}$ would result from a tidal wave with a tidal range of 0.4 m in water 5 m deep. This is sufficient for the transport of fine-grained sand. For a tidal wave with a tidal range of 2 m in water 10 m deep, the maximum velocity near the bottom would be about $1\,\mathrm{m\,s^{-1}}$. Equation (2.51) has limited applicability for currents accelerated by channels or damped by strong friction. Nevertheless, the velocity of tidal currents in shallow, enclosed seas and tidal channels is typically about $1\,\mathrm{m\,s^{-1}}$ to $2\,\mathrm{m\,s^{-1}}$. By integrating the orbital velocity of particles oscillating back and forth at the tidal frequency, one can estimate how far the tidal transport extends. In coastal areas, this tidal transport can be of the order of 10 km (Gerkema, 2019).

Many macrotidal regions (Equation (2.49)) are associated with strong tidal currents that result in tidal sedimentation. Examples include the Bay of Fundy. However, it is not the tidal range alone that determines the maximum current velocity at a given location. Rather, it is determined by the tidal prism. This is the amount of water that must flow through that point due to high and low tides, without other contributions such as river inflows. For example, if the tidal prism is small, a large tidal range will not produce significant currents. Conversely, even though the tidal range is small, some straits that connect large bodies of water have strong tidal currents. The English Channel is an example.

2.2.4.6. Conservation laws

By scalar multiplication of the velocity $\vec{\boldsymbol{v}}$ and by vectorial multiplication of the position vector $\vec{\boldsymbol{r}}$ with the equations of motion (Equations (2.43) and (2.44)), the equations for the energy and angular momentum balance of the oceanic tidal oscillation system are obtained. Integration over the perturbed world ocean volume yields the equations of energy and angular momentum balance ($\langle X \rangle$). Partial tides (Equation (2.27)) as an external excitation potential in the equations of motion (Equations (2.43) and (2.44)) allow averaging over closed tidal periods ($\overline{X}$). This allows studying perturbations of the Earth's gravitational potential caused of the ocean tides acting secularly on the Earth's rotation. In Baader (1982) and Seiler (1989) the balance equations can be found with a detailed discussion.

Energy balance equation In the world ocean, the gain of potential energy $\langle \overline{\dot{E}_t} \rangle$ by the partial tide Φ_σ^t

$$\langle \overline{\dot{E}_p} \rangle + \langle \overline{\dot{E}_t} \rangle + \langle \overline{\dot{E}_{sal}} \rangle + \langle \overline{\dot{E}_f} \rangle = 0 \tag{2.52}$$

is balanced by the dissipation by the frictional forces $\langle \overline{\dot{E}_f} \rangle$. In the past, bottom friction in shallow seas on continental shelfs was thought to be the primary sink of tidal energy (Jeffreys, 1920; Taylor, 1919). The mechanisms of bottom friction and eddy viscosity in tidal energy dissipation have been extended in particular by the analysis of satellite altimeter data. In the open ocean over rough topography, Egbert and Ray (2000) and Egbert and Ray (2001) have shown that there is a significant dissipation of 25 % to 30 % of the barotropic tidal energy. One possible mechanism is the excitation of internal tides (Munk & McDonald, 1960). Cross-slope currents will result in vertical currents as depth varies. Realistically, temperature and salinity vary along the vertical in the ocean, as does the density. Planes of equal density, called isopycnals, can be periodically raised and lowered with the vertical tidal current. Vertically mixing occurs where energy is dissipated by turbulent mixing. Energy is lost through the barotropic surface tides to generate these internal (i. e., baroclinic) tides, which can propagate freely from their source into the deep ocean and onto the shelf over long distances. This interaction of barotropic tides with steep features such as continental slopes and submarine ridges is also known as topographic wave drag.

The loading potential and the pressure gradient, averaged over a tidal period, do not represent a source or a sink of energy $\langle \overline{\dot{E}_{sal}} \rangle$ and $\langle \overline{\dot{E}_p} \rangle$, respectively (Baader, 1982; Lambeck, 1980b). However, numerical simulations of ocean tides do show changes in the energy due to these forcings. Furthermore, numerical diffusion by the Coriolis force, and thus an energy imbalance $\langle \overline{\dot{E}_{imb}} \rangle$, can result from the spatial discretization of the equations of motion in the hydrodynamic numerical models (Seiler, 1989).

The rate at which work $\dot{W}$ is done on the ocean by the partial tide Φ_σ^t and the moving seafloor provides another way to describe the energy balance equation. Integrated over the sea surface and over one tidal period, the change in kinetic and potential energy vanishes. With the impermeable boundaries between the ocean and the continents, the horizontal divergence of the energy flux also disappears. The rate at which work is done

$$\langle \overline{\dot{W}} \rangle = -\langle \overline{\dot{E}_d} \rangle \tag{2.53}$$

becomes equal to the rate at which energy is dissipated $\langle\overline{\dot{E}_d}\rangle$ (Lambeck, 1980b). $\langle\overline{\dot{W}}\rangle$ can be obtained from the nominal tide (Appendix C.1, the prograde spherical harmonic $\zeta^+_{\sigma,lm}, \epsilon^+_{\sigma,lm}$ with $s = l$ and $t = m$) of the tidal oscillation system of the same degree l and order m as the considered partial tide $\Phi^t_{\sigma,lm}$ (Lambeck, 1980b):

$$\langle\overline{\dot{W}}\rangle = 4\pi\sigma\,(1 + k_l - h_l)\,\frac{GR^2 m_\imath \varrho}{a_\imath}\left(\frac{R}{a_\imath}\right)^l \frac{\zeta^+_{\sigma,lm}}{2l+1} \times F_{lmp}(i_\imath)G_{lpq}(e_\imath)\left[\begin{array}{c}\sin\\ \cos\end{array}\right]^{l-m\ \text{even}}_{l-m\ \text{odd}}\left[\epsilon^+_{\sigma,lm} - \pi\left(\frac{r_\sigma}{2} + m\right)\right]. \tag{2.54}$$

The subscript $\imath$ refers to the tide-generating body. F_{lmp} and G_{lpq} are polynomials in the inclination $i_\imath$ and eccentricity $e_\imath$ of the orbit of the tide-generating body (Table 2.4). p can take values between 0 and l and q from $-\infty$ to $+\infty$. Their values for the particular partial tide can be taken from e. g. Lambeck (1980b). r_σ is an integer required to modify the phase $\epsilon^+_{\sigma,lm}$ and depends on the particular partial tide (Table 2.4). The remaining spherical harmonics vanish with an integration over the surface of the world's oceans and over one period of the considered partial tide $\Phi^t_{\sigma,lm}$. In this way, the average rate of energy dissipation in the world's oceans is given only by the prograde spherical harmonic of the disturbed sea surface of the same degree and order as the partial tide. In other words, the harmonic that is geographically distributed and zonally propagating like the considered partial tide $\Phi^t_{\sigma,lm}$. For the present resonant conditions of the world ocean, the phase ϵ^+ over all partial tides represents a schematic retardation of the ocean tides, as in the case of the Earth body tides (Section 2.2.3). This means that an accelerating torque acts on the orbit of the tide-generating body due to the ocean tides, and conversely a torque of the tide-generating body, which decelerates the Earth's rotation, acts on the ocean tides (Section 2.3).

Angular momentum balance equation The equation for the balance of angular momentum in the body-fixed relative system (Baader, 1982; Seiler, 1989) is given by

$$\langle\overline{\vec{\boldsymbol{M}}_a}\rangle + \langle\overline{\vec{\boldsymbol{M}}_c}\rangle = \langle\overline{\vec{\boldsymbol{M}}_p}\rangle + \langle\overline{\vec{\boldsymbol{M}}_t}\rangle + \langle\overline{\vec{\boldsymbol{M}}_{sal}}\rangle + \langle\overline{\vec{\boldsymbol{M}}_f}\rangle. \tag{2.55}$$

Where $\langle\overline{\vec{\boldsymbol{M}}_a}\rangle$ is the torque of the acceleration terms, $\langle\overline{\vec{\boldsymbol{M}}_c}\rangle$ is that of the Coriolis force, $\langle\overline{\vec{\boldsymbol{M}}_p}\rangle$ is that of the pressure gradient, $\langle\overline{\vec{\boldsymbol{M}}_t}\rangle$ is that of the partial tide, $\langle\overline{\vec{\boldsymbol{M}}_{sal}}\rangle$ is that of the loading potential, and $\langle\overline{\vec{\boldsymbol{M}}_f}\rangle$ is that of the frictional forces such as bottom friction, eddy viscosity, and topographic wave drag. A change in the Earth's rotational velocity occurs via the terms in the direction of the axis of rotation (Equation (2.8)):

$$\langle\overline{M_{a,z}}\rangle + \langle\overline{M_{c,z}}\rangle = \langle\overline{M_{p,z}}\rangle + \langle\overline{M_{t,z}}\rangle + \langle\overline{M_{sal,z}}\rangle + \langle\overline{M_{f,z}}\rangle. \tag{2.56}$$

In accordance with the work method used for the energy balance (Equations (2.53) and (2.54)), the tidal torque $\langle\overline{M_{t,z}}\rangle$ is proportional to the nominal ocean tide (Appendix C.1) (Lambeck, 1977; Ray et al., 1999).

The global polar tidal torque $\langle\overline{M_{t,z}}\rangle$ (cf. Equations (2.5) and (2.6)) average over a tidal

Table 2.4.: Relation between the partial tides and the indices *lmpq* (Lambeck, 1977), inclination functions F_{lmp}, eccentricity functions G_{lpq} (Kaula, 1966; Lambeck, 1980b), and the required integer r_σ to modify the phase $\epsilon^+_{\sigma,lm}$ (Lambeck, 1977) for the use of the work method in Equation (2.54).

Tide	*lmpq*	Origin	$F_{lmp}(i_\imath)$	$G_{lpq}(e_\imath)$	r_σ
M_2	2200	☾	$\frac{3}{4}(1+\cos i_☾)^2$	$1-\frac{5}{2}e_☾+\ldots$	0
S_2	2200	☉	$\frac{3}{4}(1+\cos i_☉)^2$	$1-\frac{5}{2}e_☉+\ldots$	0
$K_{1☾}$	2110	☾	$-\frac{3}{2}\sin i_☾\cos i_☾$	$(1-e_☾)^{-3/2}$	1
$K_{1☉}$	2110	☉	$-\frac{3}{2}\sin i_☉\cos i_☉$	$(1-e_☉)^{-3/2}$	1
O_1	2100	☾	$\frac{3}{4}\sin i_☾\,(1+\cos i_☾)$	$1-\frac{5}{2}e_☾+\ldots$	-1

cycle remains non-zero. It is balanced by an exchange of angular momentum between the ocean and the solid Earth body. In a harmonic tidal oscillations system, there is a phase difference between the tidal wave and the astronomical tidal force, and thus a tidal torque, due to the resonance properties of the tides. The individual transfer mechanisms should be considered realistic. This is due to the non-linear interactions (advection and friction) of the oceanic motion field with its permanent residual currents (Brosche & Sündermann, 1971). A purely harmonic system of tidal oscillations according to the Laplace's tidal equations also exhibits the corresponding counter-current at every point where a current is present. The integration of the current over a tidal cycle will vanish. Velocity dependent torques (friction and Coriolis) would vanish. Due to non-linear interactions, the tidal phenomena in the world's oceans, especially in the shelf areas, show deviations from harmonic behavior. Residual currents remain when integrated over a tidal cycle. Furthermore, due to integration over the disturbed sea surface, all global quantities contain non-linearities. These non-linearities do not make the transfer mechanisms disappear (Seiler, 1989). In numerical simulations, spatial discretization effects can also contribute to the transfer mechanisms in a manner analogous to an imbalance in the energy balance.

2.3. Tidal torque and tidal friction

The redistribution of mass by the tides affects the gravitational field of the Earth. As a result, the tides have gravitational interactions with celestial bodies and geostationary artificial satellites. In Section 2.3.1, this is schematically demonstrated using the Moon as an example. The gravitational potential of the tides can periodically perturb the orbital motion of the celestial bodies and artificial satellites, and also secularly perturb the orbital motion of the tide-generating body (Lambeck, 1980b). Vice versa, a torque is exerted on the tides by the gravitational potential of the tide-generating body. This is discussed in terms of a secular effect on the Earth's rotation in Section 2.3.2.

2.3.1. Description

A schematic representation of the interaction between the Moon and an Earth body equilibrium tide (Section 2.2.3) is given in Figure 2.6. The Earth rotates counterclockwise

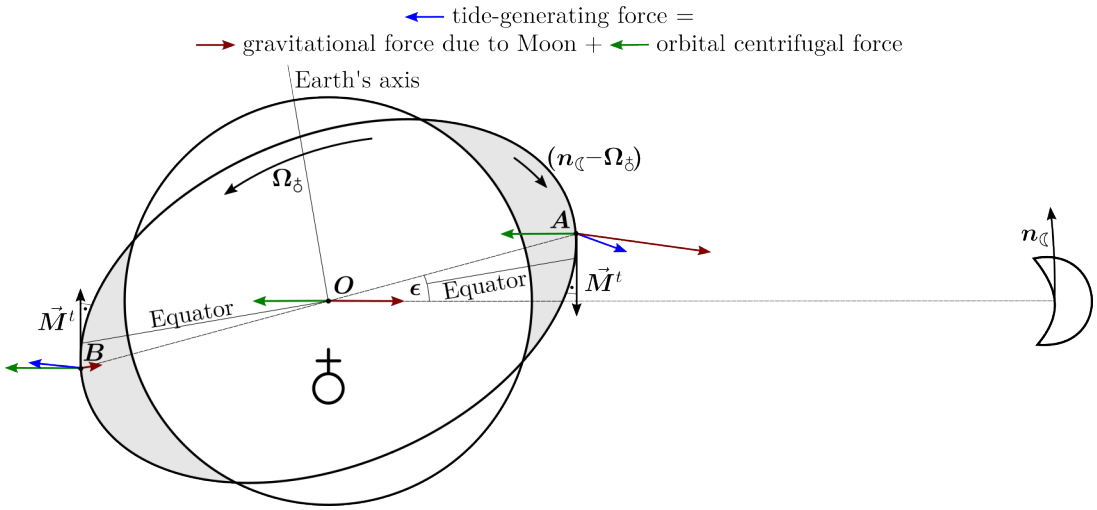

Figure 2.6.: Tidal torque of the Moon on a viscous-elastic Earth (based on Melchior (1983)). A cross-section of the Earth's equatorial plane is displayed. This is were the Moon's orbit is assumed to be.

with a period of 1 d, just as the Moon orbits the Earth with a period of one tropical month (~27 d, Table 2.2, p. 30). Thus, the lunar orbital velocity

$$|\vec{n}_{☾}| \sim \frac{|\vec{\Omega}_{♁}|}{27} \ll |\vec{\Omega}_{♁}| \tag{2.57}$$

is much lower than the Earth's rotational velocity $\vec{\Omega}_{♁}$. After the time Δt when the Moon has passed through the meridian of an observer in the Earth's rotating relative system, the maximum tidal uplift of the Earth's body is reached. This tidal bulge (represented by protuberances A and B), carried by the Earth in its rotation, must therefore rotate clockwise at the negative speed $n_{☾} - \Omega_{♁}$ in order to remain in line with the attracting lunar body. Internal friction causes a constant delay in this bulge rotation, represented by the angle ϵ of the AB line with respect to the line connecting the Earth and the Moon. A schematic representation of the forces acting on A, B, and O and their differences with respect to the force acting on O then shows that the resulting tidal torque $\vec{M}_t$ acts against the direction of the Earth's rotation $\vec{\Omega}_{♁}$ and thus acts as a secular drag on the Earth's rotation. Since the system is in equilibrium, there must be an equal and opposite torque of the Earth's body tides on the Moon. This has an accelerating effect on the Moon's orbit.

The ocean tides are an oscillating system (Section 2.2.4). Due to their resonant properties, they adjust themselves with a phase difference to their generating astronomical tidal force, which results in a tidal torque. Unlike body tides, they can be either leading or lagging locally with respect to the generating force. Correspondingly, local torques can occur that either accelerate or decelerate the Earth's rotation (Brosche & Sündermann, 1971). Integrated over the ocean surface and averaged over a tidal cycle, this results in a tidal torque for the principal tidal constituents that slows secularly the Earth's rotational velocity.

Alternatively, the tidal friction was and is considered to be at the expense of the Earth's rotational velocity (Defant, 1961; Munk & McDonald, 1960). This is due to various dissipations mechanisms such as bottom friction and topographic wave drag during oceanic tidal motion. Thus, the dissipation of tidal energy should be equivalent to the decrease in the rotational energy of the Earth, which in turn is related to the secular tidal torque and its

decrease in the rotational velocity of the Earth (Equation (2.9)). This consideration is valid for a tide that is constantly propagating westward, such as the equilibrium tide of the solid Earth body. It is different in the oceanic tidal oscillations system, where residual currents can remain in all possible directions when averaging over a tidal cycle (Section 2.2.4.6, p. 48). Thus, the western component of the residual currents has a slowing effect on the Earth's rotation, and the eastern component of the residual currents has an accelerating effect on the Earth's rotation. Purely northern or southern residual currents do not influence the Earth's rotation. Although all currents are subject to friction, not all of the energy lost to oceanic tidal friction is at the expense of the Earth's rotational velocity. Unlike the vectorial approach via tidal torque, the scalar approach via tidal friction fundamentally excludes tidal acceleration effects on Earth's rotation (Brosche & Sündermann, 1971). The effect of the ocean tides on the Earth's rotational velocity should be based on an study of the torques acting on the solid body of the Earth, not in a co-rotating system, but in an inertial system (Brosche & Sündermann, 1971). Regarding the fundamental nature of the process, namely the transfer of the vectorial quantity of angular momentum, the scalar energetic approach seems to be inadequate (Sündermann & Brosche, 1978).

2.3.2. Tidal torque

The tidal torque $\vec{\boldsymbol{M}}_t$ acting on the Earth's rotation for a given tidal disturbed volume V_δ of the Earth and given astronomical tidal potential Φ^t (Equations (2.24), (2.25) and (2.27)) can be obtained from Equation (2.5). For a given volume V of the tide-generating body and given tidal potentials Φ^{et}, Φ^{lt}, and Φ^{ot} (Equations (2.32), (2.38) and (2.47)), the opposite tidal torque $\vec{\boldsymbol{M}}_t$ of the same magnitude acting on the tide-generating body also results from Equation (2.5). For the purely harmonic partial tides (Equation (2.27)) as astronomical tidal potential Φ^t, the tidal torque $\vec{\boldsymbol{M}}_t$ can be averaged over closed periods. The global polar component of the tidal torque averaged over one period $\langle\overline{M_{t,z}}\rangle$ (Equation (2.6)) does not vanish and exerts a secular effect on the Earth's rotational velocity (Equation (2.8)). This assertion remains valid even when exclusively considering the purely harmonic component of the tides (Equation (2.41)). The tidal phases prove to be of pivotal significance (Hufschmidt, 2025). The time-averaged polar tidal torque relative to the water column has the capacity to either decelerate or accelerate the Earth's rotation rate, contingent upon the tidal phases (Appendix D.1).

At present, the time-averaged global polar tidal torque $\langle\overline{M_{t,z}}\rangle$ implies a secular decrease in the Earth's rotation rate Ω_δ (Table 3.1, p. 80). The contributions of the body tides driven by the astronomical partial tides to their total tidal torque are equal to the contributions of the partial tides to the astronomical tidal potential. For the ocean tides, the ratio of the contributions is a function of their resonance characteristics. The long-period tides with zonal potential (Equation (2.25)), however, have no contribution to the secular effect on the Earth's rotational velocity because they are symmetric in longitude and have a vanishing axial tidal torque (cf. Equation (2.6)).

Equivalently, for a viscous-elastic body of the Earth, the time-averaged global tidal torque $\langle\overline{M_{t,z}}\rangle$ can be estimated as being proportional to the sine of the phase shift $\sin\epsilon$ of its equilibrium tide (Lambeck, 1977). The phase shift is estimated to be a few hundredths of a degree, since the inelasticity and energy dissipation of the tides of the Earth body are not

well known (Sections 2.2.3 and 3.1.1).

For the oceans, the time-averaged global polar tidal torque $\langle\overline{M_{t,z}}\rangle$ can be derived from the angular momentum balance for the tides (Section 2.2.4.6 and Equation (2.55)). Precise knowledge of tidal heights and currents is required for this purpose. Instead, the nominal ocean tide (Appendix C.1) can be considered. This represents the part of the ocean tide that behaves like an equilibrium tide, comparable to the body tides. It thus reflects the secular effect of the ocean tides on the Earth's rotational velocity. The time-averaged global polar tidal torque $\langle\overline{M_{t,z}}\rangle$ becomes proportional to the nominal ocean tide (Lambeck, 1977; Ray et al., 1999). The other spherical harmonics are associated with periodic rotational variations (Lambeck, 1977; Ray et al., 1999).

A complete analysis also requires consideration of the Moon's tides through the Earth and Earth's tides through the Sun. Lambeck (1980b) gives the ratio between the effect of the Moon's tides through the Earth and the effect of the Earth's tides through the Moon as $\lesssim 0.15$. The tides on the Moon do not contribute significantly with respect to changes in the semi-major axis and the inclination of the lunar orbit. They can only be important with respect to changes in the eccentricity of the lunar orbit (Lambeck, 1980b).

The orbital angular momentum of the Earth orbiting the Sun is unaffected by any angular momentum transfers due to the ratio of the angular momenta in the Sun-Earth-Moon system. Even if all of the Earth's rotational momentum were transferred to its orbit around the Sun, the change in the new period of the Earth's orbit would be less than 15 s (Deines & Williams, 2016). Furthermore, insufficient evidence has been found for a secular change in the Earth's distance from the Sun (Simon et al., 1994), and thus for a secular change in the length of the year. Conversely, the solar torque on the Earth's tides has a significantly effect on the Earth's rotational angular momentum. This should be taken into account when considering the history of the Earth's rotation.

2.4. Tidal rhythmites

Sediment can be entrained, transported, and deposited by waves as well as tides. Multidisciplinary analyses of ancient tidal sediments have played a key role in providing information on Earth paleo-rotation and lunar paleo-orbit. From the fundamentals of tidal sedimentation in Section 2.4.1, Section 2.4.2 provides details and examples of the effects of tides on sedimentation. After the preferred environments for the formation and preservation of tidal sediments over geologic time in Section 2.4.3, approaches to the analysis of tidal sediments in Section 2.4.4 conclude this section.

2.4.1. Description

Empirical field and laboratory measurements provide the bulk of our knowledge of sediment transport. The two phases of movement initiation (erosion) and deposition are linked by sediment transport. Tides and waves both entrain and transport sediment. In general, the velocity of tidal currents is sufficient to transport gravel and sand along the bottom and clay and silt in suspension (Section 2.2.4.5). As velocity decreases, the mean grain size of the transported sediment decreases and deposition of sediment above the mean

grain size occurs. As velocity increases, the mean grain size of the transported sediment increases and erosion of sediment below the mean grain size occurs. As shown in Figure 2.7, the capacity to transport sediment depends on the third power of the current velocity, which in turn is more or less linearly related to the tidal amplitude (Boothroyd, 1985; De Boer & Alexandre, 2012; FitzGerald & Nummedal, 1983; van Rijn, 1993; P. Wang, 2012).

In contrast to the open ocean, tidal waves and currents develop asymmetrically in coastal areas and shoals. Tidal currents vary not only temporally but also spatially with depth and tidal range (Equation (2.51)). The maximum current velocity increases with tidal range and decreasing depth. Flood currents tend to be stronger and of shorter duration than ebb currents and, because of their capacity, dominate sediment displacement landward. Areas where ebb currents dominate sediment displacement seaward can be created, for example, by the amplification of ebb currents by river discharge. In addition, the asymmetric flood and ebb currents can follow different paths along which net sediment transport can occur (Allen, 1970; Bridge & Demicco, 2008; Harris et al., 1995; Johnson et al., 1982).

A finer sedimentary deposition results from a spatially and temporally slowed tidal current. Coarser deposition results from a spatially slowed and temporally accelerated tidal current. One layer can form per ebb and flood if these units grow on the order of millimeters during a tidal cycle. During the slack water phase between ebb and flood, a layer of mud can form on top of the sand layer (Figure 2.8, A, B). Such an alignment and arrangement of layered sedimentary structures is commonly known as

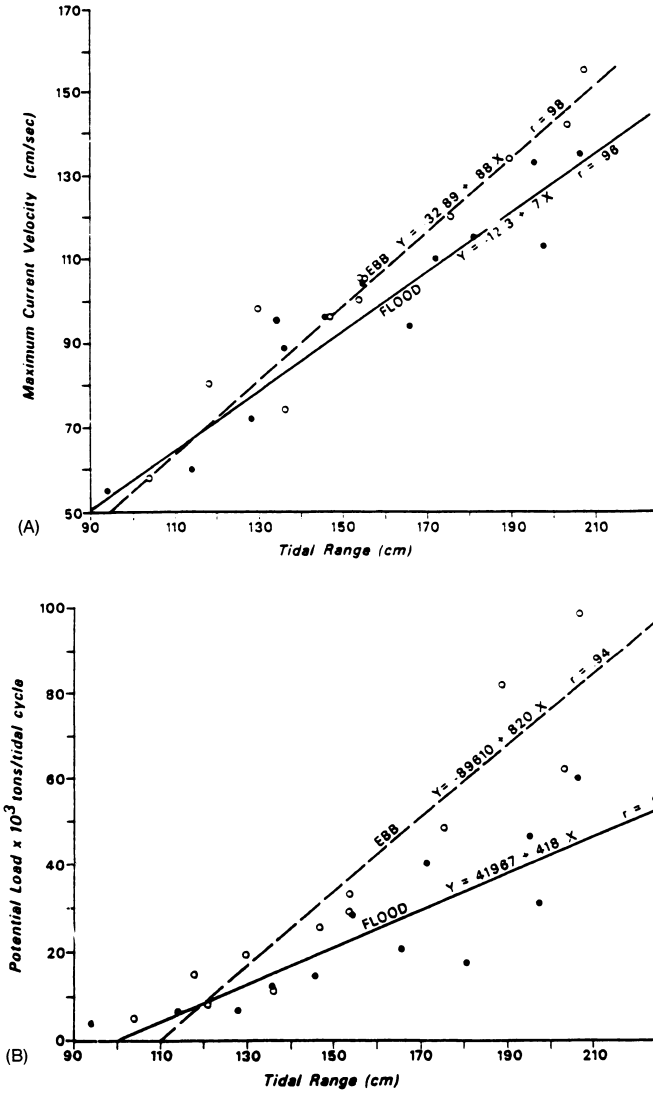

Figure 2.7.: 'Tidal-current velocity and sediment transport, Price Inlet, South Carolina. (A) Maximum current velocity versus tidal range (from FitzGerald (1977)). (B) Potential sediment transport calculated using Maddock Jr. (1969) relationship (from FitzGerald and Nummedal (1983): 'Potential load (tons/tidal cycle) has been calculated for the throat section of the main channel using Maddock Jr. (1969) relationship where bedload transport is proportional to the cube of the velocity. The individual values were calculated from velocity data measured at Price Inlet during varying tidal conditions. Except for very small tidal ranges, potential ebb transport dominates over flood.' (Boothroyd, 1985).

a laminite, and the individual layers are referred to laminae. Laminites whose vertically accreted, thinly bedded layers of medium- to fine-grained sandstone, siltstone, and mudstone are tidal in origin and exhibit periodic changes in thickness and grain size are also called tidal rhythmites (Dalrymple et al., 1991; Kvale, 2003; Mazumder & Arima, 2005; G. E. Williams, 1991). A sedimentary pattern particularly typical of tidal environments, such as tidal flats, is the herringbone cross-bedding (Reading, 1978; Reineck & Singh, 1973; G. E. Williams, 2000): The opposite directions of sediment transport during periodic successive ebb and flood phases can be represented in the sediments by successive cross-bedded sandstone layers separated by a muddy layer, forming a herringbone cross-bedding.

2.4.2. Examples

Flood and ebb deposition can form tidal rhythmites with as many as four laminae during the course of a tidal cycle (Figure 2.8). More commonly, however, tidal rhythmites are formed by pure flood or ebb deposition. That is, dominant flood or ebb currents and subordinate ebb or flood currents that are too weak to move and deposit sediment (Figure 2.8, C). In the common case where the subordinate tidal current is too weak for deposition, each pair of coarse and fine laminae represents a complete tidal cycle.

Relatively thick and thin successive sedimentary layers that alternate systematically can be left by semi-diurnal tides with a diurnal inequality, as observed in modern tidal deposits (Dalrymple et al., 1990; De Boer et al., 1989; G. E. Williams, 2000). Because of the diurnal inequality, the strength of successive semi-diurnal tidal currents can change systematically. Large tidal ranges will result in relatively thick layers of sediment, while smaller tidal ranges will result in thinner layers of sediment (Boothroyd, 1985; FitzGerald & Nummedal, 1983; G. E. Williams, 2000).

Similarly, tidal rhythmites can record the fortnightly cycle of neap and spring tides (Dalrymple et al., 1991; Smith et al., 1990; Tessier, 1993; G. E. Williams, 2000). Ideally, 28 pairs of sand-silt layers should form in a neap-spring tidal cycle for semi-diurnal tides. During the fortnightly spring tides, thicker semi-diurnal and diurnal sand layers result from the larger tidal ranges and thus faster tidal currents. The smaller tidal ranges and slower tidal currents favor the deposition of prominent muddy material during neap tides.

More than 28 occur when the subordinate tidal current is strong enough to deposit. Less than 28 may occur when the dominant current is too weak for deposition, such as during neap tides, or when erosion occurs during the spring tides. In contrast, only 14 dominant laminae follow for diurnal tidal regimes. The number of dominant laminae ranges from 14 and 28 in mixed tidal regimes. Thus, the record of the laminae can provide valuable information about the dominant tides during the depositon of the laminae. Deviations from the ideal case of cyclic rhythmites with 28 laminae are predominant in reality. Systematic thickness variations of successive neap-spring tidal cycles may further indicate other long-term tidal periods (G. E. Williams, 1991, 2000). The diurnal inequality and the neap-spring tidal cycle shown in Figure 2.9 are most commonly recorded in laminites. However, longer periods such as the lunar orbital precession are also known.

A complete tidal rhythmite is indicated by a continuous thick-thin alternation of the laminae. However, this can vary and gets disturbed frequently. Low sediment yields in summer or bioturbation can temporally disrupt tidal sedimentation. Meteorological events,

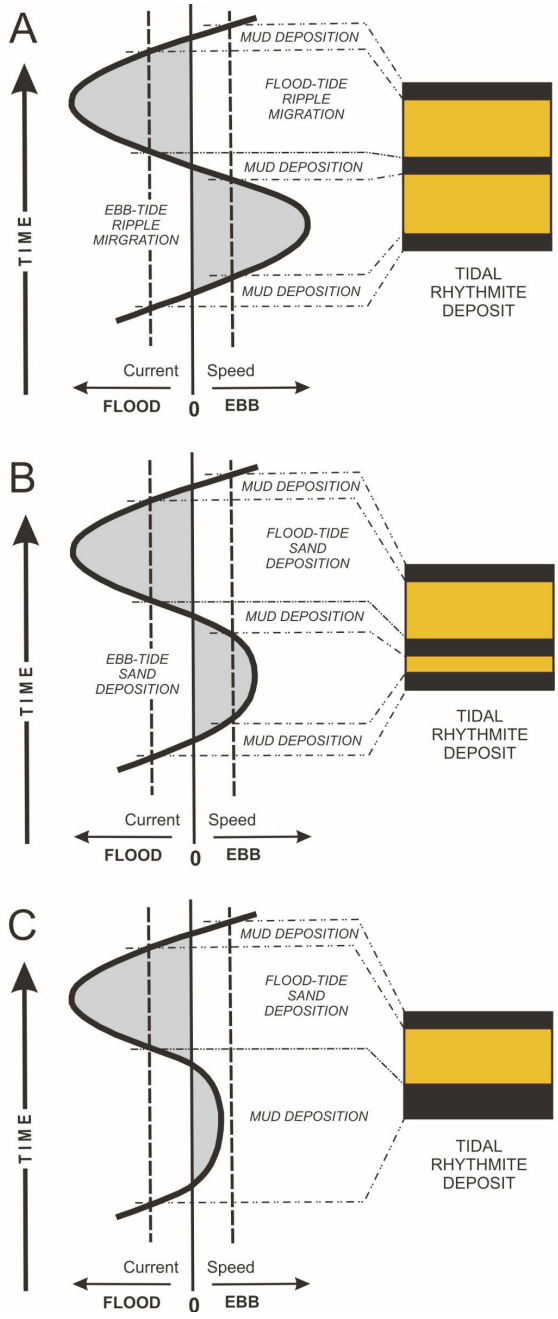

Figure 2.8.: 'Variation in tidal-current speed over a single tidal cycle and the corresponding tidal-rhythmite deposit. **A.** A symmetrical tide, with equal duration and magnitude of the flood and ebb currents, generates two sand layers of equal thickness. **B.** A flood-dominant situation, but with an ebb current that is capable of depositing a thin sand layer. The resulting alternation of thicker and thinner sand layers would mimic the pattern created by the diurnal inequality in a system such as (**C**). **C.** A highly asymmetric tide with an ebb current that is never capable of transporting sand. This situation is quite common in the tidal-rhythmite occurrences documented in modern and ancient successions. Based on Dalrymple et al. (1991).' (Dalrymple, 2010).

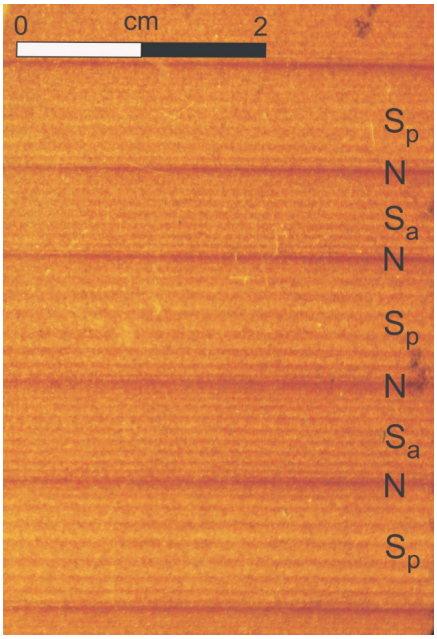

Figure 2.9.: 'Tidal rhythmites from the Elatina Formation (Neoproterozoic) of South Australia. Note how the thickness of the lighter colored coarser (silty) layers varies cyclically, from thicker during spring tides ('S') to thinner during neap tides ('N'). The subscript 'p' refers to perigee when the Moon is at its closest to Earth, whereas the subscript 'a' refers to apogee (the Earth–Moon separation is greatest). Note how the thickness of the spring-tide lamina is greater during perigee and thinner at apogee. See Williams (1991) for more details on these deposits.' (Dalrymple, 2010).

such as storms, can also lead to the incomplete formation of tidal rhythmites due to erosion. After the disturbance, there should be a return to the previous pattern. In comparison to an ideal situation, the number of tidal laminae will be lower. An evaluation of the tidal rhythmites is possible by means of the recorded neap-spring tidal cycles. As shown in Figure 2.9, the evaluation should reflect the monthly inequality caused by proximity to perigee (high spring tide) and by proximity to apogee (low spring tide). Gaps in the laminae due to insufficient tidal currents during neap tide may complicate the assignment to tidal deposits. However, each tidal indicator could also be formed by other processes and must be evaluated by the probability that the indicator is more common in tidal environments than in other environments. Often, inconclusive evidence must be used to determine tidal origin. A more comprehensive analysis of rhythmites allows to discriminate the underlying mechanisms (Archer et al., 1995).

The lunar orbital precession, with a period of 18.6 yr, leaves recognizable patterns in (sub-)recent tidal sedimentation in coastal systems (Allen, 2000). Mid-latitude tidal measurements show a 4 % to 5 % variation in tidal range over the period of lunar orbital precession (Flick et al., 2003; Oost et al., 1993; Stumpf & Haines, 1998). Sediment transport capacity may vary by 15 % to 20 % during the lunar orbital precession (Miller & Eriksson, 1997; Oost et al., 1993). The *lunar apsidal precessing* is weaker in the cyclic succession of laminae in tidally influenced sediments because of its weaker effect on tidal range (De Boer & Alexandre, 2012).

However, the data sets must be sufficiently long and complete. Furthermore, semi-diurnal tidal systems can mimic diurnal tidal systems in sediments. Tropical and synodic monthly cycles can also be similar. For a proper analysis, it is therefore necessary to be able to identify the type of the tidal regime in the sediments (Kvale et al., 1995). The analyses are still subject to the shortcomings and the incompleteness of the records. Much work remains to be done to obtain a more complete picture of the mechanisms that are important to the dynamics of specific depositional areas (Coughenour et al., 2009).

2.4.3. Environments

The macrotidal environment may create strong tidal currents. In addition, tidal rhythmites can develop in microtidal areas due to a large tidal prism. The regularity of the rhythmites is also protected by environments that are well protected from external disturbances such as storm waves or wind surges. Tidal rhythmites can form in environments ranging from estuaries, to the upper and lower slopes of deltas, to offshore intertidal deltas. In addition, particularly long and detailed rhythmites can form in a wave-protected distal ebb-tidal delta. Tidal currents can erode and suspend fine-grained sandy, silty, and muddy sediments in tidal inlets. These suspended sediments can be transported away from the coast by ebb currents across the main ebb channel to below the storm wave basis (i. e., 100 m water depth) to the marine shelf of the ebb-tidal delta (Özsoy, 1986; G. E. Williams, 2000). According to Longhitano et al. (2012, p. 5), ebb-tidal deltas ‘may be hundreds of metres to kilometres long and wide, and many tens of metres thick’, with seaward gradients of up to 12° in the terminal lobe (G. E. Williams & Gostin, 2019; Yang & Nio, 1989). In coastal areas, the distance traveled to and from typically reaches 10 km (Gerkema, 2019). The deposited laminae are relatively unaffected by the weak tidal currents (Özsoy, 1986; G. E. Williams,

2000). Only neap tides may have disturbed the deposited sand laminae. This is because neap tides could allow much fine material and distinct clayey laminae to become deposited between fortnightly groups of laminae. Such a relatively rapid drop in the depth of the ebb-tidal delta, together with low wave energy, would favor the preservation of the tidal rhythmites. Tidal deltas remain poorly understood (Dalrymple, 2010). See Willis (2005) for a detailed discussion of tidal deltas.

2.4.4. Analysis

A series of thickness data relative to the number of events (layers) can be obtained by examining the vertical sequence of tidal rhythmites (Archer et al., 1991). Thickness diagrams can be used to illustrate the cyclicity of tidal deposits. The main tidal constituents are evident from the quasi-sinusoidal harmonic fluctuations. In addition, the methods of time series analysis are used to unravel the periodicity of the tidal signals in the rhythmite records.

Harmonic analysis assumes that the observed tides are composed of a series of harmonic constituents. Their periods are equal to one of the periods of the relative astronomical motions in the Earth-Moon-Sun system (Section 2.2.2). Related to the tidal range and the resulting current velocity is the amount of sediment that can be transported and eventually be deposited as tidal rhythmites. For this reason, the paleo-periods of the Earth's rotation and the Moon's orbit can be determined by harmonic analysis of data from successive laminae with their bedding thickness as tidal rhythmites (cf. Archer et al., 1991; Kvale et al., 1995; Kvale et al., 1999; G. E. Williams, 1989b, 2000). Harmonic analysis is completed by optimized Fourier transforms, such as fast Fourier transforms, as well as probabilistic analyses and sophisticated spectral tests that can extract the periodicities and their reliability from a given data set (Archer, 1998; Archer, 1996a, 1996b; Archer & Johnson, 1997; Coughenour et al., 2009; De Azarevich & Azarevich, 2017; Kvale et al., 1995; Kvale et al., 1999; Visser, 1980; G. E. Williams, 2000; Yang & Nio, 1985).

The tidal rhythmite data can include the synodic month (new moon to new moon) and the tropical month of the Moon (maximum northerly declination to maximum northerly declination). This is in contrast to the Moon's sidereal period, which refer to a fixed celestial point. For further calculations, such as the Moon's distance from the Earth, sidereal periods are needed. However, there is a clear functional relationship between the sidereal, synodic, and tropical lunar orbital periods.

The *vernal equinox precession* is the link between sidereal month and tropical month, or the sidereal year and tropical year. By a tiny amount, the sidereal periods are longer than the tropical periods. In terms of the accuracy of tidal rhythmites, these tiny amounts can be neglected. Since there is no evidence of a change in the vernal equinox precession, they are also negligible in the history of the Earth. The tropical periods can be used as a substitute for the basic sidereal periods (Kvale et al., 1999).

The synodic month is longer than the sidereal month. This is due to the same orbital direction of the Moon around the Earth and the Earth around the Sun. There is currently exactly one more sidereal month in a year than are synodic months (Table 2.2, p. 30). Over the course of Earth's history, the current ratio of synodic months to sidereal months of 1.0808 may have changed only slightly. As the Moon approaches Earth, the Moon's periods

must decrease and the number of months per year must increase, while the length of the year remains the same. The ratio is decreasing toward 1. However, before the ratio reaches 1, the *Roche limit* will prevent the ratio from decreasing any further. A ratio of 1.08 should be sufficient for a conversion from sidereal to synodic months during the last billion years (Kvale et al., 1999).

One of the most important issues in analyzing long-term tidal periods is the non-tidal period of the year. Tidal rhythmites can also be the source of periodic, non-tidal sedimentary structures. The period of the year is an example. This occurs due to seasonal changes in ocean temperature, winds, and atmospheric pressure (Komar & Enfield, 1987; Pattullo, 1966; G. E. Williams, 2000; G. E. Williams & Gostin, 2019; Wunsch, 1972). Integrated analyses of ancient tidal rhythmites from multidisciplinary research have been instrumental in elucidating Earth paleo-rotation and lunar paleo-orbital dynamics (cf. Archer, 1996b; Archer et al., 1991; De Boer et al., 1989; Kvale et al., 1999; Oost et al., 1993; Piper, 1990; Rosenberg, 1997; Sonett et al., 1996; G. E. Williams, 2000, 2004). Modern data sets provide estimates of lunar orbital periods and Earth-Moon distance that are well within 1 % of the actual values (Kvale et al., 1999).

2.5. Summary

The various theoretical aspects of the present study were introduced and defined. Their interrelationship serves as a framework for the elaboration and methodology of the study.

The rotation of the Earth in Section 2.1, with its various fluctuations and changes in Section 2.1.1, was the starting point. By describing the Earth as part of the solar planetary system and the structure of the Earth in Section 2.1.2, the exogenous and endogenous causes were established. In particular, a significant effect on the secular decrease of the Earth's rotation rate has been identified in the ocean tides. Section 2.1.3 introduced the physical principles of the Earth's rotation.

The functional relationship between tidal mass displacements and the Earth's rotation in Section 2.2 is the first step in investigating the influence of tides. Of fundamental importance is the global material response of the Earth's solid body in Section 2.2.3 and of the oceans in Section 2.2.4 to the tidal force of the Moon and the Sun in Section 2.2.2. For example, ocean tides can be in resonance with ocean basins. Depending on the geometry of the ocean basin and the Earth's rotation rate, the tidal waves are attenuated or amplified.

A qualitative description of the secular tidal influence on the Earth's rotation rate in terms of tidal torques can be found in Section 2.3. Gravitationally, the tidal mass displacements interacts back with the Moon and the Sun, and a secular tidal torque can affect the Earth's rotation rate and the Moon's and Earth's orbits. However, the effect on the Earth's orbit is negligible.

Finally, tidal sedimentation in the form of tidal rhythmites was discussed in Section 2.4. Considerable information about the history of the Earth's rotation and the Moon's orbit can be obtained from tidal rhythmites.

Recent empirical and numerical data and methods on tidal friction and ocean tides in modern and geologic times follow in the next chapter.

3. State of the art and related work

The empirical, analytical, and numerical methods used to obtain the data, as well as the data itself, on the secular tidal evolution of the Earth's rotation rate for modern times and in the Earth's history in this chapter complement the preceding theoretical foundations with regard to the background of the present study. Observational and analytical data on the secular acceleration of the Earth's rotation rate are presented in Section 3.1 for modern times (Section 3.1.1), for Earth history (Section 3.1.2), and the Neoproterozoic period ~620 Myr ago (Section 3.1.3). In the data for modern times, the outstanding influence of the ocean tides on the secular decrease of the Earth's rotation rate and on the transfer of angular momentum between Earth and Moon can be well recognized. To be able to study their influence, modeling the spatial and temporal characteristics of ocean tides is discussed first in (Section 3.2.1). Investigations using numerical modeling of ocean tides on their effect on the secular change of the Earth's rotation rate are presented in Section 3.2.2 for modern times, for individual geological epochs, and for the Earth's history. The considerations will integrate related work.

3.1. Secular rate of Earth's rotational velocity

The deceleration of the Earth's rotation rate, as shown in Tables 3.1 to 3.5, p. 80 to 83, can be expressed in terms of the three equivalent quantities (Section 2.1.3.1): the change in the Earth's rotational energy with time $\dot{E}_{rot}$, the torque exerted along the axis of rotation M_z, and angular acceleration of the Earth $\dot{\Omega}_{\delta}$ or the increase in the length of day $\Delta l.o.d.$ This section will focus on the observed tidal deceleration of the Earth's rotation rate for modern times in Section 3.1.1, for the Earth's history in Section 3.1.2, and specifically for the Neoproterozoic Era ~620 Myr ago in Section 3.1.3.

3.1.1. Modern times

There are more than 3000 years of astronomical evidence for a decrease in the Earth's rotation rate. Based on earlier work by Stephenson et al. (1995), Stephenson et al. (2016) used reports of solar and lunar eclipses between 750 BC and 2015 AD to observe an average increase in day length of (1.78 ± 0.03) ms/cy (Section 2.1.1, p. 13). This secular increase in the length of the day has to be considered as an average integral quantity consisting of tidal and non-tidal components.

Finally, in 1969, the LLR experiment (Seitz & Müller, 2016) was launched to continuously measure the distance to the Moon using laser pulses. The time it takes for a laser pulse to travel from an observatory's telescope on Earth to a retroflector on the Moon and back to the observatory's telescope on Earth is measured. The measured times are conveniently

multiplied by the speed of light and called ranges. These ranges contain information about the Earth, the Moon, and the lunar orbit (J. G. Williams et al., 2006). Apart from astronomical observations, LLR measurements are the longest data series for the determination of variations in Earth rotation rate (Seitz & Müller, 2016). LLR data from recent decades have accuracies in the centimeter to millimeter range (Battat et al., 2023; Colmenares et al., 2023; Murphy et al., 2012; Samain et al., 1998). Additional data sources are now available from other space geodetic techniques, such as Satellite Laser Ranging (SLR). Estimates of tidal parameters from near-Earth orbits of artificial satellites can be directly applied to the secular evolution of lunar orbit and Earth rotation rate. The same parameters that cause short-period perturbations in satellite orbits also describe the secular variation of the lunar orbit (Lambeck, 1975; Lambeck & Cazenave, 1977; Lambeck et al., 1974). The LLR measurements reveal the tidal effects on the Earth's rotation, unlike the astronomical observations and the SLR approach, which consider both tidal and non-tidal effects.

For decades, the change of the Earth's oblateness and thus of the principal polar moment of inertia with a decreasing trend and periodic components has been observed, e. g. by analysis of SLR data (Cheng et al., 2013; Marchenko & Lopushanskyi, 2018). A decreasing polar moment of inertia results in an increase in rotation rate or a decrease in day length according to section Section 2.1.3. Factors include continental drift, changing coastlines, melting glaciers, sea level rise, and glaciation (Baenas et al., 2021; Deines & Williams, 2016). Signals from the exchange of angular momentum between the liquid outer core and the mantle can also be detected, which are expected to vary on millennial timescales (Baenas et al., 2021; Dumberry & Bloxham, 2006; Mitrovica et al., 2015). The most important effect is likely glacial isostatic adjustment, due to the viscous rebound of the solid Earth body from the reduced load on the polar caps following the last deglaciation (Baenas et al., 2021; J. G. Williams & Boggs, 2016). Modeling Earth's radial viscosity profile, Mitrovica and Forte (1997) found that glacial isostatic adjustment should cause a secular decrease in day length of $-0.5\,\mathrm{ms/cy}$ (Gross, 2007). It is noteworthy that this value is constistent with the difference between the observed total secular increase in day length of $(1.78 \pm 0.03)\,\mathrm{ms/cy}$ (Stephenson et al., 2016) and the increase due to the tides of $(1.78 \pm 0.03)\,\mathrm{ms/cy}$ (J. G. Williams & Boggs, 2016). Morrison et al. (2021) updated the difference to $-0.7\,\mathrm{ms/cy}$.

Following the discovery of tidal perturbations in artificial satellites orbits in the mid-1960s, it became possible to estimate the delay angle ϵ of the Earth's body tides relative to the astronomical tidal potential (Section 2.3 and Figure 2.6) from observations combining SLR and satellite altimetry data (Ray et al., 2001). By updating the lag angle of the principal lunar semi-diurnal tide M_2 to $\epsilon = (0.204 \pm 0.047)°$, Ray et al. (2001) could reduce the rather large error limits of Ray et al. (1996) by almost 50 %. Although the empirical data for estimating ϵ is not strong (Ray et al., 2001), estimates based on Earth models are in good agreement with Ray et al. (2001). Both studies were restricted to the M_2 tide. The solar tides were excluded due to superimposed atmospheric effects. The diurnal tides are smaller and less reliable to determine (Ray et al., 2001). For the lag of the ocean loading tide, no comparable useful information could be derived. The lag angle in the tides of the solid Earth body is associated with a loss of tidal energy of 0.11 TW. Ray et al. (2001) calculated this value based on work done by Platzman (1984). As shown in Table 3.2, p. 81, this is

more than an order of magnitude smaller than the M_2 tidal dissipation rate in the oceans and an order of magnitude larger than the rate in the atmosphere (Ray et al., 2001). From the altimetry and tracking analysis, Ray et al. (2001) estimated the M_2 planetary tidal dissipation to be (2.536 ± 0.016) TW, using the prograde spherical harmonic coefficients of 2^{nd} degree and 2^{nd} order of the M_2 tidal elevations (Appendix C.1). The altimetric coefficients implied an oceanic tidal dissipation of (2.421 ± 0.015) TW. The tides of the solid Earth body and the atmosphere account for the difference of 0.115 TW (Table 3.2, p. 81). It has been assumed that the ocean loading tide is only slightly delayed with $\epsilon' \approx 0$ (Zschau, 1978) and does not cause any significant dissipation as estimated in Platzman (1984). Thus, the M_2 tide of the solid Earth body contributes less than 5 % and that of the atmosphere less than 1 % to the M_2 planetary tidal dissipation (Table 3.2, p. 81).

Geodetic satellite measurements can also be used to estimate the tidal torques (Section 2.3) of the Moon and the Sun on the ocean tides (Ray et al., 1999). Using the prograde spherical harmonic coefficients of the tidal elevation of the same degree and order as those of their generating astronomical tidal constituent (Appendix C.1), Ray et al. (1999) estimated the mean polar component of the tidal torque and the tidal secular deceleration of the Earth's rotation rate (Equation (2.8)). For the EGM (Earth geopotential model) 96S (Lemoine et al., 1998), a satellite-only Earth gravity solution, the coefficients are based on optical, Doppler, laser and GPS (Global Positioning System) tracking of 40 artificial satellites (Ray et al., 1999). Using these, for example, Ray et al. (1999) examined the effect of 4 fundamental semi-diurnal and 4 fundamental diurnal ocean tides, as listed in Tables 3.1 to 3.5, p. 80 to 83. Overall, there is a slowing of the Earth's rotation rate corresponding to an increase in the length of day of 2.373 ms/cy (Table 3.1, p. 80). The M_2 tide alone causes an increase of 1.612 ms/cy (Table 3.2, p. 81). This accounts for about 70 % of the total deceleration of the Earth's rotation rate. Compared to the tidal dissipation of the M_2 tide of Ray et al. (2001), the derived decrease in the Earth's rotational energy of 2.623 TW due to the M_2 tide is about 8 % greater. The S_2 (Table 3.3, p. 82), the K_1 (Table 3.4, p. 83), and the O_1 (Table 3.5, p. 83) tides are the next largest contributions, decreasing in magnitude. With the atmospheric S_2 tide accelerating the Earth's rotation rate (Ray et al., 1999, and references therein), the increase in the length of day due to the oceanic S_2 tide of 0.224 ms/cy is reduced by −0.096 ms/cy.

The Earth's rotational acceleration in J. G. Williams and Boggs (2016) is derived by evaluating the tidal torque about its polar axis (Equation (2.8)), which causes the Earth's rotational velocity to change. The small dependence of the polar principal moment of inertia on the rotation rate is accounted for by a factor for the moment of inertia (Equation (2.7), p. 22). The evaluation combines the effect of the tides of the oceans and of the solid body of the Earth. For the body tides, the frequency-dependent Love numbers of the Earth body were taken from Petit and Luzum (2010). For the ocean tides, the Love numbers were derived from the ocean tide simulations of the FES (Finite Element Solution) 2004 model (Lyard et al., 2006) (Section 3.2.1, p. 73). According to the imaginary parts of the Love numbers for the solid Earth body and the oceans in J. G. Williams and Boggs (2016), ~5 % of the energy dissipation occurs in the body and ~95 % in the oceans, which is in agreement with Ray et al. (2001) (Table 3.1, p. 80). Following the analytical Earth rotational acceleration, the day length increases by 2.411 ms/cy (J. G. Williams & Boggs, 2016) as shown in Table 3.1, p. 80. The diurnal tides ($m = 1$) account for 0.344 ms/cy and

the semi-diurnal tides ($m = 2$) for 2.067 ms/cy (J. G. Williams & Boggs, 2016). As can be seen in Tables 3.2 to 3.5, p. 81 to 83, the M_2 tide dominates the slowing of the Earth's rotation rate and the increase in day length. However, the S_2, K_1, and O_1 tides also make a significant contribution. This extracts 3.78 TW from Earth's rotation, of which 0.122 TW is transferred to the lunar orbit and ~0.014 TW to the solar orbit, leaving 3.64 TW dissipated (J. G. Williams & Boggs, 2016). When the analytical results are adjusted to the LLR data, the tidal delay of the Earth's rotation is an increase in day length of 2.394 ms/cy. In terms of tidal energy dissipation, the two approaches differ by less than 1 % (J. G. Williams & Boggs, 2016).

Furthermore, Baenas et al. (2021) have analytically investigated the tidal secular evolution of the Earth's rotation rate using the Hamiltonian formalism of Earth rotation theories, including a dissipative torque at the core-mantle boundary (CMB). The best estimate they obtained for a two-layer Earth model with an anelastic mantle with oceans and a liquid core. As in J. G. Williams and Boggs (2016), the tides of the solid Earth body with ocean loading are described by frequency-dependent Love numbers taken from Petit and Luzum (2010). The ocean tides are implemented following J. G. Williams and Boggs (2016). As shown in Table 3.1, p. 80, the resultant increase in day length of 2.418 ms/cy, as in J. G. Williams and Boggs (2016), is mainly due to the semi-diurnal tides ($m = 2$) at 2.071 ms/cy, of which 1.959 ms/cy is due to the ocean tides alone. The diurnal tides ($m = 1$) with an increase of the day length of 0.348 ms/cy are also mainly due to the ocean tides with 0.352 ms/cy. However, the tides of the solid Earth body cause an acceleration of the Earth's rotation rate and a decrease of the day length by -0.004 ms/cy. This is due to the K_1 tide closely resonant with the oblate CMB (J. G. Williams & Boggs, 2016). With 2.067 ms/cy, the tides caused by the Moon account for 85.45 % of the increase in the length of the day, while the tides caused by the Sun contribute only 14.55 % with 0.352 ms/cy. The same underlying Love numbers explain the very good agreement of the numerical results with J. G. Williams and Boggs (2016).

The day length increases by 2.394 ms/cy as shown in Table 3.1, p. 80, due to the mean tidal deceleration of the Earth's rotation rate estimated by J. G. Williams and Boggs (2016) from LLR measurements. This involves transferring energy and angular momentum from the rotating Earth to the lunar and solar orbits. It causes the Moon to move away from the Earth at a rate of (38.30 ± 0.08) mm/yr, with the tides on the Moon reducing this rate by about 1 % (J. G. Williams & Boggs, 2016). The effect on the Earth orbit around the Sun is small, -1 mm on solar longitude after ± 1 decade (J. G. Williams & Boggs, 2016). Christodoulidis et al. (1988) already observed a tidal deceleration of the Earth rotation of (2.24 ± 0.08) ms/cy based on the analysis of SLR data (Baenas et al., 2021). Using an indirect method based on fossil data, Deines and Williams (2016) were able to estimate a confirmatory mean tidal deceleration of (2.23 ± 0.66) ms/cy (Baenas et al., 2021). Consistent with this, Stephenson et al. (2016) estimated the average increase in day length due to the tides of the solid Earth body and the oceans to be (2.3 ± 0.1) ms/cy. They relied on the empirical relationship between the observed tidal acceleration of the Moon and the deceleration of Earth's rotation due to lunar and solar tides by Christodoulidis et al. (1988).

With respect to the secular tidal increase in day length, as shown in Tables 3.1 to 3.5, p. 80 to 83, the oceanic M_2 contributes about 70 % of the total increase. Most of the planetary tidal dissipation is due to M_2, as been known for decades (Munk & McDonald,

1960). This is followed by the S_2 tides, where the atmospheric tide accelerates the Earth's rotation at $55''/cy^2$ (Table 3.3, p. 82), counteracting the increasing day length (Ray et al., 2001).

Another method of estimating tidal friction due to ocean tides (Section 3.2.2) has been established with the advent of numerical simulations of global ocean tides and high performance computers (Section 3.2.1).

3.1.2. Earth history

The annual growth rhythms of recent and fossil corals, bivalves, and calcareous plants have long been known to be driven by seasonal changes in water temperature. J. W. Wells (1963) made the discovery that corals also exhibit a diurnal growth pattern. This provided the first direct estimate for the Middle Devonian, about 380 Myr ago (Table 1.1, p. 2). The paleo-rotation rate of the Earth was about 400 d/yr (Figure 1.1) with an assumed year length equal to that of today. Subsequent studies of the growth pattern of marine invertebrate fossils generally showed, consistent with the tidal friction hypothesis (Brosche & Sündermann, 1978; Rosenberg & Runcorn, 1975), a decreasing number of days per year since the *Paleozoic* (~539 to 252 Myr ago), as shown in Figure 1.1, and thus an increasing day length through time to the present. Scrutton (1978) pointed out that the present increase in day length and lunar distance appears to be particularly high, that similarly high values occurred in the Ordovician (450 Myr ago), but that in between there were long epochs of much smaller increases (factor 2) with a minimum in the Perm (230 Myr ago).

However, the high expectations that were placed on such paleontological geochronometers have not been fully met. Concerns about the reliability of much of this Paleozoic paleontological data have been raised by extensive research by Lambeck (1980b) and Scrutton (1978). In addition, the reliability of paleo-rotation data derived from growth patterns of *Precambrian* (~4600 to 539 Myr ago) stromatolites has been the subject of controversial debate (Lambeck, 1980b; Pannella, 1975, 1976; Vanyo & Awramik, 1985).

Considerable information about the history of the Earth's rotation and the Moon's orbit can be obtained from tidal rhythmites (Section 2.4; Kvale et al., 1999; Rosenberg, 1997; Sonett et al., 1996; G. E. Williams, 1989a, 1989b, 2000). A record of neap-spring tidal cycles in modern Holocene sediments was first discovered by Visser (1980). Soon after, Allen (1981) observed tidal periods in Cretaceous rock records. The best documented tidal rhythmites are Carboniferous, with semi-diurnal to annual periodicities (Archer, 1991; M. A. Brown et al., 1990; Kvale & Archer, 1991; Kvale et al., 1995). A Neoproterozoic (~900 Myr ago) rock record from the Big Cottonwood Formation in central Utah, USA, shows a comparable range of periodicities (Chan et al., 1994). Late Neoproterozoic (~620 Myr ago) cyclic rhythmites of proposed tidal origin are best seen in the Elatina Formation in South Australia (G. E. Williams, 1988, 1989a, 1989b, 1991, 2000; G. E. Williams, 1989c, 1990, 1997, 1998b). However, little is known about the role of tides in the earliest rock record (Coughenour et al., 2009; P. G. Eriksson et al., 2013; Kagan, 1997; G. E. Williams, 2000; G. E. Williams, 1990).

Rarely can sediments be used to infer the influence of lunar apsidal precessing and lunar orbital precession. Nearly a decade or two of uninterrupted sedimentation would be required (Miller & Eriksson, 1997; Oost et al., 1993). Therefore, the detection is sporadic in the

history of Earth (Archer, 1996a; Kvale et al., 1994; Miller & Eriksson, 1997; Oost et al., 1993; G. E. Williams, 2000). Both cycles, the lunar apsidal precessing and lunar orbital precession, were detected by G. E. Williams (1989b) in the Neoproterozoic (~620 Myr ago) Elatina Formation. Miller and Eriksson (1997) recognized multi-year cyclicity in the Mississippian Bluestone Formation (358.9 Myr to 323.2 Myr ago) of southern West Virginia, USA, possibly reflecting the lunar nodal cycle.

Deines and Williams (2016, Table 1) have summarized the evolution of the Earth's rotational rate over the course of Earth's history from the final results of the various available paleontological reports shown in Figure 1.1. The data generally show a pattern of non-linear decrease in the number of days per year over the geologic history, consistent with Denis et al. (2002), Varga et al. (1998), and G. E. Williams (2000). The average length of day has increased to the present for a constant year length throughout Earth history (Simon et al., 1994; J. G. Williams & Boggs, 2016). Possible conflicting data are included as well. For example, from fossil data, ~420 d/yr to 400 d/yr are reproduced for the period from ~520 Myr to 350 Myr ago in the Paleozoic For the period from ~620 Myr ago in the Late Neoproterozoic, ~400 d/yr have also been analyzed using tidal rhythmite data (G. E. Williams, 2000). The fossil origin of the Paleozoic data might explain part of the contrast. For the Precambrian, and the more recent geological history from Mesozoic (~252 Myr to 66 Myr ago) to Cenozoic (~66 Myr ago to present) there are only a few data available. In addition, the seven available Earth-Moon distances derived from tidal rhythmites in Earth's history show a pattern of non-linear, progressively increasing distances and thus lunar cycles (Coughenour et al., 2013; De Azarevich & Azarevich, 2017; K. A. Eriksson & Simpson, 2000; Kvale & Archer, 1990; Sonett & Chan, 1998; G. E. Williams, 2000).

3.1.3. Paleo-rotation of ~620 Myr ago

Distinct cyclic rhythmites have been found in the Elatina Formation (Late Neoproterozoic ~620 Myr ago) at Pichi Richi Pass in the southwest of the Flinders Ranges and in the Reynella Siltstone at Hallet Cove south of Adelaide (Figure 3.1 and G. E. Williams, 1989a, 1991, 2000). These deposits (Figures 3.2 and 3.3) are called the Elatina and the Reynella rhythmite, respectively. Their sedimentation characteristics are indicative of a tidal origin (G. E. Williams, 1989a, 1989b, 1991, 2000; G. E. Williams, 1998b). They are of exceptional length and completeness. The rhythmites in question represent a distinctive natural data set that can be employed for the purpose of validating a paleo-oceanographic tidal model.

After a fundamental description of the two tidal rhythmites in Section 3.1.3.1, which also highlights their tidal origin, Section 3.1.3.2 presents the results of their analysis in relation to the Earth's rotation and the Moon's orbit ~620 Myr ago. Section 3.1.3.3 on the geographical environment of the tidal rhythmites concludes this section with regard to the validation of simulations of the paleo-tides.

3.1.3.1. Description

The herringbone cross-bedding pattern (Section 2.4.1) of sedimentation that is typical of tidal environments is characteristic of the Reynella rhythmite (G. E. Williams, 1989b, 1991, 2000). The Reynella and Elatina rhythmites, with their cycles of sandy and silty laminae

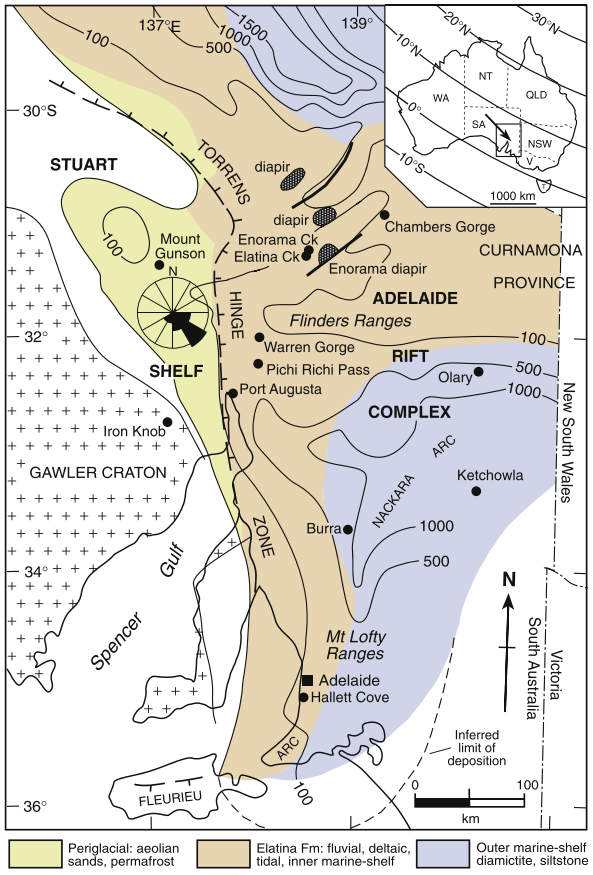

Figure 3.1: Sedimentary facies for the late Cryogenian Elatina glaciation (Yerelina Subgroup), South Australia. Permafrost regolith with primary sand-wedges and periglacial-aeolian sand sheet on the cratonic Stuart Shelf pass eastward to glaciofluvial, deltaic, subtidal and inner marine-shelf deposits of the Elatina Formation in the Adelaide Rift Complex. These pass further eastward to outer marine-shelf diamictites and mudstones-siltstones with ice-rafted detritus. Isopachs in metres. Inset shows palaeolatitudes for Australia during the Elatina glaciation (Schmidt et al., 2009). Rosette and arrow (inset) indicate palaeowind direction for aeolian sands (G. E. Williams, 1998a). Adapted from Preiss (1993). WA, Western Australia; NT, Northern Territory; SA, South Australia; QLD, Queensland; NSW, New South Wales; V, Victoria; T, Tasmania. (G. E. Williams & Gostin, 2019).

bounded by mud drapes, respectively (Figure 3.2(a, b, c, and d) and in Figure 3.3(a, b, c, and e)), demonstrate the sedimentation pattern of the neap-spring tidal cycles (Section 2.4.2 and Figure 2.9). Thick laminae appear around the center of each cycle (G. E. Williams, 1991, 2000)). In numerous instances, as demonstrated in Figure 3.2(a and d) and Figure 3.3(a, b, and c), the alternating succession of relatively thick and thin neap-spring tidal cycles indicates the monthly inequality of the tides due to the lunar proximity to perigee and apogee, respectively.

Some of the laminae of the neap-spring tidal cycles in the Reynella rhythmite are composed of two graded layers or sublaminae (Figure 3.2(c, d, and e)). This systematic alternation of successive relatively thick and thin laminae indicates, as described in Section 2.4.2, the sedimentation pattern of the diurnal inequality of the semi-diurnal tides. These have been identified as corresponding to the diurnal and semi-diurnal increments, respectively. The data indicate a mixed semi-diurnal and diurnal tidal pattern, as outlined by G. E. Williams (2000) and depicted in Figure 1.6. On occasion, semi-diurnal sublaminae are observed in the Elatina rhythmite (Figure 3.3(e)). It is likely that the tidal heights and current velocities of the lower semi-diurnal tides of the diurnal inequality were insufficient to transport sediment to the deposition site. Accordingly, they may be filtered by sedimentation (G. E. Williams, 2000).

A comparison of the thickness variations in the diurnal laminae and over the fortnightly laminae cycle of the Elatina rhythmite with observed tides of the mixed, mainly semi-diurnal tidal regime at Townsville shows a remarkable similarity (G. E. Williams, 1991, 2000). In

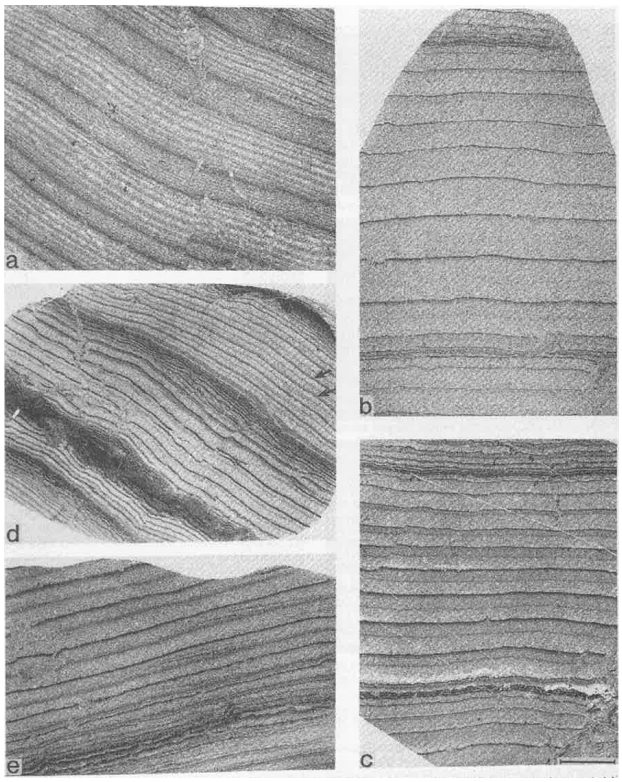

Figure 3.2: 'Thin sections of rhythmites from the Reynella Siltstone, Hallett Cove, viewed with transmitted light; opaque clayey material appears darker than translucent sandy layers. The fortnightly lamina-cycles shown comprise weakly graded diurnal laminae and semidiurnal sublaminae of very fine grained sandstone with clayey tops. Scale bars 1 cm for all photographs. **a.** Nine alternately thick and thin lamina-cycles, indicating the monthly inequality. **b.** One complete lamina-cycle containing diurnal laminae up to 8 mm thick. **c.** One complete lamina-cycle containing diurnal laminae up to 6 mm thick; semidiurnal sublaminae also evident. **d.** The uppermost lamina-cycle comprises diurnal laminae up to 3 mm thick marked by alternate darker bands, and semidiurnal sublaminae of about equal thickness; the arrows mark double mud drapes. In the cycle immediately below, the lower semidiurnal sublamina in each pair is thicker, indicating the diurnal inequality. **e.** Portions of two lamina-cycles; in the upper part of the photograph, diurnal laminae up to 6 mm thick marked by alternate darker bands contain semidiurnal sublaminae of about equal thickness.' Reproduced from G. E. Williams (1989a) with permission of Canadian Society of Petroleum Geologists, Calgary.

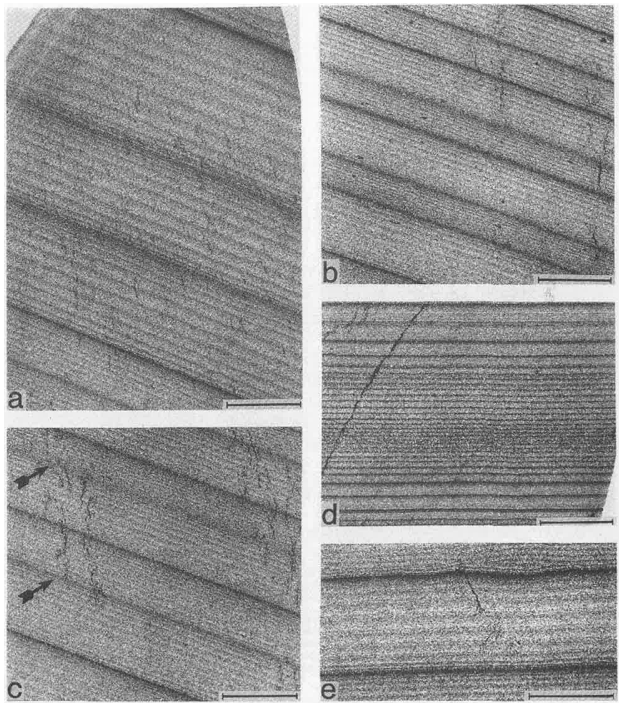

Figure 3.3: 'Thin sections of rhythmites from the Elatina, Pichi Richi Pass, viewed with transmitted light; opaque clayey material appears darker than translucent sandy layers. The specimens are from drill core. Scale bars 1 cm. **a.** Graded (upward fining) diurnal laminae up to 3 mm thick comprising a lower, paler layer of very fine grained sandstone and an upper layer of clayey siltstone; four complete fortnightly lamina-cycles of about 10 to 14 laminae are bounded by conspicuous, dark, mud drapes. **b.** Thinner laminae and lamina-cycles with alternate thick and thin lamina-cycles indicating the monthly inequality. **c.** Alternate boundaries between lamina-cycles represented by very thin silty laminae (arrows) rather than mud drapes; the lamina-cycles appear unabbreviated at these horizon. **d.** Very thin (0.5 mm to 3 mm) fortnightly lamina-cycles near the base of the rhythmite member; internal lamination between mud drapes is only discernible in a few places. **e.** Rare lamina-cycle that comprises laminae as well as sublaminae (best seen looking along the bedding) that are interpreted as semidiurnal increments.' Reproduced from G. E. Williams (1991) with permission of Canadian Society of Petroleum Geologists, Calgary.

addition, the internally self-consistent paleo-tidal and paleo-rotational values obtained from analyzing the rhythmite data support a tidal origin (G. E. Williams, 2000). A non-tidal annual signal (Section 2.4.4, p. 57) is also recorded in the deposits.

The ~10 m thick Elatina rhythmite indicate continuous depostion of 1580 neap-spring tidal cycles over a period of ~70 yr. It also contains a short record of ~4.2 yr with 1337 distinguishable diurnal sediment layers from 110 neap-spring tidal cycles (G. E. Williams, 2000). Fourier spectral analysis of the data provides a nearly noise-free spectrum with distinct peaks at the annual, semi-annual, and monthly tidal periods. The nearly undisturbed data of the Elatina rhythmite allow the influence of fluvial and other random events on the deposition to be neglected in comparison to the dominant influences of the tides on deposition (G. E. Williams, 1991).

3.1.3.2. Results

For the Neoproterozoic at ~620 Myr ago, G. E. Williams (1989a, 1989b, 1991, 2000) and G. E. Williams (1998b) was able to estimate an astonishing variety and accuracy of the Earth's paleo-rotation rate and lunar paleo-orbital rates, as shown in Table 2.2, p. 30, from the Elatina and the Reynella rhythmites. The rhythmites indicate 29.5 (currently 28.5) lunar days and 30.5 (currently 29.5) solar days per synodic month and 28.3 (currently 27.3) solar days per sidereal month, respectively. Spectral analyses derived 26.1 or 26.2 neap-spring tidal cycles (depending on the analysis) and thus 13.1 (currently 12.4) synodic months per year and 14.1 (currently 13.4) sidereal months per year. This results in 400 solar days per year (30.5 solar days per synodic month × 13.1 synodic month per year) and, assuming a non-significant annual length change from today of 31.56×10^6 s, a solar day length of 21.9 h at that time (currently 24 h).

The Elatina and Reynella rhythmites show a monthly inequality in the pattern of the neap-spring tidal cycle. Spectral analyses yielded 14.6 (currently 13.9) synodic months for the tidal year and 13.1 (currently 12.4) synodic months for the solar year, resulting in a perigee precession period of 9.7 yr (currently 8.9 yr). Even the lunar node precession period of 19.5 yr (currently 18.6 yr) could be derived from the Elatina rhythmite by means of spectral analysis (Section 2.2.2, p. 33). Due to the annual fluctuation of the sea level (Section 2.4.4, p. 57), which is independent of the tides and which usually shows highest rise in autumn, the Elatina rhythmite allowed the determination of the solar year together with the summer and winter solstices as well as the autumn and spring equinoxes.

The mean distance of the Moon from the Earth of 58.2 $R_\eth$ (currently 60.3 $R_\eth$) for ~620 Myr ago was determined in good agreement using three independent methods and parameters from celestial mechanics, such as the lunar node precession period, the number of sidereal month per year, and the number of sidereal days per year. Over the past ~620 Myr, this results in a lunar recession rate of 2.2 cm/yr. This averaged rate is only 57 % of the present rate of 3.8 cm/yr determined from LLR. Although the month was shorter about ~620 Myr ago, the length of the day was proportionally even shorter: the number of days in the month was thus larger, not smaller (Table 2.2, p. 30).

The results of the investigations of the Elatina and Reynella rhythmites, in conjunction with astronomical and astrometric observations, indicate no significant changes in the Earth's radius and principal moments of inertia over the past ~620 Myr. In particular, there

is no evidence to suggest that the Earth has undergone a rapid endogenous expansion since the Paleozoic.

The fundamental periods for the lunisolar tidal potential are thus available for ~620 Myr ago. Next, information on the geographic setting of the Elatina and Reynella rhythmites is provided for the purpose of paleo-oceanographic tidal modeling.

3.1.3.3. Geographical environment

The name Elatina Formation is derived from the late Cryogenian glaciation, which Mawson (1949) referred to as the 'Elatina glaciation' (G. E. Williams & Gostin, 2019). Also referred to as the Marinoan glaciation of ~650 Myr to 635 Myr ago (Hoffman et al., 2017; Rooney et al., 2015), this, along with the Sturtian glaciation of ~717 Myr to 660 Myr ago (Hoffman et al., 2017; Hoffman et al., 1998; Rooney et al., 2015), is proposed to have largely characterized the Cryogene with a near-global glaciation, the so-called '*Snowball Earth*' (Hoffman et al., 2017; Hoffman et al., 1998). The continental ice is proposed to have advanced to very low latitudes (Macdonald et al., 2010). This may have left an open equatorial ocean.

So far, no direct age determination for the Elatina glaciation exists (G. E. Williams et al., 2008; G. E. Williams & Gostin, 2019). A maximum and minimum age for the Elatina glaciation of ~640 Myr and ~580 Myr is given by G. E. Williams et al. (2008). G. E. Williams and Gostin (2019) suggest an age of ~635 Myr. For the Elatina tidal rhythmites, G. E. Williams (1991) gives an age of ~635 Myr. G. E. Williams (2000) gives an age of ~620 Myr.

Extensive periglacial and glacial environments with glaciofluvial, deltaic, *subtidal* and inner marine shelf deposits have been recorded in the Elatina Formation strata in the western and central Adelaide Rift Complex of South Australia (Figure 3.1 and G. E. Williams & Gostin, 2019). Early Neoproterozoic rifting of a Precambrian craton resulted in formation of the gulf-like Adelaide Rift Complex. The craton is now presented by the Gawler Craton to the west and the Curnamona Province to the east (G. E. Williams et al., 2008). The eastern Gawler Craton has permafrost regolith covered by periglacial-aeolian sand (G. E. Williams, 1998a; G. E. Williams & Tonkin, 1985; G. E. Williams et al., 2016). At best, the cratonic region has only light glaciation. The climate was frigid and highly seasonal, with paleo-westerly to paleo-northwesterly winds near sea level. Quite different is the Elatina Formation to the east, where fluvial, deltaic and inner marine shelf environments with glaciomarine deposition are dominant, especially in the central Flinders Zone. In turn, an outer marine shelf developed by subsidence along a passive margin in the Nackara Arc to the southeast and to the north (Coats & Preiss, 1987; Lemon & Gostin, 1990; Preiss, 1993; G. E. Williams et al., 2008; G. E. Williams et al., 2011).

Discrete depositional units within the Elatina Formation indicate a fluctuating ice margin. There is evidence of up to six glacial advances and retreats during the Elatina glaciation (G. E. Williams & Gostin, 2019). Neither extreme nor rapid sea level rise during the Late Cryogenian in South Australia is supported by stratigraphic sedimentary, and paleomagnetic data (G. E. Williams & Gostin, 2019). There is also no evidence for the late Cryogenian model that ice sheets of many kilometers thick covered all continents of the Earth, followed by rapid deglaciation with extreme and rapid sea level rise (P. G. Eriksson et al., 2013; G. E. Williams & Gostin, 2019). In addition, the annual non-tidal seasonal depositional pattern in the Elatina rhythmite should have been prevented because the

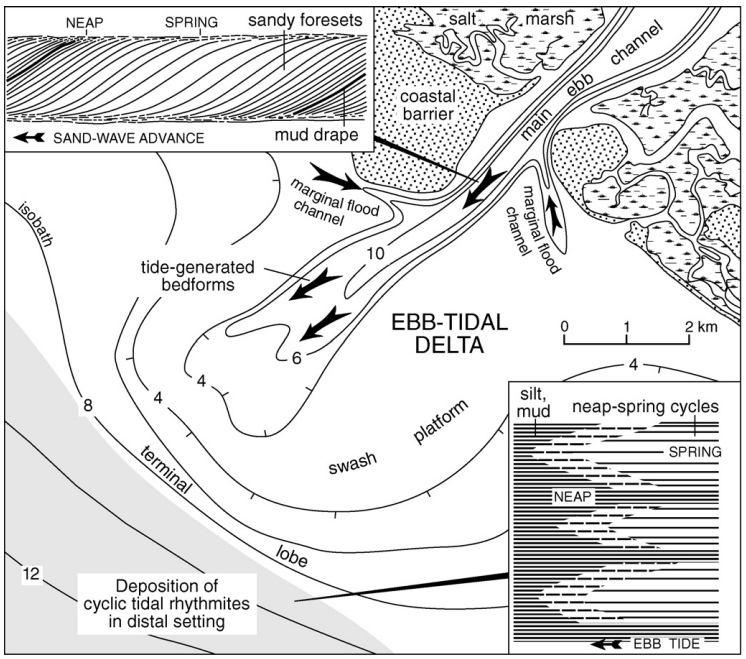

Figure 3.4: Depositional setting for the Elatina tidal rhythmites, employing a hypothetical ebb-tidal delta adapted from Imperato et al. (1988). Flood tides converge radially towards the tidal inlet, where fine-grained sediment is entrained by ebb-tidal currents and transported mainly in suspension via the main ebb channel to deeper water offshore. There the sediment settles to form neap–spring cycles comprising semidiurnal and diurnal laminae mostly of fine sand and silt (shown schematically in bottom inset), with mud bands deposited during slack water at neaps. Further offshore, the neap–spring cycles pass into marine-shelf silt and mud. Tidal bundle deposits of cross-bedded sand (top inset) are confined to proximal tidal channels. The isobaths (metres) and scale are arbitrary. Modified after Williams (2000).' (G. E. Williams et al., 2008).

ice cover would have isolated the ocean from seasonal changes. Thus, the ocean was not frozen during the deposition of the rhythmites at the Pichi Richi Pass (G. E. Williams, 2004; G. E. Williams & Schmidt, 2004). The Elatina rhythmites were deposited during an interstadial or interglacial period of high sea level (G. E. Williams et al., 2008). Glacial facies returned to the Elatina Formation when deposition ceased (G. E. Williams & Gostin, 2019).

Given the location of the Elatina rhythmite in the Pichi Richi Pass within the gulf-like Adelaide Rift Complex (Figure 3.1), this may have been an area of low wave activity. The rhythmite is remarkably unaffected by wave activity (G. E. Williams, 2000; G. E. Williams et al., 2008). Observations on the Reynella and Elatina rhythmites, together with directional paleo-currents data and paleo-geographic reconstruction of the Elatina Formation (Preiss, 1987; G. E. Williams, 1991), suggest distal ebb tidal characteristics near the margin of a marine gulf for deposition of the Reynella and Elatina rhythmites (Figure 3.4 and G. E. Williams, 2000; G. E. Williams et al., 2008). Furthermore, the site's proximity to faults suggests that water depth seaward of the ebb-tidal delta terminal lobe (Figure 3.4) rose rapidly to depths required to prevent wave disturbance (G. E. Williams, 1991). The rhythmites of the Elatina Formation are composed of very fine-grained sand, silt and clay. Ebb currents are capable (Section 2.2.4.5) of transporting such sediments in suspension several kilometers offshore. In addition, the dry periglacial hinterland would be associated with an abundance of fine-grained sand. This could enrich the amount of sediment transported in suspension.

3.2. Ocean tides

Most of the deceleration of the Earth's rotation rate, as shown in Tables 3.1 to 3.5, p. 80 to 83 and in Section 3.1.1, occurs due to the ocean tides. This is mainly due to the principal semi-diurnal lunar M_2 tide. Furthermore, a precise knowledge of the ocean tides (Section 3.2.1) is indispensable, e. g. as an essential component of nautical science and flood protection. It is also of important practical and scientific use in geophysics and geodesy.

Due to the dynamics of the oceans (Section 2.2.4), the equilibrium case does not adequately represent the majority of tides. As there is no analytical solution of the hydrodynamic tidal equations (Equations (2.43) to (2.45)) for the real ocean, the first attempts to assess ocean tides were made by measuring the tides at the coast. It has been possible to solve the equations numerically (Section 3.2.1), since the advent of high performance computers in the 1960s. The characteristics of ocean tides and their tidal friction (Section 3.2.2) vary with the position of the resonant frequencies in relation to the Earth's rotation rate. The shape of the ocean basins changes as the continents move relative to each other at a rate of a few centimeters per year. As a result, the strength of the zonal, diurnal, and semi-diurnal tides changes with an adjustment in tidal friction.

3.2.1. Modeling

Two methods, empirical and theoretical, are used to model ocean tides. The first models were created empirically by extrapolation of analyzed observations of tide gauges along the coasts and on the island. Sea level observations date back to the 17^{th} century, from 1679 in Brest, France (Wöppelmann et al., 2006), from 1682 in Amsterdam, the Netherlands (Woodworth, 1999), from 1768 in Liverpool, England (Woodworth, 1999). Predictions of the complete tidal signal were made possible by the development of the harmonic method (Section 2.2.2, p. 29 and Darwin, 1891).

Over the years, there has been an increase in the number of tide gauges in place around the world. The distribution of tide gauges is very inhomogeneous, with a large number e. g. in northern Europe and coastal regions, and almost no tide gauges in the open ocean. In the 1970s, deep-ocean bottom pressure recorders were added. These recorders measure tidal variation in sea level, which are proportional to downward pressure variations on the seafloor. The initial observing period of deep-ocean deployments of about one month was extended to more than one year in the early 1980s and to 5 years in the 1990s. Sea level variations measured by these methods are now accurate to about 1 mm (Marsh & van Sebille, 2021; Spencer & Vassie, 1997).

The theoretical approach is based on the numerical integration of the shallow-water equations (Equations (2.43) to (2.45)). For the major partial tides of the astronomical tidal potential (Equations (2.24) and (2.27)), ocean tidal models are established. These are for example the semi-diurnal tides M_2, S_2, N_2, K_2 and the diurnal tides O_1, P_1, Q_1, and K_1. Tides may be estimated with 99 % confidence using 14 harmonic constituents and their variance may be estimated with 99.99 % confidence using 80 harmonic constituents (Egbert & Ray, 2017). The simulation of global ocean dynamics was traditionally done separately from numerical circulation models. Circulation is primarily driven by the atmosphere. Global ocean dynamics are primarily driven by the gravitation of the Moon and the Sun.

This allowed the separation for computational and economical reasons. To date, almost all global oceanic models can be strictly divided into models for the baroclinic circulation and models for the barotropic tides.

Data-unconstrained (free) hydrodynamic numerical calculation of ocean tides depends only on the shallow-water equations (Equations (2.43) to (2.45)). In addition to knowledge of the bathymetry, the parametrized dissipation mechanisms are required. The hydrodynamic equations are expressed in terms of finite differences or finite elements. They are solved numerically in the time domain or in the spectral domain as an initial boundary value problem with the condition of rest or as an elliptic boundary value problem with the condition of periodicity. In contrast to the empirical method, the tidal currents are an inherent part of the theoretical method. From the calculated transports of the shallow-water equations, the currents are derived. Thus, they are even more dependent on the local bathymetry.

One of the first global tide simulations using the linearized Laplace's tidal equations was by Pekeris and Accad (1969). The first simulation using the non-linear shallow-water equations (Equations (2.43) to (2.45)) was presented by Zahel (1970). With the development of the models and the computational power, a better understanding of the physics of the tides and a more detailed representation of the ocean tides has been achieved. In addition to the consideration of Earth body tides in Zahel (1977), the complex computational procedures to account for self-attraction and loading effects have been incorporated (Accad & Pekeris, 1978; Gordeev et al., 1977; Hufschmidt, 1995; Zahel, 1978). As more powerful high performance computers and better bathymetries became available, the spatial resolution in the global models was increased from $10° \times 10°$ in 1970 to nominal model resolutions of $5'$ to $30'$ today. A resolution of $30'$ is generally appropriate for the resolution of barotropic tides in the open ocean. It has limited ability to capture variability on continental shelves and near the coast (Stammer et al., 2014; Zaron & Elipot, 2021).

A combination of empirical and theoretical methods has been developed by Schwiderski (1980). He used more than 2000 empirical tidal data as boundary values at the tide gauge stations to solve the hydrodynamic equations numerically on a $1° \times 1°$ regular latitude-longitude grid. By incorporating empirical tidal data, the data assimilation is based on an overdetermined tidal problem. The additional information provided by the measured data leads to the possibility of obtaining knowledge about the deviations between data-unconstrained model solutions and the measured tidal data. This model has been used as a reference model for more than a decade.

The current types of models with examples of models followed by validation data sets are presented in the Sections 3.2.1.1 and 3.2.1.2. Finally, the accuracy and quality of the current tidal simulations are discussed in Section 3.2.1.3.

3.2.1.1. Models

The current model types can be divided into empirical models, assimilative dynamic models constrained by observations, and free hydrodynamic models. These are introduced below with their constraints and example models.

Empirical models Since the launch of satellite altimetry missions, global ocean height measurements have become available for the first time. As a result, empirical tidal models have been derived only from the analysis of large sets of these altimetry data. The first mission was GEOSAT (GEOdetic SATellite) in 1985. This was followed, among others, by the TOPEX/Poseidon mission in 1992 and the subsequent Jason missions, the third of which is ongoing since 2016. With the availability of satellite altimeter data, tidal heights in the open ocean are now known within a few centimeters (Le Provost, 2001; Shum et al., 1997). The accuracy of numerical tidal solutions can now be assessed quantitatively (Egbert et al., 2004).

The latitude limits of the various satellite missions are the determinants of the north-south extent of the empirical models. TOPEX/Poseidon and the subsequent Jason missions cover the latitude range between ±66°. In the case of Envisat (Environmental Satellite), for example, the range is extended to ±81.5°. In the case of CryoSat-2 (Satellite for monitoring the cryosphere system), for example, even to ±88° towards true global coverage.

The altimeter measures the geocentric altitude, which includes the sum of the tides of the solid Earth body, the ocean, and its loading. Methods such as those of Cartwright and Ray (1990), Hart-Davis et al. (2021a), and Savcenko and Bosch (2012) are used to separate the contributions. The ocean tides are then determined using methods such as harmonic analysis, response analysis (Munk & Cartwright, 1966), and extended by orthogonal representation (Cartwright & Ray, 1990; Groves & Reynolds, 1975). Cartwright and Ray (1990) and Cartwright and Ray (1991) have done the fundamental work in this area on the analysis of GEOSAT data.

Empirical tidal modeling is to a large extent dependent on satellite altimetry data. It does not require knowledge of bathymetry and hydrodynamics including frictional processes. In comparison to the hydrodynamic modeling approach, the empirical modeling approach is a simple and effective method for tidal analysis and prediction. However, it provides less physical insight and understanding.

The purely empirical method of direct analysis of the altimetry data has been supplemented by semi-empirical models. In this case, the tidal analysis is based on a-priori tidal constants from a background model of the ocean tides. Outside the latitude limit of the satellites in the higher latitudes, the background model is used. The underlying background model may be responsible for some of the small-scale feature of the results (Stammer et al., 2014). The GOT (Goddard/Grenoble Ocean Tide) and EOT (Empirical Ocean Tide) model series are given as examples.

The GOT4.10 model is the latest version of the GOT series developed at the Goddard Space Flight Center, USA (Ray, 2013). The series dates back to Ray (1999) and Schrama and Ray (1994). The GOT4.10 model includes solutions for each of the ten partial tides Q_1, O_1, P_1, K_1, S_1, N_2, M_2, S_2, K_2, and M_4. The spatial resolution of the model is $30'$ on a regular latitude-longitude grid.

The EOT model series, starting with version EOT8a (Savcenko & Bosch, 2008), has been developed at Deutsches Geodätisches Forschungsinstitut, a research institute of the Technical University of Munich (DGFI-TUM), Germany. EOT20 is the most recent version (Hart-Davis et al., 2021a). In addition to the solutions for each of the ten tidal constituents of GOT4.10, EOT20 contains solutions for each of seven additional partial tides. Four of them are long-period tides. On a regular latitude-longitude grid, the spatial resolution is

7.5′.

Data-constrained models With the increase in the availability of extensive surface topographies from satellite altimetry, data assimilation methods for ocean tidal modeling have also been developed. Bennett and McIntosh (1982), McIntosh and Bennett (1984), and Zahel (1991) provide the approaches used in tidal models to date (Egbert & Ray, 2017). Note that the models assimilate sea surface heights. They do not assimilate observations of tidal currents. The derived models have replaced the previous state-of-the-art model by Schwiderski (1980) in terms of accuracy (Egbert et al., 2004). However, high-resolution data assimilation remains computationally demanding. This typically results in the use of a spatially varying grid with coarse resolution over the open ocean, and higher resolution limited to shallow seas. The model series TPXO (TOPEX/Poseidon global tide), HAMTIDE (Hamburg direct data Assimilation Methods for TIDEs), and FES are given as examples. These are widely used for predicting tidal heights, providing boundary conditions for regional ocean prediction models, and other applications.

The fully global TPXO series was established by Egbert et al. (1994) and further developed by Egbert and Erofeeva (2002). Updates are released as more accurate tidal solutions from altimetry become available. TPXO9A is the latest version.The software package OTIS (Oregon State University Tidal Inversion Software) provides the methods to assimilate the satellite altimetry data in addition to the underlying barotropic tidal model based on the Laplace's tidal equations. With the exception of the S_1 tidal constituent and the additional $2N_2$, MN_4, and MS_4 tidal constituents, the solutions include the tidal constituents of the GOT model series. In addition to the global solution with a spatial resolution of 10′, 30 regional solutions with a spatial resolution of 2′ are available for all coastal areas, including the Arctic and Antarctic. All regional solutions were obtained from the global base solution using consistent bathymetry and boundary conditions. The same altimetry datasets were used for assimilation.

The fully global HAMTIDE model was developed at the University of Hamburg, Germany (Taguchi et al., 2014; Zahel, 1995; Zahel, 1991). It includes estimates for each of the 11 major tidal constituents K_1, O_1, P_1, Q_1, M_2, S_2, N_2, K_2, $2N_2$, M_f and M_m. A regular $7.5' \times 7.5'$ latitude-longitude grid is used for calculations. The latest version is constrained between 74°N and 86°S using EOT11a data.

FES2022 is the latest version of the fully global FES global tidal model series (Carrère et al., 2022; Lionel et al., 2023). The model series has been developed and updated since Le Provost et al. (1994). With 34 tidal constituents, it contains more tidal frequencies than the other models. In addition to the major tidal constituents, it includes secondary and long-periodic tidal constituents as well as non-linear overtides. FES2022 is built on T-UGO (Toulouse-Unstructured Grid Ocean model), a 2-D/3-D ocean model developed at the Laboratoire d'Etudes en Géophysique et Océanographie Spatiales (LEGOS), France. Unstructured grids and both time-stepping and spectral methods can be applied. The SpEnOI (Spectral Ensemble Optimal Interpolation) software package was employed to assimilate altimetry data. A fully global finite element mesh comprising approximately 11 million elements is employed, representing an eightfold increase relative to the preceding version, FES2014. The native resolution ranges from about 4 km to 30 km. The results are provided on a regular latitude-longitude grid with a 2′ grid spacing. In most empirical

models, the FES model series becomes the background solution and, beyond the geographic limit of the satellite altimetry, the standard solution. The model version FES2022 exhibits substantial enhancements, particularly in the domain of shelf, coastal, and polar seas, when compared to the previous version, FES2014. The FES2014 model already demonstrated a previously unattained level of accuracy (Lyard et al., 2021). This was and is achieved in particularly through the use of more accurate bathymetry with the latest global and regional data sets, a refined and flexible resolution of the unstructured grid, and improved modeling and data assimilation procedures. FES tidal solutions are widely and successfully used e. g. in space-borne applications and in regional and coastal modeling (Lyard et al., 2021). The FES2014/2022 tidal model is currently considered to be the state-of-the-art.

Data-unconstrained models Over the last few decades, free ocean tidal models have made significant progress. This is due to higher spatial and temporal resolution and more detailed bathymetric data. In particular, the understanding of tidal dissipation (Section 2.2.4.6) has been enhanced by the use of altimeter data (Egbert & Ray, 2000; Egbert & Ray, 2001). In addition to bottom friction and eddy viscosity, this energy sink is now represented in the free barotropic ocean tidal models (2-dimensional) by a parameterized topographic internal wave drag, as discussed in e. g. Green and Nycander (2013) and Nycander (2005). Furthermore, the simulation together with the resulting excited internal tides (3-dimensional) can be made possible with a full 3-dimensional model of the stratified ocean, the so-called general ocean circulation models (Arbic et al., 2012; Arbic et al., 2010; Buijsman et al., 2015; M. Müller et al., 2010; Ngodock et al., 2016; Shriver et al., 2012; Shriver et al., 2014). The simultaneous global simulation of the oceanic barotropic tides and the baroclinic circulation was first carried out by Thomas (2002) and Thomas et al. (2001). Non-linear interactions in the region of adjacent tidal and circulation periods, such as seasonal variations and annual tides, were shown to be significant for variations in Earth's rotation (Thomas et al., 2001).

The model series OTIS, TiME (Tidal Model forced by Ephemerides), and HIM (Hallberg Isopycnal model) are given as examples of free barotropic tidal models. OTIS (p. 73 and Egbert et al., 2004), with the free barotropic model on which the TPXO tidal solutions are based, is also used as a free tidal model. The numerical discretization of the linearized Laplace's tidal equations is performed by the finite difference method on a regular latitude-longitude grid. According Egbert et al. (2004), non-linear advection and horizontal diffusion can be neglected without losing accuracy. Polar regions can be excluded from the computation. Egbert et al. (2004) used a grid with a resolution of $5'$, covering the latitudes 86°S to 82°N. In contrast, Green and Nycander (2013) used a grid with a resolution of $7.5'$, extending from 77°S to 78°N. The forcing is given by an individual tidal constituent. SAL is implemented (Egbert et al., 2004) strictly following the iterative approach of Accad and Pekeris (1978). The energy losses are parametrized with a quadratic term, which represents the bottom friction, and with different transformation schemes, which represent the excitation of internal tides (Egbert et al., 2004; Green & Nycander, 2013). OTIS has been used in a number of previous studies for the simulation of global and regional tides in the oceans of the present (e. g. Green et al., 2018), of the present and past (e. g. Egbert et al., 2004; Green, 2010), of the past (e. g. Blackledge et al., 2020; Green & Huber, 2013; Green et al., 2017; Green et al., 2020; Wilmes & Green, 2014; Wilmes et al., 2019), and of the future (e. g. Carless et al., 2016; Hayden et al., 2020; Pickering et al., 2017; Wilmes

et al., 2017).

The truly global free barotropic tidal model TiME by Weis (2006) and Weis et al. (2008) with its latest update by Sulzbach et al. (2021) and Sulzbach et al. (2022) is the result of several decades of research on the simulation of global tides at the Universität Hamburg, Germany (Brosche & Sündermann, 1971; Seiler, 1989, 1991; Thomas, 2002; Thomas & Sündermann, 1999; Thomas et al., 2001; Zahel, 1978; Zahel et al., 2000; Zahel, 1977). It was developed primarily for the investigation of the contributions of the ocean tides to the rotation of the Earth (Seiler, 1989, 1991). In contrast to the models for the pure investigation of the tidal sea surface elevations and currents, the model also contains modules for the calculation of the resulting angular momenta, torques and energy transfers. The non-linear shallow-water equations are numerically discretized by finite differences on a global regular latitude-longitude grid, in contrast to the linearized Laplace's tidal equations as used in OTIS. A user defined polar cap around the north pole avoids the polar singularity that otherwise would be the case. The original spatial resolution of $1° \times 1°$ by Seiler (1989, 1991) was increased to $20'$, $10'$ and $5'$ by Weis (2006) and Weis et al. (2008).

The forcing can be either an individual partial tide or the complete 2^{nd} degree lunisolar tidal potential (Weis, 2006). From Thomas (2002) the module for the calculation of the position of the Moon and the Sun (ephemerides) for the full tidal potential was taken over. Thomas (2002) was the first to do tidal simulations with the full tidal potential. One simulation can be used to model the total tides, which can than be assigned to the partial tides via a Fourier transformation. For the first time, the global current and sea surface elevation fields of some non-linear shallow water tides could be simulated numerically. The underlying non-linear shallow-water equations were discretized in high resolution ($5'$).

The polar rotation scheme in Sulzbach et al. (2021) allows the poles of the original latitude-longitude grid to be user defined placed on dry land grid points that are excluded from the calculation. This avoids the singularity at the North Pole instead of using an artificial polar cap and ensures more grid cells that are as uniform as possible. Thus, without numerical perturbations caused by the treatment of the polar cap, it is possible to study Arctic tides. Sulzbach et al. (2021) extended the consideration of SAL in Seiler (1989) through Accad and Pekeris (1978) parametrized approach by explicitly implementing these effects. Since Seiler (1989), the dissipation mechanisms have been represented by the parametrized turbulent eddy viscosity and a quadratic bottom friction. As an additional dissipation mechanism, Sulzbach et al. (2021) include baroclinic internal tide excitation by barotropic tides using Nycander (2005) parametrized approach. In Sulzbach et al. (2021), the focus was on extending the model to study in particular the tidal dynamics of minor and compound tides in the ocean, which is important in relation to satellite gravimetry. The extension to the 3^{rd} degree tidal potential was carried out by Sulzbach et al. (2022) to study the first data-unconstrained simulated partial tides of the 3^{rd} degree. Ray (2020) achieved the first global observation of 3^{rd} degree ocean tides.

The HIM model simulates the dynamics of the ocean using isopycnal vertical coordinates and general orthogonal horizontal coordinates (Hallberg & Rhines, 1996). The model was developed at the Geophysical Fluid Dynamics Laboratory (GFDL) of National Oceanic and Atmospheric Administration (NOAA), USA. It has been used in a barotropic version on a regular latitude-longitude grid from 86° S to 82° N with a resolution of $30'$, $15'$, and $7.5'$ in a number of tidal studies (Arbic et al., 2004; Arbic et al., 2009; Arbic et al., 2008;

Simmons et al., 2004; Skiba et al., 2013). The simulations were carried out as a run with an individual tidal constituent and as a run with multiple tidal constituents. A parametrized quadratic bottom friction, horizontal eddy viscosity, and topographic wave drag were used to model energy losses. In addition to the local scalar approximation of the SAL effects, an iterative approximation method was used.

3.2.1.2. Validation

The simulated sea surface topographies from global tidal models can be validated using satellite and in-situ data records. Pole-ward, outside of the latitudinal limits of TOPEX/Poseidon and Jason, the density of satellite data for validation and assimilation is lower. In addition, sea ice and ice shelves interfere with the satellite altimeters. The same is true for in-situ data, which represent local data. Consequently, unaccounted local details of the bathymetry and parameterizations in the models may affect the validation of global tidal models using in-situ data. Nevertheless, it is crucial to ensure that the data employed for model validation and simulation are independent.

The TICON (TIdal CONstants) tide gauge dataset was derived by Piccioni et al. (2018, 2019) from the GESLA (Global Extreme Sea Level Analysis)-2 project (Woodworth et al., 2017). TICON-3 (Hart-Davis, Dettmering, et al., 2022) was updated from GESLA-3 (Haigh et al., 2022), which allowed the number of tide gauges to be increased to 3471. Since data from several sources are available for some stations, these stations appear more than once. To ensure adequate model evaluation, the dataset provides the 40 most important tidal constituents, which include all 34 constituents of the FES2022 tidal model. In addition, the GESLA-3 datasets contain information useful for validation, such as whether the tide gauge is an ocean, coastal, or river tide gauge. The quasi-global coverage of tide gauges is very inhomogeneous, with a much higher coverage in the Northern Hemisphere, especially in Europe, North America, and Japan. High latitudes and Indian waters, for example, have almost no tide gauges. There are also few stations in the open ocean. The TICON dataset is complemented by Hart-Davis, Sulzbach, et al. (2022) and Sulzbach et al. (2022) with the TICON-td dataset containing the 3$^{\text{rd}}$ degree tidal constituents $^3M_1$, $^3M_3$, $^3N_2$, and $^3L_2$ for 134 open-ocean stations.

For the open ocean, the harmonic constants from long time series of 151 bottom pressure stations were processed by Ray (2013). The data is restricted to the open ocean. This avoids the influence of local effects on the tidal constants. Previously, the comparable open-ocean data set of 102 stations compiled by *Cristian Le Provost* and *David Cartwright* could be used for validation of global tidal models, as used by Shum et al. (1997). However, the dataset of Ray (2013) shows significant improvements, e. g. due to the many more recent multi-year bottom pressure time series (Stammer et al., 2014). This is also attributed to the international tsunami warning network. The number of available tidal components per station varies depending on the length of the time series and the noise level (Ray, 2013). For all 151 stations the main tidal constituents are included.

Stammer et al. (2014) compiled tide gauge data from 195 shallow water and shelf stations, going back to Ray et al. (2011), as well as newly added stations. The authors found that the shelf data were much less accurate than the data from the open ocean. High quality tidal analyses for tide gauges associated with the World Ocean Circulation Experiment were

performed by Ponchaut et al. (2001). A subset of 54 stations on continental coast has been subject of Stammer et al. (2014).

As another independent method to assess the accuracy of global tidal models, observations of orbital perturbations of artificial satellites due to the gravitational effects of tides (e. g. Lambeck, 1980b) can be used (Stammer et al., 2014).

Validation of simulated global tidal currents is much more limited than is the case for sea surface tidal heights. Based on moored current meters, relatively sparse and inhomogeneously distributed in-situ current measurements are available (Stammer et al., 2014). In general, moorings are more common in the western boundary current regions. However, entire regions, such as the entire South Pacific, are missing. It is also difficult to separate the barotropic component. Compared to this, tidal currents derived using data from reciprocal acoustic tomography show much lower uncertainties (Stammer et al., 2014). The measurements are almost unaffected by baroclinic tidal currents. They are integral over depth and range. However, such measurements have only been carried out at a few locations. In-situ observations of near-surface (15 m) Lagrangian currents are available with the GDP (Global Drifter Program). This is a global $5° \times 5°$ array of ~1300 satellite-tracked drifting buoys.

3.2.1.3. Evaluation

In the last decades, the different types of tidal models have evolved continuously. This has involved significant progress in tidal simulation accuracy (Shum et al., 1997; Stammer et al., 2014). In the open ocean, the simulations of different models of each type have converged to such an extent that it is difficult to distinguish between them (Stammer et al., 2014; Zaron & Elipot, 2021). However, in shelf and coastal regions and in polar seas partially or permanently covered by sea ice or ice shelves, the accuracy of the tidal simulations is up to an order of magnitude lower than that of the simulations in the open ocean (Fok, 2012; Stammer et al., 2014; Zaron & Elipot, 2021). But for the shallow water regions, the accuracy can be deceptive (Stammer et al., 2014). The accuracies of a few locations can have a negative effect on the accuracies of the majority of locations. In this context, the simulations of the model version FES2014/2022, which are comparable to other simulations in the open ocean, and show many improvements in the shallow sea and some significant improvements in the high latitudes, can be considered as the current state-of-the-art in tidal simulations (Lyard et al., 2021; Ray et al., 2019).

Among the modern altimetry-constrained tidal models, RMS (root-mean-square) residuals of up to 0.51, 3.5 and 4.5 cm for pelagic, shelf, and coastal conditions were computed in the assessment of Stammer et al. (2014) using in-situ observations of sea surface heights from tide gauges and bottom pressure recorders (Section 3.2.1.2) for the M_2 tide. In the open ocean, the very low RMS values for all modern data-constrained models of half a centimeter or better for each of the eight main tidal constituents considered correspond to a relative error (ratio of RMS residual to signal) of about 2 % for the M_2 partial tide up to 10 % for the smaller constituents K_2, P_1, and Q_1.

As expected, the free tidal models are much less accurate than the altimetry-constrained tidal models (Stammer et al., 2014). However, they have improved considerably in recent decades. The residuals for the free tidal models are an order of magnitude larger than for

the modern data-constrained tidal models. Among the free tidal models, RMS residuals of down to 5.63 cm and 23.6 cm for pelagic and shelf conditions, respectively, were obtained in the assessment by Stammer et al. (2014) using in-situ observations of the sea surface heights from tide gauges and bottom pressure records (Section 3.2.1.2) for the M_2 tide. In comparison to M_2 tidal solution of the TPXO8, the solutions of the free tidal models show RMS residuals of down to 4.65 cm and 18.6 cm for pelagic and shelf conditions, respectively. These best residuals are shown by OTIS model variant tidal solutions. Egbert et al. (2004) obtained the best residuals in the open ocean and in the shelf regions compared to the in-situ observations and in the open ocean compared to the tidal solutions of TPXO8. Green and Nycander (2013) had the best residual in the shelf regions with respect to the TPXO8 tidal solution (Stammer et al., 2014). Green and Huber (2013) were able to capture 91 % of the tidal amplitude variance in the TPXO database using OTIS simulations. The RMS residual between the simulated amplitudes and the TPXO database was 12 cm. Restricted to deep water, the RMS residual was only 7 cm. Consistent with the large M_2 tidal amplitudes in the North Atlantic due to the near-resonant conditions on the astronomical M_2 tidal potential, all six of the free tidal models considered in Stammer et al. (2014) have relatively large errors there.

Compared to in-situ observations (as used in Stammer et al. (2014), Section 3.2.1.2) the TiME model variant updated by Sulzbach et al. (2021) allowed the M_2 tidal solution to achieve an improved RMS residual of 4.83 cm in the open ocean. In the open ocean and shallow water regions, the RMS residuals were 3.39 cm and 17.95 cm, respectively, compared to the FES2014 tidal solution, which in turn improved the RMS residuals compared to TPXO8 in Stammer et al. (2014). This level of accuracy is associated with both a rigorous self-consistent treatment of the SAL effects of ocean tides and the consideration of barotropic/baroclinic energy conversion through a parametrized topographic wave drag (Egbert et al., 2004; Sulzbach et al., 2021). At a global resolution of $10'$, Sulzbach et al. (2023) achieved 70 % agreement between simulated tidal heights and current tide gauge data.

Minor tides were previously derived form data-constrained tidal solutions using admittance assumptions. With TiME, Sulzbach et al. (2021) were able to simulate them directly and with higher accuracy. Sulzbach et al. (2022) have extended TiME to the astronomical tidal potential of the 3^{rd} degree. The RMS residual of 1 mm for each partial tide solution compared to a set of tide gauges data showed good agreement.

Tidal surface currents in the world's oceans have been estimated by Poulain and Centurioni (2015), using data from the GDP (Section 3.2.1.2, p. 77). In almost all shallow seas and coastal waters, M_2 tidal currents are greater than $5\,\mathrm{cm\,s^{-1}}$. Currents greater than $40\,\mathrm{cm\,s^{-1}}$ are often observed near continental shelves. Simulations of tidal currents were compared with velocities derived from GDP data by Kodaira et al. (2016) and Zaron and Ray (2017). Zaron and Elipot (2021) found similar results when comparing simulated tidal currents from the data-constrained models FES2014, TPXO9A, and GOT4.10 with GDP data as when comparing with sea surface topographies from altimeter data. The analysis of individual drifter data sets could be a contribution to the clarification of the large residuals between the models in the vicinity of the coast (Zaron & Elipot, 2021). The evaluation of Stammer et al. (2014) with tidal currents from moored current meters and acoustic tomography data consistently showed that the numerically simulated tidal currents from data-constrained

models were more accurate than those from free models. In contrast to the amplitudes, the phases of the currents showed no significant deviations.

At least in the open ocean, which covers most of the Earth's surface, free models can now provide adequate predictions of tidal heights. However, in terms of accuracy of tidal predictions, the data-constrained models are without competition. For all types of tidal modeling, whether in the open ocean, shelf regions, of high latitudes, the need for improved bathymetric data sets is a common issue (Stammer et al., 2014). Sensitivity tests with randomly perturbed bathymetry by Egbert et al. (2004) also demonstrated the critical dependence of the quality of tidal solution on the accuracy of the bathymetry. This was also noted by Hufschmidt (1995), Thomas and Sündermann (1999), and Weis (2006).

3.2.2. Secular rate of Earth's rotational velocity

As known since Munk and McDonald (1960) and shown by the Tables 3.1 to 3.5, the tides of the oceans are responsible for most of the secular deceleration of the Earth's rotation rate. This is mainly attributable to the semi-diurnal lunar tides, with about 70 % of the planetary tidal friction being due to the oceanic M_2 tide. Numerical simulations of ocean tides can be used to determine the tidal energy dissipation and tidal torque of the world's oceans in order to estimate the effect of ocean tides on the secular change in the Earth's rotation rate. In general, tidal energy dissipation is considered to be at the expense of the Earth's rotation rate. Studies for modern times are presented in Section 3.2.2.1, for individual geologic periods in Section 3.2.2.2, and for the Earth's history in Section 3.2.2.3. It becomes evident that tidal friction has varied considerably throughout the Earth's history.

3.2.2.1. Modern times

The initial numerical simulations of ocean tides with a quantification of the angular momentum transfer in the Earth-Moon system were conducted by Brosche and Sündermann (1971) using the non-linear shallow-water equations (Equations (2.43) to (2.45)). By simulating ocean tides using the M_2 tide, discretized on a regular 10° latitude-longitude grid, they were able to support tidal friction as a cause of the secular slowing of the Earth's rotation rate. The concept of tidal friction has been substantially extended by two new elements: The time-averaged torques acting on the Earth's rotation are small compared to the extreme values, and in parts of the world's oceans, secular accelerating torques are also acting on the Earth (Section 2.2.4.6, p. 48; Section 2.3). Areas with a accelerating (eastward directed) torque essentially coincide with the part of the residual current system with a pronounced eastward component (Brosche & Sündermann, 1971). Throughout the oceans there are areas with accelerating and decelerating effects (Sündermann & Brosche, 1978). Zonally integrated, the Earth's rotation rate is decelerated between latitudes 40 °S and 10 °N. It is accelerated in a zone around 30 °N. Eventually, the resulting global torque becomes negative, slowing the Earth's rotation rate (Sündermann & Brosche, 1978). Because of the small differences in large numbers that occur, the hydrodynamic-numerical model has to be extraordinarily accurate.

Further investigations also focus on individual major tidal constituents, always including the M_2 tide. Taking into account the extreme values, this also allows for averaging over

Table 3.1.: Current secular change in the Earth's rotation rate by the tides, given by the tidal energy dissipation $\langle\overline{\dot{E}_d}\rangle$, the rotational energy rate $\langle\overline{\dot{E}_{rot}}\rangle$, the polar tidal torque $\langle\overline{M_{t,z}}\rangle$, the angular acceleration $\dot{\Omega}_{\mathfrak{F}}$, and the daylength rate $\Delta l.o.d$ as time-averaged global quantities.

Reference	Model Observ.	Tide	$\langle\overline{\dot{E}_d}\rangle$ (TW)	$-\langle\overline{\dot{E}_{rot}}\rangle$ (TW)	$-\langle\overline{M_{t,z}}\rangle$ (10^{16} N m)	$-\dot{\Omega}_{\mathfrak{F}}$ ($''$/cy^2)	$\Delta l.o.d$ (ms/cy)
Ocean							
Ray et al. (1999)	EGM96	8 tides		3.722[3]	5.104[2]	1304.0	2.373[1]
Egbert and Ray (2003)	TPXO5	8 tides	3.508		4.811[3]	1229.7[1]	2.238[1]
Taguchi et al. (2014)	HAMTIDE	8 tides	3.540		4.855[3]	1240.9[1]	2.258[1]
Sulzbach et al. (2023)	TiME21	8 tides	3.682		5.049[3]	1290.6[1]	2.348[1]
Baenas et al. (2021)	Analytical	$m=1$		0.552[3]	0.757[2]	193.5	0.352
Baenas et al. (2021)	Analytical	$m=2$		3.071[3]	4.211[2]	1075.8	1.959
Weis (2006)	TiME	total	4.800		6.582[3]	1682.5[1]	3.062[1]
Baenas et al. (2021)	Analytical	total		3.623[3]	4.968[2]	1269.3	2.360
Earth body							
Baenas et al. (2021)	Analytical	$m=1$			−0.009[2]	−2.4	−0.004
Baenas et al. (2021)	Analytical	$m=2$		0.176[3]	0.241[2]	61.7	0.112
Baenas et al. (2021)	Analytical	total		0.169[3]	0.232[2]	59.3	0.108
Ocean + Earth body							
Baenas et al. (2021)	Analytical	$m=1$		0.545[3]	0.749[2]	191.1	0.348
Baenas et al. (2021)	Analytical	$m=2$		3.246[3]	4.452[2]	1137.5	2.071
Baenas et al. (2021)	Analytical	lunar		3.240[3]	4.443[2]	1135.3	2.067
Baenas et al. (2021)	Analytical	solar		0.552[3]	0.757[2]	193.3	0.352
J. G. Williams and Boggs (2016)	Analytical	total		3.780	5.186[2]	1325.0	2.411
Baenas et al. (2021)	Analytical	total		3.792[3]	5.200[2]	1328.6	2.418
Planetary							
Christodoulidis et al. (1988)	SLR	total		3.513[3]	4.818[2]	1231.0[1]	2.240
Egbert and Ray (2001)	Space geodesy	total	3.700		5.074[3]	1296.9[1]	2.275[1]
J. G. Williams and Boggs (2016)	LLR	total		3.756[3]	5.151[2]	1316.0	2.395
Deines and Williams (2016)	Empirical	total		3.498[3]	4.796[2]	1225.5[1]	2.230

1 Derived from the values of J. G. Williams and Boggs (2016), cf. Table 3.1 section Ocean + Earth body.
2 Derived by Equation (2.8), $1\,''/\mathrm{cy}^2 = 4.686 \times 10^{-25}\,\mathrm{s}^{-2}$ (Ray et al., 1999).
3 Derived by Equation (2.9) considering $\langle\overline{\dot{E}_d}\rangle = -\langle\overline{\dot{E}_{rot}}\rangle$.

time, since closed periods can be averaged. Together with further theoretical work and more recent astronomical-geodetic observations, a largely consistent system picture has emerged (e. g. Brosche & Sündermann, 1978, 1982, 1984, 1990; Lambeck, 1977; Munk, 1997).

As numerical models, computing power and capacity, and geodetic measurement techniques have improved, oscillations in all three components of the Earth's rotation vector and their magnitudes have become addressed. Using a free barotropic partial tide model, Seiler (1989) studied the angular momentum balance of the world ocean (Section 3.2.1.1, p. 75). Her predictions were below the observational accuracy that was available at the time. Weis (2006) was the first to investigate the full effect of ocean tides on Earth rotation using the real-time approach (full 2$^{\mathrm{nd}}$ degree lunisolar tidal potential, Equation (2.25)) of the high-resolution TiME version (Section 3.2.1.1, p. 75). Compared to the also data-unconstrained simulation results of Seiler (1991), on whose model TiME is based, considerable improvements could be achieved compared to data-constrained simulation results of Zahel et al. (2000). Deviations below the observational accuracy at that time were shown by Weis (2006).

Subsequently, data-constrained ocean tidal models (Section 3.2.1, p. 73) have further

Table 3.2.: Current secular change in the Earth's rotation rate by the M_2 tide, given by the nominal tide $\zeta^+_{\sigma,lm}$, $\epsilon^+_{\sigma,lm}$, the tidal energy dissipation $\langle\overline{\dot{E}_d}\rangle$, the rotational energy rate $\langle\overline{\dot{E}_{rot}}\rangle$, the polar tidal torque $\langle\overline{M_{t,z}}\rangle$, the angular acceleration $\dot{\Omega}_{\mathfrak{F}}$, and the daylength rate $\Delta l.o.d$ as time-averaged global quantities.

Reference	Model Observ.	$\zeta^+_{2,2}$ (cm)	$\epsilon^+_{2,2}$ (°)	$\langle\overline{\dot{E}_d}\rangle$ (TW)	$-\langle\overline{\dot{E}_{rot}}\rangle$ (TW)	$-\langle\overline{M_{t,z}}\rangle$ (10^{16} N m)	$-\dot{\Omega}_{\mathfrak{F}}$ ($''$/cy^2)	$\Delta l.o.d$ (ms/cy)
Ocean								
Seiler (1989)	Seiler (1989)			2.940		4.032[3]	1030.6[1]	1.875[1]
Zahel et al. (2000)	HAMTIDE			2.375		3.257[3]	832.5[1]	1.515[1]
Egbert and Ray (2001)	TPXO4a	3.223	129.99	2.435		3.339[3]	853.5[1]	1.553[1]
Egbert and Ray (2001)	GOT99.0	3.200	129.57	2.432		3.335[3]	852.5[1]	1.551[1]
Egbert and Ray (2003)	TPXO5			2.435		3.339[3]	853.5[1]	1.553[1]
Green and Huber (2013)	OTIS			2.780		3.812[3]	974.5[1]	1.773[1]
Taguchi et al. (2014)	HAMTIDE	3.241	129.79	2.440		3.346[3]	855.3[1]	1.556[1]
Wilmes et al. (2023)	TPXO9			2.400		3.291[3]	841.3[1]	1.531[1]
Wilmes et al. (2023)	OTIS			2.500		3.428[3]	876.3[1]	1.595[1]
Sulzbach et al. (2023)	TiME21	3.399	126.92	2.494		3.420[3]	874.2[1]	1.591[1]
Ray et al. (1999)	EGM96	3.266	128.21		2.623[3]	3.597[2]	919.0	1.672[1]
Ray et al. (2001)	Space geodesy	3.206	130.01	2.420		3.319[3]	847.9[2]	1.543[1]
Earth body								
Ray et al. (2001)	Space geodesy			0.110		0.151[3]	38.6[1]	0.070[1]
Ocean + Earth body								
J. G. Williams and Boggs (2016)	Analytical				2.642[3]	3.623[2]	925.7	1.684[1]
Atmosphere								
Platzman (1991)	Observational			0.010		0.014[3]	3.5[1]	0.006[1]
Planetary								
Ray et al. (2001)	Space geodesy	3.295	128.69	2.536		3.480[3]	888.9[1]	1.617[1]
J. G. Williams and Boggs (2016)	LLR				2.613[3]	3.584[2]	915.6	1.666[1]

1 Derived from the values of J. G. Williams and Boggs (2016), cf. Table 3.1 section Ocean + Earth body.
2 Derived by Equation (2.8), $1\,''/\mathrm{cy}^2 = 4.686 \times 10^{-25}\,\mathrm{s}^{-2}$ (Ray et al., 1999).
3 Derived by Equation (2.9) considering $\langle\overline{\dot{E}_d}\rangle = -\langle\overline{\dot{E}_{rot}}\rangle$.

improved the quantification of tidal friction. However, only the scalar energy transfers in the world's oceans is usually considered. Tidal energy dissipation estimates from TPXO4a and GOT99.0 by Egbert and Ray (2001) for the M_2 tide, TPXO5 by Egbert and Ray (2003) for 8 tidal constituents including M_2, S_2, K_1, and O_1 tide, TPXO9 by Wilmes et al. (2023) for M_2, S_2, K_1, and O_1 tide, and HAMTIDE by Zahel et al. (2000) for M_2, S_2, K_1, and O_1 tide and by Taguchi et al. (2014) for a total of 8 tidal constituents and the M_2 tide are shown in Tables 3.1 to 3.5. The quantities for the secular deceleration of the Earth's rotation rate have been derived for the tables, as usual, by consideration that the tidal energy is dissipated at the expense of the Earth's rotation rate.

The tidal energy dissipation of the 8 tides in Egbert and Ray (2003) and Taguchi et al. (2014) totals 3.5 TW (Table 3.1), of which the M_2 tide contributes 69 % with 2.4 TW (Table 3.2). As in the case of the empirical and analytical values for the change in the Earth rotation rate (Section 3.1.1), S_2 (Table 3.3), K_1 (Table 3.4) and O_1 (Table 3.5) tides make the next largest contributions, with decreasing magnitude. It should be noted that the empirical and analytical estimates reflect the change in rotational energy of the Earth. Apart from the S_2 tide, the dissipation estimates of the different models are closely

Table 3.3.: Current secular change in the Earth's rotation rate by the S_2 tide, given by the nominal tide $\zeta^+_{\sigma,lm}$, $\epsilon^+_{\sigma,lm}$, the tidal energy dissipation $\langle\overline{\dot{E}_d}\rangle$, the rotational energy rate $\langle\overline{\dot{E}_{rot}}\rangle$, the polar tidal torque $\langle\overline{M_{t,z}}\rangle$, the angular acceleration $\dot{\Omega}_{\dot{+}}$, and the daylength rate $\Delta l.o.d$ as time-averaged global quantities.

Reference	Model Observ.	$\zeta^+_{2,2}$ (cm)	$\epsilon^+_{2,2}$ (°)	$\langle\overline{\dot{E}_d}\rangle$ (TW)	$-\langle\overline{\dot{E}_{rot}}\rangle$ (TW)	$-\langle\overline{M_{t,z}}\rangle$ (10^{16} N m)	$-\dot{\Omega}_{\dot{+}}$ ($''$/cy^2)	$\Delta l.o.d$ (ms/cy)
Ocean								
Seiler (1989)	Seiler (1989)			0.420		0.576[3]	147.2[2]	0.268[1]
Zahel et al. (2000)	HAMTIDE			0.381		0.522[3]	133.4[2]	0.243[1]
Egbert and Ray (2003)	TPXO5			0.376		0.516[3]	131.8[2]	0.240[1]
Taguchi et al. (2014)	HAMTIDE	1.164	134.99					
Wilmes et al. (2023)	TPXO9			0.500		0.686[3]	175.3[2]	0.319[1]
Wilmes et al. (2023)	OTIS			0.500		0.686[3]	175.3[2]	0.319[1]
Sulzbach et al. (2023)	TiME21	1.290	131.31	0.481		0.660[3]	168.6[2]	0.307[1]
Ray et al. (1999)	EGM96	0.785	145.90		0.365[3]	0.501[2]	128.0	0.233[1]
Ocean + Earth body								
J. G. Williams and Boggs (2016)	Analytical				0.422[3]	0.579[2]	148.0	0.269[1]
Atmosphere								
Ray et al. (1999)	EGM96				−0.157[3]	−0.215[2]	−55.0	0.100

1 Derived from the values of J. G. Williams and Boggs (2016), cf. Table 3.1 section Ocean + Earth body.
2 Derived by Equation (2.8), $1\,''/\mathrm{cy}^2 = 4.686 \times 10^{-25}\,\mathrm{s}^{-2}$ (Ray et al., 1999).
3 Derived by Equation (2.9) considering $\langle\overline{\dot{E}_d}\rangle = -\langle\overline{\dot{E}_{rot}}\rangle$.

matched and agree with empirical and analytical estimates (Section 3.1.1). Since these are models constrained by tidal heights from satellite altimetry, the matching of the tidal energy dissipation is reasonable, although the mathematical methods are quite different. In particular, the tidal energy dissipation can be expressed in terms of the nominal ocean tide (Appendix C.1). In this case, it depends only on tidal heights. Differences between models occur when tidal heights from different sources are assimilated, e. g. between Zahel et al. (2000) and Taguchi et al. (2014) for the M_2 tide (Table 3.2). The exception in S_2 tidal dissipation is partly due to the complicating factor of radiation forcing (Egbert & Ray, 2003). However, there are larger differences in the partitioning between shallow and deep regions (Egbert & Ray, 2003; Taguchi et al., 2014, and Section 3.2.1.3).

The progress of data-unconstrained tidal models in the simulation of tidal heights (Sections 3.2.1.1 and 3.2.1.3), especially in the open ocean, which occupies most of the Earth's surface, is also reflected in their calculated tidal energy dissipation. The free tidal models, such as the OTIS model (Section 3.2.1.1, p. 73), which is also used to simulate paleo-tides, can be based on the linearized shallow-water equations. Subsequently, the tidal dissipation rate can be determined as the difference between the rate at which work is done by the tidal force and the rate of divergence of the horizontal energy flux, employing the simulated sea surface elevations and the transport vectors. A vectorial consideration of the mean tidal torque is not feasible within the context of the underlying linearized shallow-water equations. Estimates from TiME21 by Sulzbach et al. (2023) for 8 major tidal constituents including M_2, S_2, K_1 and O_1 tides, from OTIS by Green and Huber (2013) for the M_2 tide, from TiME by Weis (2006) for the full spectrum of the 2$^{\text{nd}}$ degree astronomical tidal potential (averaged over one year) and from Seiler (1989) for the M_2, S_2, K_1 and O_1 tides are listed in Tables 3.1 to 3.5. As is done for the tidal energy dissipation of the data-constrained models

Table 3.4.: Current secular change in the Earth's rotation rate by the K_1 tide, given by the nominal tide $\zeta^+_{\sigma,lm}$, $\epsilon^+_{\sigma,lm}$, the tidal energy dissipation $\langle\overline{\dot{E}_d}\rangle$, the rotational energy rate $\langle\overline{\dot{E}_{rot}}\rangle$, the polar tidal torque $\langle\overline{M_{t,z}}\rangle$, the angular acceleration $\dot{\Omega}_{\dot{\sphericalangle}}$, and the daylength rate $\Delta l.o.d$ as time-averaged global quantities.

Reference	Model Observ.	$\zeta^+_{2,1}$ (cm)	$\epsilon^+_{2,1}$ (°)	$\langle\overline{\dot{E}_d}\rangle$ (TW)	$-\langle\overline{\dot{E}_{rot}}\rangle$ (TW)	$-\langle\overline{M_{t,z}}\rangle$ (10^{16} N m)	$-\dot{\Omega}_{\dot{\sphericalangle}}$ ($''$/cy^2)	$\Delta l.o.d$ (ms/cy)
Ocean								
Seiler (1989)	Seiler (1989)			0.200		0.274[3]	70.0[2]	0.127[1]
Zahel et al. (2000)	HAMTIDE			0.353		0.484[3]	123.7[2]	0.225[1]
Egbert and Ray (2003)	TPXO5			0.343		0.470[3]	120.1[2]	0.219[1]
Taguchi et al. (2014)	HAMTIDE	2.839	131.72					
Wilmes et al. (2023)	TPXO9			0.300		0.411[3]	105.0[2]	0.191[1]
Wilmes et al. (2023)	OTIS			0.400		0.549[3]	140.3[2]	0.255[1]
Sulzbach et al. (2023)	TiME21	3.187	135.57	0.334		0.458[3]	117.0[2]	0.213[1]
Ray et al. (1999)	EGM96	2.828	39.45		0.343[3]	0.470[2]	120.0	0.218[1]
Ocean + Earth body								
J. G. Williams and Boggs (2016)	Analytical				0.270[3]	0.370[2]	94.5	0.172[1]

1 Derived from the values of J. G. Williams and Boggs (2016), cf. Table 3.1 section Ocean + Earth body.
2 Derived by Equation (2.8), $1\,''/\text{cy}^2 = 4.686 \times 10^{-25}\,\text{s}^{-2}$ (Ray et al., 1999).
3 Derived by Equation (2.9) considering $\langle\overline{\dot{E}_d}\rangle = -\langle\overline{\dot{E}_{rot}}\rangle$.

done, the derived quantities for the secular deceleration of the Earth's rotation rate are also provided.

The global tidal energy dissipation of the 8 major tidal constituents in Sulzbach et al. (2023) was 3.7 TW (Table 3.1). Consistent with the other estimating approaches, the M_2

Table 3.5.: Current secular change in the Earth's rotation rate by the O_1 tide, given by the nominal tide $\zeta^+_{\sigma,lm}$, $\epsilon^+_{\sigma,lm}$, the tidal energy dissipation $\langle\overline{\dot{E}_d}\rangle$, the rotational energy rate $\langle\overline{\dot{E}_{rot}}\rangle$, the polar tidal torque $\langle\overline{M_{t,z}}\rangle$, the angular acceleration $\dot{\Omega}_{\dot{\sphericalangle}}$, and the daylength rate $\Delta l.o.d$ as time-averaged global quantities.

Reference	Model Observ.	$\zeta^+_{2,1}$ (cm)	$\epsilon^+_{2,1}$ (°)	$\langle\overline{\dot{E}_d}\rangle$ (TW)	$-\langle\overline{\dot{E}_{rot}}\rangle$ (TW)	$-\langle\overline{M_{t,z}}\rangle$ (10^{16} N m)	$-\dot{\Omega}_{\dot{\sphericalangle}}$ ($''$/cy^2)	$\Delta l.o.d$ (ms/cy)
Ocean								
Seiler (1989)	Seiler (1989)			0.160		0.219[3]	56.0[2]	0.102[1]
Zahel et al. (2000)	HAMTIDE			0.179		0.245[3]	62.6[2]	0.114[1]
Egbert and Ray (2003)	TPXO5			0.173		0.237[3]	60.6[2]	0.110[1]
Taguchi et al. (2014)	HAMTIDE	2.591	136.79					
Wilmes et al. (2023)	TPXO9			0.200		0.274[3]	70.0[2]	0.127[1]
Wilmes et al. (2023)	OTIS			0.200		0.274[3]	70.0[2]	0.127[1]
Sulzbach et al. (2023)	TiME21	2.767	136.89	0.199		0.273[3]	69.8[2]	0.127[1]
Ray et al. (1999)	EGM96	2.732	45.09		0.203[3]	0.278[2]	71.0	0.129[1]
Ocean + Earth body								
J. G. Williams and Boggs (2016)	Analytical				0.213[3]	0.292[2]	74.4	0.135[1]
Planetary								
J. G. Williams and Boggs (2016)	LLR				0.198[3]	0.272[2]	69.4	0.126[1]

1 Derived from the values of J. G. Williams and Boggs (2016), cf. Table 3.1 section Ocean + Earth body.
2 Derived by Equation (2.8), $1\,''/\text{cy}^2 = 4.686 \times 10^{-25}\,\text{s}^{-2}$ (Ray et al., 1999).
3 Derived by Equation (2.9) considering $\langle\overline{\dot{E}_d}\rangle = -\langle\overline{\dot{E}_{rot}}\rangle$.

tide contributed 2.5 TW (Table 3.2), about 70 %, with a further split of 0.5 TW from the S_2 tide (Table 3.3), 0.3 TW from the K_1 tide (Table 3.4), and 0.2 TW from the O_1 tide (Table 3.5). Wilmes et al. (2023) obtained comparable dissipations. There are only minor deviations from the reference values of the empirical and analytical methods (Section 3.1.1) and the unrivaled data-constrained models for tidal heights (Section 3.2.1.3).

In contrast, the dissipation of 2.78 TW determined by Green and Huber (2013) for the M_2 tide (Table 3.2) seems too high. For Green and Huber (2013), the dissipation rate was comparable to that obtained by Egbert and Ray (2001) from altimetry data, since only the equatorward dissipation of 60° was considered. However, Egbert and Ray (2001) also provided a total global dissipation of 2.438 TW in their Table 2.

In addition to more detailed bathymetric data, this degree of accuracy is related, in particular, to the consideration of the barotropic/baroclinic energy conversion by means of a parameterized topographic wave drag in TiME21 and OTIS (Sections 3.2.1.1 and 3.2.1.3) This may also explain the overestimated dissipation rates of Seiler (1989) and Weis (2006) (Tables 3.1 to 3.5), which are due to the generally overestimated tidal heights.

3.2.2.2. Geologic epochs

The numerical reconstruction of tides of ancient oceans are obtained using free data-unconstrained tidal models. This requires a detailed knowledge of paleobathymetry. Plate tectonics, however, keeps the ocean basins continuously opening and closing, and the lithospheric plates moving against each other on the asthenosphere (Section 2.1.2.3, p. 17). The age of the seafloor increases with distance from the trench system. It is generally not older than ~200 Myr (Torge, 2001). This place a limit on our knowledge of the ancient oceanic lithosphere. On a timescale of about 100 Myr to 250 Myr, ocean basins formed and disappeared in the Phanerozoic (Boulila et al., 2018; Daher et al., 2021; Nance & Murphy, 2013; Zaffos et al., 2017). The timescale may have been different in the Precambrian (M. Brown et al., 2020; Daher et al., 2021; Evans, 2013; Piper, 2018). The distribution of the continents was significantly different during the *Eon*s. During the Proterozoic the world ocean was much shallower than it was during the Phanerozoic (Denis et al., 2002).

An objective method for reconstructing open-ocean paleobathymetry is provided by the geometric rules of plate tectonics and seafloor spreading (e. g. Stein & Stein, 1992). Much progress has been made in reconstructing paleobathymetry younger than ~200 Myr (Herold et al., 2014; R. D. Müller et al., 2008; R. D. Müller et al., 2016; Seton et al., 2012). In the years before and until today, for example, simplified depth schemes have been established together with the hydrological cycle and mass conservation as well as a hypsometric analysis in cases of missing ocean crust (e. g. Sündermann & Brosche, 1978).

The comings and goings of the oceans in Earth's history must have modified the frequency spectrum of the oceanic normal modes, the resonance properties of the ocean, and thus the spatial and temporal characteristics and energetics of the ocean tides. This, in turn, must have been reflected in the decrease in the Earth's rotation rate. Figure 1.1 strongly indicates that, on average, the decrease was significantly less in the *Proterozoic* (~2500 to 539 Myr ago) than in the *Phanerozoic* (~539 Myr ago to the current time). This suggests a relationship with the evolution of the land-water-distribution in Earth's history. Further, the Earth's rotation rate, as described by the Coriolis parameter, shapes locally the structure

and energetics of the ocean tides (cf. Section 2.2.4.3). A faster rotating Earth with a larger Coriolis parameter will have a smaller Rossby radius. The shortened horizontal length scales of the tides together with the higher tidal frequencies can then result in tides of lower intensity. However, due to the smaller lunar distance, this is counteracted by the stronger astronomical tidal force. Modeling of global ocean tides for different periods of Earth's history and results obtained from solving the spectral problem confirm this (e. g. Blackledge et al., 2020; Brosche & Sündermann, 1978, 1982, 1990; Daher et al., 2021; Hansen, 1982; Kagan & Maslova, 1994; Webb, 1982a).

Paleontological Earth rotation rates have been used to validate the simulations of paleo-ocean tides (Figure 1.1). Sedimentary records of paleo-ocean tidal regimes, such as tidal rhythmites, could provide another option, especially for tidal modeling of coastal shelf systems, but also generally to a lesser extent for global modeling due to the lower resolution (e. g. Collins et al., 2018; Collins et al., 2021; Green et al., 2020; M. R. Wells et al., 2010). Another option for the geologic past back to about ~200 Myr is geologic and paleo-climatic data on astronomical cycles such as eccentricity from the deep-sea cores of the International Ocean Discovery Program (IODP). Calculating these cycles in astrochronology requires considering tidal friction and dynamic ellipticity (Laskar et al., 1993; Lourens et al., 1996; Lourens et al., 2001; Quinn et al., 1991; Zeebe & Lourens, 2022).

Permian One of the first numerical tidal reconstructions of a former ocean was presented by Sündermann and Brosche (1978). For the M_2 ocean tides of the Upper Permian (250 Myr to 230 Myr ago), they showed an angular momentum transfer between Earth and Moon that was smaller by a factor of 2 compared to modern times, consistent with Scrutton (1978) (Section 3.1.2). The tidal amplitudes were comparable to those of modern times.

The state at this time was characterized by a single large continent, Pangaea, extending from the South Pole to near the North Pole. Since information on global paleo-depths is rather scarce, a schematic bottom topography with two different depths was used, based on the paleo-geographic maps of Dietz and Holden (1970). A representative depth of 241 m was used for the shallow self areas and 3746 m were used for the deep ocean. The boundary between shelf seas and deep ocean was set by them at a depth of 1500 m. With this 2-depth model for the modern topography, the angular momentum transfer was reduced by 35 % compared to the real depth topography. On a $4° \times 4°$ regular latitude-longitude grid, the non-linear shallow-water equations were computed using Zahel (1977). Earth tides as well as a parametrized bottom friction and a lateral eddy viscosity were taken into account.

Similar results using the linearized Laplace's tidal equations for the M_2 tidal constituent on a $4° \times 4°$ grid were obtained for the Permian by Ooe (1989). Earth tides, parametrized local SAL effects, and a parametrized linear bottom friction and lateral eddy viscosity were considered. The tidal torque was evaluated as a function of the nominal ocean tide (Appendix C.1) to estimate the tidal secular change in the Earth's rotational energy. Little response of the nominal ocean tide was found for the parameterization of the friction terms and some response for the 1- and 2-depth models for modern conditions. The 2-depth model derived for present-day conditions (Defant, 1961; Hansen, 1982) with about 8 % of the Earth's surface for shelf seas at 200 m depth and about 62.5 % of the Earth's surface for deep ocean at 4200 m depth was the best fit. These configurations were then applied to the Permian ocean of Dietz and Holden (1970).

Phanerozoic An even more sophisticated picture of the history of the Earth-Moon system, which agrees well with the paleontological clock data given by Scrutton (1978), was obtained by Krohn et al. (1981) for the Upper Cretaceous (70 Myr ago) and by Krohn and Sündermann (1982) for the Middle Silurian (420 Myr ago) and the Middle Ordovician (450 Myr ago). Large differences in the land-water distribution and in the extent of shallow shelf seas characterize these time periods. The Upper Cretaceous was a time of global oceanic transgression. The continental shelves underwent an expansion. In the Permian, the supercontinent Pangaea was formed. During the Middle Silurian, the large continent of Gondwana at the South Pole and a ring of the smaller continents formed a nearly closed ocean with more shallow shelf seas than at any time in the Phanerozoic. Both poles were covered by oceans in the Middle Ordovician. Gondwana and most of the smaller continents were located at low to mid-latitudes in the Southern Hemisphere. The method was the same as that used by Sündermann and Brosche (1978) to calculate the paleo-tides of the M_2 tidal constituent and the corresponding tidal torques.

The tidal heights of the considered epochs showed no significant change from modern situation. For the Upper Cretaceous, as for the Upper Permian in Sündermann and Brosche (1978), there is a significantly lower angular momentum transfer compared to the present value, at which the length of the day changed less than today. For the Silurian and Ordovician, on the other hand, the tidal torques are of the same or even higher order of magnitude than in modern times. As in Brosche and Sündermann (1971) and Sündermann and Brosche (1978), there are areas of the ocean with tidal torques slowing down the Earth's rotation rate and areas with accelerating tidal torques in all epochs considered.

Green and Huber (2013) found that tidal dissipation in the early Eocene (55 Myr ago) was barely half of what it is in modern times. Numerical tidal simulations with a resolution of $15'$ were performed based on an OTIS variant (p. 73 and Section 3.2.1.1). In these simulations, the generation of internal tides by topographic wave drag was considered as an additional dissipation mechanism to bottom friction. For the Eocene, climate model data on ocean stratification was used to represent the topographic wave drag. Significantly lower tidal heights for the considered M_2 tidal constituent occurred especially in the Atlantic Ocean, which was narrower than at present. This is explained by the modern Atlantic's almost resonant properties for the M_2 tide (Green & Huber, 2013). Numerical tidal simulations for the Permian-Triassic (252 Myr ago), the Miocene (25 Myr ago), and the Pliocene (3 Myr ago) were added by Green et al. (2017) along with a recalculation for the Cretaceous (116 Myr ago) using M. R. Wells et al. (2010). The method was the same as that used by Green and Huber (2013), but focused on the tidal energy dissipation of the M_2 tides. Total tidal energy dissipation during the last 252 Myr was lower than the modern dissipation for the periods under consideration. However, dissipation in the deep ocean was generally higher than modern dissipation. Both total and deep ocean dissipation were at the minimum 252 Myr ago. This confirms the result of Sündermann and Brosche (1978) and Krohn et al. (1981) on the tidal torque and the angular momentum transfer in the Earth-Moon system of the Upper Permian and Upper Cretaceous, obtained by coarser methods. Deines and Williams (2016) also compiled comparatively smaller decreases in daylength change from the Permian through the Mesozoic to the Cenozoic (cf. Figure 1.1).

On the other hand, the tidal heights of Sündermann and Brosche (1978) and Krohn et al. (1981), which were comparable to modern tidal heights, are contradicted by the significantly

lower tidal heights for the periods considered by Green and Huber (2013) and Green et al. (2017). This could be related to the additional dissipation mechanism of topographic wave drag together with the much more detailed bathymetries used by Green and Huber (2013) and Green et al. (2017).

Neogene and Quaternary On a geologic time scale, the lifetime of the oceanic resonance is shown to be very short. Brosche and Hövel (1982) investigated how the angular momentum transfer between the Earth and the Moon changes between 20 Myr ago and 10 Myr in the future as the European and American continental plates drift apart, using numerical simulations of the global M_2 ocean tides with a $4° \times 4°$ regular latitude-longitude grid.Already on this timescale, angular momentum transfer increases by a factor of 2, with a rapid increase followed by an equally rapid decrease in tidal energy and torque over 5 Myr. In comparison, the Earth's rotation is currently slowing down considerably. A study by Thomas and Sündermann (1999) calculated the global M_2 and O_1 ocean tides, their evolution and their influence on angular momentum balance for realistic topographies since the LGM (last glacial maximum, 22 000 to 18 000 BC). They showed that even in this relatively short time span, the angular momentum transfer rate can vary by up to 10 %. Both studies are based on the non-linear shallow-water equations and the tidal torque approach.

Studies on the sensitivity of tidal response to water depth (propagation rate, resonance) and basin geometry (resonance) have been refined several times for the LGM to the present, with its large sea-level changes (e. g. Egbert et al., 2004; Green, 2010; Griffiths & Peltier, 2008; Griffiths & Peltier, 2009; Sulzbach et al., 2023; Uehara et al., 2006; Wilmes & Green, 2014; Wilmes et al., 2019). The development of free data-unconstrained models in recent decades (Section 3.2.1.1, p. 74), has allowed these refinements along with more recent bathymetries. However, the focus have been on the tidal system with tidal energy dissipation and energy balance. The studies are numerically simulated using the linearized shallow-water equations, in contrast to the previous studies on the tidal torque and Sulzbach et al. (2023). Basically, the friction mechanisms considered are bottom friction and the internal tides generation by the topographic wave drag.

As the global mean sea level dropped by ~130 m and the extent of the ice sheets increased during the LGM, the continental shelves were exposed and the ocean basins reshaped. Especially in the Atlantic, the semi-diurnal tides intensified. This was associated with an increase in tidal energy dissipation by a factor of 2 to 3 in favor of those in the deep ocean (topographic wave drag) and at the expense of those mainly on the continental shelves (bottom friction). According to Wilmes et al. (2023), once the global mean sea level had fallen by more than 100 m during the glacial period, the tidal energy available for mixing the oceans by topographic wave drag could double. In climate simulations by Schmittner et al. (2015) and Wilmes et al. (2019), an enhanced Atlantic Meridional Overturning Circulation (AMOC) was shown by considering the tidal energy dissipation of the LGM. During the subsequent Deglacial and Holocene (since 11 700 years ago), the continental shelves were again flooded. As a result, their share of tidal energy dissipation increased again, while that of the deep ocean decreased. Wilmes et al. (2023) also estimated tidal dissipation for the last four glacial cycles, dating back 430 000 years, with behavior similar to the last glacial cycle.

The amplification of the M_2 ocean tidal resonance during the last glacial periods allows

paleobathymetry to become the dominant factor in the evolution of the tidal system and tidal energy dissipation, while ocean stratification and sea ice have shown little influence. This makes the need to accurately model topographic wave drag and the resulting challenge posed by poorly known ocean stratification, even for the LGM, secondary, at least for the last glacial periods. Sulzbach et al. (2023) also found an enhanced tidal resonance for the diurnal O_1 ocean tides for the LGM, which could affect tidal level of up to several meters.

However, only about the last tenth of Earth's history is covered by these simulations, which go back as far as 450 Myr. Older maps of the world's oceans were not available at the time.

Cryogenian and Ediacaran For the Neoproterozoic, Li et al. (2008) presented a synthesis of the formation (1300 Myr to 900 Myr ago) and breakup (>600 Myr ago) of the supercontinent Rodinia with paleo-geographic data. In addition, Scotese (2009) provided the evolutionary timeline of the two Neoproterozoic supercontinents Rodinia (1100 Myr to 750 Myr ago) and Pannotia (650 Myr to 550 Myr ago). Paleo-geographic maps were generated for the Cryogenian (750 and 690 Myr ago), Ediacaran (600 Myr ago), and Cambrian (540 Myr ago). Besides the location of ancient plate boundaries with subduction zones and mid-ocean ridges, even ancient mountain ranges, sea ways and shelves were inferred. Paleo-geographic reconstructions covering the last billion years were developed by Merdith et al. (2021). Due to seafloor spreading, however, the exact paleobathymetry must remain unknown.

To quantify the energetic effects of cryogenic tides in the context of the hypothesized Snowball Earth (Section 3.1.3.3), numerical simulations of ocean tides for the period 750 Myr to 600 Myr ago were presented by Green et al. (2020) using Scotese (2009). For the bathymetry, the shelf seas were set at a depth of 200 m and the subduction zones at a depth of 5900 m. The mid-ocean ridges were set to dip linearly at 5° from the apex at 2500 m depth. Once these depths were established, the depth of the deep ocean was determined. The assumption was that the volume of the modern oceans was preserved. In the case of glaciations, the depth was reduced by 500 m.

The M_2 ocean tides were simulated with an OTIS variant (p. 73 and Section 3.2.1.1) with a resolution of $15'$. Apart from bottom friction, the tidal conversion depending on the ocean stratification via topographic wave drag was also considered as energy dissipation mechanism. The unknown cryogenic ocean stratification was represented as mixed for glaciated and non-glaciated periods based on modern observations. To simulate thick ice cover of the ocean during glaciations, the bottom friction was doubled. The M_2 tidal constituent was adjusted as described by G. E. Williams (2000) (cf. Table 2.2, p. 30) for the Late Neoproterozoic Earth rotation rate and lunar orbit.

During the hypothesized Snowball Earth (Section 3.1.3.3), the cryogenic ocean experienced a tidal system whose amplitudes were reduced by about ⅔ compared to modern times, and thus only had 10 % to 50 % of the modern tidal energy dissipation (Green et al., 2020). In the time-averaged global case considered here, however, the amplitudes and phases of the tidal oscillation systems together describe the tidal energy dissipatioon. This is because it is then equal to the rate at which the tide-generating potential does work on the ocean (cf. Equation (2.54)). The applied land-water-distribution with a quasi-hemispheric ocean due to Rodinia and Pannotia supercontinents, together with the proposed cryogenic global glaciations, should have created conditions that counteract tidal resonance and suggest weak

tides (Green et al., 2020). Nevertheless, this thesis is contradicted by the study conducted by Webb (1980), which demonstrates that tides of considerable intensity can occur even in hemispherical oceans.

A strong increase in tidal energy dissipation occurred in interglacial conditions. These were modeled with their melting ice in the simulations by a high sea level combined with reduced friction and tidal conversion. For example, at the end of the Marinoan glaciation about 635 Myr ago, tidal energy dissipation increased from 0.2 to 1.4 TW within 5 Myr (cf. p. 87 and Brosche and Hövel (1982)). The simulation for the period 630 Myr ago showed locally over 2 m high tidal amplitudes along the coast of the tidally influenced Elatina Formation (Section 3.1.3). This is consistent with the mesotidal environment estimated by G. E. Williams (2000). The late cryogenic glaciation was 'the tidally quietest period in all previous deep simulations', Green et al. (2020) concluded.

However, Wunsch (2016) and previous discussion of the LGM (Section 3.2.2.2) suggest that the removal of highly dissipative shelf seas by glaciations would increase, not decrease, tidal amplitudes. Thus, the ocean tides of a cryogenic Snowball Earth could have been significantly higher than modern tides (Wunsch, 2016). Because of the explicitly simulated tides based on realistic paleo-geographic maps, Green et al. (2020) suggested that their results differ from the conceptual approach of Wunsch (2016). Moreover, the 11.3 % stronger astronomic tidal force resulting from the reduction in the distance to the Moon in the Late Cryogenian to 96.5 % of the modern distance (G. E. Williams, 2000, cf. Table 2.2, p. 30), should have been capable of compensating for the estimated low tidal energy dissipation (G. E. Williams, 2023).

On the other hand, G. E. Williams (2023) points out that Green et al. (2020) incorrectly assumed that Elatina was postglacial. Cyclic tidal rhythmites in South Australia have been shown to be associated with early and late cryogenic (~660 Myr and ~635 Myr) glacial sequences and interglacial strata (G. E. Williams, 2023). Their analyses suggest strong tides in shallow waters at continental margins at low latitudes, without assuming global ice-covered oceans (G. E. Williams, 2023).

3.2.2.3. Earth history

The dynamic of plate tectonics give rise to alterations in the configuration of ocean basins and the resonance characteristics of the oceans. In order to avoid contradictions with paleontological and sedimentological records, it is essential to consider the influence of plate tectonics when studying the Earth rotation rate from tides on the geological time scale. Hansen (1982) and Webb (1982a, 1982b) were the first to study the evolution of the Earth's rotation rate and the Moon's orbit using idealized ocean and orbital models that account for the changing resonance properties of the oceans. Backward simulations of the M_2 tide for 10 paleo-geographic maps of the Precambrian based on Piper (1982a, 1982b) indicated that the angular momentum transfer was smaller than in modern times during the Earth 's history (Nerge, 1998). The Moon could not have approached the Roche limit in Earth history, according to these simulations. A validation of the model results with paleontological data was not given. Bills and Ray (1999) have matched with remarkable consistency the numerical estimate of Webb (1982b) and the observational estimates from tidal sediments of the evolution of the Moon's semi-major axis over the last 1000 Myr.

Using a relatively simple model that parameterizes rather than explicitly describes the effects of changing ocean configurations, Tyler (2021) was able to simulate tidal evolution over the last 2500 Myr without the Moon approaching the Roche limit. Primarily, the tidal evolution was determined by the resonance properties of the oceans, and not by the increase in astronomical tidal forcing or its frequencies (Poliakow, 2004; Tyler, 2021).

A semi-analytical physical model that is consistent with the current tidal energy dissipation rate and the age of the Moon has been provided by Farhat et al. (2022). Without fitting the model to any available geologic data, the solution fits a large set of these geological data and makes the solution unique. For this purpose, Farhat et al. (2022) extended previous analytical treatments of ocean tides for global and hemispheric configurations. The resulting tidal torques were used in a reduced planar orbital model describing the angular momentum transfer between the Earth's rotation and the Moon's orbital motion to reconstruct the distance between the Earth and the Moon.

The tidal terms were introduced in calculating the Earth's precession and rotation over several million years by Laskar et al. (1993), Néron de Surgy and Laskar (1997), and Quinn et al. (1991), while the resulting change in solar insolation was discussed by Berger et al. (1989). The evolution of the Earth-Moon system under tidal friction was of great importance in the astronomical calculation of solar insolation for a period from 250 Myr ago to 250 Myr from now in Laskar et al. (2004). Apart from possible changes in dynamic ellipticity, tidal friction inaccuracies were the largest contributors to uncertainties in the studies. Even though Laskar et al. (2011) improved the model for the evolution of Earth rotation, tidal friction remained the most important unknown parameter for the evolution of precession and obliquity as the largest uncertainty.

3.3. Summary

A tidal increase in day length of 2.4 ms/cy is suggested by analyses of space-borne geodetic and satellite altimetric information, global numerical simulations of ocean tides, and analytical approaches. Earth's lunar tides account for about 85 % of the increase, while solar tides account for only about 15 %. Most of the increase, about 95 %, is due to the ocean tides. The M_2 tide alone accounts for about 70 % of the total increase, indicating its proximity to resonance. Meanwhile, the M_2 tide of the solid Earth body accounts for less than 5 % and that of the atmosphere for less than 1 %. The S_2, K_1, and O_1 tides also make a significant contribution. There is a transfer of energy and angular momentum from the rotation of the Earth to the orbits of the Moon and the Sun. The result is the recession of the Moon from the Earth at a rate of 3.8 cm/yr. The effect on the Earth orbiting the Sun can be neglected.

In numerical ocean tide simulations, the tidal friction of the Earth-Moon system is obtained from the time-averaged global tidal torque and tidal energy dissipation. Generally, only scalar energy transfer in the oceans is treated. It is considered that the tidal energy is dissipated at the expense of the Earth's rotation rate. The vectorial angular momentum approach, on the other hand, suggests a tidal torque that can accelerate instead of decelerate the Earth's rotations rate at the local scale.

The free data-unconstrained ocean tide models are now comparable to the altimetry-

constrained models in terms of tidal friction. They are only dependent on the shallow-water equations, and require bathymetry and parametrized dissipation mechanisms. An improved treatment of the SAL effects and the consideration of internal tide generation has significantly improved the accuracy of the free models.

The characteristics of the ocean tides and their tidal friction vary with the position of the resonant frequencies in relation to the Earth's rotation rate. As the continents move relative to each other at a rate of a few centimeters per year, the shape of the ocean basins changes. Even the shorter glacial cycles, with exposure of continental shelves and large changes in water depth, have an effect. This alters tidal strength and tidal friction. Modeling of global ocean tides, mostly the M_2 tide, for different periods of the Phanerozoic and the Late Neoproterozoic, as well as results of solving the spectral problem confirm this. The results are consistent with paleontological Earth rotation rates.

A unique record of the history of Earth rotation and lunar orbit in the Late Neoproterozoic, ~620 Myr ago, are the tidal rhythmites of the Elatina Formation in South Australia. An interstadial or interglacial period of high sea level during deposition is indicated by the rhythmites. Distal ebb tidal characteristics near the margin of a marine gulf and rapidly increasing water depth seaward of the ebb-tidal delta terminal lobe have been proposed as the depositional site. This provides outstanding information for the numerical reconstruction and validation of ocean tides for this distant time period.

4. Research design and evaluation

Following the theoretical embedding and an overview of the state of art and related work, the central concept of the present study can now be presented. The methodology and approach utilized to reconstruct the ocean tides of the Late Neoproterozoic ~620 Myr ago and the associated tidal friction are described in detail. This chapter outlines the approach by which the research question will be addressed (Section 4.1), the data that will be used (Section 4.2), the resources and tools that will be employed (Section 4.3), and the manner of implementation (Section 4.4). The conclusion is an evaluation of the implementation under modern conditions in order to make a statement about the reliability of the approach for the Late Neoproterozoic ~620 Myr ago (Section 4.5).

4.1. Approach

Numerical simulations are employed to characterize the spatial and temporal attributes of Late Neoproterozoic ocean tides, which occured ~620 Myr ago, and to assess their potential to facilitate the deposition of the Elatina tidal rhythmites (Section 3.1.3). An additional area of interest is the documented increase in day length and lunar distance recorded by the Elatina tidal rhythmites. The simulations (Sections 4.1.1 and 4.1.2) consider the global tidal oscillation system (Equations (2.43) to (2.45)) and its instantaneous energy and angular momentum budgets (Equations (2.52) and (2.55)). The budgets include the transfer of angular momentum from the Earth's rotation via the ocean tides to the Moon's orbit through the tidal torque, which is relevant for the increase in day length and lunar distance (Sections 2.1.3.1 and 2.3). The time-averaged global polar tidal torque is the fundamental quantity describing the process in its essence. It necessitates a considerable higher degree of accuracy in the simulations than the tidal oscillation system. To conduct the simulations it is necessary to consider the lunisolar tidal potential (Section 4.1.3) and to have knowledge of the depth distribution and coastlines (Section 4.1.4) for the specific time period under consideration. The methodology employed for the implementation and evaluation of the approach is outlined in Section 4.1.5.

The objective of this study is to establish a first-order estimation in order to provide an approximation for an evaluation of the simulation results. This evaluation is conducted in conjunction with independent geological data concerning the tidal spectrum and the evolution of the lunar orbit and Earth rotation rate. In the current study a data-unconstrained barotropic tidal model was used. The next two Sections 4.1.1 and 4.1.2 describe how the decision was taken.

4.1.1. Initial simulation approach

In order to account for the influence of tidal friction exerted by the time-averaged global tidal torque, it would be appropriate to implement the non-linear shallow-water equations (Equations (2.43) to (2.45)) within the model. Due to the non-linearity inherent in the system, the tidal velocities can exhibit an inharmonic course, which, in turn, can lead to a non-vanishing time-averaged global tidal torque of the individual partial tides in the oceans (Section 2.2.4.6, p. 48). However, recent developments in oceanography and Earth system research are progressing towards coupled models that take into account the interrelationship between baroclinic circulation and barotropic tidal processes (Section 3.2.1.1, p. 74). The initial approach utilized the global circulation model MPIOM (Max Planck Institute Ocean Model), which can be augmented by a tidal module incorporating the complete 2^{nd} degree lunisolar potential (Jungclaus et al., 2006; Marsland et al., 2003; M. Müller et al., 2010; Thomas, 2002; Thomas et al., 2001). The spatial discretization may be performed with a curvilinear bipolar grid, with the position of the poles selected freely. A dedicated general geodetic module, developed with a user-defined interface to the specific ocean model MPIOM, provided the angular momentum balance and tidal torque in the usual manner within the body-fixed geocentric Cartesian coordinate system.

The preliminary approach was to describe the complete 2^{nd} degree lunisolar tidal potential in accordance with the ephemerides. Therefore, a single simulation can adequately represent the entirety of ocean tides. However, as all lunisolar tidal forces were considered, it is not possible to average the tidal torque over periods that are exactly closed. By employing an averaging method over a simulation period deemed sufficiently lengthy—for instance, over 200 yr for modern times—the resulting mean tidal torque did not yield a convergent result. This discrepancy can be attributed to the observation that the time-averaged global tidal torque was found to be up to four orders of magnitude smaller than its instantaneous values. It was therefore concluded that longer simulation periods were unsuitable for consideration.

4.1.2. Final simulation approach

The approach of simulating individual partial tides, which is widely used in this field, has been selected. Averaging across exactly closed periods subsequently yields a stable time-averaged global tidal torque. The semi-diurnal principal tides (M_2 and S_2) and the diurnal declinational tides (K_1 and O_1) were selected for examination. These tides are dominant with respect to the lunisolar tidal potential (Section 2.2.2, Equation (2.27), and Table 2.3) and the ocean tides (Section 3.2.1). From another perspective, these tides demonstrate the temporal pattern of the ocean tides (Section 2.2.4.4 and Equation (2.50)). Furthermore, the calculations necessitates only long-term, secular effects, as short-term phenomena with astronomical cycles, such as those resulting from lunar orbital eccentricity, are negated over geological time scales.

In conclusion, the tidal model TiME by Weis (2006) as presented in Section 3.2.1.1, p. 75, and Section 3.2.2.1 has been utilized. A detailed description is presented in Sections 4.3.1 to 4.3.3. The model incorporates modules for energy and angular momentum budgets, as the original model was developed by Seiler (1989) with regard to contributions to Earth rotation (Section 3.2.2.1 and Tables 3.2 to 3.5).

Modern tidal models have demonstrated that their parameterizations of dissipation, including topographic wave drag, are sufficient for accurately simulating tidal processes under modern conditions (Section 3.2.1.3). It remains unclear whether these parameterizations can be applied to geological conditions such as higher and lower sea levels and topographies with a supercontinent. Furthermore, the stratification of the ocean is poorly understood, even in recent times (Egbert et al., 2004). This introduces additional uncertainty regarding dissipation due to topographic wave drag and the transformation from barotropic to baroclinic tides in the distant past. Given the uncertainties concerning the Late Neoproterozoic context, the process of tidal transformation due to topographic wave drag will not be considered. The parameterization for the modern conditions will be adopted unchanged for the tidal simulations to the Late Neoproterozoic. In consideration of the cyclic tidal rhythmites observed in South Australia, whose analysis indicates the occurrence of strong tides in shallow waters on continental margins and the absence of global ice-covered oceans (G. E. Williams, 2023), the geographical environment of modern times has been presumed to remain unaltered throughout the Late Neoproterozoic. Accordingly, a Snowball Earth scenario has been ruled out according to G. E. Williams (2023) (Section 3.2.2.2).

In principle, simulations with a resolution of $30'$ allow an adequate representation of barotropic tides in the open ocean for modern times (Section 3.2.1.3 and Stammer et al., 2014; Zaron & Elipot, 2021). However, their characteristics on the continental shelves and near the coast are only described to a limited extent. The two-depth distribution assumed for the Late Neoproterozoic ~620 Myr ago to represent the unknown ocean depth does not account for additional features of the ocean topography, such as trenches and ridges, beyond the inclusion of shelves and the open ocean. Furthermore, uncertainties exists with regard to the coastline. Given the above considerations, resolving the simulations to a regular latitude and longitude grid of $1°$ is considered sufficient.

4.1.3. Tide-generating paleo-potential

The resonance conditions and spatial characteristics of the ocean tides are influenced not only by the excitation frequencies, but also by the Earth's rotational speed. In order to describe the lunisolar partial tides under consideration and the Coriolis parameter, the configuration of the Earth-Moon-Sun system in the Late Neoproterozoic, as proposed by G. E. Williams (2000), cf. Section 3.1.3 and Table 2.2, has been adopted (Section 4.2.1).

The solid Earth's body tides are typically described as being directly proportional to the lunisolar tidal potential (Section 2.2.3). However, due to the inelastic nature of the solid Earth's body, the propagation of the tides is delayed in comparison to the lunisolar tidal potential. With regard to the geological timescale, the inelastic properties of the Earth's body are assumed to remain unchanged. This also applies to the manner in which the Earth's body responds to the load exerted by ocean tides.

4.1.4. Paleobathymetry

In addition to the formulation of the lunisolar tidal potential for the selected time epoch, the compilation of the associated bathymetry of the world ocean represents a crucial prerequisite for the operation of the tidal model. The critical dependence of tidal solution quality on

bathymetric precision was also demonstrated in sensitivity tests conducted by Egbert et al. (2004), in which randomly perturbed bathymetry was employed.

The uncertainties regarding the age of the Elatina tidal rhythmites (Section 3.1.3.3) will be addressed through the consideration of a selection of three recent paleogeographic reconstructions for different time slices of the Late Neoproterozoic, as provided by Scotese (2017) and Scotese and Wright (2018). Two of the reconstructions are similar, while the third differs significantly. The paleogeographic reconstructions represent the unknown bathymetry (Section 3.2.2.2) through continental shelves and a deep ocean, each with a defined depth, considering an ocean volume comparable to modern conditions. Furthermore, the different reconstructions allow for the estimation of the influence of a supercontinent on the spatial and temporal characteristics of the tidal system, as well as on its properties, including the time-averaged global tidal torque.

4.1.5. Implementation

The tidal model is initially subjected to a series of sensitivity tests for calibration purposes (Section 4.4.2). The reliability of the approach for the Late Neoproterozoic ~620 Myr ago will be evaluated under modern conditions (Section 4.5.1), including an assessment of the influence of the two-depth distribution (Section 4.5.2). Tidal maps are utilized to demonstrate the evolution of the spatial and temporal characteristics of the ocean tides for the individual partial tides.

The Elatina and Reynella tidal rhythmites from South Australia (Section 3.1.3) provide a valuable opportunity to evaluate the Late Neoproterozoic tidal simulations, as they offer observational data on the tidal spectrum of the Australian continental plate. The tidal range enables inferences to be drawn regarding the potential for sedimentation (Section 2.4). The form factor and type of the tidal regime permit the drawing of conclusions regarding the periodicity of a deposit (Section 2.4). The type of coastal tidal regimes are of particular interest for the evaluation based on the local geological data of the Elatina and Reynella tidal rhythmites.

The time-averaged global polar tidal torque and the power supplied by the partial tides on the ocean are determined and analyzed in terms of their distribution globally and zonally. This allows for a more detailed investigation of the shorter day length recorded by the Elatina and Reynella tidal rhythmites ~620 Myr ago.

The final tidal simulations, presented in Chapter 5, are conducted under identical conditions for all four bathymetries, one representing the modern era and three representing the Late Neoproterozoic. The simulations initiated with the modern sidereal day length for the Coriolis parameter and the modern lunisolar partial tides, and then alternated with the sidereal day length and the lunisolar partial tides for the Late Neoproterozoic. The distinct bathymetric conditions facilitate the visualization of the impact of ocean basin geometry on the tidal oscillation system. Moreover, the different sidereal day length enables the visualization of the impact of the Earth's rotation rate on the ocean tides. Additionally, the variation of the lunisolar partial tides demonstrates how the excitation frequencies impact the resonance conditions of ocean tides. The aforementioned effects on the global balance quantities of the tidal oscillation system can also be separated.

4.2. Data base

This section presents the lunisolar partial tides and the Coriolis parameter (Section 4.2.1) as well as the bathymetries (Section 4.2.2), which were utilized in the tidal simulations for the modern times and the Late Neoproterozoic.

4.2.1. Lunisolar tidal potential and Coriolis parameter

The configuration of the Earth-Moon-Sun system proposed by G. E. Williams (2000) is utilized to describe the lunisolar tidal potential and the Coriolis parameter in the Late Neoproterozoic ~620 Myr ago. A detailed description can be found in Section 3.1.3. For a summarized version, please see Table 2.2. This configuration encompasses a mean solar day of 21.9 h and an unaltered solar distance in comparison with modern conditions. Three of the six fundamental periods of the lunisolar tidal potential (Section 2.2.2), the tropical year, the perigee precession, and the lunar orbital precession are directly covered (Table 2.2). From the provided data on sidereal and synodic months, the remaining fundamental period of the tropical month can be derived (Table 2.2). The local temporal reference via the local mean lunar time (Section 2.2.2, p. 29) can be obtained by means of the relation to the mean solar day, together with the tropical year and the tropical month (Table 2.2). The remaining fundamental period of the perihelion precession, along with the mean tropical year, describes the influences on the lunisolar tidal potential resulting form the Earth's orbital ellipse. Given the relative moderate eccentricity of Earth's orbit, these effects are of limited consequences with regard to the overall lunisolar potential, and are consequently beyond the scope of this study. In this context, the treatment of the phase of the partial tides remains an open question. Since real-time simulations are not required, tidal phases are not considered in this study.

With regard to the partial tides M_2, S_2, K_1, and O_1 encompassed by this study, their angular frequencies σ and periods are tabulated in Table 4.1 for modern times and for ~620 Myr ago. Equation (2.27) in conjunction with Table 2.3 demonstrates how the angular frequencies and periods of the considered partial tides are composed of the fundamental tidal periods presented in Table 2.2.

In contrast to the solar tidal potential, the lunar tidal potential reached a higher intensity ~620 Myr ago than it does in modern times. As stated by G. E. Williams (2000), the Earth's distance from the Sun ~620 Myr ago was identical to that observed in modern times. Consequently, the geodetic functions (Table 2.3 and Equation (2.26)) for the solar partial tides and thus their strength remained unaltered. Conversely, the reduced distance between Moon and Earth ~620 Myr ago, compared to modern times (Table 2.2), has the effect of increasing the lunar geodetic functions for the period ~620 Myr ago by a factor of 1.113, in relation to those of modern times. In this estimation, the Earth's radius was held constant between the periods of ~620 Myr ago and modern times (Section 3.1.3.2 and G. E. Williams, 2000). The same applies to the mass of the Earth $m_{\oplus}$ and the gravitational constant G. Moreover, it is assumed that the ratio of the partial tides to each other and the amplitude coefficients c_σ of the partial tides have remained unaltered in comparison to modern times. In the simulations, the amplitude coefficients presented in Table 2.3 were employed for the partial tides M_2, S_2, K_1, and O_1, both for modern times and for the time slice ~620 Myr ago.

Table 4.1.: Tidal amplitude coefficients c, geodetic functions $G_{1,2}$, tidal frequencies σ and tidal periods of modern times and of ~620 Myr ago derived from G. E. Williams (2000).

Tide	Era	c	$G_{1,2}$	σ ($^\circ\,h^{-1}$)	Period (h)
M_2	modern	0.9081	1.000	28.984 104	12.42
	~620 Myr ago		1.113	31.797 183	11.32
S_2	modern	0.4229	1.000	30.000 000	12.00
	~620 Myr ago		1.000	32.876 712	10.95
K_1	modern	0.5308	1.000	15.041 069	23.93
	~620 Myr ago		1.113	16.479 452	21.85
O_1	modern	0.3768	1.000	13.943 036	25.82
	~620 Myr ago		1.113	15.317 731	23.50

Accordingly, the potential of the semi-diurnal principal and diurnal declinational lunar tides (M_2 and O_1) has been considered to have an amplitude of 1.113 times that of modern times, while the semi-diurnal principal solar tide S_2 has been considered to have an identical amplitude in comparison to modern times in the simulations for the time slice ~620 Myr ago. The solar contribution of 32 % to the diurnal declinational tide K_1 (Table 2.3) has been simulated together with the lunar contribution of 68 % to the diurnal declinational tide K_1 (Table 2.3) in accordance with standard practice. In consideration of the scope of the present study, the entire diurnal declinational lunisolar tide K_1 has been incorporated into the simulations for the time slice ~620 Myr ago at a factor of 1.113 greater than in modern times.

In addition, the mean sidereal day for the modern era and for ~620 Myr ago (Table 2.2) has been applied to the Coriolis parameter f in the shallow-water equations (Equations (2.43) to (2.45)) as part of the simulations performed. The gravity acceleration g, which encompasses the mean centrifugal acceleration associated with the Earth's rotation, is assumed to be constant at the modern value, since the difference of less than $0.004\,m\,s^{-2}$ is considered negligible.

4.2.2. Bathymetry

For modern times, a 1° resolution bathymetry (Figure 4.1a) was extracted from the GEBCO (General Bathymetric Chart of the Oceans) bathymetry with a resolution of 5′, as utilized by Weis (2006). An optimization and smoothing of the topography have not been carried out within the scope of the present study.

In line with the actual paleogeographic reconstruction of the Late Neoproterozoic as detailed in Section 3.2.2.2, p. 88, the paleobathymetries by Scotese (2017) and Scotese and Wright (2018) have been applied in this study. The reconstructions were already available in 1° resolution with respect to both latitude and longitude. In accordance with the geologic data provided by G. E. Williams (2000) for the Late Neoproterozoic (~620 Myr ago), paleogeographic data could be provided for the periods of ~600 Myr and ~630 Myr ago. The reconstruction from ~750 Myr ago was also employed to account for the varying position of the supercontinent Rodinia in the Late Neoproterozoic. With the

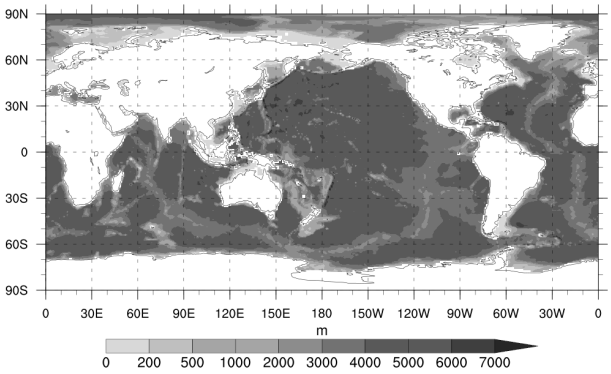

(a) Modern bathymetry extracted from 5′ GEBCO bathymetry of Weis (2006).

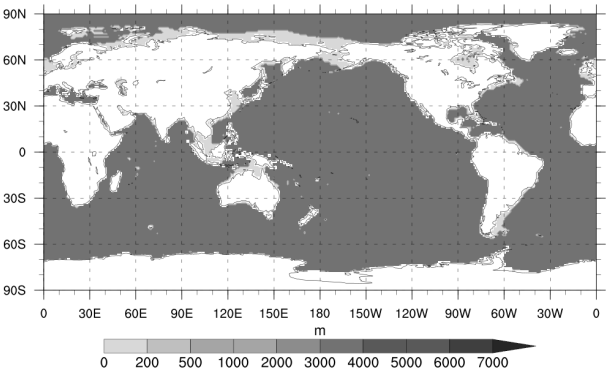

(b) Modern two-depth bathymetry derived from Figure 4.1a.

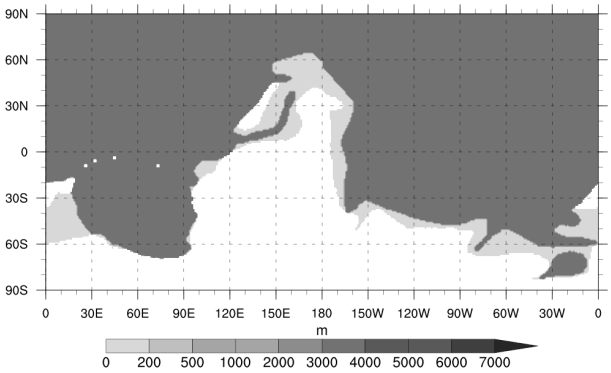

(c) Two-depth bathymetry of ~600 Myr ago derived from Scotese (2017) and Scotese and Wright (2018).

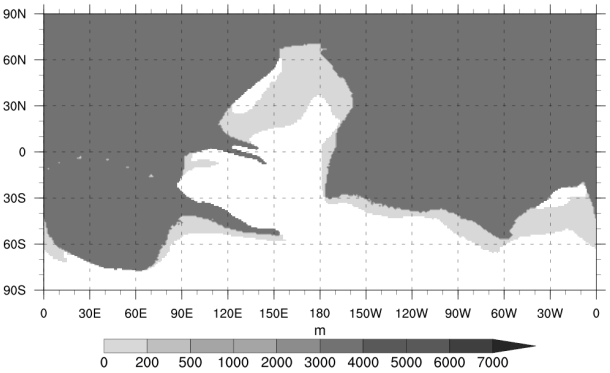

(d) Two-depth bathymetry of ~630 Myr ago derived from Scotese (2017) and Scotese and Wright (2018).

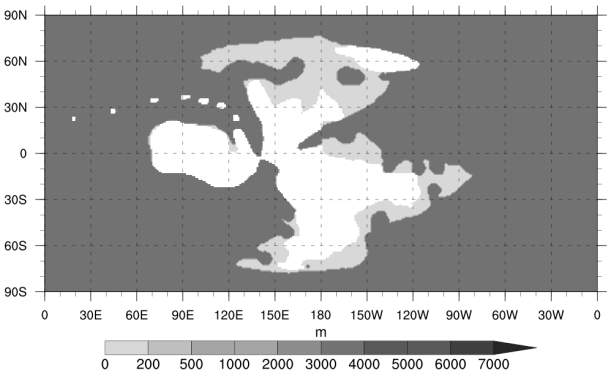

(e) Two-depth bathymetry of ~750 Myr ago derived from Scotese (2017) and Scotese and Wright (2018).

Figure 4.1.: Land-water distribution and bathymetry in m of modern times, ~600 Myr ago, ~630 Myr ago, and ~750 Myr ago at 1° resolution. Two-depth bathymetries with shelf seas at 160 m depth and open ocean at 3480 m depth.

exception of the transitions between the continental shelves and the deep ocean, a two-depth distribution was identified, with the shelf seas having a depth of 160 m and the open ocean a depth of 3480 m. The maximum depth of the flooded continents was set at 200 m (Scotese, 2020). These depths, which correspond to the average of the modern ocean of ~3500 m (Scotese, 2020), ensure that the volume of the paleo-oceans aligns with the modern value. However, it is possible that the depth has been a few hundred meters shallower, as the

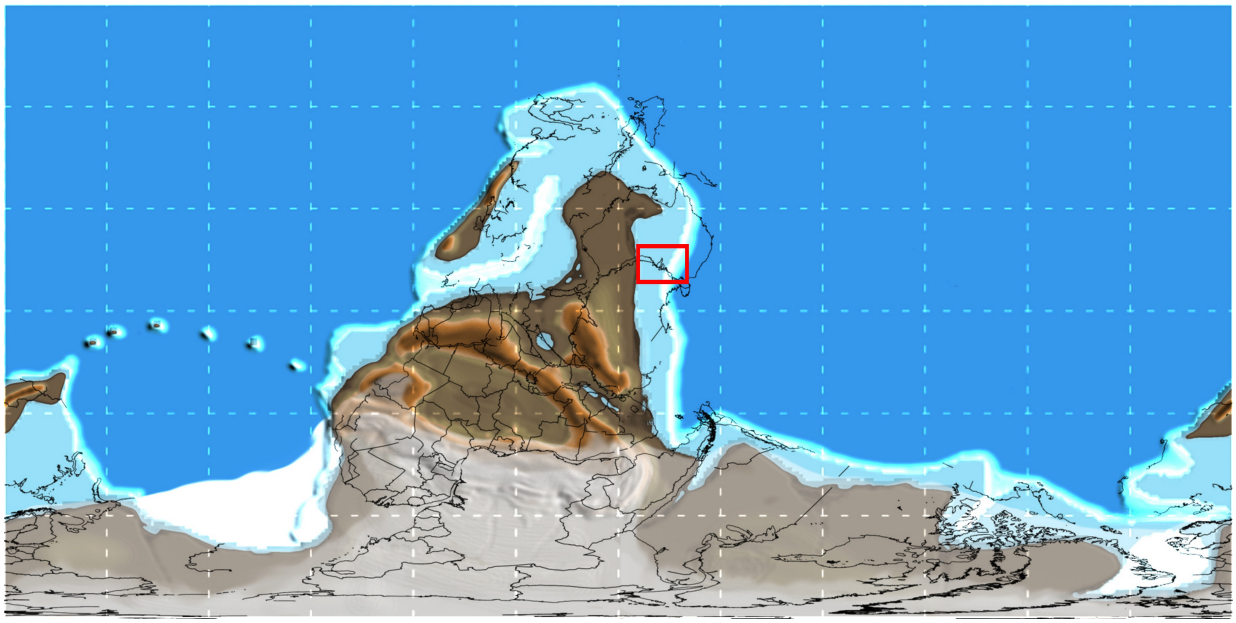

(a) ~600 Myr ago.

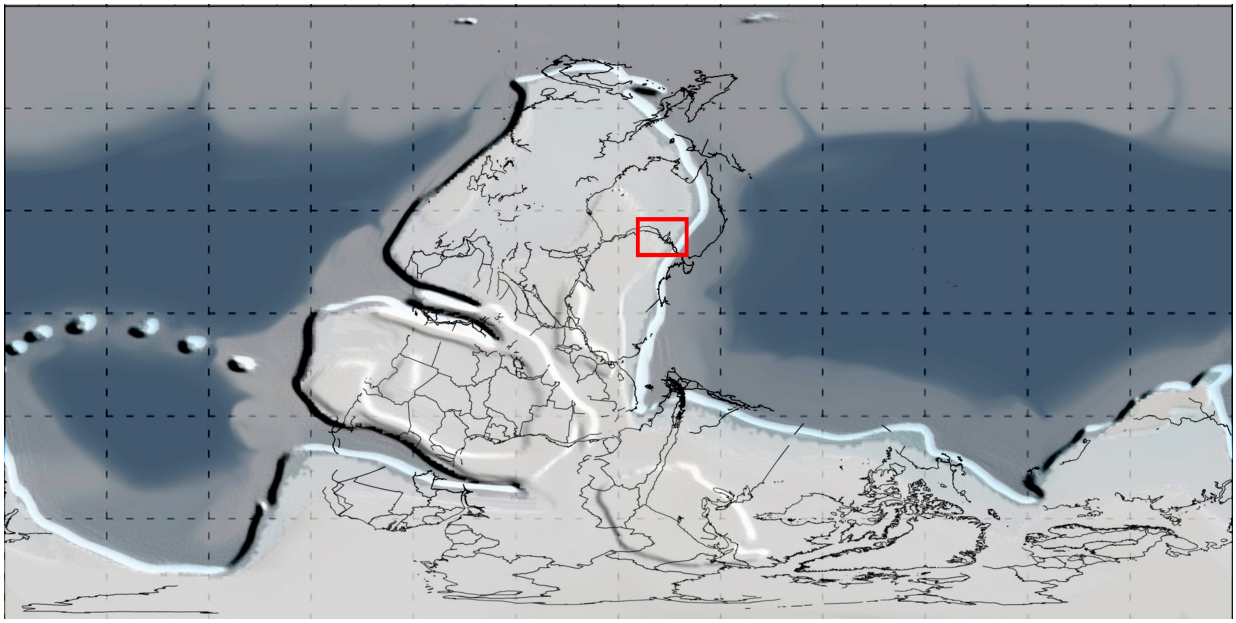

(b) ~630 Myr ago.

Figure 4.2.: Topographies of Scotese (2017) and Scotese and Wright (2018).

effects of plate tectonics were more pronounced at that time (Scotese, 2020). In contrast to the reconstructions used by Green et al. (2020) for paleotidal simulations of the Late Neoproterozoic, subduction zones and mid-ocean ridges were not taken into account.

The transitions between the continental shelf and the open ocean were eliminated in favor of a pure two-depth distribution. Depths of up to 200 m were assigned to the shelf seas and set at a depth of 160 m. Depths greater than 200 m were assigned to the open ocean and set at a depth of 3480 m. As shown in Figures 4.1c and 4.1d, the supercontinent Rodinia extents like a brace along a meridian from 20° S over the South Pole to 70° N in

similar reconstructions for the time periods ~600 Myr and ~630 Myr ago. In the southern region, the deep open ocean is divided into two semi-enclosed basins, separated by an island with an associated shelf that connects the island to Rodinia. This is located at about 10° E in the land-water distribution ~600 Myr ago and at about 15° W in the land-water distribution ~630 Myr ago. The open boundary of the basins extends between about 20° S and 30° S, aligning closely with the southern boundary of the southern equatorial waveguide. In contrast, the reconstruction for ~750 Myr ago (Figure 4.1e) demonstrates that Rodinia extends along a meridian from 80° S over the equator to 80° N, with a peninsula present at the equator in the west. An open ocean of nearly hemispherical shape, bounded by a meridian, was situated to the west and east of Rodinia ~750 Myr ago. Additionally, the Northern Hemisphere exhibited an almost hemispherically open ocean ~630 Myr and ~600 Myr ago (Figures 4.1c and 4.1d).

Furthermore, Figure 4.2 present the underlying reconstruction by Scotese (2017) and Scotese and Wright (2018) for ~600 Myr and ~630 Myr ago, with the position of the current continents, including Australia, shown. The maps are centered on the equator at 180° W and the red-outlined rectangle indicates the western part of the modern southern coastline of Australia, encompassing the Spencer Gulf and the Flinders Ranges with the Elatina Formation (Section 3.1.3). In the reconstruction ~600 Myr ago, the rectangle lies between 9° to 18° N and 159° to 174° W (Figure 4.2a). ~630 Myr ago the region was situated further north, between 17° to 26° N, within the same longitude range (Figure 4.2b).

To assess the impact of a two-depth distribution, the modern bathymetry was also transformed into a two-depth distribution (Figure 4.1b) as part of a sensitivity analysis.

4.3. Resources

This section provides a detailed description of the tidal model employed in the simulations, as outlined in Section 4.3.1. It also presents the parameterization of dissipation and the selection of additional model parameters utilized in the simulation, as detailed in Section 4.3.2. The geodetic module will be addressed in the subsequent step, (Section 4.3.3). Finally, Section 4.3.4 outlines the methodology for evaluating and analyzing the simulations.

4.3.1. Ocean tide model

The subsequent simulations based on the tidal model TiME developed by Weis (2006) on the basis of Seiler (1989) and Thomas (2002), as described in Section 3.2.1.1, p. 75, and Section 3.2.2.1. The non-linear shallow-water equations (Equations (2.43) to (2.45)) are implemented and solved on a global regular latitude-longitude Arakawa-C grid using a semi-implicit finite difference algorithm, as described in detail by Backhaus (1985) and Backhaus (1983). $\Delta\varphi$ and $\Delta\lambda$ are the angular distances between the sea level points ζ and the velocity points u, v in latitude and longitude, respectively. To circumvent a polar coordinate singularity, the grid is bounded by a spherical cap extending from the latitude φ_p towards the North Pole. An analogous description of the South Pole is not incorporated into the model, as the current location of Antarctica renders the calculation of latitudes between 78° S and 90° S superfluous.

The spatial differential operators are approximated by central differences. The temporal differential operators are discretized with forward differences; Δt is the time step resulting from the tidal period P and the number of time steps per tidal period N with $N \in \mathbb{N}$ according to

$$\Delta t = \frac{P}{N}. \tag{4.1}$$

Since Seiler (1989), the tidal energy dissipation term $\vec{\boldsymbol{F}}_f$ is composed of two components: the bottom friction

$$\vec{\boldsymbol{F}}_{bf} = r\vec{\boldsymbol{v}}|\vec{\boldsymbol{v}}| \tag{4.2}$$

parameterized according to the standard quadratic law, where $r = 0.003$ represents a dimensionless drag coefficient, and turbulent effects due to horizontal eddy viscosity by

$$\begin{aligned}\vec{\boldsymbol{F}}_{ev} = {} & \frac{A_h}{R^2}\left(\frac{1}{\cos\varphi}\frac{\partial^2}{\partial\lambda^2} + \frac{\partial^2}{\partial\varphi^2} - \tan\varphi\frac{\partial}{\partial\varphi} - \left(1+\tan^2\varphi\right)\right)\begin{pmatrix}u\\v\end{pmatrix} \\ & - \frac{A_h}{R^2}\left(2\tan\varphi\frac{\partial}{\partial\lambda}\right)\begin{pmatrix}v\\u\end{pmatrix}\end{aligned} \tag{4.3}$$

parameterized according to the Reynolds shear stress, where A_h represents the horizontal exchange coefficient. The horizontal exchange of water masses by means of small-scale processes that take place within a model grid box is prescribed and parameterized here. It therefore is a function of the spatial dimensions of the grid boxes. The relation accounts for the varying grid cell areas by employing the following approach for the zonal and meridional exchange coefficients:

$$A_z = A_h \cos\varphi \quad \text{and} \quad A_m = A_h.$$

The exchange coefficient A_h is fundamental to achieving a stable and convergent numerical solution of the global tidal oscillation system. The solution, which is not strictly harmonic due to the presence of non-linear interactions, can be approximated asymptotically. This is opposed by the maximum exchange coefficient of a stable numerical solution

$$A_h = \frac{R^2\left(\Delta\lambda\right)^2\cos\varphi_p}{4\Delta t} \tag{4.4}$$

due to the resolution of the space-time discretization (Seiler, 1989). An increase in the exchange coefficient A_h, accompanied by a reduction in the time step Δt and a constant space discretization in latitude $\Delta\varphi$ and longitude $\Delta\lambda$, results in a global dampening of the tidal amplitude and a delay in the tidal phase of the sea surface elevations. The tidal transports are also dampened, as the transport field is described consistently with the mass distribution. The determination of the horizontal exchange coefficient A_h necessitates a process of calibration and adjustment through empirical investigation (Section 4.4.2).

In consideration of global ocean tides, the solid and considered impermeable coastlines

define the boundary. Half-slip Dirichlet boundary conditions

$$\vec{\boldsymbol{v}}\vec{\boldsymbol{e_n}} = 0 \quad \text{and} \quad \vec{\boldsymbol{v}}\vec{\boldsymbol{e_t}} = \frac{1}{2}\vec{\boldsymbol{v}}^{o}\vec{\boldsymbol{e_t}} \tag{4.5}$$

are used as boundary conditions. $\vec{\boldsymbol{e_n}}$ and $\vec{\boldsymbol{e_t}}$ denote the normalized normal and tangential vectors of the bounding land surface. $\vec{\boldsymbol{v}}^{o}$ is the velocity at the wet grid point closest to the coast. On the one hand, it is required that the mass flow normal to the boundary vanishes, and on the other hand, that the mass flow tangential to the boundary satisfies the half-slip condition. The initial condition is chosen to be the state of rest ($\vec{\boldsymbol{v}} = 0$) and no sea surface elevation ($\zeta = 0$). It is a fully determined initial boundary value problem that does not depend on any empirical data other than the depth distribution and the coastlines.

4.3.2. Model parameterization

The space-time discretization is addressed, which defines the maximum horizontal exchange coefficient A_h of the eddy viscosity parameterization (Equation (4.4)). The high resolution of the final regular latitude and longitude grid of $5'$ by Weis (2006) is reduced to

$$\Delta\varphi = \Delta\lambda = 1^{\circ}.$$

The reduction of the zonal resolution $\Delta\lambda$ at two specific latitudes in the direction of the North Pole, resulting from the limitation of the time step by the smallest grid cell (Equation (4.4)), is therefore rendered unnecessary. In order to conduct tidal simulations with the Late Neoproterozoic bathymetries, the model is extended to encompass latitudes between 78° S and 90° S. Additionally, a polar cap analogous to the North Pole is incorporated into the model for the South Pole. The radius of the polar caps is increase from 2.5° to

$$\Delta\varphi_p = 3^{\circ}. \tag{4.6}$$

The adjustment experiments, as detailed in Sections 4.4.2.1 to 4.4.2.3, yield a time step of about $\Delta t = 2\,\text{min}$ for the semi-diurnal tide simulations and of about $\Delta t = 4\,\text{min}$ for the diurnal tide simulations. A minimum depth of 15 m is established.

The model parameterization encompasses also the impact of the bottom friction and eddy viscosity. A bottom friction coefficient of $r = 0.003$ is implemented, consistent with other models in the field. In accordance with the investigations of e. g. Hufschmidt (1995), Seiler (1989), Thomas (1996), and von Storch et al. (2023), the adjustment of the model for modern times encompasses solely the eddy viscosity with the horizontal exchange coefficient A_h (Section 4.4.2). Adjustment experiments conducted with a semi-diurnal partial tide forcing yield an optimum exchange coefficient of $A_h = 250 \times 10^4\,\text{m}^2\,\text{s}^{-1}$, while experiments conducted with a diurnal partial tide forcing yielded an optimum exchange coefficient of $A_h = 75 \times 10^4\,\text{m}^2\,\text{s}^{-1}$.

In the tide-generating potential Φ^{tg} (Equation (2.46)) of the shallow-water equations, the Love numbers according to Equation (2.35) are used for the impact of the solid Earth's body tides. The SAL potential Φ^{sal} of the tide-generating potential Φ^{tg} is simplified as a local parameter approach (Equation (2.48)) according to Accad and Pekeris (1978) with $\varepsilon = 0.1$ (Seiler, 1989; Weis, 2006).

The semi-implicit solution of TiME addresses tidal sea surface elevation iteratively through successive over-relaxation (SOR), with a relaxation parameter of 1.3 retained throughout. To facilitate the analysis of the time-averaged global tidal torque, the convergence criterion is reduced to 10^{-6} m.

4.3.3. Geodetic module

The geodetic module of TiME provides the global instantaneous and time-averaged energy and angular momentum balance in accordance with Section 2.2.4.6, Equations (2.52) and (2.55). Furthermore, the kinetic and potential energy within the system and the oceanic angular momentum (relative and rotational angular momentum), Equation (2.3), are calculated. Angular momenta and torques are presented in the standard body-fixed geocentric Cartesian coordinate system. The z-axis is aligned with the Earth's mean axis of rotation, the x-axis is located at the height of the equator through the prime meridian, and the y-axis is perpendicular to the x- and z-axes at the height of the equator in an easterly direction. Detailed discussions, e. g. of the semi-implicit solving schemes and the instantaneous and time-averaged global balances and their individual terms, can be found in Seiler (1989, 1991), Weis (2006), and Weis et al. (2008).

In the context of the initial work with the MPIOM ocean model, a low-level module of modular structure was developed for the calculation of the global angular momentum balance and the tidal torque. A freely programmable interface permits the coupling to an ocean model, which provides the sea surface elevation and the relative velocity field. To facilitate further developments of TiME, the revised angular momentum budgets were integrated with TiME in place of the existing budgets. Subsequently, the geodetic module of the TiME model, which is closely integrated with TiME, underwent a substantial rewrite. The low-level module defines the data types, fundamental algorithms, and associated calculations. Revisions were made to TiME with regard to its coupling with TiME and the access it provides to the individual acceleration terms required for the balances. As part of the modification, TiME was divided into functional procedures and modules. This enables the structured and consistent access to the required grid quantities, sea surface elevations, undisturbed water depths, velocities, and accelerations from the model for the purpose of coupling the low-level module via the interface. The interface allows the user to specify the quantities of the balances, energies, oceanic angular momentum, and moments of inertia to be calculated in a user-defined manner.

As a user-defined interface, the position vectors of the grid points of the scalar fields (moments of inertia) and the vector fields (angular momentum and torque) and the cross product of the position vectors and the unit vectors of the vector fields of the grid points of vector fields must be provided in the body fixed Cartesian coordinate system. Furthermore, the interface defines the initialization and calculation of the geodetic quantities.

4.3.4. Analysis procedures

4.3.4.1. Tidal mapping procedures

The tidal sea surface elevations are represented graphically with their amplitudes and phases (Equation (2.41)) using tidal maps (Section 2.2.4.1). The graphical representation

of the type of the tidal regimes employs the amplitude ratio of the diurnal tides (K_1 and O_1) to the semi-diurnal tides (M_2 and S_2), quantified as the form factor F, as detailed in Equation (2.50) and on p. 45. Furthermore, the time-averaged global polar tidal torque and the power supplied by the partial tides on the ocean are calculated, and their mean values per water column or unit area are analyzed graphically by the global and zonal distributions.

4.3.4.2. Comparative tidal elevation procedures

RMS The reliability of tidal models is typically evaluated by comparing the simulated individual tidal elevations with those from alternative models or with tide gauge data (Section 3.2.1.3). A statistical measure used to assess the magnitude of discrepancies is the RMS residual

$$rms_\sigma = \sqrt{\frac{1}{2N}\sum_{\jmath=1}^{N}\left|\zeta^a_{\sigma,\jmath} - \zeta^b_{\sigma,\jmath}\right|^2} \quad \text{with}$$
$$\zeta^{a,b}_{\sigma,\jmath} = \zeta^{0(a,b)}_{\sigma,\jmath} e^{\imath(\sigma t - \phi^{a,b}_{\sigma,\jmath})},$$

where a and b represent the data sets to be compared. $\zeta^{a,b}_{\sigma,\jmath}$ denotes the tidal elevations due to the partial tide with the frequency σ in the complex representation of Equation (2.41) at point $\jmath$. N is the number of data points to be compared. In accordance with standard practice (e. g. Stammer et al., 2014; Sulzbach et al., 2021; Taguchi et al., 2014; Zaron & Elipot, 2021), the real and imaginary components of the tidal elevation are treated as statistically independent, with a factor of $1/2$.

Correlation coefficient The correlation coefficient

$$r^{ab}_\sigma = \frac{\left|\sum_{\jmath=1}^{N}\left(\zeta^a_{\sigma,\jmath} - \overline{\zeta^a_\sigma}\right)\left(\zeta^b_{\sigma,\jmath} - \overline{\zeta^b_\sigma}\right)^*\right|^2}{\sum_{\jmath=1}^{N}\left|\zeta^a_{\sigma,\jmath} - \overline{\zeta^a_\sigma}\right|^2 \sum_{\jmath=1}^{N}\left|\zeta^b_{\sigma,\jmath} - \overline{\zeta^b_\sigma}\right|^2} \qquad 0 \le r^{ab}_\sigma \le 1$$

is employed as a means of quantifying the extent of dependency exhibited by the data sets under comparison. A correlation function of zero indicates that the two data sets are statistically independent. $\overline{\zeta^{a,b}_\sigma}$ is the respective mean value of the N samples.

Form factor The type of the simulated tidal regimes, comprising of the M_2, S_2, K_1, and O_1 tides, is analyzed using the form factor F (Equation (2.50) and p. 45). A negative difference in the form factors $F^a - F^b < 0$ and in the periodicities suggests a more pronounced semi-diurnal oscillation system of a compared to b, a positive difference suggests a more diurnal oscillation system.

4.3.4.3. Nominal tide

The nominal ocean tide (Appendix C.1) is employed as an evaluation factor with regard to its relationship, on the one hand, to the global tidal sea surface topography and, on

the other hand, to the tidal torque (Sections 2.2.4.6 and 2.3.2) and to the tidal energy dissipation as a time-averaged global quantity (Section 2.2.4.6 and Equation (2.54)).

4.4. Implementation

Following an overview of the infrastructure utilized for the tidal simulations and its subsequent evaluation and analysis in Section 4.4.1, the model adjustment via the horizontal exchange coefficient under modern conditions is detailed in Section 4.4.2. Lack of data for Late Neoproterozoic prevents calibration under analogous conditions. The calibration is evaluated under modern conditions using detailed bathymetry and schematized two-depth distribution in the section Section 4.5. The procedure for carrying out the simulations, including start and scheduling, is finally addressed in Section 4.4.3.

4.4.1. Infrastructure

The model calculations were performed on the current high-performance computer system, designated „Levante“, and its predecessor, „Mistral“, at the German Climate Computing Center Hamburg (DKRZ). Moreover, the cluster operated by the Scientific Computing working group of the Department of Computer Science at the University of Hamburg was incorporated into the research. Additionally, test calculations were conducted on conventional laptops.

The TiME model as well as the geodetic module and interface written in the Fortran programming language were compiled using GFortran (GCC). The model runs were controlled by shell scripting (bash jobs).

The pre- and post-processing implemented in ncl, python, and shell scripting was primarily conducted on the high-performance computer system of the DKRZ.

4.4.2. Model Adjustment

A series of simulations with modern M_2 and K_1 tidal forcing with modern detailed bathymetry were conducted as part of the model adjustment. Given the proximity of their excitation frequencies to those of the M_2 and K_1 tides, it was not considered reasonable to conduct adjustment studies of the S_2 and O_1 tides. The horizontal exchange coefficient A_h was selected as the adjustment parameter (Section 4.3.2), which was incrementally increased from its minimum value to its maximum value (Equation (4.4)) over a series of time steps Δt.

4.4.2.1. Tidal elevation

Figure 4.3 shows the RMS residuals rms and correlation coefficients r^{ab} in relation to the empirical tidal data of Ray (2013), presented in Section 3.2.1.2. A stable M_2 and K_1 tidal simulation was achieved with all number of time steps per tidal period N or at all time steps Δt (Equation (4.1)) with a horizontal exchange coefficient of $A_h = 10 \times 10^4\,\mathrm{m^2\,s^{-1}}$ (not shown). An initial increase in the exchange coefficient is followed by a decrease in the residuals, reaching the optimum value. This is subsequently followed by an increase in the

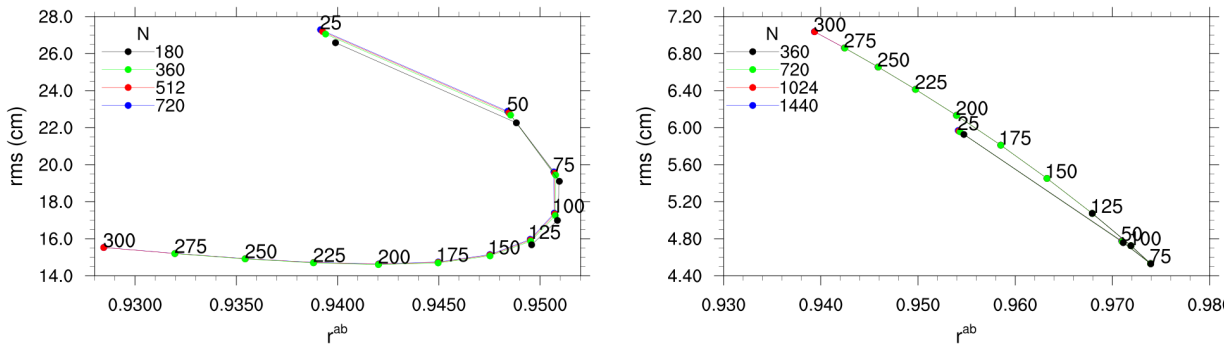

(a) M_2 tide. (b) K_1 tide.

Figure 4.3.: Model adjustment for the modern M_2 and K_1 tide using the horizontal exchange coefficient A_h and the number of time steps per tidal period N or the time step Δt (Equation (4.1)). RMS residuals rms and correlation coefficients r^{ab} refer to the empirical data from Ray (2013). The exchange coefficient A_h are given as labels in $10^4\,\mathrm{m^2\,s^{-1}}$.

residuals up to the region of unstable simulations. The correlation coefficient demonstrates an inverse behavior. As the number of time steps per tidal period N is increased or the time step Δt is reduced (Equation (4.1)), the maximum exchange coefficient of a stable simulation increases (Equation (4.4)). For example, the maximum exchange coefficient for a stable simulation with $N = 180$ (M_2) or $N = 360$ (K_1) is $A_h = 125 \times 10^4\,\mathrm{m^2\,s^{-1}}$, while for $N = 720$ (M_2) or $N = 1440$ (K_1), it is $A_h = 500 \times 10^4\,\mathrm{m^2\,s^{-1}}$ (not shown).

In the stable region of the simulations, the RMS residuals and correlation coefficients are almost independent of the time step. Therefore, the largest possible time step can be selected for the optimum RMS residual and correlation coefficients without comprising the accuracy of the results. The range of the RMS residual and the correlation coefficient for the M_2 and K_1 tides is roughly 100 % of the optimal RMS residual and 3 % and 4 % of the optimal correlation coefficient, respectively. With respect to the M_2 tide, the exchange coefficient corresponding to the optimal RMS residual of $A_h = 200 \times 10^4\,\mathrm{m^2\,s^{-1}}$ is distinct from that associated with the most accurate fit for the correlation coefficient, which is $A_h = 75 \times 10^4\,\mathrm{m^2\,s^{-1}}$. In contrast, for the K_1 tide, both the RMS residual and the correlation coefficient are best achieved with $A_h = 75 \times 10^4\,\mathrm{m^2\,s^{-1}}$.

4.4.2.2. Time-averaged global polar tidal torque

Figure 4.4 presents the simulated time-averaged global polar tidal torque $\langle\overline{M_{t,z}}\rangle$ of the M_2 and K_1 tide for the varying horizontal exchange coefficient A_h and time steps Δt. Analogous to the RMS residuals rms and correlation coefficients r^{ab} in Figure 4.3, the tidal torques are almost independent of the time step. The exchange coefficient of the optimal correlation coefficient yields a tidal torque for the M_2 tide, which exerts the greatest deceleration on the Earth's rotation rate. This deceleration decreases by about 15 % with both decreasing and increasing exchange coefficients. However, the reference tidal torques provided in Section 3.2.2.1 and Table 3.2 correspond to lower deceleration. In contrast, the K_1 tidal torque shows a different pattern, exhibiting an increase in deceleration of the Earth's rotation rate by more than 38 % as the exchange coefficients increase. Nevertheless, the tidal torques within the range of the exchange coefficients with the optimal RMS residual

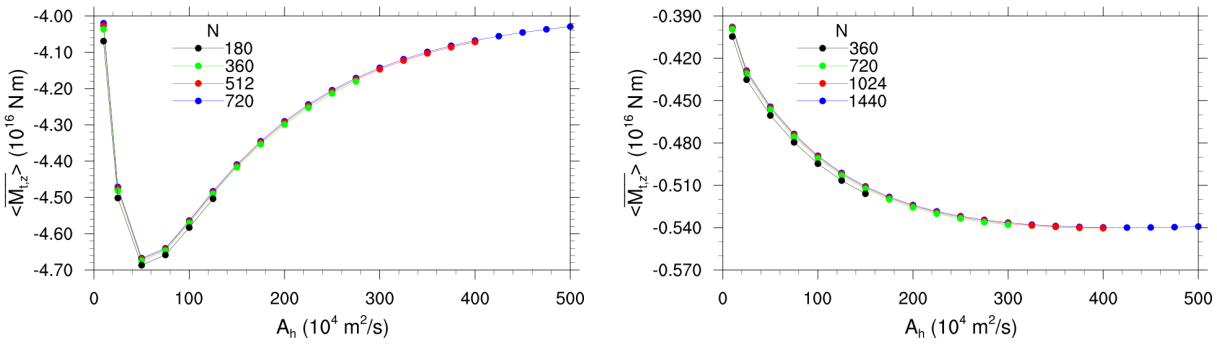

(a) M_2 tide. (b) K_1 tide.

Figure 4.4.: Model adjustment for the modern M_2 and K_1 tide using the horizontal exchange coefficient A_h and the number of time steps per tidal period N or the time step Δt (Equation (4.1)) based on the simulated time-averaged global polar tidal torques $\langle\overline{M_{t,z}}\rangle$.

and correlation coefficient align most closely with the reference values given in Section 3.2.2.1 and Table 3.4. The patterns of the time-averaged global power $\langle\overline{\dot{E}_t}\rangle$ supplied by the M_2 and K_1 tidal constituents to the ocean and the time-averaged global energy dissipation $\langle\overline{\dot{E}_f}\rangle$ due to bottom friction and eddy viscosity with the successively increasing horizontal exchange coefficient (not shown) evolve in a manner analogous to the patterns of the time-averaged global polar tidal torque $\langle\overline{M_{t,z}}\rangle$.

4.4.2.3. Parameterization

In the simulations conducted with the semi-diurnal M_2 and S_2 tidal constituents, the horizontal exchange coefficient $A_h = 200 \times 10^4\,\mathrm{m^2\,s^{-1}}$, which yielded the optimal RMS residual rms, was replaced with $A_h = 250 \times 10^4\,\mathrm{m^2\,s^{-1}}$. This alternative coefficient was selected because its time-averaged global polar tidal torque $\langle\overline{M_{t,z}}\rangle$ is closer to the reference values (Table 3.2), and the RMS residual exhibited only minor deviations, amounting to less than 2 % from the optimal RMS residual. Given the narrow bandwith of the correlation coefficients r^{ab}, the exchange coefficient with the optimal correlation coefficient of $A_h = 75 \times 10^4\,\mathrm{m^2\,s^{-1}}$ was not included in the selection. This was because its RMS residual is more than 34 % higher than the optimal residual, and its tidal torque deviates the most from the reference values (Table 3.2). For the semi-diurnal tidal simulations, the largest feasible time step Δt was utilized, with a total of $N = 360$ time steps per tidal period.

In the simulations involving the diurnal K_1 and O_1 tidal constituents, an exchange coefficient of $A_h = 75 \times 10^4\,\mathrm{m^2\,s^{-1}}$ was employed, which corresponds to that of the optimal RMS residual, that of the optimal correlation coefficient, and that of the optimal time-averaged global polar tidal torque for the K_1 tidal constituent (Figures 4.3 and 4.4). The largest feasible time step Δt for simulations of the diurnal tides with $N = 360$ time steps per tidal perod is approximately twice that of the time step used for simulations of the semi-diurnal tidal constituents M_2 and S_2.

4.4.3. Simulation procedure

The following describes the procedure for conducting each simulation, commencing with an estimate of the simulation's accuracy. To mitigate the impact of truncation errors on the instantaneous and particularly time-averaged global balancing quantities, all calculations were performed with double precision (64-bit) and 15 significant decimal places. Seiler (1989) employed a fourfold precision for the global balancing quantities, which resulted in a truncation error of $\mathcal{O}(10^{-8})$ of the smallest term in angular momentum balance. Nevertheless, this degree of precision is not suitable to the Neoproterozoic era, given the inherent uncertainties involved. The larger errors in the conservation of energy were addressed by Weis (2006) with a refined semi-implicit numerical solution scheme. This resulted in the kinetic energy being independent of the time step. However, an estimation of the numerical errors on the energy balance was not provided. In the present study, however, the energy budgets are of secondary importance, as it is the tidal torque in relation to the Earth's rotation rate that is the primary focus of analysis.

In consideration of the physical assumptions, an error rate of up to 10 % can be deduced for the time-averaged global values of the angular momentum budgets (Seiler, 1989). Consequently, it can be reasonably assumed that the required accuracy for tidal simulations of the Neoproterozoic is satisfied in both numerical and physical respects.

The tidal simulations are initiated in a state of rest and the tidal motion, comprising currents and sea surface topography, evolves until the oceanic system has adapted to the partial tidal forcing. At this point, the simulation is terminated. Following a period of less than 100 simulated tidal cycles, stable tidal oscillation systems are established. The time-averaged global angular momenta and torques typically evolve at a rate that is at least three orders of magnitude below their extreme values. These low terms are a consequence of non-linearities (Section 2.2.4.6, p. 48). When considering reasonable simulation time frames with partial tidal forcing, only the time-averaged global tidal torque shows a constant value. In contrast, the other quantities show comparatively large fluctuations. In this study, only the mean polar tidal torque (Equations (2.5) and (2.6)) is considered. A model ocean is defined periodic if the time-averaged global polar tidal torque is found to have five constant decimal places. Following a simulation period of less than 200 tidal cycles, all simulations conducted (modern and paleo land-water distributions, two-depth distribution, tidal potential and day length of modern times and ~620 Myr ago) yielded a periodic model ocean.

4.5. Evaluation

The model described in Sections 4.3.1 and 4.3.3, which is referred to in the subsequent text as TiME(1°), is evaluated with the implementation described in Section 4.4 and the parameterization described in Sections 4.3.2 and 4.4.2.3. With regard to the tidal simulations for the Late Neoproterozoic ~620 Myr ago, the reliability of the simulations for modern times is first examined with the detailed bathymetry (Figure 4.1a) in Section 4.5.1. In comparison, the implementation with the modern two-depth distribution (Figure 4.1b) is analyzed in Section 4.5.2. The purpose is to evaluate the implementation under modern conditions in order to ascertain the reliability of the approach for the Late Neoproterozoic

~620 Myr ago.

In regard to the analysis of the tidal simulations for the Late Neoproterozoic ~620 Myr ago, the evaluation encompasses not only global tidal maps but also maps of the form factor and type of the tidal regime at global, regional, and local levels (Sections 4.5.1.2, 4.5.2.2 and 4.5.2.3. By analyzing the form factor and type of the tidal regimes, it is possible to estimate the periodicity of a deposit. The tidal range provides insight into the potential for deposits. With regard to the modern detailed bathymetry, the tidal elevations themselves are evaluated in Section 4.5.1.1.

In Sections 4.5.1.3 and 4.5.2.4, a detailed analysis is conducted of the fundamental quantity, the time-averaged global polar tidal torque, in relation to the documented increase in length of day recorded by the Elatina Formation. In these sections, the basis for this is established with regard to modern conditions. The characteristic properties of the time-averaged global quantity are analyzed on the basis of the underlying global and zonal distribution per water column. Due to the limited number of references (Brosche & Sündermann, 1971), the analysis is comprehensive. The impact of the schematized two-depth distribution is presented alongside the analysis for the modern detailed bathymetry in Section 4.5.2.4. Finally, an examination of the nominal tide is conducted in Sections 4.5.1.4 and 4.5.2.5, due to its relationship with the tides and the time-averaged global polar tidal torque and energy dissipation. Subsequently, the influence of the Earth-Moon-Sun configuration and the supercontinent Rodinia in the Late Neoproterozoic ~620 Myr ago can be analyzed.

4.5.1. Modern simulations with detailed bathymetry

Following the evaluation of the tidal elevations of the simulations with modern detailed bathymetry by TiME(1°), as outlined in Section 4.5.1.1, the evaluation of the global type of the tidal regime is presented in Section 4.5.1.2. Section 4.5.1.3 addresses the time-averaged global polar tidal torque, while Section 4.5.1.4 discusses the nominal tides. Section 4.5.1.5 provides a synthesis of the evaluation.

4.5.1.1. Tidal elevation

The simulated tides with the modern detailed bathymetry are presented in tidal charts in Figure 4.5. They visually match very well with the tidal maps of the EOT20 tidal atlas, derived from altimetry data (Hart-Davis et al., 2021a; Hart-Davis et al., 2021b). The later are presented in Figures 2.4 and 2.5.

As is customary, the evaluation encompasses the analysis of the individual tidal sea surface elevations, with a statistical comparison (Section 4.3.4.2) drawn between the data set of 151 tide gauge stations, as compiled by Ray (2013) and the global tidal atlas FES2022 (CNES, 2024), both of which were presented in Section 3.2.1.2. The comparison with FES2022 is limited to the geographical latitudes between 60° S and 60° N, where the altimetry data are available in high density and quality. Furthermore, the comparison is carried out for all depths and for depths above 1000 m (open sea). Table 4.2 summarizes the RMS residuals rms and correlations coefficients r^{ab}.

A strong and positive correlation was found with the reference data sets, with the correlation coefficient r^{ab} exceeding 0.88 throughout. The differences between the RMS

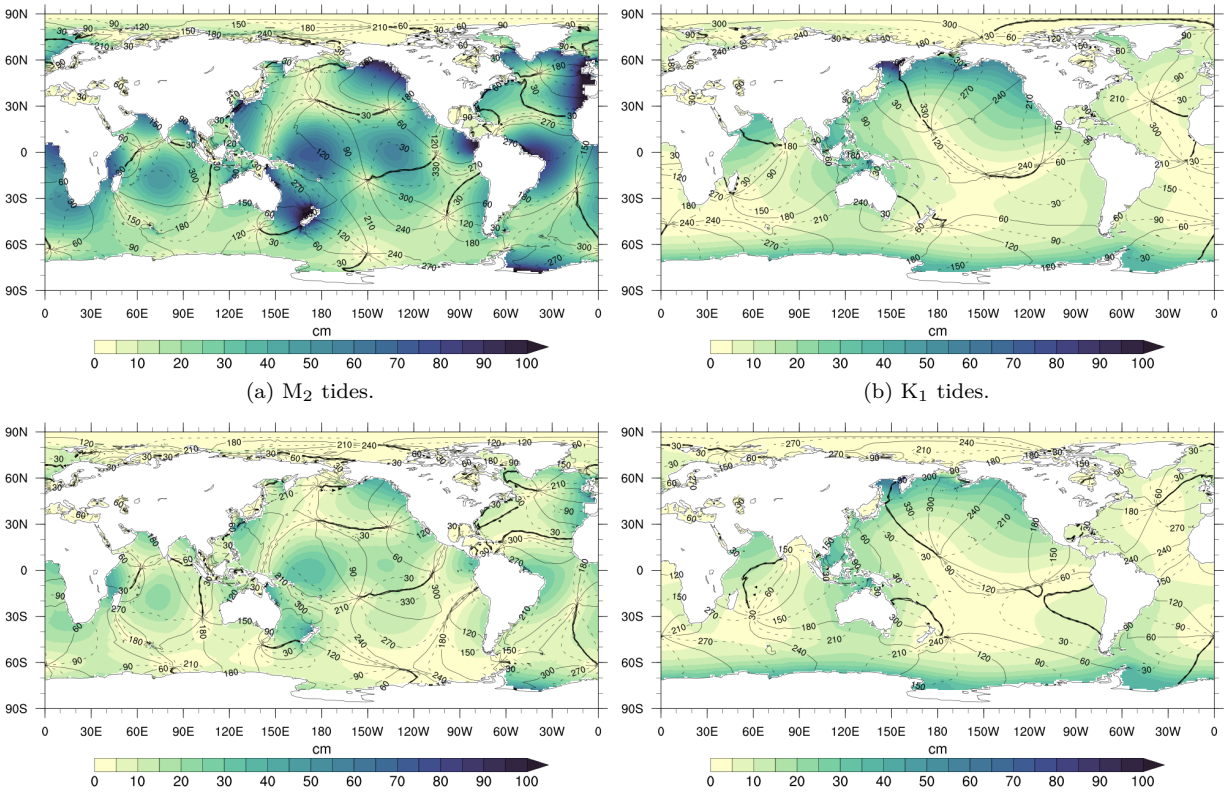

(a) M_2 tides. (b) K_1 tides.

(c) S_2 tides. (d) O_1 tides.

Figure 4.5.: Tidal maps of modern times. Colors show amplitudes in cm, black lines show contours of the same phase in degrees.

Table 4.2.: Model evaluation for modern times with the RMS residual rms and the correlation coefficient r^{ab} with Ray (2013), FES2022 (open ocean), and FES2022 (CNES, 2024). The power supplied by the lunisolar partial tides on the ocean $\langle\overline{\dot{E}_t}\rangle$ and the polar tidal torque $\langle\overline{M_{t,z}}\rangle$ as global temporal averages are given as additional metrics (cf. Tables 3.2 to 3.5). According to Equation (2.53), the power supply $\langle\overline{\dot{E}_t}\rangle$ is equivalent to the energy dissipation $\langle\overline{\dot{E}_d}\rangle$ when the time-averaged global quantities are taken into account.

Tide	r^{ab}	rms (cm)	$\langle\overline{\dot{E}_t}\rangle$ (TW)	$-\langle\overline{M_{t,z}}\rangle$ (10^{16} N m)
M_2	0.94/0.92/0.82[1]	14.91/14.30/22.57[1]	2.919[2]	4.213[2]
S_2	0.91/0.88/0.81[1]	6.86/6.96/9.30[1]	0.478[2]	0.672[2]
K_1	0.97/0.96/0.91[1]	4.53/3.87/5.98[1]	0.344[2]	0.479[2]
O_1	0.98/0.98/0.93[1]	3.68/3.09/4.43[1]	0.212[2]	0.316[2]

1 Ray (2013)/FES2022(open ocean)/FES2022.
2 TiME(1°).

residuals and the correlation coefficients with regard to the open ocean and all depths for all tides clearly demonstrate the deficiencies of TiME(1°) in shallow seas and the satisfactory simulation of the tides in the open ocean (Section 3.2.1). Given the focus of the study, further investigation into results for all depths is not feasible. The exceptionally high correlation

coefficients for the diurnal tides suggest an optimal representation and configuration of TiME(1°) in relation to their excitation frequencies. Although the correlation coefficients for the semi-diurnal tides are comparatively lower, they can be considered to be of a high quality, particularly in view of the very low resolution in comparison and the approximations of TiME(1°). Consequently, the geometry of the ocean basins, which largely determines the resonance conditions, may not be sufficiently resolved to achieve a higher correlation for the semi-diurnal tides that are in proximity to resonance.

The RMS residuals for the M_2 tides show an increase of about 10 cm compared to the reference values in Section 3.2.1.3, which indicates that the residuals are relatively high. However, considering the locally parametrized SAL effect and neglecting the energy conversion into internal tides as well as the comparatively low resolution of TiME(1°), the residuals can be considered as very good. No reference values could be identified from free tidal models for the S_2, K_1, and O_1 tides. Weis (2006) reports significantly higher residuals, however, these residuals pertain to a pelagic data set that was frequently utilized for evaluation prior to the pelagic data set of Ray (2013). In comparison to the global distribution of tidal heights presented in Figure 4.5, the residuals appear to be relatively minor.

4.5.1.2. Global tidal regime type

The type of the simulated tidal regime is shown in Figure 4.6 (Section 4.3.4.2) in relation to that of the state-of-the-art global tidal atlas FES2022 (CNES, 2024), presented in Sections 3.2.1.1 and 3.2.1.3. Overall, the difference in the form factors is small at $|F(\text{TiME}(1°)) - F(\text{FES}(2022))| < 0.25$ (Figure 4.6a). Larger differences are mainly confined to the polar seas, the shallow shelf seas, and the Antarctic Circumpolar Current. In addition, there are notable differences in the northwestern Pacific and eastern Indian Oceans along the prominent Kural, Japan and Mariana Trenches, as well as from the South China Basin to the North Australian Basin and onward to the Western Australian Basin. These regions, which include deep-sea trenches and adjacent oceanic ridges, along with island realms such as those in Indonesia and the Philippines, have in common that they are beyond the 1° resolution of the simulated tides. Nevertheless, not all regions exhibiting deep sea trenches and pronounced depth gradients demonstrate a correlation with strong changes in the form factor. This is evidenced, for example, by the presence of trenches along the East Pacific coastline and the trenches situated east of Australia and north of New Zealand.

The alternation in the resonance proximity of the diurnal and semi-diurnal tides in the North Pacific, which is linked to the smoothing effect of the ocean basin geometry, could prove to be a pivotal factor. In contrast, the eastern Pacific off South America exhibits a distinct pattern. Neither the diurnal nor the semi-diurnal tides show a resonance proximity, and the smoothing of the large depth gradients along the deep-sea trench demonstrates minimal change in the form factor. Similarly, east of Australia and north of New Zealand, where the semi-diurnal tides are pronounced in comparison to the diurnal tides, the form factor remains virtually unchanged when the steep depth gradients along the deep-sea trenches are smoothed by the 1° resolution bathymetry in comparison to the high-resolution FES2022 tidal atlas.

The influence of the different form factors on the tidal regime type is shown in Figure 4.6b.

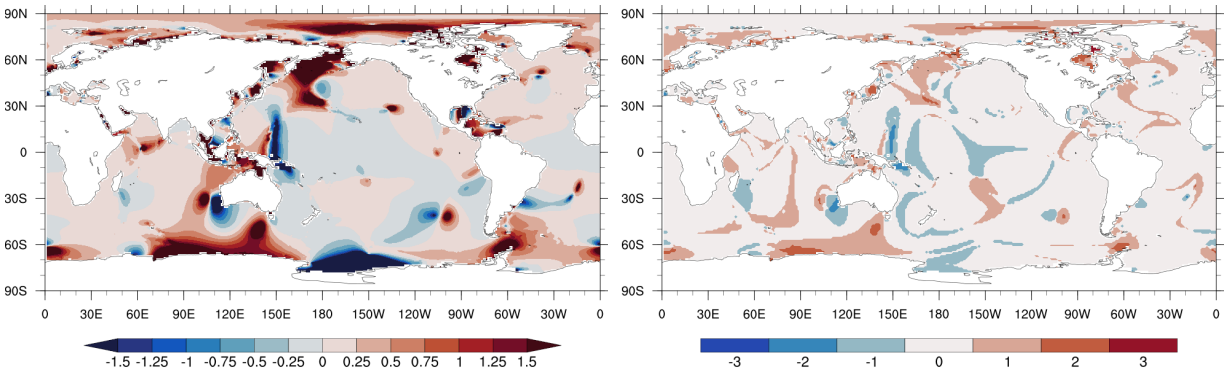

(a) F(TiME(1°)) - F(FES(2022)). (b) Type(TiME(1°)) - Type(FES(2022)).

Figure 4.6.: Form factor F (Equation (2.50)) of TiME(1°) in relation to FES2022 (CNES, 2024). Tidal regime type 0: semi-diurnal at $F < 0.25$, 1: mixed mainly semi-diurnal at $0.25 \geq F < 1.5$, 2: mixed mainly diurnal at $1.5 \geq F < 3.0$, 3: diurnal at $F \geq 3.0$. Negative differences indicate a more pronounced semi-diurnal tidal oscillation system of TiME(1°) compared to FES2022 and positive differences indicate a more pronounced diurnal tidal regime.

Overall, the tidal regime type of TiME(1°) is in good agreement with the tidal regime type of the FES(2022) tidal atlas. Even the larger differences in the form factors predominantly lead to a change in tidal regime type of ±1. Larger changes are only locally limited.

4.5.1.3. Time-averaged global polar tidal torque

To provide additional context, the polar tidal torques and the power supplied by the lunisolar partial tides to the ocean are used as global temporal means. The results are shown in Table 4.2. Reference values are contained in Tables 3.2 to 3.5. According to Equation (2.53), the power supply $\langle \overline{\dot{E}_t} \rangle$ is equivalent to the energy dissipation $\langle \overline{\dot{E}_d} \rangle$ when the time-averaged global quantities are taken into account. The range of reference energy dissipation and polar tidal torque is 1.17 times the lowest value, resulting from the oceanic M_2 and O_1, and 1.34 times the lowest value, resulting from the oceanic S_2 and K_1 tides. This demonstrates that the global temporal mean values are highly susceptible to alterations in the tidal sea surface elevations, which can be classified as minor in comparison to the water depths. The significant uncertainties are present in all tides, regardless of the excitation frequency and proximity to resonance. With regard to the S_2 and K_1 tides, the energy dissipation and polar tidal torque are at the upper end of the range of reference values, whereas with regard to the M_2 and O_1, they exceed this range. This supports the statement that the free tidal models tend to overestimate the tidal sea surface elevations in the open ocean. Nevertheless, no account is taken here of the influence exerted by the phase of the elevations.

4.5.1.4. Nominal tide

Alternatively, there is a functional relationship between the nominal tide (Appendix C.1) and the time-averaged global power supply or energy dissipation via the work method (Section 2.2.4.6, p. 47). Table 4.3 shows the nominal tides $\zeta^+_{\sigma,lm}, \epsilon^+_{\sigma,lm}$ according to Appendix C.1 and the time-averaged global energy dissipation $\langle \overline{\dot{E}_d} \rangle$ determined from them according to

Table 4.3.: Model evaluation for modern times with the nominal tide $\zeta^{+}_{\sigma,lm}, \epsilon^{+}_{\sigma,lm}$ (Appendix C.1) and energy dissipation $\langle\overline{\dot{E}_d}\rangle$ as global temporal average by the work method (see Equations (2.53) and (2.54)). The values are given for TiME(1°), TiME21 (Sulzbach et al., 2021), and FES2022 (CNES, 2024) in that order. Further reference values are given in Tables 3.2 to 3.5.

Tide	$\zeta^{+}_{2,2}$ (cm)	$\epsilon^{+}_{2,2}$ (°)	$\zeta^{+}_{2,2} \sin \epsilon^{+}_{2,2}$ (cm)	$\langle\overline{\dot{E}_d}\rangle$ (TW)
M_2	3.650/3.399/3.222	123.69/126.92/129.66	3.037/2.717/2.480	2.995/2.680/2.446
S_2	1.403/1.290/1.152	133.13/131.31/134.88	1.024/0.969/0.816	0.478/0.452/0.381
	$\zeta^{+}_{2,1}$ (cm)	$\epsilon^{+}_{2,1}$ (°)	$\zeta^{+}_{2,1} \cos\left(\epsilon^{+}_{2,1} + \frac{\pi}{2}\right)$ (cm)	
K_1	3.510/3.187/2.953	137.52/135.58/132.97	-2.370/-2.231/-2.161	0.355/0.334/0.324
			$\zeta^{+}_{2,1} \cos\left(\epsilon^{+}_{2,1} - \frac{\pi}{2}\right)$ (cm)	
O_1	3.034/2.767/2.626	133.03/136.89/137.21	2.218/1.891/1.784	0.219/0.187/0.176

Equation (2.54) for the simulations with TiME(1°) in relation to the global tidal atlas TiME21 (Sulzbach et al., 2021) and FES2022 (CNES, 2024).

The energy dissipations for the simulated partial tides by TiME(1°) in Table 4.3 are comparable to the power supply of the partial tides to the ocean in Table 4.2, with a range of less than 4 %. In comparison to the dissipations derived from the FES2022 tidal atlas, the dissipation resulting from each of the tides simulated with TiME(1°) is greater than 20 %, with the exception of the K_1 tides, which exhibit about 10 % higher dissipation. The dissipations derived from the FES2022 tidal atlas are within the lower range of the reference ranges for dissipation presented in Tables 3.2 to 3.5. This finding is consistent with the comparison of the power supply to the ocean by the partial tides and the dissipations in the reference tables Tables 3.2 to 3.5. For TiME21, the derived dissipations are in turn closer to FES2022. With the exception of the S_2 tides, where the dissipation is 18 % higher, the dissipation is less than 10 % higher than for FES2022.

The nominal tides in Table 4.3 demonstrate that, in addition to the amplitudes, the phases contribute to the higher dissipation of TiME(1°) and TiME21 compared to FES2022. With the exception of the K_1 tides, where the phase error reduces the amplitude error, thereby reducing the overall error. For TiME21, the phase errors are comparable to the amplitude errors. In contrast, for TiME(1°), the amplitude errors exceed those of the phase errors, with both consistently exceeding those of TiME21, in alignment with the dissipations.

4.5.1.5. Evaluation

In summary, the tidal oscillation system for modern times is adequately represented by the implemented model version TiME(1°) for the purpose of the present study. First and foremost, the tidal maps exhibit a high degree of correspondence with those of the state-of-the-art empirical tidal model, EOT20 (Hart-Davis et al., 2021a; Hart-Davis et al., 2021b). The type of the tidal regime is well reproduced. Deficits only manifest in regions that cannot be adequately represented with the comparatively coarse resolution of 1° (e. g., coastlines, shelves, steep deep-sea trenches in the Northwest Pacific and extensive island realms such

as Indonesia and the Philippines) and concurrently exhibit a resonance proximity of both the semi-diurnal and the diurnal tides.

The statistical methods demonstrate the impact of the approximations inherent to the TiME(1°) model version, including the relatively coarse resolution of 1°, the local parameter approach for SAL, and the exclusion of topographic wave drag, among other factors. Nevertheless, satisfactory results were obtained in comparison.

In regard to the global balance quantities, such as energy supply and dissipation, as well as the polar tidal torque as time averages, the comparison yielded results indicating an increase up to and beyond the upper limit of the reference values. The nominal tide yielded consistent energy dissipation when used with the work method. In comparison, it can be confirmed that, as with all free models, the amplitudes are overestimated. Additionally, the phases lag behind. Collectively, these discrepancies result in an increase in energy dissipation under modern conditions by up to 25 % of the smallest reference value. With the exception of the K_1 tides, where the phases are ahead, the increase in energy dissipation due to the overestimation of the amplitudes is reduced to approximately 10 %.

In consideration of the aforementioned factors, it can be concluded that the tidal oscillation system for all four tidal constituents is adequately captured with respect to the focus of this study.

4.5.2. Modern simulations with two-depth distribution

A quantification of the impact of the modern two-depth distribution (Figure 4.1b) on the tidal oscillation systems and their time-averaged global polar tidal torques and power supply remains to be conducted. Following the evaluation of the tidal elevations of the simulations with modern two-depth distribution by TiME(1°), as outlined in Section 4.5.2.1, the evaluation of the global tidal regime type is presented in Section 4.5.2.2. The local tidal regime type is examined in Section 4.5.2.3 at various locations in Australian coastal waters. A detailed investigation of the time-averaged global polar tidal torque and power supply is provided in Section 4.5.2.4, while the intermediate quantity between the tidal system and the power supply, as well as the tidal torque, the nominal tide, is discussed in Section 4.5.2.5. Section 4.5.2.6 contains a synthesis of the evaluation.

4.5.2.1. Tidal elevation

The temporal and spatial characteristics of the individual tidal systems of the two-depth distribution shown in Figure 4.7 are comparable to those of the detailed bathymetry shown in Figure 4.5. The amphidromic systems have evolved with a consistent direction of rotation but distinct phase lags, with some instances of slight offset. Of particular note are the significant phase shifts observed in the central Pacific region as evidenced by the S_2 tides (Figures 4.5c and 4.7c). A further examination of this topic would exceed the scope of the present study. The regions with amphidromic and anti-amphidromic systems align well, although the amplitudes themselves have decreased significantly. It is therefore not meaningful to make statistical comparisons.

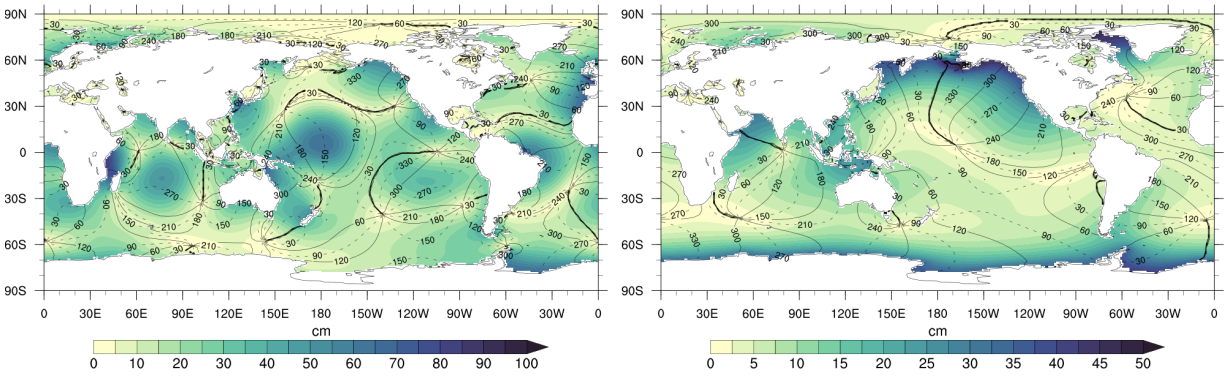

(a) M_2 tides. (b) K_1 tides.

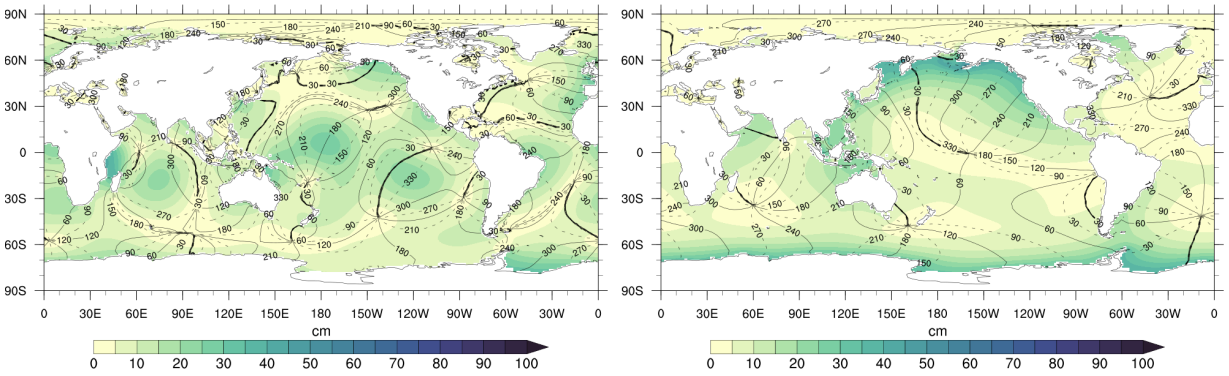

(c) S_2 tides. (d) O_1 tides.

Figure 4.7.: Tidal maps of modern times for two-depth distribution. Colors show amplitudes in cm, black lines show contours of the same phase in degrees.

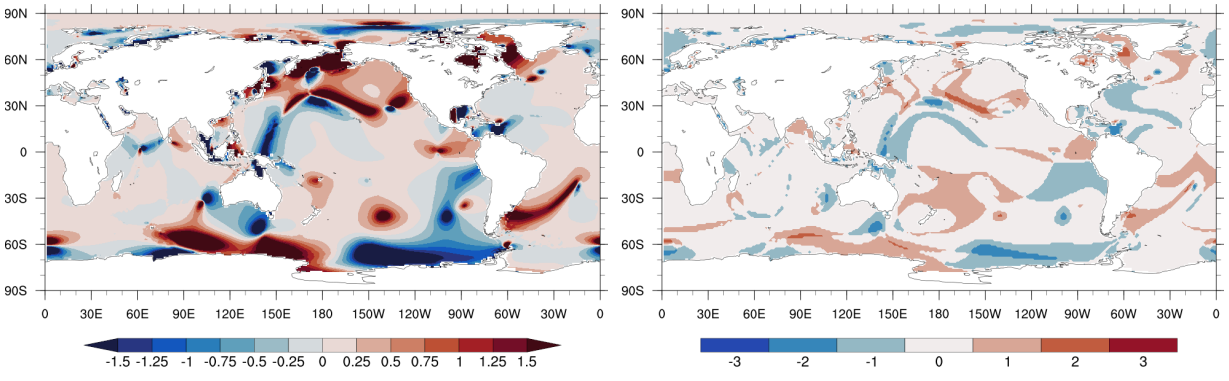

(a) F(TiME(1° 2-depth) - F(TiME(1°)). (b) Type(TiME(1° 2-depth) - Type(TiME(1°)).

Figure 4.8.: Form factor F (Equation (2.50)) of TiME(1°) with two-depth distribution in relation to TiME(1°) with detailed bathymetry. Tidal regime type 0: semi-diurnal at $F < 0.25$, 1: mixed mainly semi-diurnal at $0.25 \geq F < 1.5$, 2: mixed mainly diurnal at $1.5 \geq F < 3.0$, 3: diurnal at $F \geq 3.0$. Negative differences indicate a more pronounced semi-diurnal tidal oscillation system of the two-depth distribution compared to that of the detailed bathymetry and positive differences indicate a more pronounced diurnal tidal regime.

4.5.2.2. Global tidal regime type

The impact of the two-depth distribution on the tidal regime type is demonstrated in Figure 4.8 through the use of the form factor (Section 4.3.4.2). The pattern of the form factor differences in Figure 4.8a is analogous to that seen in the form factor differences between TiME(1°) and FES2022 in Figure 4.6a. The majority of larger differences between the two-depth distribution form factors and the detailed bathymetry form factors with $|F(\text{TiME}(1^\circ \text{ 2-depth}) - F(\text{TiME}(1^\circ))| > 0.25$ are confined to the polar seas and shallow seas, as well as the Antarctic Circumpolar Current. Similarly, in the North Pacific, large differences in form factors occur in the regions of the deep-sea trenches and adjacent oceanic ridges, but they are more pronounced than those in Figure 4.6a. They also extend into the regions of the Aleutian Trench and the Emperor and Hawaiian Ridges. Additionally, smaller regions in the eastern Pacific along the coast near the deep-sea trenches are affected by larger form factor differences. Even the South Atlantic is affected by strong differences in the region from the Falkland Plateau across the Argentine Basin to the Mid-Atlantic Ridge. As expected, the extreme smoothing of not only steep but all depth gradients with only one depth correlates with large form factor differences, especially at locations with steep depth gradients, according to the comparison between TiME(1°) and FES2022 in Section 4.5.1.2 and Figure 4.6. In this case, regions without pronounced diurnal or semi-diurnal tides are also affected by large form factor differences, such as the South Atlantic.

Overall the global tidal regime type for the two-depth distribution aligns closely with that of the tidal regime for the detailed bathymetry (Figure 4.8b). Even the more pronounced differences in the form factors predominantly result in a change in tidal regime type of ± 1. Larger changes are only limited to local areas.

4.5.2.3. Local tidal regime tpye

The local evaluation of the coastal tidal regime type is based on data from sites in Australia and makes reference to the geological data of G. E. Williams (2000), which dates back ~620 Myr. The initial site of investigation is Spencer Gulf in South Australia, where the Elatina Formation (Figure 3.1) is located as the origin of the geological data. Townsville on the coast of Queensland, Australia, represents a further site based on the analysis of the Elatina Rhythmites in conjunction with modern tide data from this region, as presented by (G. E. Williams, 2000). The potential geographical environments for the deposition of the Elatina Rhythmites are distal ebb-tidal deltas (Sections 2.4.3 and 3.1.3.3). Corner Inlet, located at the southernmost point of the Australian state Victoria, represents a modern example of ebb-tidal delta (G. E. Williams, 2023). It marks the final site.

Recent Australian tidal data is accessible via the AusTides 2024 Edition, which correspond to the Australian National Tide Tables in paper form as an electronic product. Additional information is available at Australian Hydrographic Office (2024). Two stations, Whalers Bay (W) and Shelf Edge (S), were selected at the entrance to Spencer Gulf (Figures 4.9a and 4.9d). The Townsville station is also available (Figures 4.9a and 4.9b). For the Corner Inlet, the Rabbit Island (R) station was selected in close proximity to the entrance (Figures 4.9a and 4.9c).

As shown in Figure 4.10 the tidal amplitudes ζ_σ^0 (Equation (2.41)) for the M_2, S_2, K_1, and O_1, as well as the form factor F resulting from them (Equation (2.50)), have been

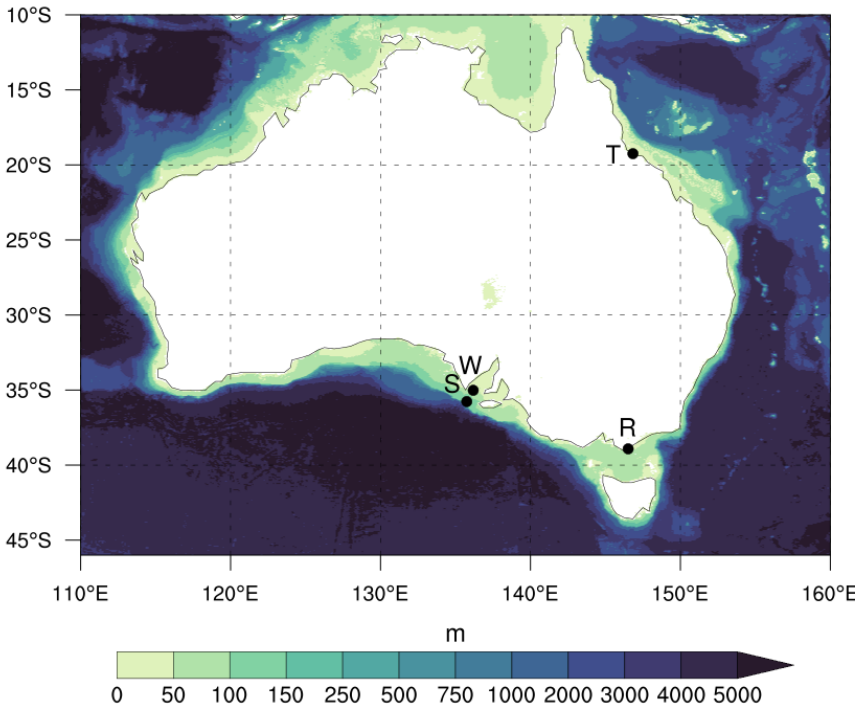

(a) Map of Australia.

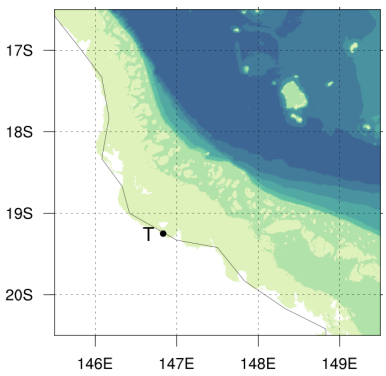

(b) Tidal station Townsville (T).

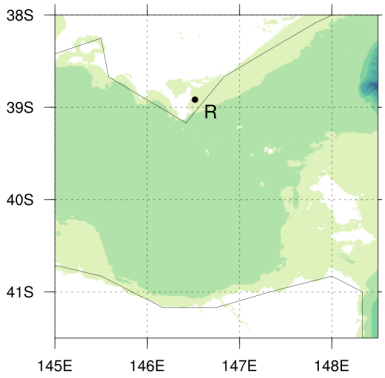

(c) Tidal station Rabbit Island (R) close to the Corner Inlet.

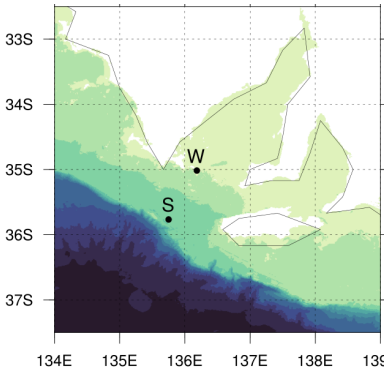

(d) Tidal stations Whalers Bay (W) and Shelf Edge (S) close to the Spencer Gulf.

Figure 4.9.: Australian tidal data stations Townsville (T), Rabbit Island (R) close to the Corner Inlet, and Whalers Bay (W) and Shelf Edge (S) close to the Spencer Gulf of AusTides 2024 Edition selected for evaluation. Colors show the depth in m.

derived using AusTides 2024 Edition, the state-of-the-art tidal atlas FES2022 (CNES, 2024), presented in Sections 3.2.1.1 and 3.2.1.3, and the tidal simulations by TiME(1°) that incorporate detailed bathymetry and the two-depth distribution (Figures 4.1a and 4.1b). The high-resolution tide atlas FES2022, which was further refined in the shallow seas, demonstrates nearly identical tidal amplitudes and form factors for all stations relative to AusTides. The TiME(1°) simulations yield tidal amplitudes that can differ significantly from those derived using AusTides, particularly in the case of the two-depth distribution.

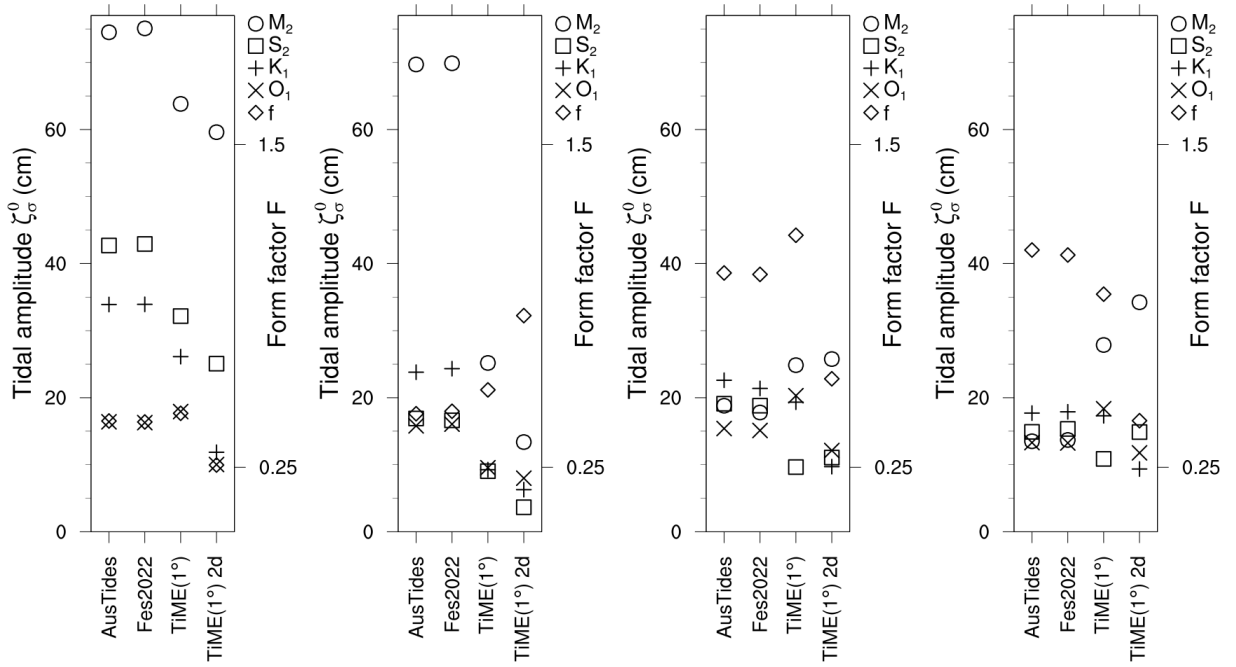

(a) Townsville (T). (b) Rabbit Island (R). (c) Whalers Bay (W). (d) Shelf Edge (S).

Figure 4.10.: Tidal amplitudes ζ^0_σ (Equation (2.41)) and form factors F (Equation (2.50)) of the stations Townsville (T), Rabbit Island (R), Whalers Bay (W), and Shelf Edge (S) derived by using AusTides 2024 Edition related to FES2022, TiME(1°) with detailed bathymetry (TiME(1°)) and two-depth distribution (TiME(1°) 2d).

The station Rabbit Island exhibits the most pronounced reductions in tidal amplitudes across all tides. It is evident that the semi-diurnal tides are significantly dampened in comparison to the diurnal tides (Figure 4.10). The simulations with the two-depth distribution demonstrate a more pronounced behavior than those with detailed bathymetry. In contrast to the other stations, the form factor does not exhibit a shift towards semi-diurnal type, but rather towards diurnal type relative to AusTides.

For the remaining stations—Townsville, Whalers Bay, and Shelf Edge—the simulations of TiME(1°) using detailed bathymetry and two-depth distribution demonstrate comparable alterations in the form factor relative to those exhibited by AusTides. However, the values differ between the Townsville station on the one hand and the Whalers Bay and Shelf Edge stations on the other. In the case of the detailed bathymetry, the form factors are found to be comparable to those derived using AusTides. Conversely, the simulations employing the two-depth distribution demonstrate a greater intensity of semi-diurnal tides in comparison to the diurnal tides, accompanied by a notable reduction in form factor, yet the tidal regime retains a mixed, mainly semi-diurnal type. The behavior of the individual tidal amplitudes for the Townsville station, with their reduction relative to AusTides, corresponds to the behavior for the Rabbit Island station. In contrast, the situation is different for the Whalers Bay and Shelf Edge stations off the Spencer Gulf, where the semi-diurnal M_2 tides show larger amplitudes than those derived using AusTides. The simulations with the two-depth distribution serve to further accentuate this effect. Like the tidal amplitudes and form

factors derived using AusTides for both stations, the simulations with TiME(1°) yield comparable tidal amplitudes and form factors for both stations.

The tidal systems in the vicinity of the Rabbit Island Station, with its extensive and flat continental shelf between Australia and Tasmania, cannot be adequately resolved with TiME(1°). The impact of the 1° resolution for the tidal dynamics on the shelf becomes more pronounced in the simulations with the highly simplified two-depth distribution.

The situation is distinct at the stations Townsville and in Spencer Gulf, where the relatively narrow continental shelves exhibit a rapid transition to the deep oceanic depths. The geological data of the Elatina Formation indicate a relatively rapid decrease in depth seaward below the storm wave basis (i. e., 100 m water depth) for the distal ebb-tidal delta. This excludes the possibility of wave disturbance to the deposits, as discussed in (Sections 2.4.3 and 3.1.3.3). In accordance with the specified conditions, TiME(1°) is capable of reproducing the ratio of diurnal to semi-diurnal tides and the tidal regime type at the local level; however, it is not possible to draw conclusion about the potential for sedimentation based on the tidal range. Nevertheless, the tidal regime type of a deposit can be inferred. This also applies to simulations with the two-depth distribution.

4.5.2.4. Time-averaged polar tidal torque

General The effect of the two-depth distribution on the global balance quantities, such as time-averaged global polar tidal torques and power supply by the lunisolar partial tides to the ocean, are shown in Figures 4.11 and 4.12. As for the tides simulated with the detailed bathymetry (Figures 4.11a, 4.11c, 4.11e and 4.11g), a negative time-averaged global polar tidal torque, which decelerates the Earth's rotation rate, results for all tides simulated with the two-depth distribution (Figures 4.11b, 4.11d, 4.11f and 4.11h). The time-averaged global power supply to the ocean by the lunisolar partial tides under consideration is positive for both the detailed bathymetry (Figures 4.12a, 4.12c, 4.12e and 4.12g) and the two-depth distribution (Figures 4.12b, 4.12d, 4.12f and 4.12h). With the exception of the O_1 tides, the two time-averaged global quantities are approximately half the magnitude of the quantities for the detailed bathymetry. For the O_1 they are about 80 % of the detailed bathymetry values.

In addition to the time-averaged global quantities, the time-averaged quantities per water column are presented in Figures 4.11 and 4.12, with both global and zonal distributions. A common feature of all simulations presented in Figure 4.11 is the alternation between regions exhibiting negative and positive time-averaged polar tidal torques per water column, or alternatively, regions that exert a decelerating and accelerating effect on the Earth's rotation rate. The distribution of the regions, in conjunction with the overlaid tidal phases and tidal amplitudes, substantiates the established correlation in Appendix D.1 between the direction and magnitude of the tidal torque and the tidal phase of the purely harmonic component of the tides. As an example, consider the western South Pacific around 160° E for the semi-diurnal M_2 and S_2 tides (Figures 4.11a and 4.11c). A region with a pronounced positive tidal torque is situated between Australia and New Zealand. Additionally, a region with a pronounced negative tidal torque is located to the north of this region. The absolute tidal torques are nearly equivalent in both regions. The tidal amplitudes, which are one determining factor for the tidal torque (Appendix D.1), are slightly higher in the southern

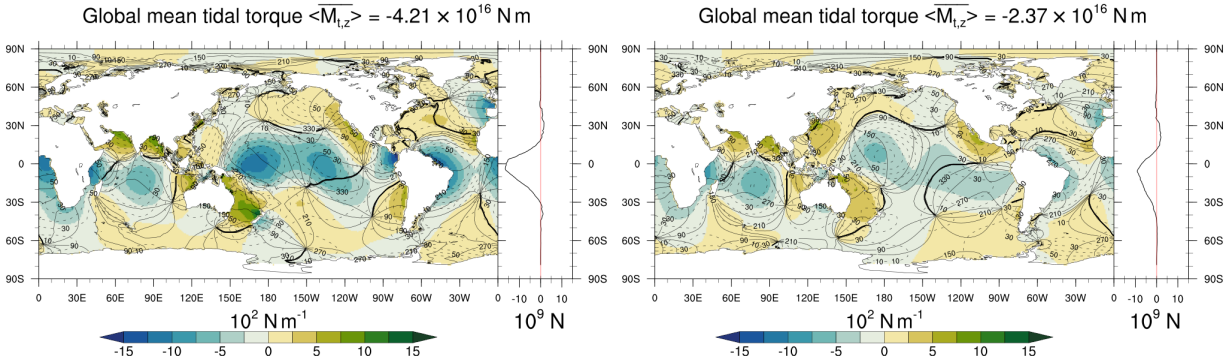

(a) M_2 tides, detailed bathymetry.

(b) M_2 tides, two-depth distribution.

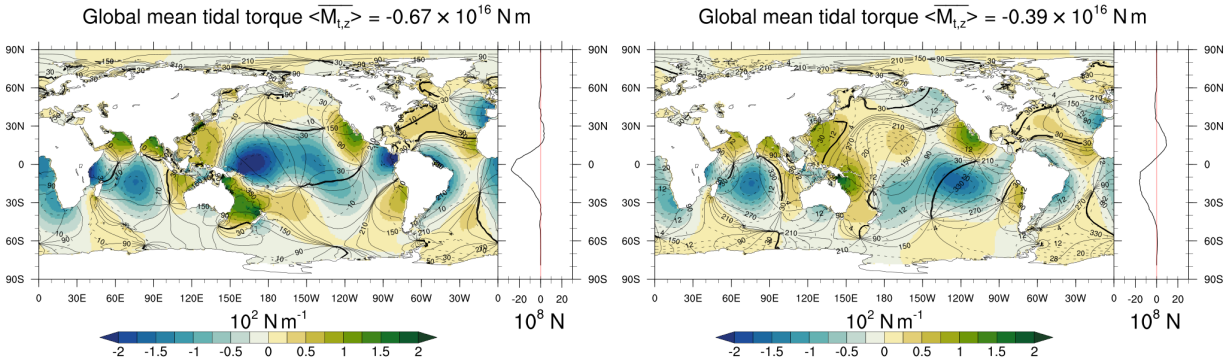

(c) S_2 tides, detailed bathymetry.

(d) S_2 tides, two-depth distribution.

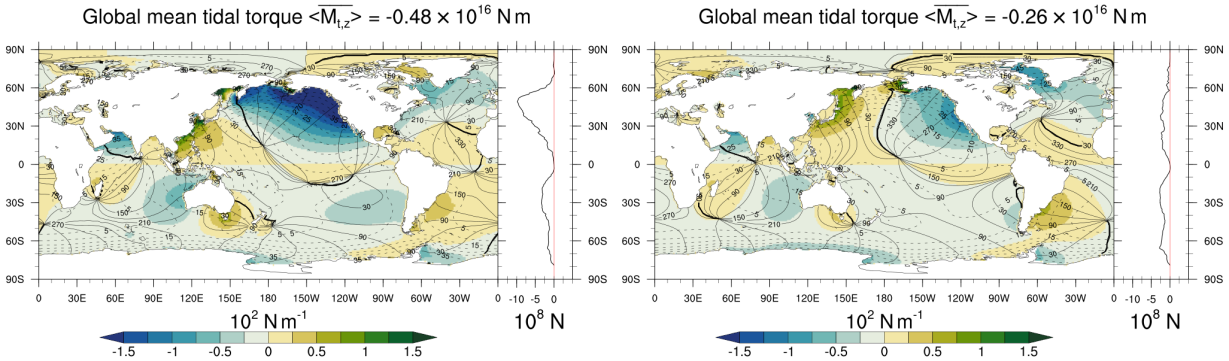

(e) K_1 tides, detailed bathymetry.

(f) K_1 tides, two-depth distribution.

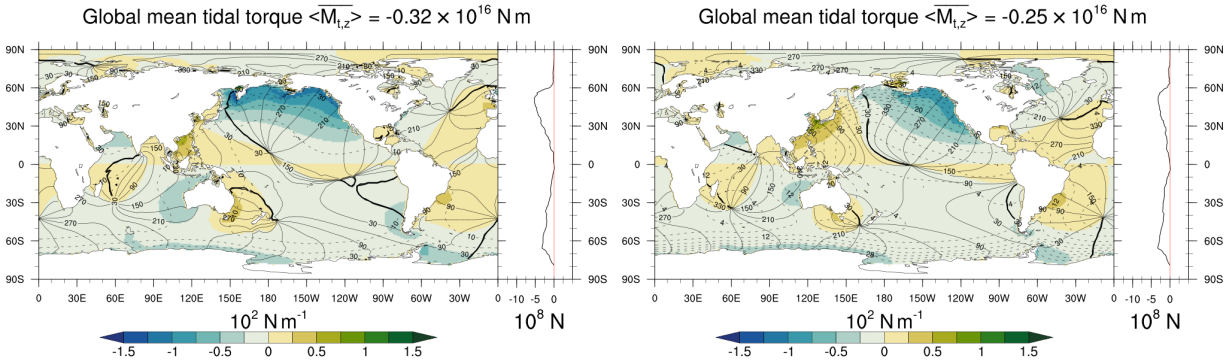

(g) O_1 tides, detailed bathymetry.

(h) O_1 tides, two-depth distribution.

Figure 4.11.: Time-averaged polar tidal torques $\overline{M_{t,z}}$ per water column of modern times. Their zonal integration is shown to the right of the maps. The globally integrated time-averaged polar torques are given above the maps. Positive torques accelerate and negative torques decelerate the Earth's rotation rate. Overlaid are the tidal amplitudes in cm as dashed contour lines and the tidal phases in ° as solid contour lines. The left column is derived from tidal simulations with modern detailed bathymetry, the right column is derived from tidal simulations with modern two-depth distribution. Note: There are different value ranges.

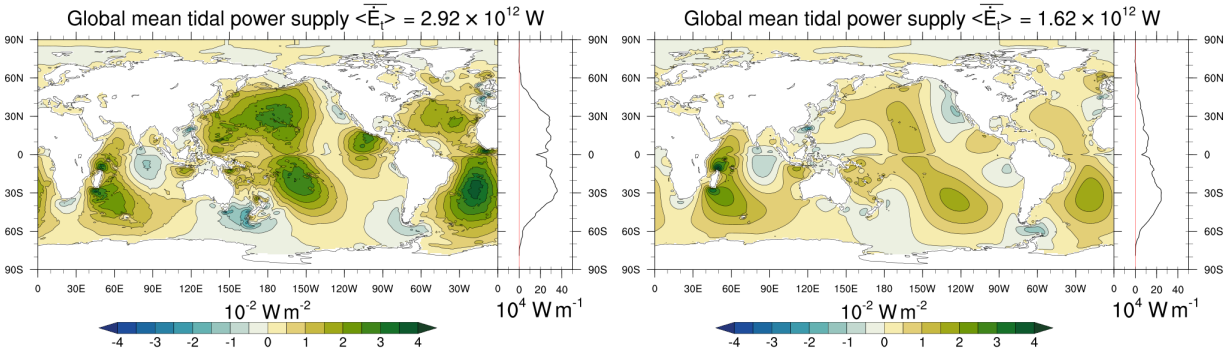

(a) M_2 tides, detailed bathymetry.

(b) M_2 tides, two-depth distribution.

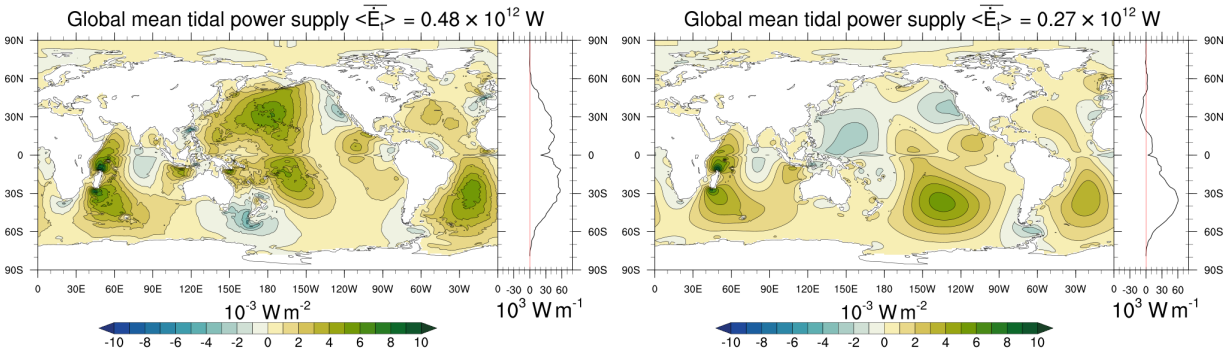

(c) S_2 tides, detailed bathymetry.

(d) S_2 tides, two-depth distribution.

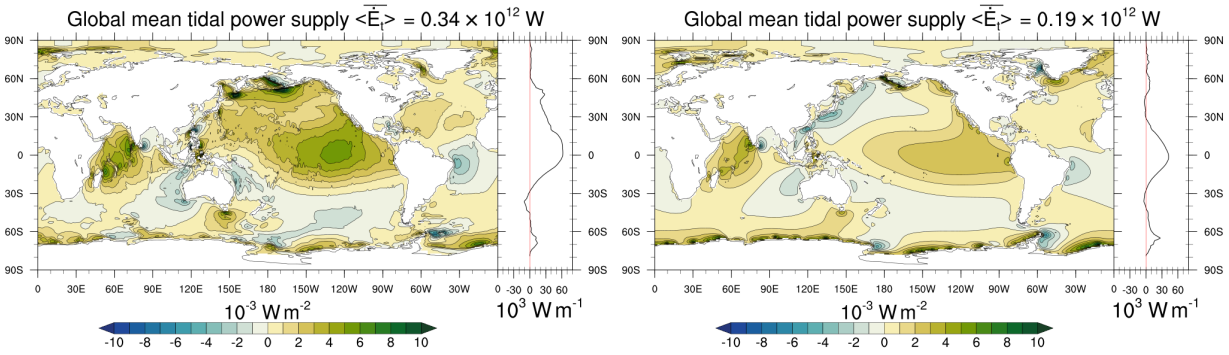

(e) K_1 tides, detailed bathymetry.

(f) K_1 tides, two-depth distribution.

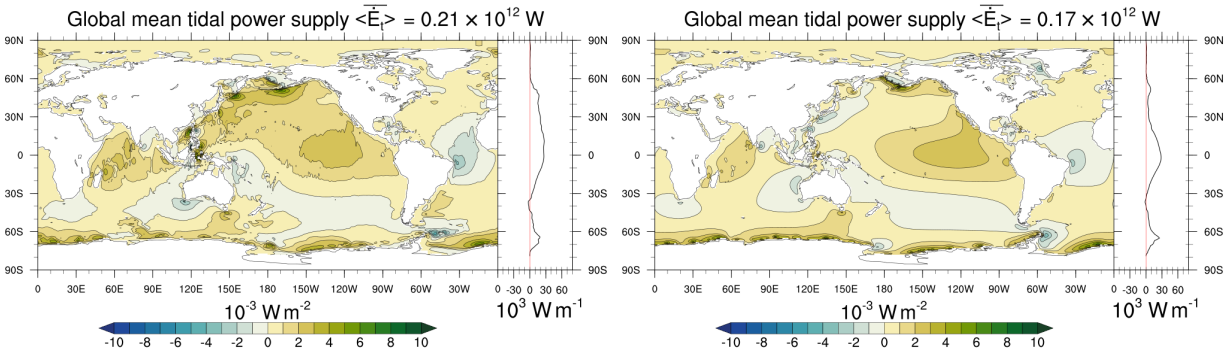

(g) O_1 tides, detailed bathymetry.

(h) O_1 tides, two-depth distribution.

Figure 4.12.: Time-averaged power supply $\overline{\dot{E}_t}$ per water column by the lunisolar partial tides of modern times. Their zonal integration is shown to the right of the maps. The globally integrated time-averaged power supply are given above the maps. The left column is derived from tidal simulations with modern detailed bathymetry, the right column is derived from tidal simulations with modern two-depth distribution. Note: There are different value ranges.

region than in the northern region (Figures 4.5a and 4.5c). Conversely, the zonal gradients of the M_2 and S_2 partial tides[a] or the zonal tidal force (Equation (D.7) and Table 2.3), an additional factor influencing the tidal torque, exhibits a lower magnitude in the southern region, characterized by its higher southern latitude, in comparison to the northern region. The tidal phases, which are also instrumental in determining the tidal torque, exhibit notable differences between the two regions. In the northern region, the tidal phases fall within the range of a negative tidal torque, while in the southern region they fall within the range of a positive tidal torque, namely in the section where the zonal tidal force has a stronger influence on the tidal elevation (Appendix D.1 and Figure D.1a). Consequently, the tidal phases can compensate for the aforementioned lower contributions to the resulting tidal torque compared to the northern region.

A second example is the North Pacific for the diurnal K_1 and O_1 tides (Figures 4.11f and 4.11h). The example for the O_1 tides is slightly shifted in longitude relative to the example for the K_1 tides; however, its discussion can be readily transferred to the example for the O_1 tides. East of the longitude of about 180°, there is a region exhibiting a pronounced negative time-averaged polar tidal torques per water column, while west of this region is characterized by pronounced positive tidal torques. In contradiction to the preceding example, the zonal tidal force (Equation (D.7) and Table 2.3) is distributed evenly in both regions. Kelvin waves propagate along the entire coastline of the North Pacific and interfere with each other to form an amphidromic patter that covers almost the entire North Pacific with a similar tidal amplitude distribution in both regions (Figures 4.7b and 4.7d). The cotidal lines, originating at the amphidromic point, extend in a star shape across the North Pacific. The tidal phases in the eastern region range from about 210° at about 130° W to about 360° at about 180° W, and cover the interval of negative time-averaged tidal torques per water column (Appendix D.1 and Figure D.1b). In contrast, the tidal phases in the western region are situated between about 0° at about 180° W and about 180° at about 130° E, encompassing the interval for a positive tidal torque. The cotidal line of the 0° tidal phase coincides with the boundary between the two regions at a longitude of about 180°, corresponding to the boundary between positive and negative tidal torque at this longitude.

As shown in Figures 4.11a to 4.11d, the tidal torques per water column of the semi-diurnal M_2 and S_2 tides exhibit considerable extremes in regions situated primarily around the equator between 30° S and 30° N. These regions broadly align with the regions of high tidal range, as evident in Figures 4.5a, 4.5c, 4.7a and 4.7c. Similarly, the extreme values of the zonal gradients of the sectoral semi-diurnal tidal potentials (Footnote a, p. 123) also manifest themselves in the regions concerned (Equation (D.7) and Table 2.3). Furthermore, regions with extreme values are present in the Tasman Sea and the West European Basin, which, in turn, roughly correspond to regions with high tidal ranges. It should be noted that not all regions with high tidal amplitudes, such as the Gulf of Alaska and the Weddel Sea, demonstrate the presence of extreme tidal torques. This is due to the phase factor in addition to the tidal amplitude and the exciting partial tide, the phase of the tides is also a contributing factor in the polar tidal torque. As detailed in Appendix D.1 and Figure D.1a, the tidal oscillations in both regions are approximately in phase or 180° out of phase with

[a] The gradients of the lunisolar partialtides M_2, S_2, K_1, and O_1 can be estimated from the contribution of the nominal tides to the tidal sea surface elevation in Figure 4.13, since they propagate like the partial tide in question.

the zonal tidal force. Accordingly, the zonal tidal force is incapable of acting on the tidal elevations on a time-averaged basis and generating a tidal torque.

As shown in Figures 4.11e to 4.11h, the time-averaged polar tidal torques per water column of the diurnal K_1 and O_1 tides indicate a significant dominance of extremes in the Northern Hemisphere, particularly in the regions of the northeast and northwest Pacific around 45° N. In these regions, a pronounced resonance proximity of the diurnal tides can be observed (Figures 4.5b, 4.5d, 4.7b and 4.7d). Moreover, the zonal gradients of the tesseral diurnal tidal potentials (Appendix D.1 and Figures D.1b and D.1c) reach their extreme values in these regions (Footnote a, p. 123), as well as in those around 45° S. In a symmetrically manner with respect to the equator, the regions around 45° S exhibit high tidal torques, although these are significantly less pronounced than in the Northern Hemisphere, in accordance with the tidal maps in Figures 4.5b, 4.5d, 4.7b and 4.7d. Nevertheless, the ocean surrounding Antarctica, which also has high tidal amplitudes but lower zonal gradients of the tesseral tidal potentials, is also characterized by strong negative time-averaged polar tidal torques per water column. The high amplitudes are attributed to the Kelvin wave (Section 2.2.4.3), with which the diurnal tides propagate along the edge of the Antarctic. In conjunction with the tidal phases that fall within the interval exhibiting negative time-averaged polar tidal torques per water column around Antarctica (Appendix D.1 and Figure D.1c), the lower zonal tidal forces are sufficient to generate these substantial negative tidal torques.

The alternation of regions that receive power on average over time and regions that release power on average over time is also a common feature of all the simulations shown in Figure 4.12. In this context, the zonal and meridional gradients of the tidal potential and the currents are of interest (Section 2.2.4.6 and Equations (2.25) and (2.52)). Once the currents are in phase with the gradients of the lunisolar partial tide, power is supplied to the affected ocean regions. Conversely, if the currents are in antiphase, power is withdrawn from the affected regions.

With respect to the semi-diurnal sectoral tidal potentials, the meridional gradients have their extreme values (Footnote a, p. 123) in the regions around 30° S and 30° N. Significant zonal gradients also occur at these latitudes. As can be seen in Figures 4.12a to 4.12d, regions with extreme values in the power supplied to the ocean are observed to occur in a symmetrical pattern around the equator for the semi-diurnal tides M_2 and S_2. The regions with the greatest power supplied by the ocean per water column, averaged over time, are primarily concentrated in the Southern Hemisphere, specifically in the Indian Ocean south of India, the Tasman sea, and the Drake Passage. In the Northern Hemisphere, the simulations indicate the presence of a region exhibiting a maximum in the north-eastern Pacific.

In addition to the zonal gradients of the diurnal tesseral tidal potentials, which exhibit extreme values in regions around 45° S and 45° N, the meridional gradients, with their extreme values concentrated around the equator, are found between about 30° S and 30° N. Similarly, regions situated around the equator exhibit considerable extremes in the diurnal K_1 and O_1 tides with respect to the power supply (Figures 4.12e to 4.12h). In the simulations with detailed bathymetry, power is predominantly supplied to the Northern Hemisphere, with further extreme values observed in the northwestern Pacific region. In this region, the diurnal tides are in close proximity to resonance (Figures 4.5b and 4.5d), resulting in the consistent occurrence of strong currents. In contrast, the Southern Hemisphere experiences a more extensive supply of power from the ocean. Notwithstanding this, the ocean around

Antarctica also receives a considerable amount of power, with extreme values being recorded. This latitude region is distinguished by notable zonal and meridional gradients of the diurnal tesseral tidal potentials, along with high tides (Figures 4.5b and 4.5d) related to strong currents.

Two-depth distribution The impact of the two-depth distribution on the polar tidal torque and the tidal power supply as time averages is demonstrated by a comparison of the tidal simulations with the modern two-depth distribution with those with the modern detailed bathymetry. Additionally, effects on the underlying tidal oscillation system can be deduced from this analysis.

The tidal simulations with the two-depth distribution reproduce the patterns of the global and zonal distributions of the time averages of the polar tidal torque and the power supply per water column to a large extent compared to the tidal simulations with the detailed bathymetry (Figures 4.11 and 4.12). As with the tidal oscillation systems in Figures 4.5 and 4.7, the distributions of the two-depth distribution are consistently less pronounced. The extreme values show a significant decrease. As seen in Figure 4.12, the zonal distributions demonstrate that the ocean in the Northern Hemisphere receives considerably less power overall in all tidal simulations with the two-depth distribution than in those with the detailed bathymetry. In contrast, the zonal distributions for the Southern Hemisphere are comparable.

Analogous to the evaluation of the type of the simulated tidal regime in Figure 4.8, there are significant discrepancies in the North Pacific, with occasional reversals in the observed signs. This is especially noticeable in the power supplied to the ocean by the partial tide S_2 (Figures 4.12c and 4.12d), K_1 (Figures 4.12e and 4.12f), and O_1 (Figures 4.12g and 4.12h). With regard to the S_2 tides, the North Pacific demonstrates a significant release of power with the occurrence of extrem values. This phenomenon is less pronounced in the case of the K_1 tides, while the O_1 tides exhibit an even more attenuated release of power.

The tidal currents in this region, which in the simulations with the detailed bathymetry appear to be mainly in phase with the tidal force, have been transformed into large-scale mainly counter-phase currents in the simulations with the two-depth distribution. In this region, which is characterized by deep-sea trenches and ocean ridges, the steep and all other depth gradients are completely smoothed out with the two-depth distribution. As the mass distribution is described consistently with the transport field, the phases of the sea surface elevations are also shifted in an equivalent manner. This phenomenon is particularly evident in the S_2 tides as shown in Figures 4.5c and 4.7c and to a lesser extent, in the K_1 tides as shown in Figures 4.5b and 4.7b, and in the O_1 as shown in Figures 4.5d and 4.7d. The distribution in the Southern Hemisphere remains unaffected by such changes. With the exception of a general decrease in power supply per water column, the Southern Hemisphere is practically unaffected by the two-depth distribution.

The time-averaged polar tidal torques per water column resulting from the simulations with the two-depth distribution, as shown in Figure 4.11, exhibit a similar behavior to the power supply from the simulations with the two-depth distribution in comparison to the simulations with the detailed bathymetry, as presented in Figure 4.12. As outlined in Appendix D.1 and Figure D.1, the shift in tidal phases in the North Pacific for the two-depth distribution is sufficient for the S_2, K_1, and O_1 tides to cause a large-scale sign

change in the time-averaged polar tidal torques per water column (Figures 4.11c to 4.11h). As indicated in Figure 4.11, the zonal distributions, with the exception of the M_2 tides, demonstrate that in the tidal simulations with the two-depth distribution in the Northern Hemisphere, a markedly weaker Earth rotation rate decelerating tidal torque is generated than in the simulations with detailed bathymetry. This phenomenon is analogous to the power supply shown in Figure 4.12. For the S_2 tides, the shifts in the tidal phase are so pronounced that the tidal torques per water column, zonally integrated, can even accelerate the Earth's rotation rate. In contrast, the zonal distributions for the tidal simulations with the two-depth distribution, such as for the power supply in Figure 4.12, exhibit a comparable characteristic for the Southern Hemisphere as for the detailed bathymetry.

It can be concluded that the tides in the North Pacific undergo significant changes due to the two-depth distribution for modern conditions. This implies that changes in sign can occur in the time-averaged polar tidal torque and in the tidal power supply per water column. However, the effects on the aforementioned quantities in the Atlantic, Indian Ocean, and South Pacific are relatively minor.

4.5.2.5. Nominal tide

To gain further insight into the effect of the two-depth distribution on energy dissipation and the polar tidal torque, Figure 4.13 demonstrates the global distribution of the modern nominal tide $\zeta^{+}_{\sigma,lm}, \epsilon^{+}_{\sigma,lm}$ (Appendix C.1) as a component of the tidal sea surface elevation (Equation (C.3)). The amplitudes $\zeta^{+}_{\sigma,lm}$ and phases $\epsilon^{+}_{\sigma,lm}$ of the nominal tide are both subject to modification. The amplitudes are approximately 70 % of those of the simulations with the detailed bathymetry, and the phases are approximately 10° to 15° ahead. Notably, the O_1 tides exhibit a nominal tide amplitude that is only approximately 4 % below that simulated with the detailed bathymetry.

In accordance with the time-averaged global balance quantities of energy dissipation and polar tidal torque, the contribution of the nominal tide is found to be approximately half that of the detailed bathymetry. The O_1 tides represents a consistent exception, with the contribution from the nominal tide approximately 80 % of that from the detailed bathymetry.

4.5.2.6. Evaluation

The tidal simulation conducted under modern conditions indicate that the Atlantic, Indian, and South Pacific Oceans exhibit a relatively minor response to the two-depth distribution. However, the North Pacific demonstrates a notable reaction.

A remarkable correlation exists between the regions exhibiting high and low tidal amplitudes, as simulated with the two-depth distribution, and those simulated with the detailed bathymetry. The amplitudes themselves show a considerable decrease. The evolution of the amphidromic systems demonstrates a correlation with the direction of rotation, although notable phase shifts are evident. Regions with significant phase shifts play a pivotal role in all other analyzed quantities.

The tidal regime type is adequately reproduced by the simulations with the two-depth distribution. The deficits that occur when comparing TiME(1°) to FES2022 also manifest themselves here with greater intensity and extent when comparing to the simulations with detailed bathymetry. Of particular note is the Northwest Pacific with its deep-sea trenches

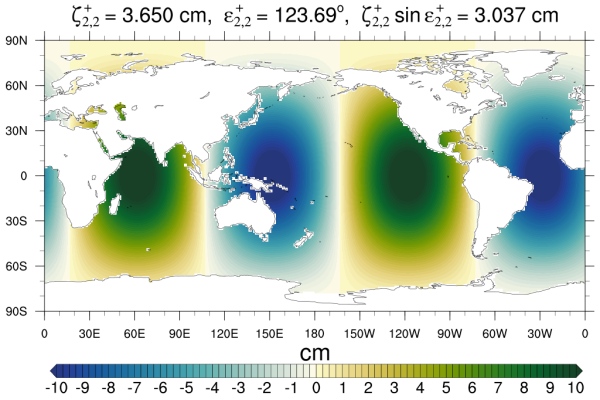

(a) M_2 tides, detailed bathymetry.

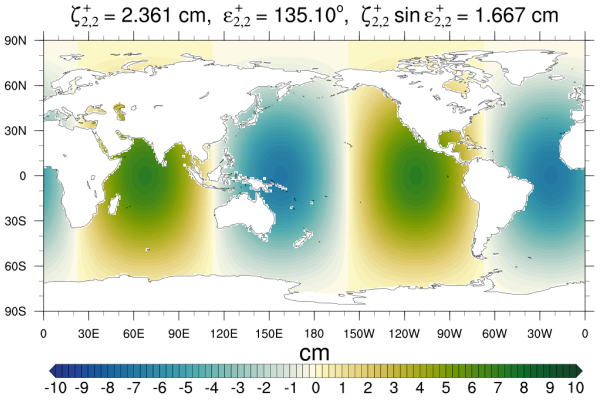

(b) M_2 tides, two-depth distribution.

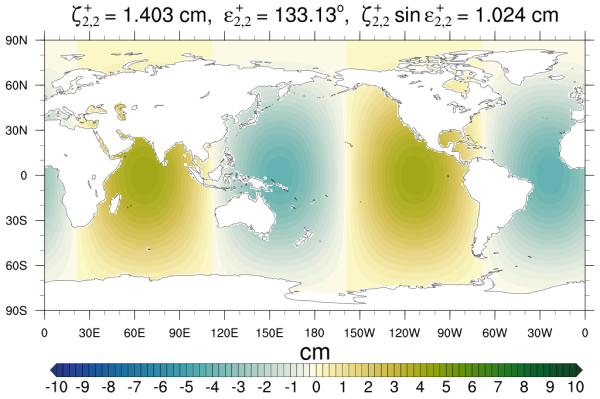

(c) S_2 tides, detailed bathymetry.

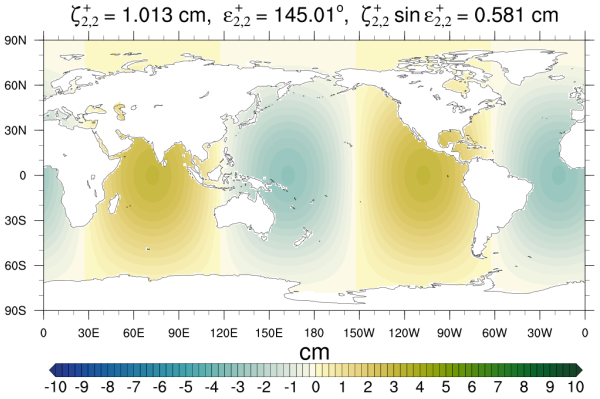

(d) S_2 tides, two-depth distribution.

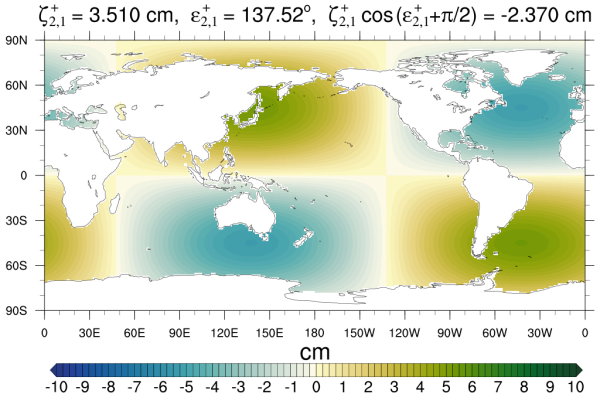

(e) K_1 tides, detailed bathymetry.

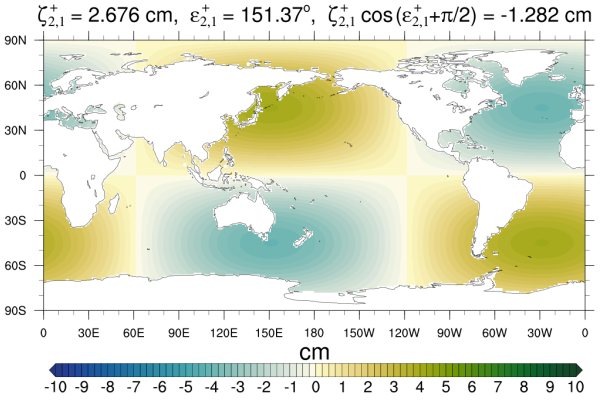

(f) K_1 tides, two-depth distribution.

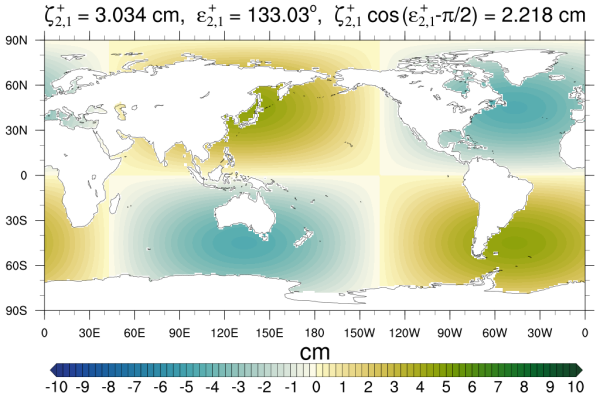

(g) O_1 tides, detailed bathymetry.

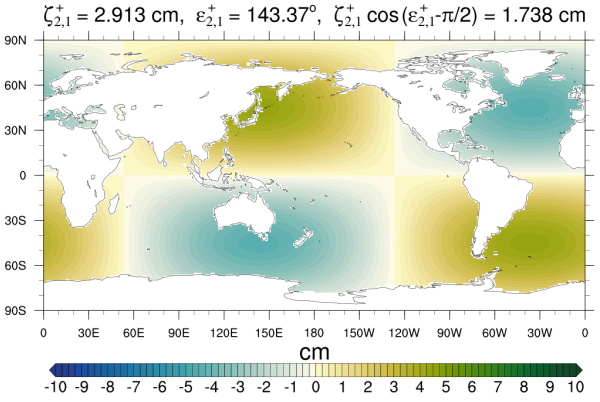

(h) O_1 tides, two-depth distribution.

Figure 4.13.: Contribution of the nominal tide ζ^+_{st}, ϵ^+_{st} (Appendix C.1) to the tidal sea surface elevations (Equation (C.3)) in cm. The nominal tide ζ^+_{st}, ϵ^+_{st} and its contribution to the energy dissipation as global temporal average by the work method (Equations (2.53) and (2.54)) are given above the maps. The left column is derived from tidal simulations with modern detailed bathymetry, the right column is derived from tidal simulations with modern two-depth distribution.

and adjacent ocean ridges and the resonance proximity of the diurnal and semi-diurnal tides. These significant changes occur only regionally.

Given the geographical conditions of a relatively narrow continental shelf with a rapid transition to the great depths of the deep sea, as previously mentioned in the context of the deposition of the Elatina rhythmites, TiME(1°) is capable of adequately simulating the ratio of diurnal to semi-diurnal tides and the tidal regime type at the local level. However, the tidal range does not permit any inferences to be drawn regarding the potential for sedimentation. Nevertheless, conclusions can be drawn regarding the periodicity of a deposit, which also applies to simulations with the two-depth distribution.

The nominal tides of the simulations with the two-depth distribution exhibit amplitudes of 70 % and 10° to 15° larger in phase compared to the simulations with the detailed bathymetry. The results demonstrate the impact of tidal phases on the reduction of polar tidal torque and energy dissipation as time-averaged global quantities. The simulations with the two-depth distribution exhibited a reduction of approximately 50 % in these quantities compared to the simulations with the detailed bathymetry. The O_1 tides represent an exception, exhibiting a nominal tidal amplitude that is 4 % lower and time-averaged global quantities that demonstrate a reduction of approximately 20 %. As a consequence of the phase shifts in the tides, the transports are also impacted, given that the shallow-water equations describe the transports consistently with the tidal elevations.

The global distribution of polar tidal torque and tidal energy supply as time-averaged quantities per water column, obtained from simulations with the detailed bathymetry, is reproduced to a lesser extent by simulations with the two-depth distribution. It is notable that in a pattern characteristic of the respective tidal band, regions with negative and positive values are present in alternation. This implies that the Earth's rotation rate with respect to the polar tidal torque decelerates at negative values and accelerates at positive values. The phase of the tides exerts a decisive control on the direction of the tidal torque. In terms of power supply, energy is released from the ocean at negative values and supplied to the ocean at positive values. When considered at the global scale, the Earth's rotation rate is decelerated, while the partial tides supply potential energy to the ocean.

As with the form factor, notable discrepancies are evident in the North Pacific, including reversal in the sign between the simulations with the detailed bathymetry and those with the two-depth distribution. In the case of the S_2 tidal torques, instead of a zonal effect that slows down the Earth's rotation rate, an accelerating effect is observed.

The North Pacific exhibits distinctive and pronounced alterations that are not observed in other oceans, including the Atlantic, the Indian Ocean, and the South Pacific. The occurrence in the North Pacific can be described as an extraordinary phenomenon, although not one that persists over an extended period of time. The region in question is distinguished by a complex array of factors that render it challenging to represent using the two-depth distribution. These include the resonant proximity to diurnal and semi-diurnal tides, steep-sea trenches and the adjacent oceanic ridges, and extensive island areas. Even the simulations with the resolution of 1° of the detailed bathymetry are inadequate for representing the region. From a geological perspective, such phenomena have an extremely short lifespan. In this regard, the presented two-depth distribution can be applied to the tidal simulations for the Late Neoproterozoic ~620 Myr ago. In particular, within the scope of the present study.

4.6. Summary

The approach used in the present study to simulate and analyze the ocean tides in Late Neoproterozoic oceans ~620 Myr ago is presented in detail (Section 4.1) and the methods to carry it out are fully explained. This encompasses the definition of the required data (Section 4.2) and the resources, which include the data-unconstrained barotropic tide model TiME (Weis, 2006) with the geodetic module and the analysis tools (Section 4.3). The semi-diurnal M_2 and S_2 tides and the diurnal K_1 and O_1 tides are selected for examination. The configuration of the Earth-Moon-Sun system with a day length of 21.9 h put forth by G. E. Williams (2000) is employed to delineate the lunisolar partial tides and the Coriolis parameter of ~620 Myr ago (Section 4.2.1 and Table 4.1). Paleobathymetries from Scotese (2017) and Scotese and Wright (2018) have been provided for the time slices ~600 Myr, ~630 Myr, and ~750 Myr ago (Figure 4.1). The latter is very different from the first two, which are very similar. One depth for the continental shelves (160 m) and one for the open ocean (3480 m) represent the bathymetry (Section 4.2.2).

The TiME(1°) model, adapted for the purposes of the present study, was adjusted (Section 4.4.2) and evaluated (Section 4.5.1) for modern conditions. The local parameter approach for SAL and the exclusion of topographic wave drag, combined with the resolution of 1°, yielded satisfactory results (Table 4.2). The nominal tides confirm that, as is the case with all data-unconstrained models, the tidal amplitudes are overestimated and the phases lag behind (Table 4.3). Therefore, the polar tidal torque and energy dissipation, globally averaged over a period, are at the upper end of the reference values. In comparison, the modern two-depth distribution results in approximately half the polar tidal torques and energy supplies, globally averaged over a period (Section 4.5.2). For the O_1 tides there is only a reduction of about 20 %. The amphidromic systems evolve in a comparable manner in terms of their spatial distribution and direction of rotation (Figures 4.5 and 4.7). However, there is a notable decrease in tidal amplitudes, alongside the occurrence of significant phase shifts. The nominal tides are roughly 30 % smaller and about 10° to 15° advanced (Figure 4.13). The O_1 have only a 4 % smaller nominal amplitude.

A noteworthy aspect of the simulations with both depth distributions is the alternating occurrence of regions in which the Earth's rotation rate is slowed down and accelerated by tidal torques (Figure 4.11), and in which potential energy is absorbed and released (Figure 4.12). The occurrence of maxima and minima of the partial tide gradients in regions of high tidal range facilitates the occurrence of high tidal torques, contingent on the tidal phase. Similarly, regions with low tidal range and/or partial tide gradients can develop high tidal torques when the tidal phase is well aligned. The Northwest Pacific region undergoes notable alterations when the simulations with the two depth distributions are contrasted. This also applies to the type of the global tidal regime (Figures 4.6 and 4.8). The region, which is characterized by steep deep-sea trenches and island territories such as Indonesia and the Philippines, cannot be adequately resolved even with the 1° resolution of the detailed bathymetry. In this region there is a resonance proximity of diurnal and semi-diurnal tides, which nevertheless have an extremely brief half-life on the geological time scale. The Atlantic, Indian, and Southern Pacific Oceans exhibit only minimal impacts, apart from a notable reduction in the quantities under consideration.

For a shelf of limited width with a rapid transition to the deep-sea, TiME(1°) simulates the

ratio of diurnal to semi-diurnal tides and the tidal regime type locally adequate. The tidal range does not permit the drawing of conclusions regarding the potential for sedimentation. However, statements can be made regarding the periodicity of sedimentation, which also applies to the simulations with the two-depth distribution.

The tidal oscillation systems and their periodicities are adequately represented for the purpose of the this study. Overall, the evidence indicates that a pure two-depth distribution can be employed to simulate tides for the Late Neoproterozoic ~620 Myr ago.

5. Results

Following the implementation and evaluation of the research approach, the final tidal simulations for the Late Neoproterozoic ~620 Myr ago were conducted. The findings are set forth herein. The procedure, conditions and assumptions employed in the tidal simulations pertaining to ~620 Myr ago have been previously outlined in Section 4.1. TiME(1°) was used as the tidal model, as detailed in Sections 4.3.1 and 4.3.3, with the parameterization from Sections 4.3.2 and 4.4.2.3 and evaluated for modern conditions in Section 4.5. The analysis encompassed the resources outlined in Section 4.3.4 and utilized for the evaluation in Section 4.5. The implementation is analogous to that in Sections 4.4.1 and 4.4.3.

As part of the tidal simulations conducted, the modern land-water distribution (Figure 4.1b) and those that existed ~750 Myr, ~630 Myr, and ~600 Myr ago (Figures 4.1c to 4.1e) were considered along with the two-depth distribution from Section 4.2.2. Simulations were done for the partial tides M_2, S_2, K_1, and O_1. For each partial tide and each land-water distribution, four versions were simulated: each partial tide for the modern period and for ~620 Myr ago, each for the modern day length and for ~620 Myr ago (Section 4.2.1 and Table 4.1). This approach facilitates the representation of the respective influence of the varied partial tide and day length. The combinations of the modern tidal force with the paleoday length and the paleotidal force with the modern day length must be considered as theoretical considerations; they cannot occur on Earth due to the conservation of angular momentum. The geographic conditions were retained, and the hypothesis of a Snowball Earth was excluded (Section 4.1.2).

The presentation of the results will focus on the simulations of the M_2 and K_1 tides, with the results for the S_2 tides being analogous to those for the M_2 tides and the results for the O_1 tides being analogous to those for the K_1 tides. The tidal forces that were considered ~620 Myr ago were either greater than or equal to modern values, and the tidal periods and day length ~620 Myr ago were shorter than modern values (Table 4.1). In the following, these conditions ~620 Myr ago are also referred to as the paleotidal force, paleotidal period, and paleoday length, or as the shorter tidal period and shorter day length. Moreover, all subsequent comparisons of quantities for the paleoconditions are inherently relative to modern conditions.

Section 5.1 focuses on the subject of tidal sea surface elevations. Geological data will subsequently be utilized in Section 5.2 to evaluate the various tidal regime types. In Section 5.3, the discussion shifts to the nominal tides in conjunction with the time-averaged global polar tidal torques. Finally, Section 5.4 examines the composition of the time-averaged global polar tidal torques based on the global distributions of the torques per water column.

5.1. Tidal elevation

The tidal sea surface topographies of the modern and paleo land-water distributions for the tidal force and day length in modern times and ~620 Myr ago are shown in Figures 5.1 and 5.2 for the M_2 tides and in Figures 5.3 and 5.4 for the K_1 tides. The relatively high tidal amplitudes of the modern conditions are no exception for either the semi-diurnal or the diurnal tides. In some cases they are exceeded (e. g. Figures 5.1f, 5.2c and 5.2d). The simulations demonstrate a marked deficiency in the resolution of tides along the extensive continental shelves of the paleo land-water distributions (Section 4.5.1.5 and Figures 4.1c to 4.1e). The discrete depth distribution can be clearly seen in some places (e. g. Figures 5.1b, 5.2a and 5.2b). At the shelf edges, significant upwelling with vertical velocity can occur, allowing a discrete transition from the open ocean to the shelf for tidal propagation (Section 2.2.4.3). However, no large-scale effects have been identified.

Initially, Section 5.1.1 delineates the effects of the conditions ~620 Myr ago on tidal propagation. Subsequently, Sections 5.1.2 and 5.1.3 provide a detailed analysis of the M_2 and K_1 tides, respectively. In both instances, the effects occurring for all land-water distributions are considered first. The tidal oscillation systems for the respective land-water distributions are subsequently examined. A striking similarity can be observed between the tides for the analogous land-water distributions ~630 Myr and ~600 Myr ago (Figures 5.2 and 5.4). Consequently, both land-water distributions are treated together in the following discussion. Finally, a summary is provided in Section 5.1.4.

5.1.1. Tidal propagation

The periods of the partial tides and the length of the sidereal day are both equivalent to about 0.91 of their modern values (Table 4.1) in accordance with the conservation of angular momentum. Consequently, the critical latitude of Poincaré waves remains constant for both time periods (Section 2.2.4.3). Other quantities that determine tidal propagation are also affected by these decreases, including the tidal wavelengths due to the tidal periods, the Coriolis parameter, and the Rossby radius due to the length of day (Section 2.2.4.3).

In contrast to the paleo land-water distributions characterized by the single supercontinent Rodinia, the modern land-water distribution characterized by dispersed continents gives rise to a substantially longer coastline. This, in turn, facilitates the development of Kelvin waves on a far greater scale, given that these waves require a vertical boundary to propagate (Section 2.2.4.3). A significantly longer coastline in the mid- and high-southern latitudes is shown by the land-water distributions ~630 Myr and ~600 Myr ago in Figures 4.1c and 4.1d with the position of Rodinia around the South Pole compared to the land-water distribution ~750 Myr ago in Figure 4.1e. This enables the propagation of diurnal tides as Kelvin waves to a greater degree in ocean regions south of about 30° S, where Poincaré waves are excluded due to the critical latitude for the diurnal tides (Section 2.2.4.3). The almost hemispherically open paleo-oceans and the relatively short paleo-coastlines favor tidal dynamics that are different from modern ones (Sections 5.1.2 and 5.1.3).

In relation to the development of the tidal oscillation systems as a function of the tidal period and day length, there is potential interest in the tidal propagation as Kelvin or Poincaré waves. The propagation velocity of non-dispersive Kelvin waves is independent of

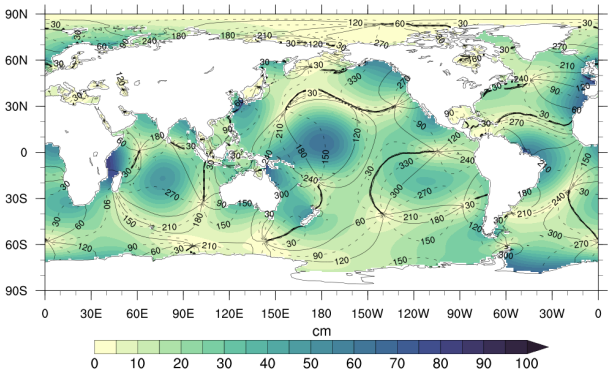

(a) Modern tidal force and modern sidereal day.

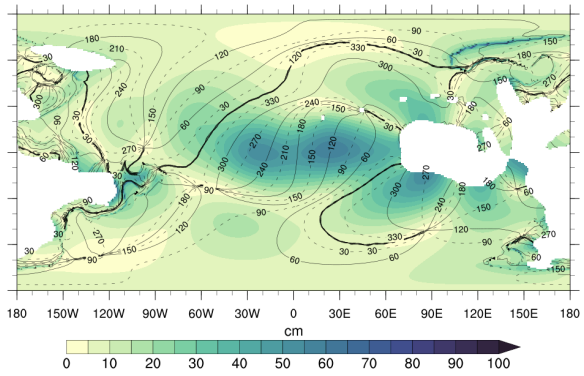

(b) Modern tidal force and modern sidereal day.

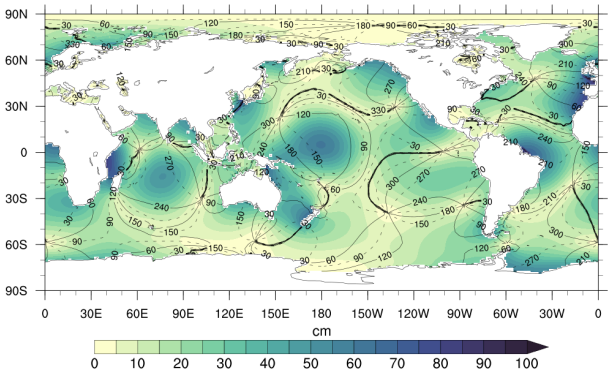

(c) Modern tidal force and sidereal day of ~620 Myr ago.

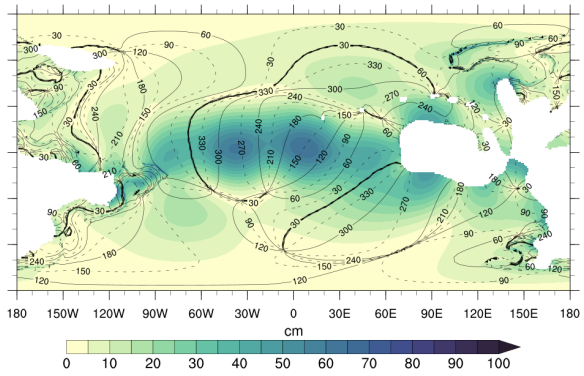

(d) Modern tidal force and sidereal day of ~620 Myr ago.

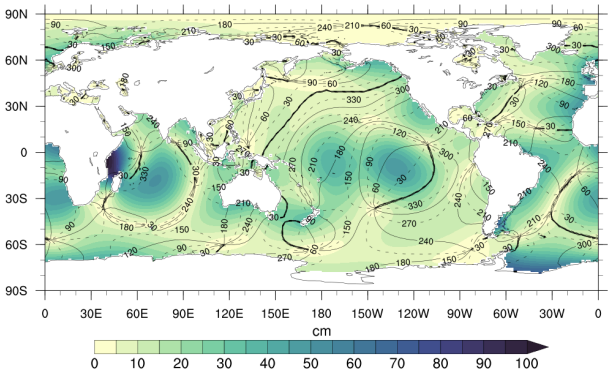

(e) Tidal force of ~620 Myr ago and modern sidereal day.

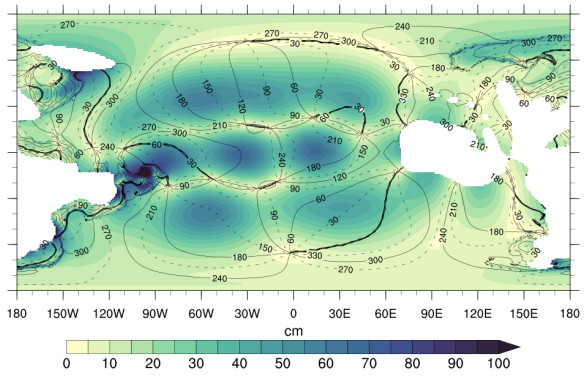

(f) Tidal force of ~620 Myr ago and modern sidereal day.

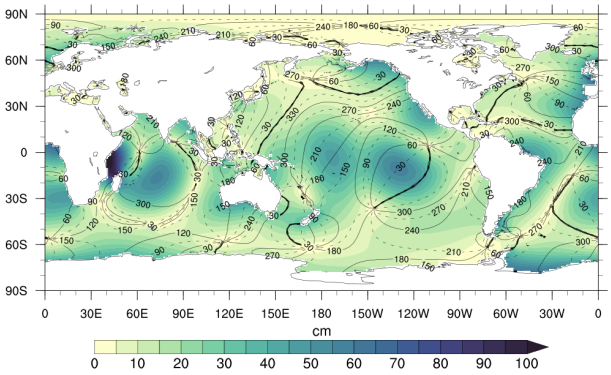

(g) Tidal force and sidereal day of ~620 Myr ago.

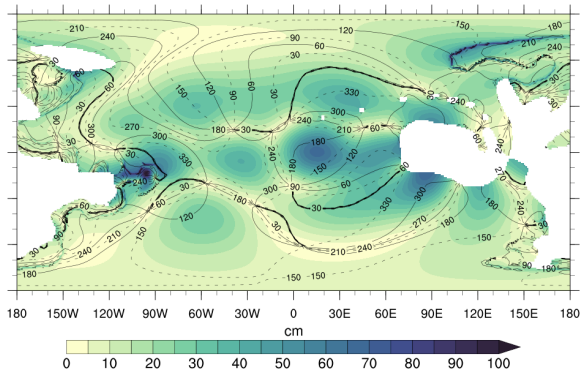

(h) Tidal force and sidereal day of ~620 Myr ago.

Figure 5.1.: M_2 tidal maps for land-water distribution of modern times (left column) and ~750 Myr ago (right column) with the two-depth distribution. Colors show amplitudes in cm, black lines show contours of the same phase in degrees of the tidal sea level oscillation.

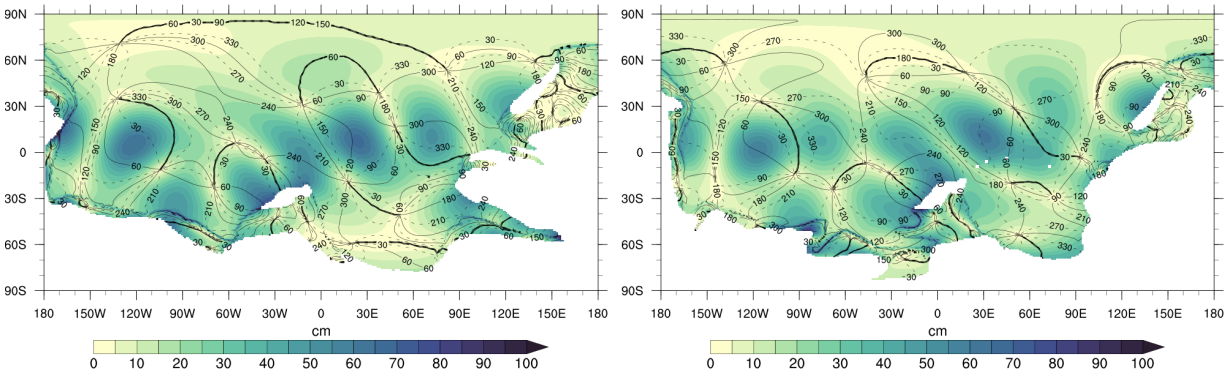

(a) Modern tidal force and modern sidereal day.

(b) Modern tidal force and modern sidereal day.

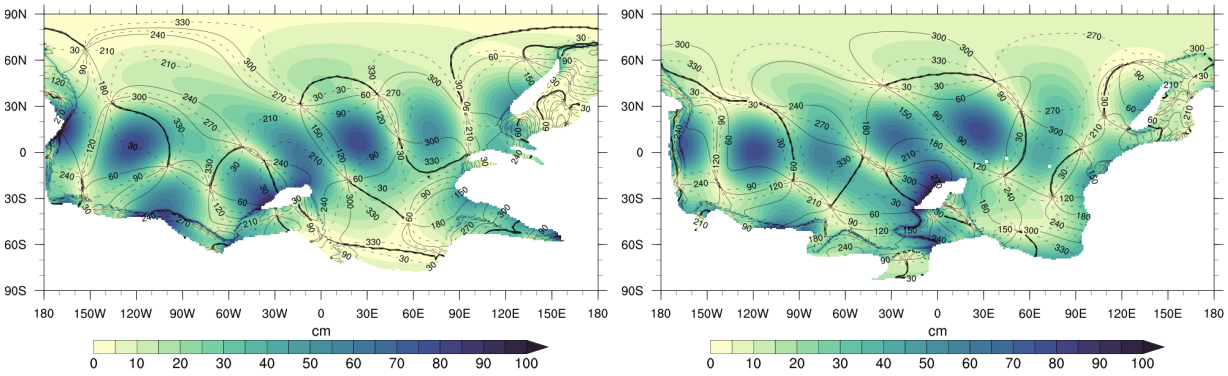

(c) Modern tidal force and sidereal day of ~620 Myr ago.

(d) Modern tidal force and sidereal day of ~620 Myr ago.

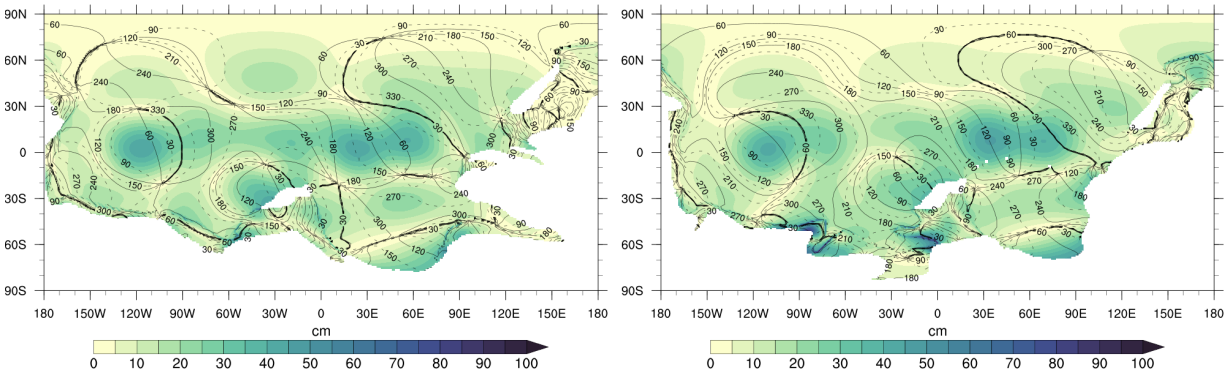

(e) Tidal force of ~620 Myr ago and modern sidereal day.

(f) Tidal force of ~620 Myr ago and modern sidereal day.

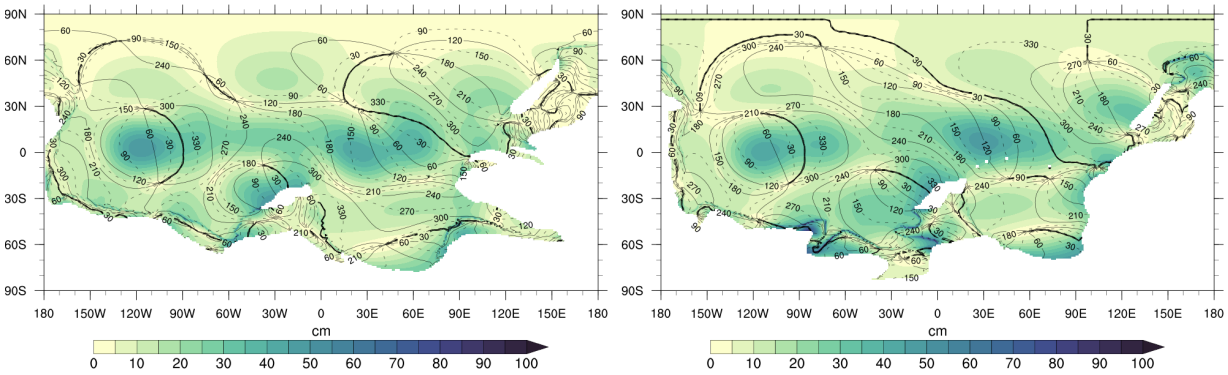

(g) Tidal force and sidereal day of ~620 Myr ago.

(h) Tidal force and sidereal day of ~620 Myr ago.

Figure 5.2.: M_2 tidal maps for land-water distribution of ~630 Myr ago (left column) and ~600 Myr ago (right column) with the two-depth distribution. Colors show amplitudes in cm, black lines show contours of the same phase in degrees of the tidal sea level oscillation.

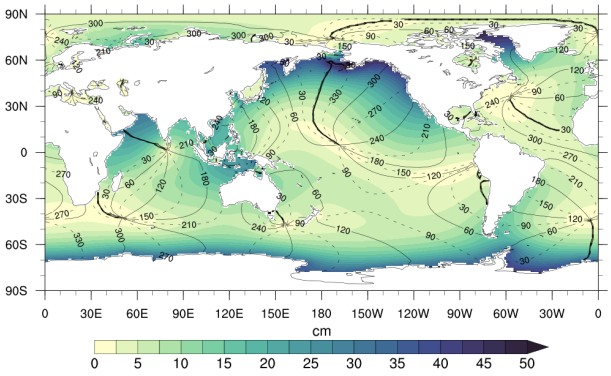

(a) Modern tidal force and modern sidereal day.

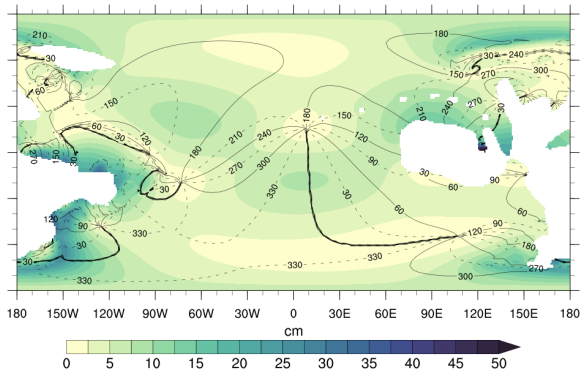

(b) Modern tidal force and modern sidereal day.

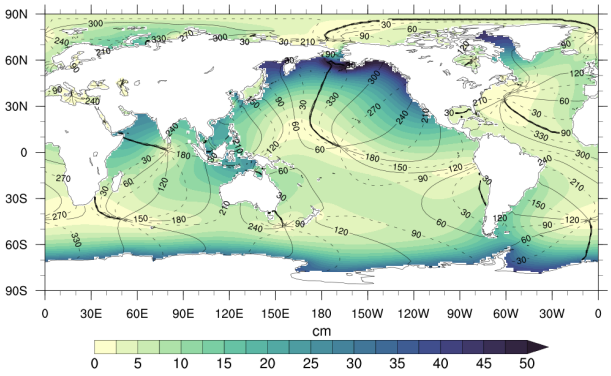

(c) Modern tidal force and sidereal day of ~620 Myr ago.

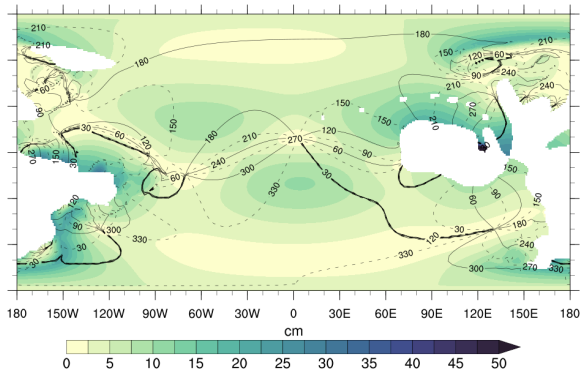

(d) Modern tidal force and sidereal day of ~620 Myr ago.

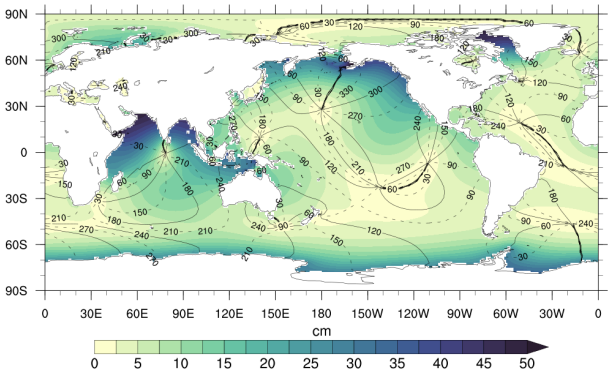

(e) Tidal force of ~620 Myr ago and modern sidereal day.

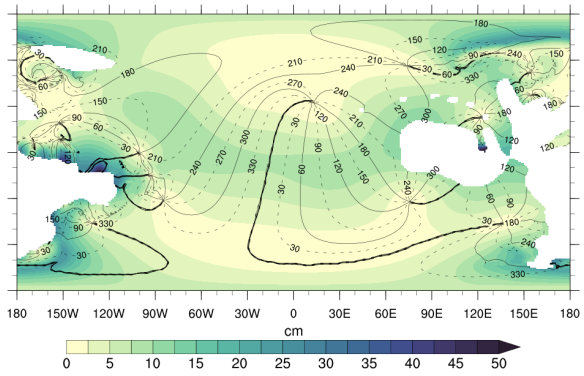

(f) Tidal force of ~620 Myr ago and modern sidereal day.

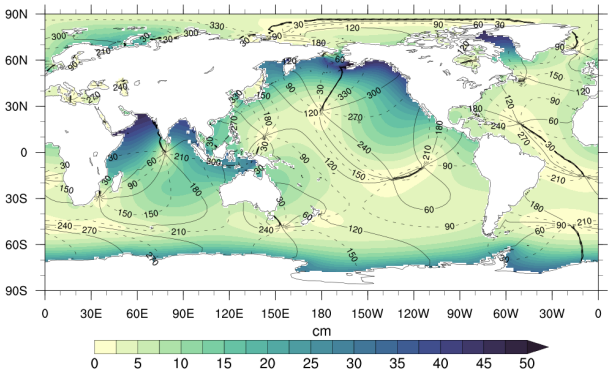

(g) Tidal force and sidereal day of ~620 Myr ago.

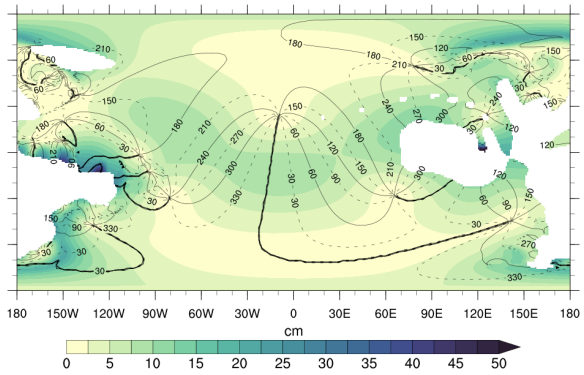

(h) Tidal force and sidereal day of ~620 Myr ago.

Figure 5.3.: K_1 tidal maps for land-water distribution of modern times (left column) and ~750 Myr ago (right column) with the two-depth distribution. Colors show amplitudes in cm, black lines show contours of the same phase in degrees of the tidal sea level oscillation.

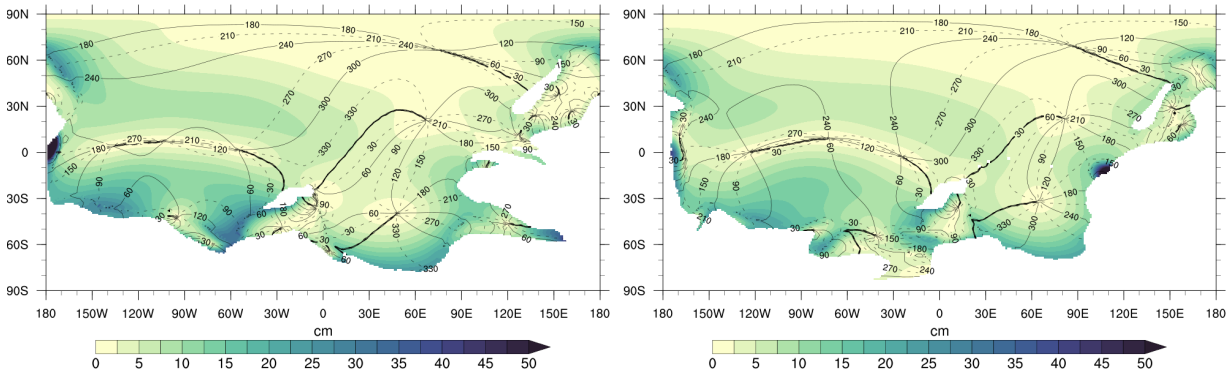

(a) Modern tidal force and modern sidereal day.

(b) Modern tidal force and modern sidereal day.

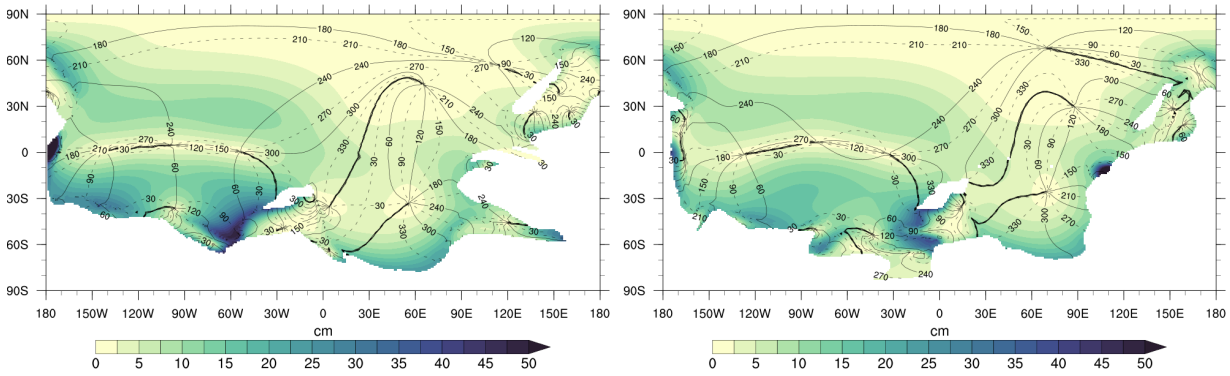

(c) Modern tidal force and sidereal day of ~620 Myr ago.

(d) Modern tidal force and sidereal day of ~620 Myr ago.

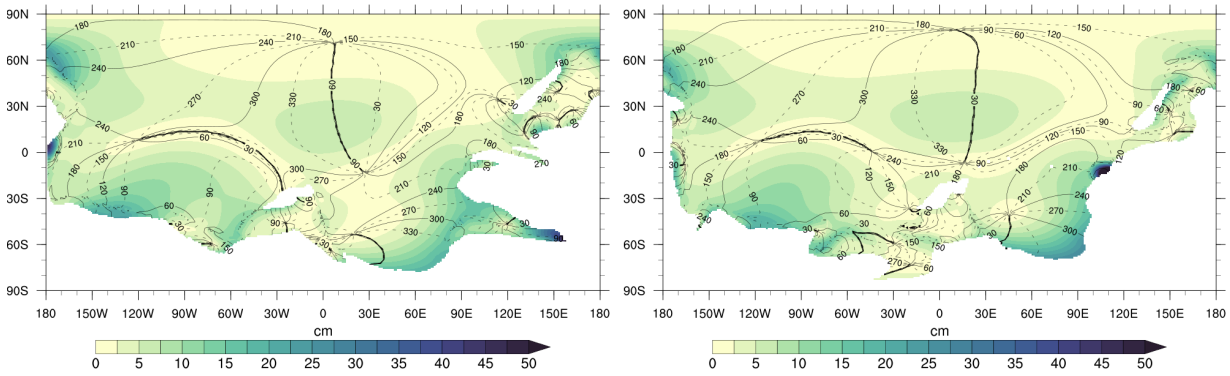

(e) Tidal force of ~620 Myr ago and modern sidereal day.

(f) Tidal force of ~620 Myr ago and modern sidereal day.

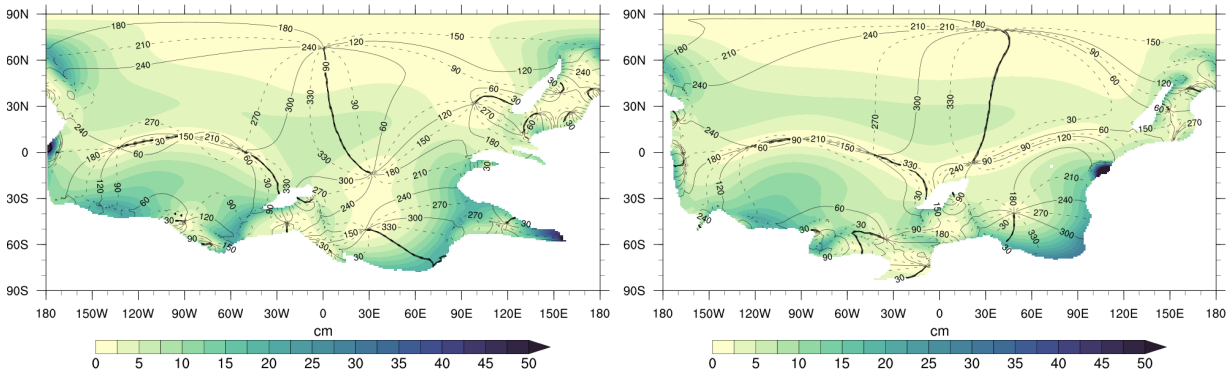

(g) Tidal force and sidereal day of ~620 Myr ago.

(h) Tidal force and sidereal day of ~620 Myr ago.

Figure 5.4.: K_1 tidal maps for land-water distribution of ~630 Myr ago (left column) and ~600 Myr ago (right column) with the two-depth distribution. Colors show amplitudes in cm, black lines show contours of the same phase in degrees of the tidal sea level oscillation.

the tidal period and day length (Section 2.2.4.3). A shift in the wavelength is only observed in conjunction with a change in the tidal period. Conversely, the propagation velocity of dispersive Poincaré waves is governed by tidal period and day length (LeBlond & Mysak, 1978). The wavelengths have a higher potential for change, consequently, for constructive or destructive interference. In the context of both tidal period and day length in modern times and ~620 Myr ago, the quotient of both quantities in the dispersion relation and the propagation velocity remain constant. The tidal period and day length have undergone a mutually dependent change in a manner consistent with the conservation of angular momentum over the past ~620 Myr.

5.1.2. M_2 tide

The tidal oscillation systems for the paleo land-water distributions can exceed the relatively high tidal amplitudes for modern times (Figures 5.1 and 5.2). This is evident for the distribution ~750 Myr ago for the paleotidal force and the modern day length (Figure 5.1f), as well as for the distributions ~630 Myr and ~600 Myr ago for the modern tidal force and the paleoday length (Figures 5.2c and 5.2d). The influence of the day length is evident in the tidal oscillation systems. In systems characterized by the same tidal force, but with the shorter day length ~620 Myr ago, tidal amplitudes may exhibit substantial increases (Figures 5.2c and 5.2d) or decreases (Figure 5.1h), while the amphidromic systems remain relatively stable displaying only minor phase shifts.

In modern conditions, regions with relatively high tidal amplitudes are predominantly located along the coastline (Figure 5.1a). This distribution can be attributed to the presence of Kelvin waves, which are facilitated by the relatively extended coastline of the dispersed continents. The paleo land-water distributions with the supercontinent Rodinia demonstrate different characteristics in this respect (Figures 5.1 and 5.2). The occurrence and intensity of regions with relatively high tidal amplitudes is greater in the open ocean than in coastal regions. Amphidromic systems are identified in open ocean with their nodes near 30° S and 30° N and regions with relatively high amplitudes around the equator. These systems exhibit a pattern of stringed cells, arising from the interference of counter-propagating Poincaré waves in the equatorial waveguide, which can be conceptualized as an infinite channel of constant width (Section 2.2.4.3). Furthermore, the phase distribution displays a westward propagating tidal wave, indicative of Poincaré waves. A total of four waveguides are apparent. Firstly, the two equatorial waveguides are evident, extending from 0° to about 30° S and 30° N, respectively. Adjacent to this, a further waveguide is constituted by the critical latitude of Poincaré waves for semi-diurnal tides at about 75° S and 75° N (Section 2.2.4.3), as is clearly evident in Figure 5.1f

5.1.2.1. Modern land-water distribution

In general, the tidal amplitudes for the tidal force and day length ~620 Myr ago are moderately lower than the modern values (Figures 5.1a and 5.1g) despite the stronger tidal force. There are local exceptions with higher amplitudes like the East African waters off Madagascar.

The amphidromic systems in the Indian and Atlantic Oceans remain almost the same for

the shorter tidal period and day length (Figures 5.1a, 5.1c, 5.1e and 5.1g), both individually and combined. However, there are phase shifts. The tidal oscillation system in the Pacific exhibits comparable behavior for the shorter day length ~620 Myr ago (Figures 5.1c and 5.1g), when the tidal force remained unchanged. However, the shorter tidal period and the resulting shorter wavelength ~620 Myr ago make it more difficult for Kelvin waves to occur and suppress the anti-amphidrome in the western central Pacific and the amphidrome in the western North Pacific (Figures 5.1e and 5.1g). Instead, a progressive Poincaré wave with significantly lower tidal amplitudes develops across the entire width of the North Pacific. In the central Pacific south of the equator, two neighboring regions characterized by relatively high tidal amplitudes emerge. The amplitudes of these regions exhibit a moderate increase in conjunction with the shorter day length ~620 Myr ago (Figure 5.1g). Similarly, the North Pacific exhibits a moderate increase in tidal amplitudes along its coastlines.

5.1.2.2. Land-water distribution ~750 Myr ago

Within the open ocean surrounding the equator, there exist regions characterized by relatively high tidal amplitudes (Figures 5.1b, 5.1d, 5.1f and 5.1h). The distribution pattern of regions exhibiting relatively high amplitudes remains practically unchanged under the different conditions, with significant differences in the height of the amplitudes. For the paleotidal force, the amplitudes in the northern and southern waveguides exhibit a substantial increase in height (Figures 5.1f and 5.1h). The amplitudes in the western open ocean underwent a substantial decline in response to the shorter day length (Figure 5.1h). Conversely, the shorter day length for the modern tidal force results in a moderate increase in amplitude heights (Figure 5.1d).

Kelvin waves occur only sporadically along the coastlines, such as along the extensive northern continental shelf (Figure 4.1e). In all conditions, Kelvin waves propagate along the northern extended shelf's edge, capable of developing higher amplitudes for the paleotidal force (Figures 5.1f and 5.1h). The amphidromes primarily demonstrate the direction for Poincaré waves, and the westward wave propagation along the equator corresponds to that of Poincaré waves (Section 2.2.4.3). The regions exhibiting relatively high tidal amplitudes remain almost the same for the shorter day length ~620 Myr ago at unchanged tidal force (for the modern tidal force: Figures 5.1b and 5.1d; for the paleotidal force: Figures 5.1f and 5.1h), although the amphidromic systems are affected by variations.

In the northern open ocean, Poincaré waves propagate from the eastern edge along the equatorial waveguide to the west and in the adjacent northern waveguide to the northwest and west towards the east coast of Rodinia. The semi-enclosed basin north of the equator, in conjunction with the substantial shelf area situated further north, functions as an effective barrier for the Poincaré waves. With respect to the paleotidal force (Figures 5.1f and 5.1h), the northern waveguide exhibits considerably higher tidal amplitudes.

Along the southwestern edge of Rodinia, Kelvin waves develop in all conditions (Figures 5.1b, 5.1d, 5.1f and 5.1h), encompassing the ocean basin in this region to a considerable extent. From the adjoining southeastern periphery of the southern open ocean, Poincaré waves propagate northwestward toward the equator. In the equatorial waveguide the waves exhibit a westward propagation towards the eastern coastline of Rodinia. The easternmost extension of Rodinia south of the equator, characterized by its substantial protruding shelf

(Figure 4.1e), impedes the further propagation of the Poincaré wave in a southerly direction. Along the southern east coast of Rodinia, Kelvin waves are also absent in the context of the modern tidal force, as evidenced in Figures 5.1b and 5.1d. In contrast, the presence of Kelvin waves is evident for the paleotidal force (Figures 5.1f and 5.1h). From the high latitudes towards the equator, along the coastline or the shelf edge of Rodinia, they are pronounced in the case of the modern day length (Figure 5.1f), and from the mid-latitudes, they are weakly pronounced in the case of the paleoday length (Figure 5.1h). Kelvin waves also propagate around the easternmost extent of Rodinia south of the equator along the protruding shelf, where they interfere with the westward-traveling Poincaré waves in the equatorial waveguide, giving rise to a localized amplitude trapping effect.

5.1.2.3. Land-water distribution ~630 Myr and ~600 Myr ago

In the open ocean surrounding the equator, regions characterized by relatively high tidal amplitudes emerge, as evidenced in Figures 5.2a, 5.2c, 5.2e and 5.2g for the land-water distribution ~630 Myr ago and in Figures 5.2b, 5.2d, 5.2f and 5.2h for the land-water distribution ~600 Myr ago. Regions exhibiting relatively high tidal amplitudes remain relatively stable across the varying tidal force and day length; however, shifts in amphidromic systems are evident. The regions undergo a substantial decrease in tidal amplitude for the paleotidal force (Figures 5.2e to 5.2h), while the tidal amplitudes for the paleoday length exhibit a moderat increase, with the tidal force remaining unaltered (Figures 5.2c, 5.2d, 5.2g and 5.2h). For the modern tidal force with the paleoday length, tidal amplitudes can exceed the maximum levels recorded in modern times (Figures 4.5a, 5.2c and 5.2d).

From the easternmost edge of the northern open ocean, Poincaré waves propagate westward along the equatorial waveguide towards the east coast of Rodinia. This is shown in particular in Figures 5.2e to 5.2h for the paleotidal force, wherein the Poincaré waves exhibit the capacity to propagate up to the periphery of the Rodinia shelf. Nevertheless, the amplitudes diminish considerably towards the shelf edge. In the context of the modern tidal force, Kelvin waves characterized by relatively high amplitudes emerge along the shelf edge, thereby impeding the propagation of the Poincaré waves. With lower amplitudes, the Poincaré waves can also propagate further west in the adjacent northern waveguide, especially for the paleotidal force (Figures 5.2e to 5.2h). In this instance as well, the Poincaré waves are able to propagate to the edge of the substantial northernmost continental shelf (Figures 4.1c and 4.1d). In the vicinity of the nexus, where the southern edge of the waveguide intersects with the shelf edge, the development of an amphidromic node with correspondingly diminished amplitudes in its surrounding region commences. For the modern tidal force (Figures 5.2a to 5.2d), an amphidromic system, characteristic of Kelvin waves, acts as a barrier to further propagation in the northwestern open ocean. Along the edge of the northernmost shelf, Kelvin waves with relatively high amplitudes manifest.

The southern equatorial waveguide is distinguished by the presence of westward-directed Poincaré waves, as evidenced particularly by Figures 5.2e to 5.2h for the paleotidal force. In the region further south, the eastern basin (Section 4.2.2)—whose open boundary roughly coincides with the southern equatorial waveguide's edge—is distinguished for the modern tidal force by circumferential Kelvin waves (Figures 5.2a to 5.2d), exhibiting relatively moderate tidal amplitudes at the boundaries. For the paleotidal force, the Kelvin waves are

forced back into the southern bay and replaced by Poincaré waves (Figures 5.2e to 5.2h).

Kelvin waves propagate in the western basin at the easternmost edge, as shown in Figure 5.2, in all conditions, extending from the north of the island along the continental shelf edge to the southwest. For the land-water distribution ~630 Myr ago and the modern tidal force (Figures 5.2a and 5.2c), and for the land-water distribution ~600 Myr ago and the modern tidal force with the paleoday length (Figure 5.2d), the Kelvin waves extend to the southern shelf edge of Rodinia at about 50° to 60° W. The subsequent region in a northwesterly direction to about 120° W exhibits a minimal phase change of the tides for the modern tidal force, particularly with regard to the land-water distribution ~630 Myr ago (Figures 5.2a and 5.2c). Further towards the western basin edge, the distance to the southern equatorial waveguide is too small to separate between the two waveguides.

5.1.3. K_1 tide

The K_1 tides propagate from the open ocean into the surrounding shelf areas and increase in amplitude (Figures 5.3 and 5.4). This phenomenon occurs for all land-water distributions, regardless of selected tidal force or day length. The highest tidal amplitudes manifest along coastlines and shelf edges. The propagation of K_1 tides is determined by the propagation of Kelvin waves. Poincaré waves are constrained to the area between approximately 30° S and 30° N for the diurnal tides (Section 2.2.4.3). In contrast to the modern land-water distribution, the paleo land-water distributions in the nearly hemispherically open oceans (Figures 5.3b, 5.3d, 5.3f, 5.3h and 5.4) around the equator exhibit Poincaré waves and regions with relatively high amplitudes. The relatively high modern tidal amplitudes are attained or exceeded in some relatively small regions by the tidal oscillation systems of the paleo land-water distribution (Figures 5.3 and 5.4). The nearly hemispherically open oceans of the paleo land-water distributions, particularly at high latitudes, exhibit relatively extensive regions with almost no tidal propagation, featuring minimal tidal amplitudes and phase differences. These characteristics are virtually absent for the modern land-water distribution due to the substantially extended coastline of the dispersed continents, even at high latitudes, which promotes tidal propagation by Kelvin waves.

5.1.3.1. Modern land-water distribution

The tidal oscillation system for the modern land-water distribution exhibits stability with respect to the variations in tidal force and day length (Figures 5.3a, 5.3c, 5.3e and 5.3g). Along the coastlines of all continents, there are extensive regions characterized by relatively high tidal ranges. The Kelvin waves that predominate tidal propagation extend profoundly into the open ocean. Within the North Pacific and Indian Oceans, the interference of Kelvin waves is virtually omnipresent. The South Pacific region serves as an exception, exhibiting only minimal tidal dynamics.

Notwithstanding the slightly higher tidal amplitudes, the tidal oscillation system for a selected tidal force is nearly equivalent for the longer modern day length and the shorter day length ~620 Myr ago (Figures 5.3c and 5.3g). This phenomenon can be attributed to the prevalence of non-dispersive Kelvin waves (Section 5.1.1). While the tidal amplitudes exhibit an increase in the Indian Ocean due to the stronger tidal force ~620 Myr ago, they

underwent a moderate decrease in the Pacific and Atlantic Oceans (Figures 5.3e and 5.3g). Two new amphidromes are emerging in the central Atlantic. The existing amphidrome in the central Pacific is shifting northward. This shift is leading to a significant reduction in the extent of the region with relatively high amplitudes in the northern Pacific. In the eastern South Pacific, the presence of two newly formed smaller amphidromes serves to further attenuate the already minimal tidal amplitudes.

5.1.3.2. Land-water distribution ~750 Myr ago

The spatial distribution pattern of the tidal amplitudes remains largely unaltered regardless of the selected tidal force and day length (Figures 5.3b, 5.3d, 5.3f and 5.3h). Along the coastline of the supercontinent Rodinia, regions with relatively high amplitudes can develop, corresponding to the propagation of Kelvin waves. In the northern region, the waters along the eastern coastline persist in a state of near-tidal absence. In the equatorial waveguides of the nearly hemispherically open ocean, eastward-moving Poincaré waves are evident, especially for the paleotidal force (Figures 5.3f and 5.3h). In vast regions extending from approximately 30° S and N towards the poles, tidal propagation is nearly absent. Poincaré waves are excluded, and the necessary vertical boundaries for Kelvin waves are missing. The configuration of Rodinia, in conjunction with its geographical position, rules out the possibility of extensive regions characterized by high amplitudes in the vicinity of Rodinia.

In relation to the paleotidal force (Figures 5.3f and 5.3h), the tidal amplitudes demonstrate a moderate increase in regions exhibiting relatively high tides. The tidal oscillation system gains momentum particularly in the open ocean around the equator. At the same tidal force, the tidal oscillation system for the shorter day length in the vicinity of Rodinia is analogous to that for the longer modern day length. In the open ocean, phase shifts occur in the dispersive Poincaré waves (Section 5.1.1).

5.1.3.3. Land-water distribution ~630 Myr and ~600 Myr ago

For the selected tidal forces and day lengths, the spatial and temporal distribution patterns of the tidal oscillations system remain relatively stationary (Figure 5.4). Kelvin waves generate extensive regions along a substantial part of Rodinia's coastline, where the tidal amplitudes increase towards the coastline. The configuration of Rodinia, with its extensive ocean basins and its geographical location like a brace around the South Pole (Section 4.2.2), allows Kelvin waves and their interference to occupy extensive regions far into the open ocean for the propagation of K_1 tides. The propagation patterns in the western northern open ocean, extending from the equator to about 60° N, are distinguished by relatively high amplitudes accompanied by minimal phase change, akin to an anti-amphidrome. This region is considered ambiguous. For the paleotidal force (Figures 5.4e to 5.4h), tidal amplitudes exhibit a significant decrease in regions with relatively high amplitudes. Conversely, they show a slight increase in conjunction with the shorter day length for unaltered tide (Figures 5.4c, 5.4d, 5.4g and 5.4h).

In the eastern northern open ocean, the Kelvin waves are associated with two amphidromes for the modern tidal force (Figures 5.4a to 5.4d), which cause the tidal amplitudes in large parts of the open ocean to approach zero. This phenomenon is also applicable to the paleotidal force, wherein the amphidromes undergo a partial shift further northwest into

the open ocean (Figures 5.4e to 5.4h) or are not fully developed due to a relatively strong decrease in the Kelvin waves (Figures 5.4f and 5.4h). Along the periphery of the substantial northernmost continental shelf, Kelvin waves with relatively high amplitudes can propagate and extend as far as the North Pole. As these waves travel southward toward the equator along the shelf's edge in the western northern open ocean, encompassing the Rodinia protrusion at about 15° to 30° N, they undergo a process of decay. At the equator, the reflection process of the Kelvin waves as they propagate further south appears to trap the tides locally, resulting in an accumulation of high amplitude tides. This phenomenon is particularly evident in the context of the modern tidal force (Figures 5.4a to 5.4d).

The southern open ocean is distinguished by the presence of regions exhibiting relatively high tidal amplitudes, particularly in the western sector. The propagation of Kelvin waves is evidenced by their extension across the entire width and their reach toward the equator. As the Kelvin waves travel northward along the shelf edge in the western ocean, they accumulate in the reflection process south of the equator, reaching high amplitudes, especially for the modern tidal force (Figures 5.4a to 5.4d). The eastern basin is characterized by a circumferential Kelvin wave, whereby the region exhibiting relatively high amplitudes is comparatively diminished in extent relative to the western basin. In the case of the modern tidal force (Figures 5.4a to 5.4d), the tidal amplitudes are lower and comparable for the paleotidal force (Figures 5.4e to 5.4h).

5.1.4. Summary

The simulated M_2 and K_1 tides for tidal force and day length in modern times and ~620 Myr ago have been presented in detail based on the corresponding tidal sea surface topographies. The simulations incorporate the two-depth distribution. For the land-water distribution of modern times and ~630 Myr and ~600 Myr ago, the shorter tidal period of the stronger paleotidal force results in a weakening of the tidal amplitudes and an increase in tidal phase. Conversely, the shorter day length results in an increase of the tidal amplitudes and a decrease in tidal phase. The paleotidal force exerts a more pronounced influence within this context. In contrast, the land-water distribution ~750 Myr ago exhibits a tidal oscillation system that responses in a nearly opposite manner.

The tidal amplitudes of modern conditions are no exception. In some cases, the tides for the paleo land-water distributions even exceed them. The spatial distribution pattern of the M_2 and K_1 tides remains virtually unaltered worldwide in all conditions for the individual land-water distributions. The extent and intensity of regions with relatively high tides can vary significantly depending on the resonance proximity, with the location of the amphidromes being relatively stable. For the individual land-water distributions, the propagation processes of the M_2 and K_1 tides are found to be largely independent of the tidal force and day length.

The M_2 and K_1 tides for modern land-water distribution respond slightly to tidal force and day length ~620 Myr ago. This phenomenon can be attributed to the dominance of non-dispersive Kelvin waves in the M_2 and K_1 tidal propagation, which have a velocity that is independent of day length. The relative long coastline and multiple large ocean basins, enables the predominance of Kelvin waves and their interference under all conditions. Extensive regions characterized by relatively high tides develop along the coastlines, extending

far into the open oceans. The coastlines situated at mid to high latitudes facilitate the propagation of diurnal tides as Kelvin waves within oceanic regions, where Poincaré waves are excluded.

Along the substantial shorter coastline of the paleo land-water distributions, the tidal propagation remains predominantly influenced by Kelvin waves. In the nearly hemispherical oceans, dispersive Poincaré waves dominate around the equator. This phenomenon enable the tides to respond more dynamically to tidal force and day length ~620 Myr ago. The occurrence and intensity of regions with relatively high tidal amplitudes for the M_2 tides is greater in the open ocean than in coastal regions. For the K_1 tides they are almost comparable. The position of Rodinia around the South Pole in the land-water distributions ~630 Myr and ~600 Myr ago allows Kelvin waves and their interference with relatively high M_2 and K_1 tides in the two associated extensive ocean basins at mid to high southern latitudes. In general, the M_2 and K_1 tides for the land-water distributions ~630 Myr and ~600 Myr ago exhibit greater stability in response to the paleo-conditions compared to the land-water distribution ~750 Myr ago.

In conjunction with the evaluation of the two-depth distribution for modern conditions, the tidal oscillation systems of the paleo land-water distributions are considered robust against more realistic depth distributions. Nevertheless, it must be acknowledged that the tidal amplitudes have been found to be underestimated.

5.2. Tidal regime type

The impact of the paleotidal forces and the paleoday length on the type of tidal regime for the modern and the paleo land-water distributions is shown in Figures 5.5 and 5.6 using the form factor (Section 2.2.4.4). The tidal regime type is predominantly semi-diurnal to mixed, mainly semi-diurnal. For the paleo land-water distributions to an even larger extent than for the modern land-water distribution (Section 2.2.4.4). Regions exhibiting a semi-diurnal tidal regime are present in all land-water distributions, particularly within the low latitudes surrounding the equator (Figures 5.1 and 5.2). In accordance with the spatial distribution of tidal amplitudes for the semi-diurnal and diurnal tides (Figures 5.1 and 5.2 and Figures 5.3 and 5.4, respectively), regions characterized by mixed, mainly diurnal to diurnal nature, are predominantly located along the coastlines or shelf edges. These diurnal regions demonstrate a decrease in both size and extent in the paleo land-water distributions relative to their modern counterparts, attributable to the much shorter coastlines.

In the modern land-water distribution, regions exhibiting one of the two diurnal tidal regimes demonstrate a moderate decline in intensity and extent with decreasing day length (Figures 5.5a, 5.5c, 5.5e and 5.5g). In contrast, these regions demonstrate amplification in response to the paleotidal force. The tidal regime for the land-water distribution ~750 Myr ago exhibits a contrasting behavior (Figures 5.5b, 5.5d, 5.5f and 5.5h). A comparable behavior is evident by the tidal regimes of the land-water distribution ~630 Myr and ~600 Myr ago (Figure 5.6), with the exception that, for the land-water distribution ~630 Myr ago, the shorter day length of the modern tidal forces results in an augmentation of the regions exhibiting both diurnal types (Figure 5.6c).

The tidal regime for the region of the Elatina Formation (Section 4.2.2 and Figure 4.2)

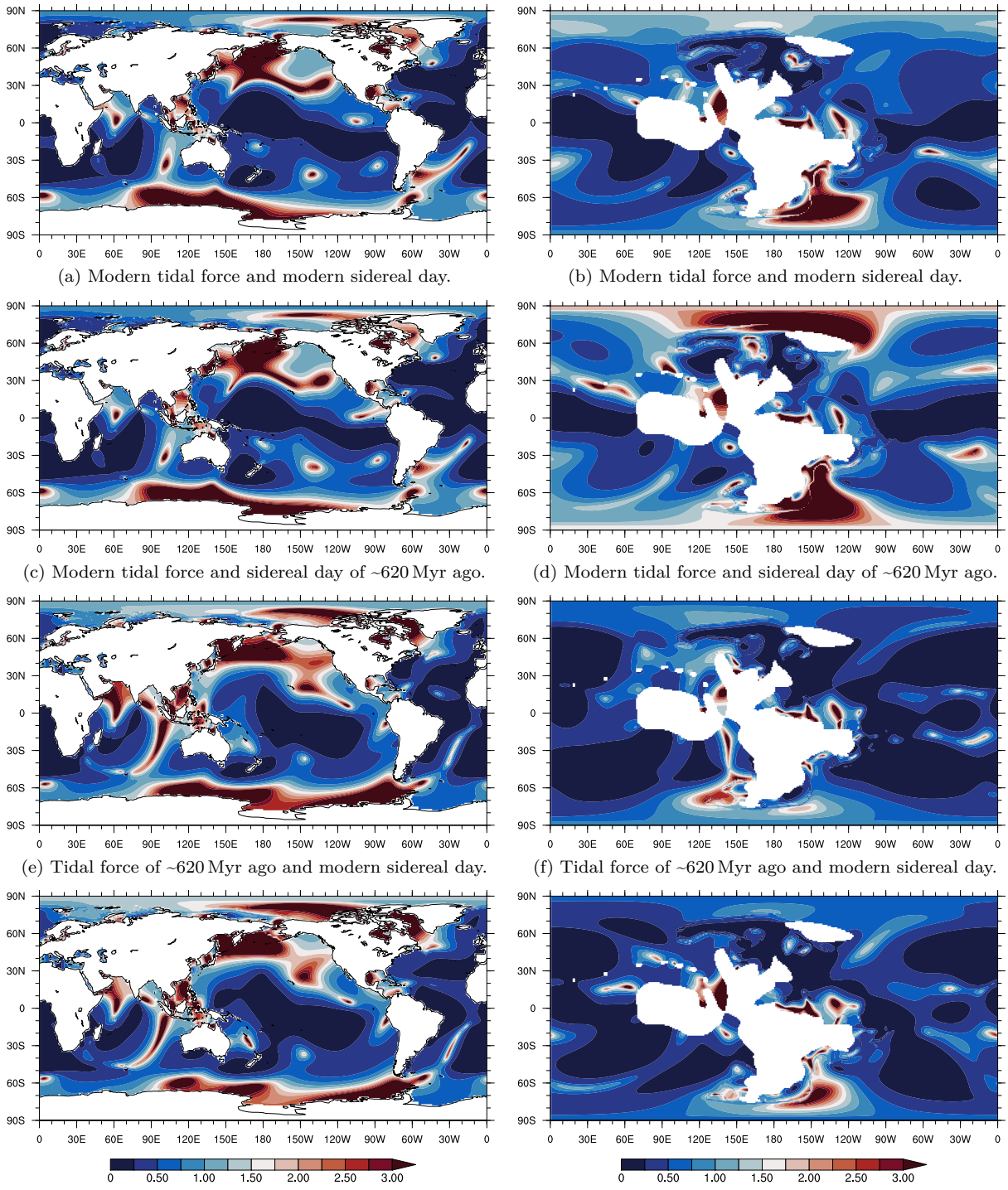

(a) Modern tidal force and modern sidereal day.

(b) Modern tidal force and modern sidereal day.

(c) Modern tidal force and sidereal day of ~620 Myr ago.

(d) Modern tidal force and sidereal day of ~620 Myr ago.

(e) Tidal force of ~620 Myr ago and modern sidereal day.

(f) Tidal force of ~620 Myr ago and modern sidereal day.

(g) Tidal force and sidereal day of ~620 Myr ago.

(h) Tidal force and sidereal day of ~620 Myr ago.

Figure 5.5.: Form factors for land-water distribution of modern times (left column) and ~750 Myr ago (right column) with the two-depth distribution. Where the tidal regime type is semi-diurnal at $F < 0.25$, mixed mainly semi-diurnal at $0.25 \geq F < 1.5$, mixed mainly diurnal at $1.5 \geq F < 3.0$, and diurnal at $F \geq 3.0$.

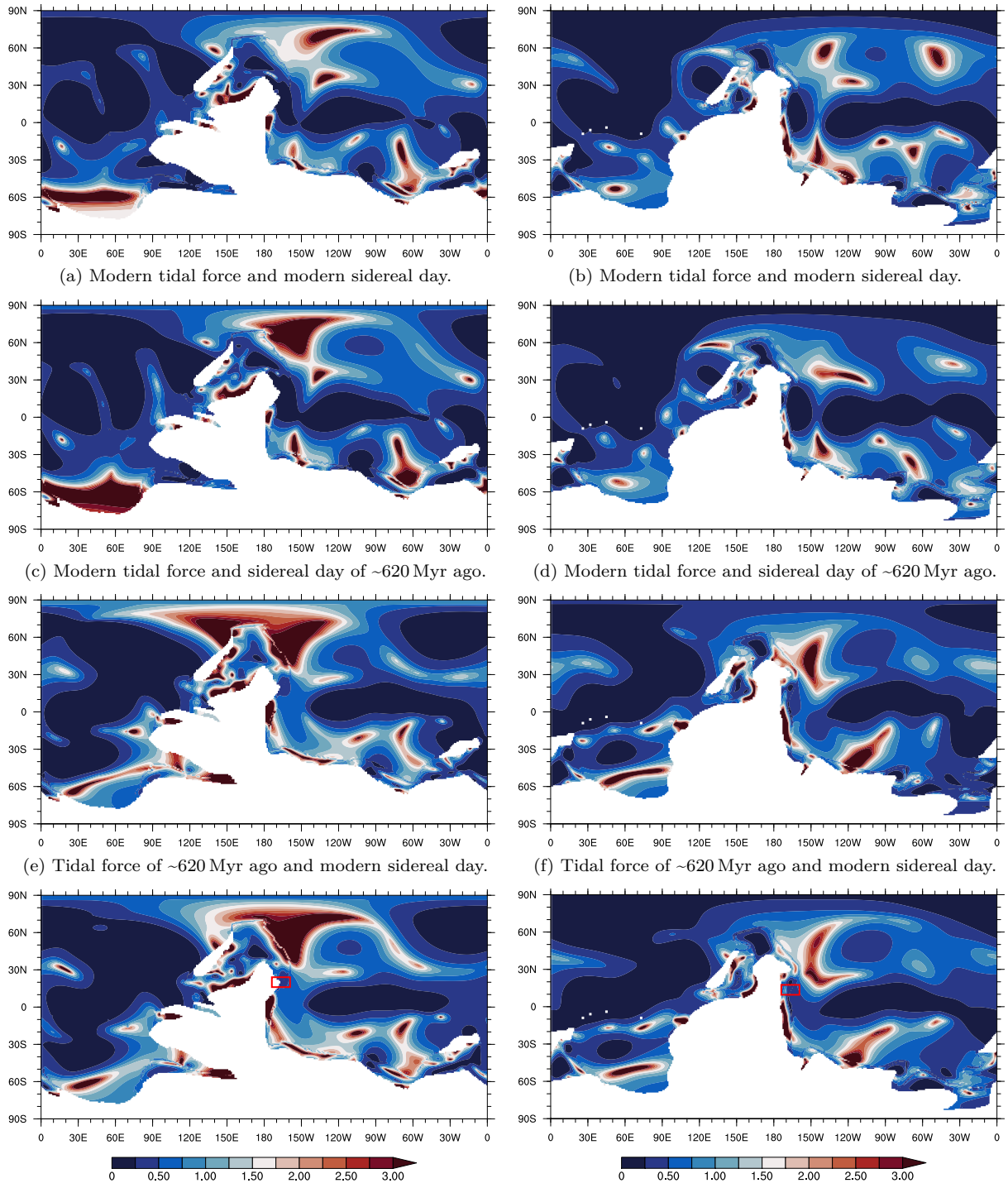

(a) Modern tidal force and modern sidereal day.

(b) Modern tidal force and modern sidereal day.

(c) Modern tidal force and sidereal day of ~620 Myr ago.

(d) Modern tidal force and sidereal day of ~620 Myr ago.

(e) Tidal force of ~620 Myr ago and modern sidereal day.

(f) Tidal force of ~620 Myr ago and modern sidereal day.

(g) Tidal force and sidereal day of ~620 Myr ago.

(h) Tidal force and sidereal day of ~620 Myr ago.

Figure 5.6.: Form factors for land-water distribution of ~630 Myr ago (left column) and ~600 Myr ago (right column) with the two-depth distribution. Where the tidal regime type is semi-diurnal at $F < 0.25$, mixed mainly semi-diurnal at $0.25 \geq F < 1.5$, mixed mainly diurnal at $1.5 \geq F < 3.0$, and diurnal at $F \geq 3.0$.

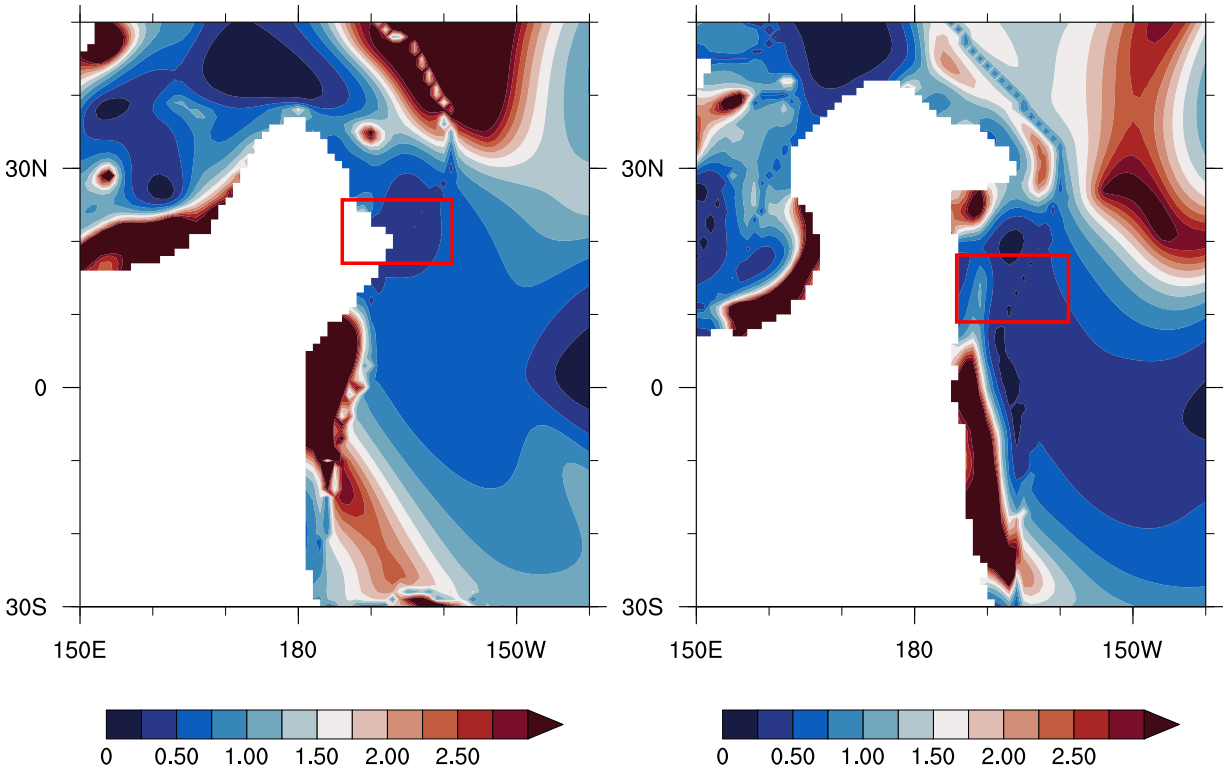

(a) Tidal force and sidereal day of ~620 Myr ago.

(b) Tidal force and sidereal day of ~620 Myr ago.

Figure 5.7.: Form factors for land-water distribution of ~630 Myr ago (left column) and ~600 Myr ago (right column) with the two-depth distribution. Where the tidal regime type is semi-diurnal at $F < 0.25$, mixed mainly semi-diurnal at $0.25 \geq F < 1.5$, mixed mainly diurnal at $1.5 \geq F < 3.0$, and diurnal at $F \geq 3.0$.

is indicated for the land-water distributions ~630 Myr ago and ~600 Myr ago by a red-outlined rectangle in Figures 5.6g and 5.6h for the tidal force and day length ~620 Myr ago. Figures 5.7a and 5.7b offer a more detailed representation of the region. The land-water distribution ~630 Myr ago shows a pronounced semi-diurnal tidal regime for the tidal force and day length from ~620 Myr ago, which transitions into a mixed mainly semi-diurnal regime. A comparable tidal regime emerges in the land-water distribution ~600 Myr ago. As Figure 5.7b shows, in this instance, the transition from the coastline and from the open ocean towards the edge of the narrow shelf (Figure 4.1c) is characterized by a shift from a mixed mainly semi-diurnal tidal regime towards a mixed mainly diurnal regime. The region of the Elatina Formation is surrounded by partially extensive diurnal tidal regimes (Figures 5.7a and 5.7b). Given the inherent uncertainties, the tidal regime is in relative good agreement with the sedimentation patterns of the Elatina Formation (Section 3.1.3), indicating a mixed semi-diurnal and diurnal tidal regime (Figures 3.2 and 3.3) with a trend towards a mixed, mainly semi-diurnal tidal regime (Figure 1.6). Inferences regarding the sedimentation potential of the tidal regime from the tidal range cannot be derived from the simulations (Section 4.5.2.3).

As shown in Figures 5.6e to 5.6h, the tidal regime for the region of the Elatina Formation is robust with respect to the day length in conjunction with the paleotidal force. This also

applies to the modern tidal force (Figures 5.6a to 5.6d), for which the tidal regime in the region of the Elatina Formation shows a tendency towards a semi-diurnal regime. To a lesser extent, the diurnal regimes persist in the vicinity.

The characteristic of the diurnal tides for the region of the Elatina Formation and further north and south of it can be considered stable and robust in terms of tidal force and day length. This finding is corroborated by the results presented in Section 5.1.3.3, on the K_1 tides, which are shown in Figure 5.4. The weakening of the tides in the region of the Elatina Formation due to the influence of the Rodinia protrusion on the Kelvin waves, independent of the changes in tidal force and day length, is considered to be relatively robust. The trapping effect at the equator warrants further examination, given the region's atypical, relatively extensive straight shelf edge, which intersects the equator perpendicular. However, it can be reasonably inferred that Kelvin waves with relatively moderate to high amplitudes are present in the region.

The profound impact of the semi-diurnal tides on the tidal regime within the Elatina Formation and the adjacent regions to the north and south for the modern tidal force is attributable to the pronounced Kelvin waves, as detailed in Section 5.1.2.3, and illustrated in Figures 5.2a to 5.2d for the M_2 tides. A divergent pattern emerges for the paleotidal force (Figures 5.2e to 5.2h), characterized by the Poincaré waves of the two northern waveguides that extend to the shelf edge. The Poincaré waves in the waveguides exhibit a high degree of strength, which contributes to the relative stability of the semi-diurnal tides in this region. The transition from Kelvin to Poincaré waves for the paleotidal force is further substantiated by the M_2 tides for the modern land-water distribution in the western North Pacific and North Atlantic (Figures 5.1e and 5.1g).

5.2.1. Summary

An analysis of the tidal regime types of the modern and paleo land-water distributions for tidal force and day length in modern times and ~620 Myr ago has been presented. The tidal regime type is predominantly semi-diurnal to mixed, mainly semi-diurnal. This is consistent with the tidal oscillation systems and applies to the paleo land-water distributions to a greater extent than to the modern land-water distribution. Due to their significantly reduced coastline, the diurnal tides are capable of propagating to a lesser extent as Kelvin waves. In the range of mid-to-high latitudes Poincaré waves are excluded as a propagation mechanism for diurnal tides.

The spatial distribution patterns for the different tidal forces and day lengths are generally comparable for the respective land-water distributions. However, these patterns may exhibit variations in their development and extent, ranging from the modern tidal force to the stronger paleotidal force with its shorter tidal period and from the modern day length to the shorter day length.

Accordingly, the first tidal investigation on the sedimentation patterns of the Elatina rhythmites has been conducted. Given the inherent uncertainties, the simulated tidal regimes for the Elatina Formation ~620 Myr ago have the potential to generate the sedimentation pattern characteristic of the Elatina rhythmites. The resolution of the simulations in conjunction with the two-depth distribution, as outlined in their evaluation, does not allow any conclusions to be drawn about the sedimentation potential of the tidal regime based on

the tidal range. However, Green et al. (2020) were able to identify a sufficient tidal range for sedimentation using tidal simulations.

5.3. Nominal tide and time-averaged global polar tidal torque

A quantitative relationship between a tidal oscillation system and its tidal torque, as a time-averaged global quantity, is provided by its nominal tide (Appendix C.1). The ocean tide coefficient is calculated using the amplitude and phase of the nominal tide. It is proportional to the tidal energy dissipation (Equations (2.53) and (2.54)) and the polar tidal torque (Section 2.3.2) as time-averaged global quantities in the ocean.

Figure 5.8 presents the nominal tides and ocean tide coefficients for the M_2 and K_1 tides as a function of tidal force and day length for the modern and paleo land-water distributions. The power supply by the partial tides and the polar tidal torques, as calculated by the simulations, are contrasted as global time averages. These quantities show a direct proportionality to the ocean tide coefficients (Figure 5.8a.3 to Figure 5.8a.5 and Figure 5.8b.3 to Figure 5.8b.5). The proportionality factor, which is contingent on the orbit of the tide-generating body and day length (e. g. Equation (2.54)), exhibits variability across different tidal forces and day lengths. Deviations may emerge due to how the quantities are computed. The time-averaged global balance quantities are determined during the simulation. Therefore, the calculation includes the harmonic and non-linear components of the tides (Section 4.3.1). The nominal tides and ocean tide coefficients are based on the harmonic component output by the simulations. However, the deviations are relatively minor. For instance, consider the M_2 paleotidal force with the modern day length for the land-water distribution ~750 Myr ago (Figure 5.8a.3 to Figure 5.8a.5). Further considerations are confined to the ocean tide coefficients and the time-averaged global polar tidal torques.

Sections 5.3.1 and 5.3.2 introduce the amplitudes and phases of the nominale tides. Section 5.3.3 discusses the ocean tide coefficients, along with the impact of the nominal tidal amplitudes and phases on them. Finally, Section 5.3.4 provides a quantitative analysis of the time-averaged global polar tidal torques.

5.3.1. Nominal tidal amplitude

The nominal tidal amplitude is defined as one of the spherical expansion coefficients of the harmonic component of the tidal sea surface topographies (Appendix C.1). It is directly related to the spatial distribution pattern and magnitude of the global tides. The resonance proximity of tidal propagation exerts the predominant influence on the development of the nominal tidal amplitudes in relation to the paleotidal force and paleoday length (Figure 5.8a.1 and Figure 5.8b.1). The spatial distribution patterns for the M_2 and K_1 tides remain virtually unchanged under all conditions for the individual land-water distributions (Section 5.1.4). Due to the comparable tidal oscillation systems for the similar land-water distributions ~630 Myr and ~600 Myr ago (Sections 5.1.2.3 and 5.1.3.3), the resulting nominal tidal amplitudes are nearly identical (Figure 5.8a.1 and Figure 5.8b.1).

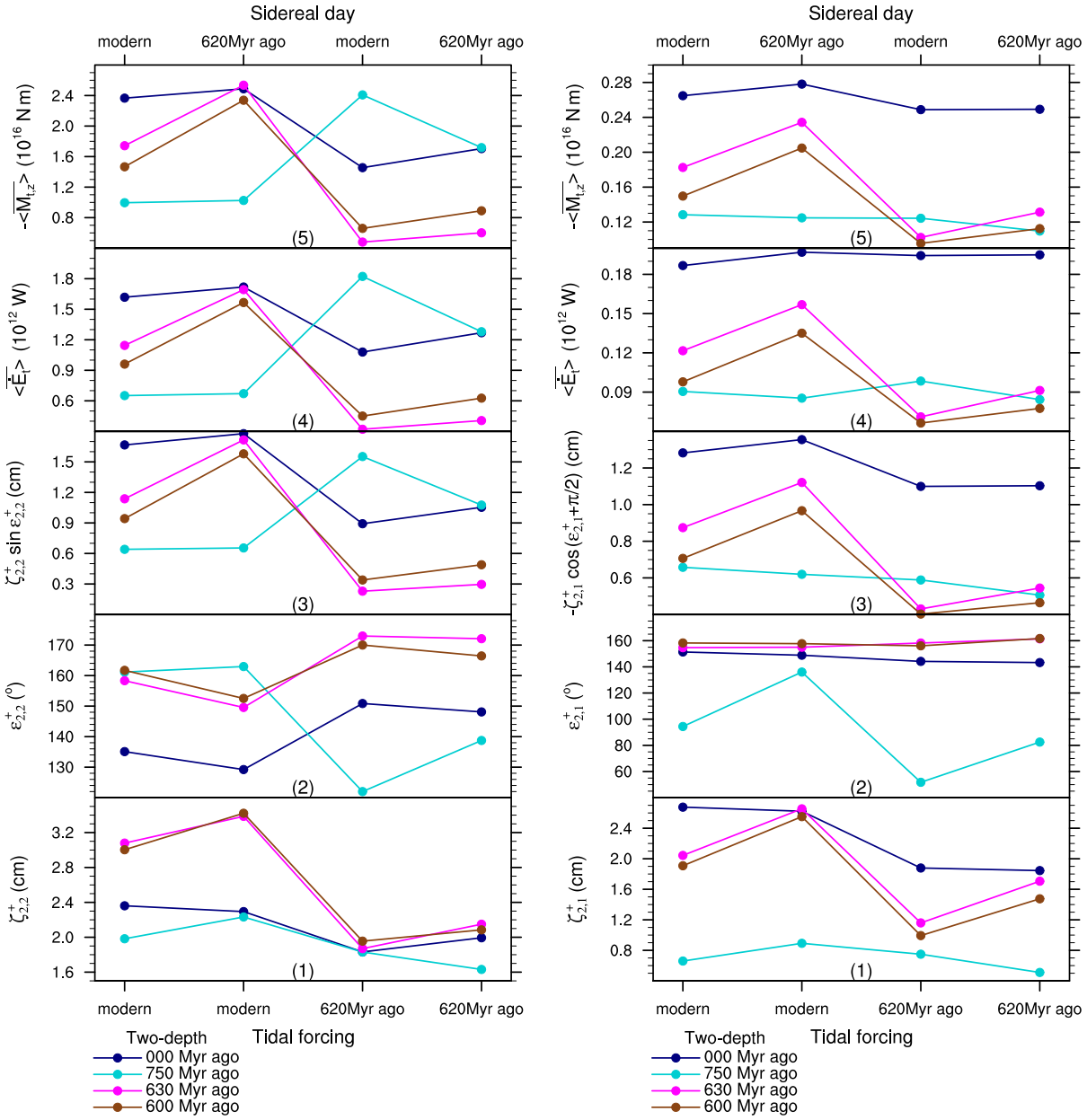

(a) M_2 tides. (b) K_1 tides.

Figure 5.8.: M_2 (a) and K_1 (b) nominal tidal amplitude ζ_{st}^{+} in cm (1), nominal tidal phase ϵ_{st}^{+} in ° (2), its contribution $\zeta_{22}^{+} \sin \epsilon_{22}^{+}$ and $\zeta_{21}^{+} \cos\left(\epsilon_{21}^{+} + \pi/2\right)$ in cm (3), respectively, to energy dissipation as global temporal average by the work method (Equations (2.53) and (2.54)), power supply $\langle \overline{\dot{E}_t} \rangle$ by the partial tides in W (4) and the polar tidal torque $\langle \overline{M_{t,z}} \rangle$ in N m (5) as global temporal averages as a function of the tidal force for modern times and ~620 Myr ago (bottom x-axis) and the length of the sidereal day for modern times and ~620 Myr ago (top x-axis). The simulated quantities with the two-depth distribution of land and water for modern times, ~600 Myr, ~630 Myr, and ~750 Myr ago are shown.

The sequence of regions exhibiting relatively high modern M_2 tides surrounding the equator within the nearly hemispherically open ocean for the land-water distribution ~630 Myr and ~600 Myr ago (Section 5.1.2.3) yields the most significant nominal tidal

amplitudes (Figure 5.8a.1). In contrast, the relatively extensive regions with comparatively high amplitudes for the modern land-water distribution (Section 5.1.2.1), which can extend across all latitudes due to the dispersed location of the continents, result in nominal tidal amplitudes that are up to about 50 % smaller (Figure 5.8a.1). Due to the greater decrease in tidal amplitudes for the paleotidal force for the land-water distribution ~630 Myr and ~600 Myr ago relative to the modern land-water distribution (Sections 5.1.2.1 and 5.1.2.3) the nominal tidal amplitudes are approaching each other (Figure 5.8a.1). Despite the presence of regions exhibiting comparable high tidal amplitudes for the land-water distribution ~750 Myr ago (Section 5.1.2.2), it yields the lowest nominal tidal amplitudes (Figure 5.8a.1). However, due to their geographical location, a significant number of these regions contribute only to a reduced or negligible extent to the nominal tidal amplitude.

For the K_1 tides, the highest nominal tidal amplitudes occur for the modern land-water distribution (Figure 5.8b.1). The basis is that the regions with relatively high amplitudes are located in mid-to-high latitudes and are relatively extensive (Section 5.1.3.1). Regions that are predominantly located in mid-to-high latitudes and that exhibit comparable tidal amplitudes for the land-water distribution ~630 Myr and ~600 Myr (Section 5.1.3.3) result in significantly lower to comparable nominal tidal amplitudes (Figure 5.8b.1). The nominal tidal amplitudes for the land-water distribution ~750 Myr ago are the lowest (Figure 5.8b.1) due to the sparse regions with relatively high tidal amplitudes along the coastline of Rodinia and relatively high tidal amplitudes in the equatorial waveguides (Section 5.1.3.2)

The paleotidal force in conjunction with the paleoday length results in a decrease of the nominal tidal amplitudes by about 15 %, 18 % and 30 %, and 31 % for the M_2 tides (Figure 5.8a.1) and by about 31 %, 23 %, 17 %, and 23 % for the K_1 tides (Figure 5.8b.1) of the land-water distributions in modern times and ~750 Myr, ~630 Myr and ~600 Myr ago, respectively. With regard to the land-water distribution in modern times and ~630 Myr and ~600 Myr ago, the nominal amplitudes respond more strongly to the paleotidal force than to the paleoday length (Figure 5.8a.1 and Figure 5.8b.1). The decreasing resonance of the tides in terms of magnitude (Sections 5.1.2.1, 5.1.2.3, 5.1.3.1 and 5.1.3.3) is evident.

In the context of the land-water distributions ~630 Myr and ~600 Myr ago, notable increases in nominal amplitude are observed for the paleoday length (Figure 5.8a.1 and Figure 5.8b.1), attributable to the enhanced resonance proximity of the tides. For M_2 tides, their propagation as dispersive Poincaré waves surrounding the equator in the nearly hemispherical ocean (Section 5.1.2.3) is contingent on the day length (LeBlond & Mysak, 1978). With regard to K_1 tides, the underlying region is located west of the shelf connection between the island and Rodinia, between the two ocean basins in the southern ocean (Section 5.1.3.3). However, within a global context, the tidal propagation manifests as Kelvin waves. Due to the configuration of the shelf edge, it is inevitable that reflection will occur, which must be associated with other wave types, such as Poincaré waves (Section 2.2.4.3).

The nearly complete absence of response to the paleoday length of the M_2 and K_1 tides for the modern land-water distribution (Figure 5.8a.1 and Figure 5.8b.1, respectively) can be attributed to the predominant tidal propagation as non-dispersive Kelvin waves (Section 5.1.2.1 and Section 5.1.3.1, respectively). The relatively high contribution of Poincaré waves to the propagation of M_2 and K_1 tides for the land-water distribution ~750 Myr ago (Sections 5.1.2.2 and 5.1.3.2) can imply that the nominal amplitude is no

less sensitive to the day length than to the tidal force and period (Figure 5.8a.1 and Figure 5.8b.1).

The tidal propagation processes between the M_2 and K_1 tides are relatively comparable for the individual land-water distributions (Section 5.1). As a result, there is a potential for an analogous response of the nominal tidal amplitude to the paleotidal force and the paleoday length between the M_2 and K_1 tides (Figure 5.8a.1 and Figure 5.8b.1, respectively).

5.3.2. Nominal tidal phase

The nominal tidal phase denotes one of the spherical expansion coefficients of the harmonic component of the tidal sea surface topography (Section 2.2.4.3). It is directly related to the propagation processes and temporal characteristics of the global tides. The propagation processes of the M_2 and K_1 tides demonstrate a high degree of independence from the tidal force and the day length for the individual land-water distributions. Additionally, a parallel can be drawn between the M_2 and K_1 tides. The propagation processes of tides are largely governed by the individual land-water distributions (Section 5.1).

The nominal tidal phases of the M_2 and K_1 tides for all land-water distributions are confined to the second quadrant (Figure 5.8a.2 and Figure 5.8b.2, respectively). However, an exception to this pattern emerges for the land-water distribution ~750 Myr ago, where the K_1 tides of the paleotidal force exhibit phases in the first quadrant (Figure 5.8b.2). The comparable tidal oscillation systems, evidenced by the similar land-water distributions ~630 Myr and ~600 Myr ago (Sections 5.1.2.3 and 5.1.3.3), yield nearly identical nominal tidal phases (Figure 5.8a.2 and Figure 5.8b.2). Furthermore, the nominal tidal phases for the modern land-water distribution are consistently smaller by about 20° for the M_2 tides (Figure 5.8a.2) and up to about 20° for the K_1 tides (Figure 5.8b.2) relative to those for the land-water distributions ~630 Myr and ~600 Myr ago. This phenomenon can be attributed, at least in part, to the presence of overlapping propagation processes (Section 5.1).

For the land-water distribution ~750 Myr ago, the nominal phase of the M_2 (Figure 5.8a.2) and K_1 tides (Figure 5.8b.2) demonstrates a relatively substantial range. Specifically, the marked increases in the nominal tidal phases in response to the paleoday length at the same tidal force, as detailed in Section 5.1.1, can be attributed to the enhanced prevalence of Poincaré waves in tidal propagation under all conditions (Section 5.1.2.2; Section 5.1.3.2). Conversely, the paleotidal force characterized by a shorter tidal period at the same day length result in analogous decrease in the phases.

For the land-water distribution in modern times, ~630 Myr and ~600 Myr ago, the nominal tidal phases of the M_2 (Figure 5.8a.2) and K_1 tides (Figure 5.8b.2) show relatively minor fluctuations in response to paleoday length at the same tidal force. According to Section 5.1.1, this can be attributed for the modern land-water distribution to the predominant tidal propagation as non-dispersive Kelvin waves under all conditions (Sections 5.1.2.1 and 5.1.3.1). The Poincaré waves that occur at paleotidal force in the propagation of the M_2 tides in the North Pacific exhibit minor fluctuations between the modern and paleoday length (Section 5.1.2.1). However, with the advent of Poincaré waves, there is a notable increase in the nominal tidal phase in response to the paleotidal force (Figure 5.8a.2).

With regard to the land-water distribution ~630 Myr and ~600 Myr ago, Kelvin waves in the propagation of the M_2 tides are accompanied by interfering Poincaré waves around

the equator (Section 5.1.2.3). Both exhibit slight fluctuations in phase in response to the paleoday length, while the tidal force remains the same. The propagation of the K_1 tides exhibits a predominant influence from Kelvin waves (Section 5.1.3.3), and even the response to the paleotidal force results in minor fluctuations in the nominal tidal phase (Figure 5.8b.2). This phenomenon also pertains to modern land-water distribution.

5.3.3. Ocean tide coefficient

The absolute ocean tide coefficients are subject to a range of values, depending on the nominal tidal phase, with a maximum value equal to the nominal tidal amplitude (Figure 5.8a.3 and Figure 5.8b.3). The nominal tidal phases of the M_2 and K_1 tides for all land-water distributions are confined to the second quadrant (Figure 5.8a.2 and Figure 5.8b.2, respectively). As the phase increase, the absolute ocean tide coefficients approach zero and converge toward the nominal tidal amplitude as the phase decrease. The opposite applies to the land-water distribution ~750 Myr ago for the K_1 tides of the paleotidal force at phases in the first quadrant (Figure 5.8b.2). In particular, the nominal tidal phases around 170° of the M_2 tides ~620 Myr ago (Figure 5.8a.2) and around 160° of the K_1 tides (Figure 5.8b.2) for the land-water distributions ~630 Myr and ~600 Myr ago, demonstrate a clear reduction in the contribution of the nominal tidal amplitude to the ocean tide coefficient by the nominal tidal phase. In contrast, the contribution attains a near-maximal level for the land-water distribution ~750 Myr ago for the K_1 tides (Figure 5.8b.2) with phases approaching 90° for the modern tidal force and day length and for the tidal force and day length ~620 Myr ago.

In general, the paleo land-water distributions result in significantly lower absolute ocean tide coefficients in comparison to the modern land-water distribution (Figure 5.8a.3 and Figure 5.8b.3). For the M_2 tides (Figure 5.8a.3), the coefficients for the modern land-water distribution can be attained and even exceeded by those for the paleo land-water distributions. With the exception of the land-water distribution ~750 Myr ago, the stronger tidal force, characterized by a shorter period, ~620 Myr ago, results in a substantial decline in the absolut ocean tide coefficients for the M_2 and K_1 tides (Figure 5.8a.3 and Figure 5.8b.3, respectively).

For the similar land-water distributions ~630 Myr and ~600 Myr ago, the nominal tides are nearly identical. However, slight discrepancies in nominal tidal phases can lead to a divergence of up to about 40 % in the ocean tide coefficients of the M_2 tide. For the K_1 tides, the ocean tide coefficients exhibit a maximum discrepancy of about 23 %, attributable to minute variations in the nominal tidal amplitude. Nevertheless, the magnitude of the ocean tide coefficients remains unaltered.

The following discourse pertains to an examination of the ocean tide coefficients of the M_2 and K_1 tides in regard to tidal forcing in modern times (Sections 5.3.3.1 and 5.3.3.3, respectively) and ~620 Myr ago (Sections 5.3.3.2 and 5.3.3.4, respectively).

5.3.3.1. M_2 tidal forcing of modern times

The modern M_2 tides yield the highest ocean tide coefficients for the modern land-water distribution (Figure 5.8a.3). In conjunction with the modern day length, the ocean tide coefficients for the land-water distributions ~750 Myr, ~630 Myr, and ~600 Myr ago are

about 38 %, 68 %, and 57 % of the coefficient for the modern land-water distribution. As the day length decreases, the coefficients increase, with the exception of the nearly constant coefficient for the land-water distribution ~750 Myr ago.

The substantial increases for the land-water distributions ~630 Myr and ~600 Myr ago at the paleoday length are attributable to the considerable increases in the already highest nominal tidal amplitudes (Figure 5.8a.1). This is accompanied by a relatively minor decrease in the nominal tidal phases (Figure 5.8a.2) within a phase range where minor fluctuations correspond to a relative substantial change in the ocean tide coefficient. Both phenomena can be explained by the tidal propagation as Poincaré waves in the equatorial waters of the nearly hemispherical oceans (Section 5.1.2.3). The shorter day length ~620 Myr ago results in increased interference. Relatively large regions with relatively high tidal amplitudes in equatorial waters strengthen, while the tidal phases slightly decrease. Consequently, the contribution of the nominal tidal amplitude to the ocean tide coefficient is less attenuated than it is at modern day length.

In the context of the modern land-water distribution at the paleoday length, a marginally higher coefficient is evident. The two tidal oscillation systems for the modern and the paleoday length are comparable on the basis of the predominant tidal propagation as non-dispersive Kelvin waves (Section 5.1.2.1). This results in a moderately reduced nominal tidal amplitude (Figure 5.8a.1) and tidal phase (Figure 5.8a.2) for the shorter paleoday length. The nominal tidal phases (Figure 5.8a.2) are smaller by about 23° than those for the land-water distributions ~630 Myr and ~600 Myr ago. This difference serves to reverse the difference to the considerably higher nominal tidal amplitudes (Figure 5.8a.1) for the land-water distributions ~630 Myr and ~600 Myr ago in the ocean tide coefficients (Figure 5.8a.3).

Despite the prevalence of Poincaré waves in the tidal propagation for the land-water distribution ~750 Myr ago (Section 5.1.2.2), the shorter day length ~620 Myr ago results only in a slightly larger nominal tidal phase (Figure 5.8a.2), accompanied by a relatively strong increase in the nominal tidal amplitude (Figure 5.8a.1). The slightly higher nominal tidal phase at above 160° for the shorter day length is sufficient to reduce the contribution of the nominal tidal amplitude to the coefficient almost in line with the coefficient for the longer modern day length.

5.3.3.2. M_2 tidal forcing of ~620 Myr ago

The remarks on the relationship between tidal propagation and ocean tide coefficients for the modern tidal force (Section 5.3.3.1) also apply to the tidal force ~620 Myr ago. The characteristics of the tidal oscillation systems for the respective land-water distributions are similar for the two tidal forces and day lengths (Section 5.1.2). However, these characteristics can vary significantly in development and extent.

For the tidal force and day length ~620 Myr ago, the ocean tide coefficients for the land-water distributions ~750 Myr, ~630 Myr, and ~600 Myr ago are 102 %, 28 %, and 46 % of the coefficient for the modern land-water distribution (Figure 5.8a.3). Relativ to the modern tidal force and day length, the coefficients for the land-water distribution in modern times, and ~750 Myr, ~630 Myr, and ~600 Myr ago are approximately 63 %, 168 %, 26 % and 52 %, respectively. Despite the lowest nominal tidal amplitudes (Section 5.3.1 and Figure 5.8a.1)

and due to the lowest nominal tidal phases (Section 5.3.2 and Figure 5.8a.2), the coefficient for the land-water distribution ~750 Myr ago ranges from the lowest coefficient for the modern tidal force to the highest coefficient for the tidal force ~620 Myr ago.

The paleoday length exerts an opposing influence to that of the paleotidal forcing on the ocean tide coefficients, attenuating its effects. The paleotidal force results in a damping, and the paleoday length results in an increase in the ocean tide coefficients for the land-water distribution in modern times and ~630 Myr and ~600 Myr ago. A divergent pattern emerges in the land-water distribution ~750 Myr ago, marked by a substantial increase in the ocean tide coefficients for the paleotidal force and a considerable decrease for the paleoday length at the paleotidal force.

The decreasing interference of the Kelvin and Poincaré waves at the paleotidal force, which have significantly reduced tidal amplitudes for the land-water distributions ~630 Myr and ~600 Myr ago (Section 5.1.2.3), can clearly seen in the nominal tidal amplitudes (Section 5.3.1 and Figure 5.8a.1). In addition, the nominal tidal phases are increasing (Section 5.3.2 and Figure 5.8a.2). Together, these two factors cause the coefficients to drop sharply (Figure 5.8a.3). In the context of the modern land-water distribution for the paleotidal force, the occurrence of Poincaré waves characterized by relatively moderate amplitudes in the North Pacific (Section 5.1.2.1) can be associated with the smaller nominal tidal amplitudes (Section 5.3.1 and Figure 5.8a.1) and larger nominal tidal phases (Section 5.3.2 and Figure 5.8a.2). Consequently, the coefficients undergo a substantial reduction.

5.3.3.3. K_1 tidal forcing of modern times

The modern K_1 tides yield the highest absolute ocean tide coefficients for the modern land-water distribution (Figure 5.8b.3). In conjunction with the modern day length, the absolute ocean tide coefficients for the land-water distributions ~750 Myr, ~630 Myr, and ~600 Myr ago are about 51 %, 68 %, and 55 % of the coefficient for the modern land-water distribution. The response of the absolute coefficients to the shorter paleoday length is comparable to that observed with the modern M_2 tidal force (Section 5.3.3.1). The absolute coefficients exhibit an increase as the day length undergoes a decrease, with the exception of the absolute coefficient for the land-water distribution ~750 Myr ago, which remains relatively constant.

The tidal propagation processes for the respective land-water distributions related to the modern M_2 tidal force can largely be transferred (Sections 5.1.2 and 5.1.3). This also pertains to the remarks concerning the coefficients associated with the modern M_2 tides (Section 5.3.3.1). However, the contribution of Kelvin waves to the tidal propagation increases because Poincaré waves are excluded from the propagation of diurnal tides in the mid-to-high latitudes.

5.3.3.4. K_1 tidal forcing of ~620 Myr ago

The highest absolute ocean tide coefficients are found for the modern land-water distribution at the tidal force of ~620 Myr ago (Figure 5.8b.3). In conjunction with the shorter day length ~620 Myr ago, the absolute ocean tide coefficients for the land-water distributions ~750 Myr, ~630 Myr, and ~600 Myr ago are about 46 %, 49 %, and 42 % of the modern absolute coefficient, respectively. In relation to the modern tidal force and day length, the absolute ocean

tide coefficients for the land-water distributions in modern times and ~750 Myr, ~630 Myr and ~600 Myr ago are approximately 86 %, 77 %, 62 %, 66 %, respectively (Figure 5.8b.3). As with the M_2 paleotidal force (Figure 5.8a.3), the absolute coefficients for the land-water distribution in modern times and ~630 Myr and ~600 Myr ago decrease significantly. The absolute coefficient associated with the land-water distribution ~750 Myr ago exhibits minimal variation instead of undergoing a substantial increase.

The paleoday length counteracts the paleotidal force, thereby weakening its effect on the absolute ocean tide coefficients for the land-water distribution in modern times and ~630 Myr and ~600 Myr ago. The paleotidal force results in a damping, and the paleoday length results in an increase in the absolute coefficients. The situation is different for the land-water distribution ~750 Myr ago, where the absolute coefficient for the paleotidal force and paleoday length decrease slightly.

The development of the ocean tide coefficients for the tidal force ~620 Myr ago (Figure 5.8b.3) is analogous to that for the M_2 tides (Figure 5.8a.3). Moreover, the tidal propagation processes for the respective land-water distributions relative to M_2 tidal force can be predominantly transferred as outlined in Sections 5.1.2 and 5.1.3. Given the exclusion of Poincaré waves from the propagation of diurnal tides in the mid-to-high latitudes, the contribution of Kelvin waves to the propagation increases. In summary, the remarks provided on the coefficients in relation to the M_2 tidal force ~620 Myr ago can be adopted. However, the value ranges of the nominal tidal amplitudes (Figure 5.8b.1) and phases (Figure 5.8b.2) for the individual land-water distributions are established such that the coefficient for the land-water distribution ~750 Myr ago is nearly equal to the coefficients for the land-water distributions ~630 Myr and ~600 Myr ago (Figure 5.8b.3). Notably, it does not surpass the coefficient for the modern land-water distribution, as is observed for the M_2 tides.

5.3.4. Time-averaged global polar tidal torque

The development of the ocean tide coefficients (Section 5.3.3) derived from the nominal tides (Sections 5.3.1 and 5.3.2) for the individual land-water distributions as a function of tidal force and day length in modern times and ~620 Myr ago can be applied to the simulated time-averaged global polar tidal torques (Figure 5.8a.3 and Figure 5.8a.5 for M_2 tides and Figure 5.8b.3 and Figure 5.8b.5 for K_1 tides). The coefficients reflect the impact of the harmonic component of the tides, and the torques consider the impact of both harmonic and non-linear components. Therefore, the deviations between the two allow the impact of the non-linear components to be estimated. Subsequently, the torques are discussed quantitatively, and their deviations from the coefficients are evaluated.

The M_2 and K_1 tides of the individual land-water distributions exhibit a negative time-averaged global polar tidal torque for tidal force and day length in modern times and ~620 Myr ago (Figure 5.8a.5 and Figure 5.8b.5, respectively). This results in a decrease in the Earth rotation rate. The most significant time-averaged global polar tidal torque of the modern M_2 tides at the modern day length is -2.37×10^{16} N m, and it is determined for the modern land-water distribution (Figure 5.8a.5). The torques associated with the land-water distributions ~750 Myr, ~630 Myr, and ~600 Myr ago are estimated to be about 42 %, 73 %, and 62 % of the torque for the modern land-water distribution.

Conversely, for the M_2 tides and the day length ~620 Myr ago, the most significant torque of -1.72×10^{16} N m is obtained for the land-water distribution ~750 Myr ago, exhibiting an increase of approximately 172 %. This is closely followed by the torque of -1.70×10^{16} N m for the modern land-water distribution, with a decrease of about 28 %. The weakest torques are calculated with a decrease of about 66 % and 40 % for the land-water distributions ~630 Myr and ~600 Myr ago, respectively. This is in the order of magnitude of the torques for the K_1 tides (Figure 5.8b.5) The ratio of the torques for the land-water distributions ~750 Myr, ~630 Myr, and ~600 Myr ago to the torque for the modern land-water distribution significantly changes to about 101 %, 35 %, and 52 %, respectively.

The time-averaged global polar tidal torques of modern K_1 tides at modern day length are, in general, one order of magnitude smaller than those of M_2 tides (Figure 5.8b.5 and Figure 5.8a.5, respectively). In the context of the land-water distributions ~750 Myr, ~630 Myr, and ~600 Myr ago, the torques are estimated to be about 50 %, 69 %, and 58 % of the torque for the modern land-water distribution (Figure 5.8b.5). For the K_1 tidal force and day length ~620 Myr ago, the torques decrease to about 96 %, 85 %, 72 %, and 73 % of the torques in relation to modern tidal force and day length for the land-water distributions in modern times and ~750 Myr, ~630 Myr, and ~600 Myr ago, respectively. Conversely, the absolute changes are comparatively minimal. However, for the paleo land-water distributions, the torques are about 44 % to 52 % of those for the modern land-water distribution. These ratios are closely related to the land-water distribution. The propagation of K_1 tides is associated with the potential for Kelvin waves to manifest. Poincaré waves are confined to the latitude range of about $-30°$ to $30°$ in regard to the propagation of diurnal tides. In comparison to the modern land-water distribution, with continents dispersed across all latitudes and a comparatively extensive coastline, the paleo land-water distributions by the supercontinent Rodinia offer only limited potential for the propagation of diurnal tides.

In comparison with the ocean tide coefficients (Section 5.3.3), the torques typically respond to the tidal force and day length ~620 Myr ago by approximately 5 % less. The observed peaks are 1 % and 11 % less, respectively. It can be stated that the majority of the torques' response is attributable to the harmonic component of the tides. A more thorough investigation is beyond the scope of the present study.

An evaluation of the time-averaged global polar tidal torques associated with the paleo land-water distributions can be made in accordance with Equation (2.8) based on the evolution of the rate of change of days per year, as outlined by Deines and Williams (2016). The relatively high rate of change exhibited in Figure 1.1 for the period approximately ~750 Myr ago nearly corresponds to the modern rate. De Azarevich and Azarevich (2017) have found that it may have been even higher at this time. A notable inflection point is evident at around ~620 Myr ago. Assuming a continuous progression, a steady decline from approximately 456 d per year around ~850 Myr ago to approximately 400 d per year around ~620 Myr ago, followed by a relatively rapid increase (Figure 1.1).

The torques for tidal force and/or day length ~620 Myr ago, in conjunction with the land-water distribution ~750 Myr ago, lend support to the observational data to a limited extent. This distribution can be associated with a comparable rate of change, albeit with high variance, for tidal force and/or day length ~620 Myr ago relative to the modern rate of change. Given the relatively high rates of change between ~850 Myr and ~750 Myr ago, it is reasonable to infer that the tidal period and day length between ~750 Myr and ~620 Myr

ago have increased in a similar way to how they did between ~620 Myr ago and modern times.

The inflection point, associated with relatively weak rates of change in its vicinity, is supported by the torques for the tidal force and day length ~620 Myr ago, and their variance. As discussed in Sections 5.1.2.3 and 5.1.3.3, the comparable tidal oscillation systems ~620 Myr ago for the similar land-water distributions ~630 Myr and ~600 Myr ago demonstrate a stability of the tidal oscillation systems and the derived quantities, such as the torque, despite the potential tectonic activity during this period. Both the global and zonally integrated distributions and characteristics of the tidal torques per water column are comparable, as is the case for the tidal oscillation systems. A pivotal factor in this regard is the tidal propagation driven by Kelvin waves, characterized by a propagation velocity which remains unaffected by the tidal period and day length. Due to the location around the South Pole, in contrast to the land-water distribution ~750 Myr ago, the formation of ocean basins is possible, which can result in increased tidal propagation as Kelvin waves (Sections 5.1.2.3 and 5.1.3.3).

Furthermore, as discussed in Appendix D.1 and Section 5.4, the decrease in day length following the inflection point ~620 Myr ago in the observed data (Figure 1.1) cannot be rule out.

5.3.5. Summary

The development of the nominal amplitudes and phases of the M_2 and K_1 tides in relation to tidal force and day length in modern times and ~620 Myr ago has been investigated for the modern and paleo land-water distributions. They are consistent with the response of the tidal oscillation system for the individual land-water distributions. The nominal tidal amplitude for the modern conditions exhibits a substantial decrease for the individual land-water distributions under the conditions ~620 Myr ago. The nominal tidal phases are confined to the second quadrant. With the exception of the land-water distribution ~750 Myr ago, for which the K_1 tidal force ~620 Myr ago exhibits phases in the first quadrant.

The tidal propagation characterized by Kelvin waves for the land-water distributions in modern times and ~630 Myr and ~600 Myr ago is reflected in nominal tidal amplitudes and phases that hardly respond to the day length. Conversely, pronounced responses to tidal force can occur. Additional Poincaré waves and their interference in the nearly hemispherically open oceans ~630 Myr and ~600 Myr ago, can result in substantial responses. The nature of the response exhibits a high degree of similarity between the land-water distributions. For the similar land-water distributions ~630 Myr and ~600 Myr ago, the nominal tides are nearly identical. With respect to the land-water distribution ~750 Myr ago, the tidal propagation is dominated by Poincaré waves, as reflected in the relatively strong, opposite responses of the nominal tidal phase to the tidal force and day length. In all conditions, the lowest nominal tidal amplitudes with minimal fluctuations are achieved.

Subsequently, a discussion of the ocean tide coefficients derived from the nominal tides followed. These correspond to the harmonic component of the tides. The simulated time-averaged global polar tidal torques are comparable to the ocean tide coefficients. They incorporate the harmonic and non-linear components of the tides. The deviations are typically within the range of 5 %. In all conditions, the torques result in a deceleration of

the Earth's rotation rate for the modern and the paleo land-water distributions.

In general, the torques for the paleo land-water distributions correspond to 35 % to 73 % of the torque for the modern land-water distribution. Using the land-water distribution ~750 Myr ago, the strongest torque is achieved with 101 % of the torque for the modern land-water distribution for the M_2 tidal force and the day length ~620 Myr ago. In the context of the ocean tide coefficients, this is due to the lowest nominal tidal phase occurring at the lowest nominal tidal amplitude. A counterexample is demonstrated by the land-water distributions ~630 Myr and ~600 Myr ago, in which a high nominal tidal phase at high nominal tidal amplitude yields a low coefficient.

The paleotidal force causes the torques to weaken relatively strongly for the land-water distributions in modern times and ~630 Myr and ~600 Myr ago. The paleoday length associated with the tidal force in modern times and ~620 Myr ago results in less strong strengthening of the torques, thereby weakening the impact of the paleotidal force. In the context of the coefficients, this is derived from a comparable development of the nominal tidal amplitudes. The nominal tidal phases result in a reduction of the contribution of the nominal tidal amplitudes by a minimum of about 50 %. The weakest torques are predominantly associated with the land-water distribution ~750 Myr ago and remain largely unaltered in response to the paleotidal force and the paleoday length. A substantial strengthening of the torque engenders the strongest torque for the M_2 tidal force ~620 Myr ago being provided by the land-water distribution ~750 Myr ago.

5.4. Time-averaged polar tidal torque

The underlying development of the composition of the global tidal torques is shown in Figures 5.9 and 5.10 for the M_2 tides and in Figures 5.11 and 5.12 for the K_1 tides. These figures present the global and zonally integrated distributions of the time-averaged polar tidal torques per water column. Similar to the modern case (Figure 4.11), regions exhibiting a positive torque, thereby accelerating the Earth's rotation rate, alternate with regions exhibiting a negative torque, thereby decelerating the Earth's rotation rate, under all conditions. Although positive and negative torques are comparable in strength, negative torques predominate. As stated in Appendix D.1 and Section 4.5.2.4, the tidal phase is associated with both the direction and magnitude of the tidal torque per water column. To show this more clearly, the tidal amplitudes and phases (Figures 5.1 to 5.4) are overlaid as line contours on the globally distributed tidal torques per water column.

A more detailed discussion regarding the M_2 tides is provided in Section 5.4.1, while Section 5.4.2 focusses on K_1 tides. In both instances, the effects occurring for all land-water distributions are considered first. The time-averaged polar tidal torques per water column in global and zonally integrated distributions are subsequently examined for the individual land-water distributions. A striking similarity can be observed between the distributions for the analogous land-water distributions ~630 Myr and ~600 Myr ago (Figures 5.10 and 5.12). Consequently, both land-water distributions are addressed collectively in the following discussion. Finally, a summary is provided in Section 5.4.3.

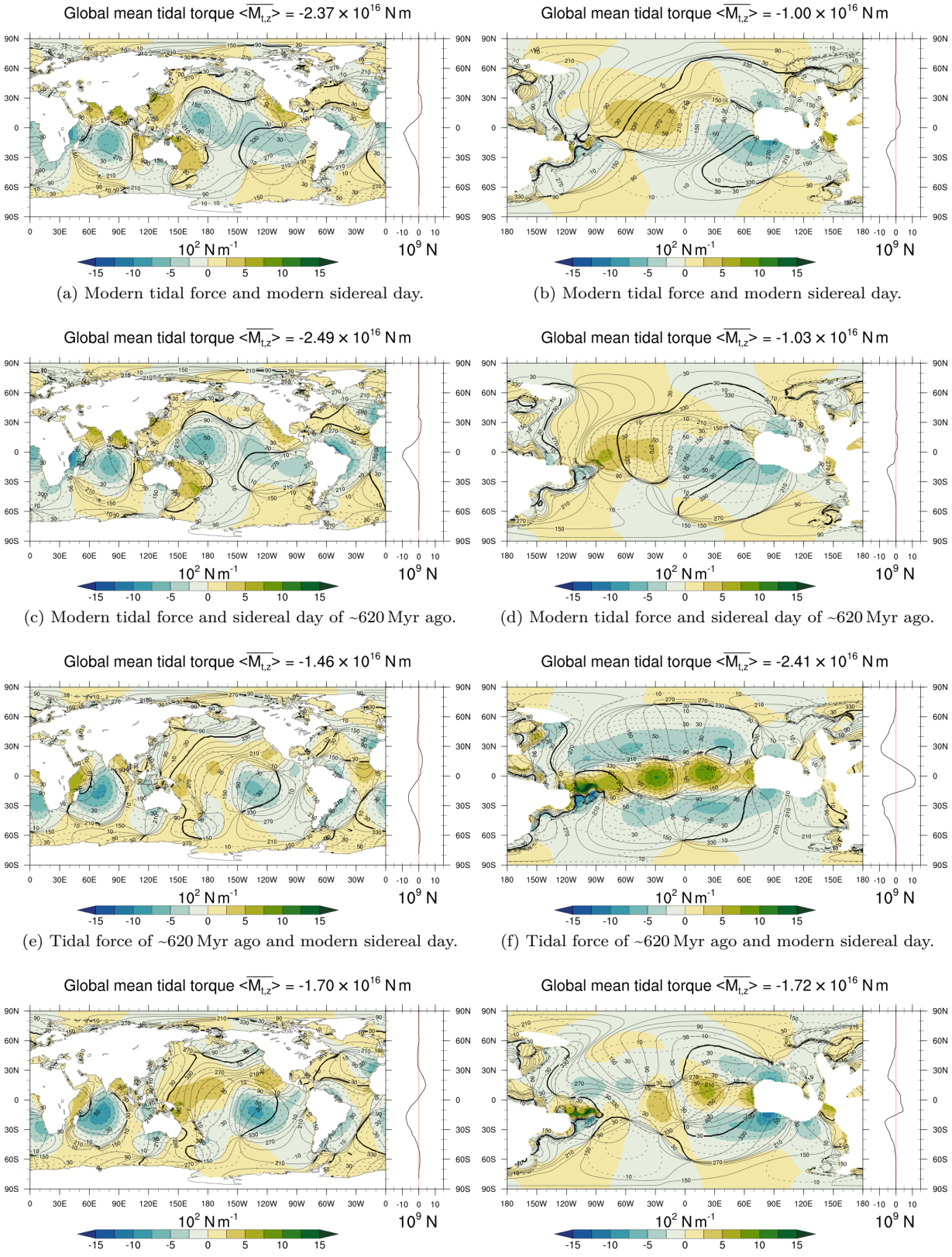

(a) Modern tidal force and modern sidereal day.

(b) Modern tidal force and modern sidereal day.

(c) Modern tidal force and sidereal day of ~620 Myr ago.

(d) Modern tidal force and sidereal day of ~620 Myr ago.

(e) Tidal force of ~620 Myr ago and modern sidereal day.

(f) Tidal force of ~620 Myr ago and modern sidereal day.

(g) Tidal force and sidereal day of ~620 Myr ago.

(h) Tidal force and sidereal day of ~620 Myr ago.

Figure 5.9.: M_2 time-averaged polar tidal torques $\overline{M_{t,z}}$ per water column for land-water distribution of modern times (left column) and of ~750 Myr ago (right column) with the two-depth distribution. Their zonal integration is shown to the right of the maps. The globally integrated time-averaged polar torques are given above the maps. Positive torques accelerate and negative torques decelerate the Earth's rotation rate.

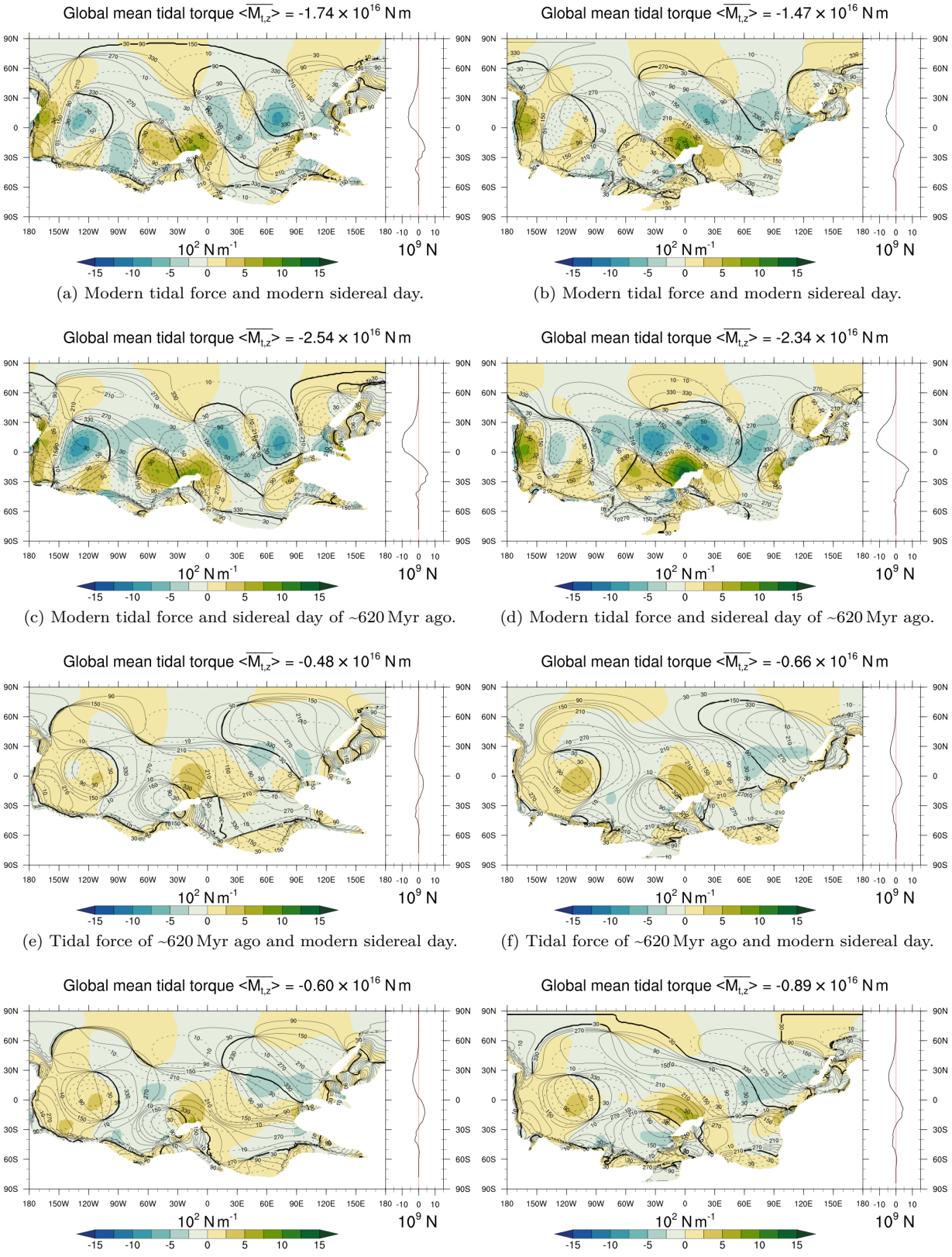

(a) Modern tidal force and modern sidereal day.

(b) Modern tidal force and modern sidereal day.

(c) Modern tidal force and sidereal day of ~620 Myr ago.

(d) Modern tidal force and sidereal day of ~620 Myr ago.

(e) Tidal force of ~620 Myr ago and modern sidereal day.

(f) Tidal force of ~620 Myr ago and modern sidereal day.

(g) Tidal force and sidereal day of ~620 Myr ago.

(h) Tidal force and sidereal day of ~620 Myr ago.

Figure 5.10.: M_2 time-averaged polar tidal torques $\overline{M_{t,z}}$ per water column for land-water distribution of ~630 Myr ago (left column) and of ~600 Myr ago (right column) with the two-depth distribution. Their zonal integration is shown to the right of the maps. The globally integrated time-averaged polar torques are given above the maps. Positive torques accelerate and negative torques decelerate the Earth's rotation rate.

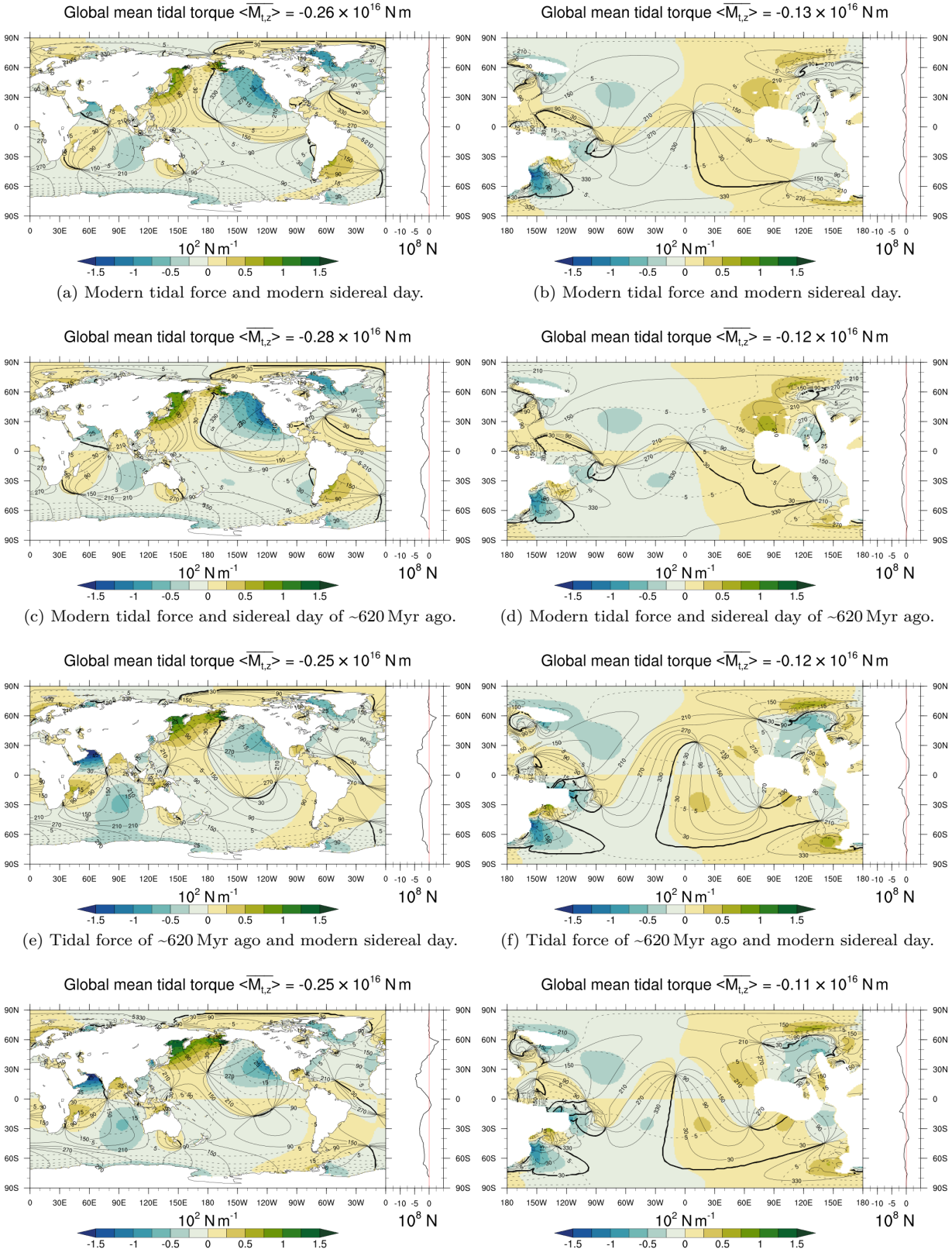

(a) Modern tidal force and modern sidereal day.

(b) Modern tidal force and modern sidereal day.

(c) Modern tidal force and sidereal day of ~620 Myr ago.

(d) Modern tidal force and sidereal day of ~620 Myr ago.

(e) Tidal force of ~620 Myr ago and modern sidereal day.

(f) Tidal force of ~620 Myr ago and modern sidereal day.

(g) Tidal force and sidereal day of ~620 Myr ago.

(h) Tidal force and sidereal day of ~620 Myr ago.

Figure 5.11.: K_1 time-averaged polar tidal torques $\overline{M_{t,z}}$ per water column for land-water distribution of modern times (left column) and of ~750 Myr ago (right column) with the two-depth distribution. Their zonal integration is shown to the right of the maps. The globally integrated time-averaged polar torques are given above the maps. Positive torques accelerate and negative torques decelerate the Earth's rotation rate.

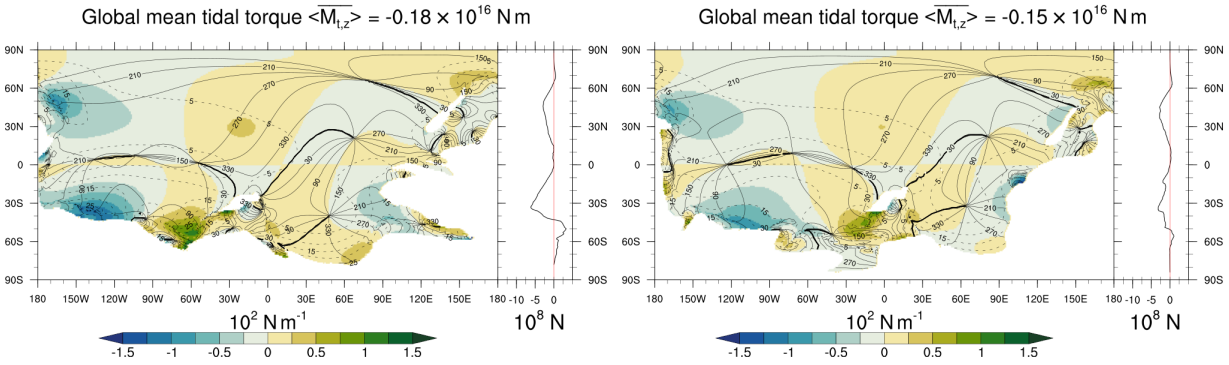

(a) Modern tidal force and modern sidereal day.

(b) Modern tidal force and modern sidereal day.

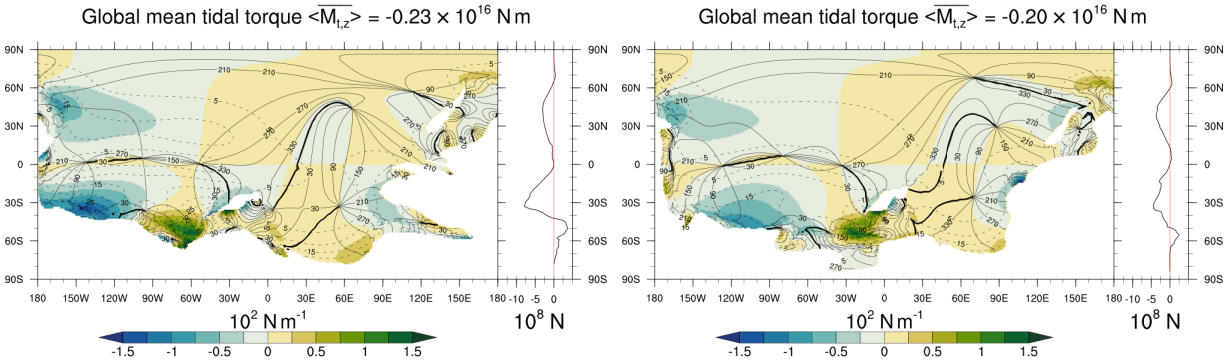

(c) Modern tidal force and sidereal day of ~620 Myr ago.

(d) Modern tidal force and sidereal day of ~620 Myr ago.

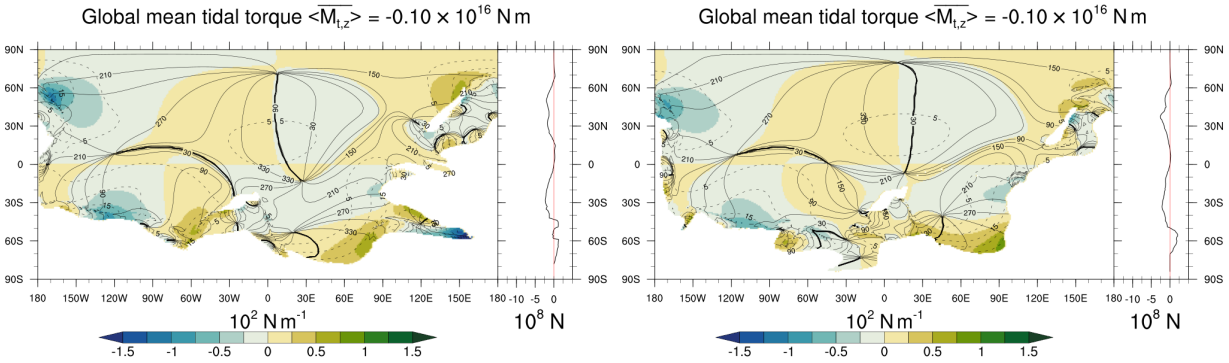

(e) Tidal force of ~620 Myr ago and modern sidereal day.

(f) Tidal force of ~620 Myr ago and modern sidereal day.

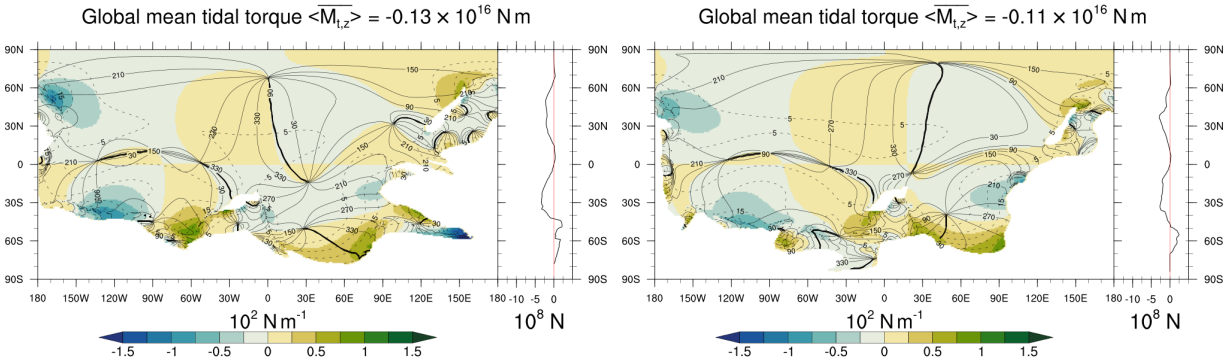

(g) Tidal force and sidereal day of ~620 Myr ago.

(h) Tidal force and sidereal day of ~620 Myr ago.

Figure 5.12.: K_1 time-averaged polar tidal torques $\overline{M_{t,z}}$ per water column for land-water distribution of ~630 Myr ago (left column) and of ~600 Myr ago (right column) with the two-depth distribution. Their zonal integration is shown to the right of the maps. The globally integrated time-averaged polar torques are given above the maps. Positive torques accelerate and negative torques decelerate the Earth's rotation rate.

5.4.1. M_2 tides

Relatively strong, time-averaged polar tidal torques per water column occur under all conditions in the regions around the equator between 30° S and 30° N for any land-water distribution (Figures 5.9 and 5.10). These regions correspond to a high degree with the regions of relatively high tidal amplitudes (Section 5.1.2 and Figures 5.1 and 5.2). In the context of the modern land-water distribution, characterized by the predominance of tidal propagation as Kelvin waves, these regions are situated along the coastlines, with the potential to extend significantly into the open ocean (Section 5.1.2.1). For the paleo land-water distributions, these regions are located in the nearly hemispherically open oceans in accordance with the prevailing tidal propagation as Poincaré waves with significant interference in the equatorial waveguides (Sections 5.1.2.2 and 5.1.2.3). For the land-water distributions ~630 Myr and ~600 Myr ago, these regions are additionally found in the two basins in the south along the coastline as the tides propagate there as Kelvin waves (Section 5.1.2.3).

The second quantity that determines the polar tidal torque (Section 2.2.4.6 and Equations (2.6), (2.25) and (2.55)) is the zonal gradient of the sectoral semi-diurnal tidal potential. The zonal gradient distribution also manifests with the extreme values in the regions previously mentioned (Footnote a, p. 123). While zonally integrated strong positive tidal torques can occur in these regions (Figures 5.9f, 5.9h, 5.10a, 5.10c, 5.10d and 5.12b), negative tidal torques predominate. Further, the zonal integrated distributions of M_2 tidal torques per water column (Figures 5.9 and 5.10) and M_2 tidal oscillation systems (Figures 5.1 and 5.2) demonstrate that semi-diurnal zonal tidal forces at high latitudes are insufficient to generate significant polar tidal torques.

The strongest positive and negative time-averaged polar tidal torques per water column are observed for the paleo land-water distributions (Figures 5.9 and 5.10). This also applies to the distribution of the zonally integrated torques per water column. These elements balance each other to generate a negative time-averaged global polar tidal torque. In the context of the modern land-water distribution, positive torques per water column are observed to be considerably diminished under all conditions, leading to comparatively low positive zonally integrated torques per water column (Figures 5.9a, 5.9c, 5.9e and 5.9g).

5.4.1.1. Modern land-water distribution

The decline in the strength of the time-averaged global polar tidal torque of about 28 % for the tidal force and day length ~620 Myr ago versus modern tidal force and day length occurs primarily in the central Pacific (Figures 5.9a, 5.9c, 5.9e and 5.9g). In the context of the modern tidal force and both day lengths, the amphidrome in the western Central Pacific is associated with an anti-amphidrome, which exhibits substantial negative tidal torques per water column (Figures 5.9a and 5.9c). Conversely, for the tidal force ~620 Myr ago and both day lengths, progressive Poincaré waves develop with significantly lower tidal amplitudes over the entire width of the central and northern Pacific, yielding relatively weak positive tidal torques per water column (Figures 5.9e and 5.9g). The negative tidal torques experienced in the eastern central Pacific region are amplified by an anti-amphidrome, which is situated between the two amphidromic nodes in the eastern and southern Pacific. The shorter day length ~620 Myr ago enhances the aforementioned effects. The positive tidal

torques in the western central and northern Pacific, as well as the negative tidal torques in the eastern central and southern Pacific, are strengthened. Consequently, the substantial negative tidal torques surrounding the equator for the modern tidal force (Figures 5.9a and 5.9c) are shifted to a certain extent, weakened at about 20° S for the tidal force ~620 Myr ago (Figures 5.9e and 5.9g). Significantly augmented positive tidal torques north of the equator are incorporated in a zonally integrated manner.

Within the Atlantic and Indian Ocean, the tidal torques per water column demonstrate minimal response to the tidal force and day length ~620 Myr ago (Figures 5.9a, 5.9c, 5.9e and 5.9g), akin to the tidal oscillation system (Section 5.1.2.1). In the Indian Ocean, the negativ tidal torques per water column exhibit a substantial increase in strength, as do the tidal amplitudes, in the anti-amphidromic region. In the coastal marginal regions, positive tidal torques experience a weakening tendency toward the north, while negative tidal torques in East African and West Australian waters undergo a change in direction. However, these effects are found to be negligible for the zonally integrated time-averaged polar tidal torques per water column.

5.4.1.2. Land-water distribution ~750 Myr ago

The increase in the strength of the time-averaged global polar tidal torque for tidal force and day length ~620 Myr ago compared to the modern tidal force and day length by about 72 % occurs in low to mid-latitudes in the nearly hemispherically open ocean (Figures 5.9b, 5.9d, 5.9f and 5.9h). The pivotal aspect is related to the tidal propagation, predominantly driven by Poincaré waves and their subsequent interference, contingent on the tidal force and day length in the open ocean (Section 5.1.2.2). In the context of the modern tidal force and both day lengths (Figures 5.9b and 5.9d), the tidal phases of the westward propagating Poincaré waves at about 0° longitude segment the equatorial waveguides east of it into a region exhibiting marked negative tidal torques and west of it into a region demonstrating marked positiv tidal torques (Appendix D.1 and Figure D.1a). The tidal phase range is the critical factor in this relationship, as regions exhibiting the strongest torques per water column demonstrate only a weak correlation with regions that exhibit relatively high tidal amplitudes. A substantial negative zonally integrated tidal torque manifests exclusively in the vicinity of 20° S. Conversely, the low tidal amplitudes in the northern and southern waveguides are associated with negligible torques, even when integrated zonally.

A completely different distribution pattern of the time-averaged polar tidal torques per water column emerges for the tidal force ~620 Myr ago (Figures 5.9f and 5.9h). The interference of the Poincaré waves with anti-amphidromes stringed together in an equatorial belt (Section 5.1.2.2), in conjunction with the prevailing tidal phases (Appendix D.1 and Figure D.1a), results in the generation of exclusively positive tidal torques per water column at the modern day length (Figure 5.9f). The strength of these torques correlates strongly with the height of the tidal amplitudes due to the tidal phase range. In the regions north and south of the equatorial belt, the interference of the Poincaré waves is associated with exclusively negative torques per water column. Although the tidal amplitudes are comparable to those of the equatorial belt, the tidal phases (Appendix D.1 and Figure D.1a) result in significantly weaker torques per water column. These torques continue to correlate with the height of the tidal amplitudes. Overall, however, the negative torques per water

column more than offset the relatively strong positive tidal torques in the equatorial belt. This results in the strongest negative time-averaged global polar tidal torque under all conditions for all land-water distributions. The pattern weakens significantly for the shorter day length ~620 Myr ago (Figure 5.9h). It begins to decay. This is analogous to the tidal oscillation system and the associated interference of the Poincaré waves (Section 5.1.2.2). The time-averaged global polar tidal torque for tidal force and day length ~620 Myr ago (Figure 5.9h) undergoes a substantial reduction in strength relative to the torque for the modern day length (Figure 5.9f), approaching the torque of the modern land-water distribution (Figure 5.9g).

5.4.1.3. Land-water distribution ~630 Myr and ~600 Myr ago

The decline in the strength of the time-averaged global polar tidal torque for the land-water distributions ~630 Myr and ~620 Myr ago of about 66 % and 40 %, respectively, for the tidal force and day length ~620 Myr ago versus modern tidal force and day length occurs in the whole open ocean between the two continental landmasses of Rodinia (Figure 5.10). The globally distributed torques per water column exhibit a consistent weakening that is associated with the global decrease in tidal amplitudes and the shift in tidal phases (Section 5.1.2.3). In consideration of modern tidal force and both day lengths (Figures 5.10a to 5.10d), regions manifesting relatively high tidal torques demonstrate a discernible correlation with regions exhibiting relatively high tidal amplitudes. This effect is largely offset by the tidal phase shifts (Appendix D.1 and Figure D.1a) associated with the tidal force ~620 Myr ago and both day lengths (Figures 5.10e to 5.10h). In conjunction with the global decline in tidal amplitudes, this phenomenon leads to a comparatively pronounced weakening of the time-averaged global polar tidal torques. At equal tidal force, the two day lengths exert minimal influence on the global and zonally integrated distributions of the tidal torques per water column. However, the strength of the tidal torques exhibits an increase in conjunction with the shorter day length ~620 Myr ago, as do the tidal amplitudes.

The development of the time-averaged polar tidal torques per water column as a function of tidal force and day length is closely linked to the tidal propagation of Poincaré waves in the equatorial waveguides. In the context of the modern tidal force, a sequence of anti-amphidromes, distinguished by relatively high tidal amplitudes, are associated with the interference of Poincaré waves within the equatorial waveguides (Section 5.1.2.3), yielding almost exclusively negative, relatively strong tidal torques per water column (Figures 5.10a to 5.10d). The shorter day length ~620 Myr ago significantly amplifies this effect, primarily due to the considerably higher tidal amplitudes compared to modern day length. Within the eastern and western basins of the Southern Hemisphere, the Kelvin waves, characterized by their relatively moderate tidal amplitudes, result in relatively weak and negligible torques. This phenomenon occurs despite the presence of optimal tidal phases favorable for strong tidal torques (Appendix D.1 and Figure D.1a), due to the decline of the zonal tidal force toward the polar regions. Conversely, along the eastern periphery of Rodinia and in the vicinity of the island situated between the eastern and western basins, the Kelvin waves can generate substantial regions characterized by relatively robust positiv tidal torques per water column, attributable to the tidal phases. This phenomenon is particularly evident for the day length ~620 Myr ago. The disruption in the interference of the Poincaré waves for the

tidal force ~620 Myr ago (Section 5.1.2.3) considerably weakens the anti-amphidromes for the modern tidal force (Figures 5.10e to 5.10h). The substantial diminished tidal amplitudes, in conjunction with the tidal phases that have been shifted towards weak tidal torques (Appendix D.1 and Figure D.1a), result in the attenuation of the torques per water column within the equatorial waveguides. A comparable phenomenon is observed in the Kelvin waves of the southern ocean and the subsequent tidal torques.

5.4.2. K_1 tides

Relatively strong, time-averaged polar tidal torques per water column occur under all conditions in the regions around 45° S and 45° N for any land-water distribution (Figures 5.11 and 5.12). These regions correspond to a high degree with the regions of relatively high tidal amplitudes (Section 5.1.3 and Figures 5.3 and 5.4). In accordance with the prevailing Kelvin waves that dominate tidal propagation, the regions exhibiting the strongest torques are located along the coastlines, decreasing toward the open ocean.

The second quantity that determines the polar tidal torque (Section 2.2.4.6 and Equations (2.6), (2.25) and (2.55)) is the zonal gradient of the tesseral diurnal tidal potential. The zonal gradient distribution also manifests with their extreme values in the regions previously mentioned (Footnote a, p. 123). While zonally integrated strong positive tidal torques can occur in these regions (Figures 5.11e, 5.11g, 5.12a, 5.12c, 5.12d and 5.12f to 5.12h), negative tidal torques predominate. Further, the zonal integrated distributions of K_1 tidal torques per water column (Figures 5.11 and 5.12) and K_1 tidal oscillation systems (Figures 5.3 and 5.4) demonstrate that diurnal zonal tidal forces at high latitudes are insufficient to generate significant polar tidal torques. Additionally, tidal torques per water column are observed to be zero at the equator, a consequence of the zonal tidal forces being null.

It is evident that regions exhibiting weak to medium torques predominate over those with strong torques (Figures 5.11 and 5.12). The strength of the local torques per water column is comparable for the various land-water distributions (Figures 5.11 and 5.12). In line with the negligible tidal propagation in the nearly hemispherically open paleo-ocean basins in mid-to-high latitudes (Section 5.1.3), there are marked regions with negligible torques per water column (Figures 5.11b, 5.11d, 5.11f, 5.11h and 5.12). The modern land-water distribution, with continents dispersed across all latitudes and a relatively long coastline, results in a significantly different spatial distribution of torques (Figures 5.11a, 5.11c, 5.11e and 5.11g). Additionally, significantly larger numbers of strong torques per water column can develop. Generally, the time-averaged global polar tidal torques for the paleo land-water distributions are approximately 50 % of those for the modern land-water distribution (Section 5.3.4).

5.4.2.1. Modern land-water distribution

The resulting decline of approximately 4 % in the time-averaged global polar tidal torque for the tidal force and day length ~620 Myr ago, as compared to the modern tidal force and day length, can be disregarded within the context of the absolute values (Figures 5.11a and 5.11g). A comparable global distribution of the time-averaged polar tidal torques per water column is evident for both tidal forces in Figures 5.11a and 5.11c and Figures 5.11e

and 5.11g, respectively. However, notable variations emerge in the characteristics of regions exhibiting relatively strong positive and negative torques, particularly evident in the zonally integrated distribution. The distributions of the zonally integrated torques per water column for the two day lengths at the same tidal force in Figures 5.11a and 5.11c and Figures 5.11e and 5.11g, respectively, are nearly identical, indicating a nearly identical global distribution of the torques for these conditions. This phenomenon can be attributed to the nearly identical tidal oscillations systems resulting from the typical tidal propagation by Kelvin waves (Section 5.1.3.1), which are independent of the Earth rotation rate (Section 2.2.4.3).

The Southern Hemisphere exhibits a moderate increase in the strength of the negative tidal torque per water column in the Indian Ocean and a moderate decrease in the strength of the positive tidal torque per water column in the Argentine basin for the tidal force ~620 Myr ago (Figures 5.11e and 5.11g). These phenomena can be attributed to the evolution of the tidal amplitudes in these regions (Section 5.1.3.1). However, beyond this point, the global and zonal distribution remains indistinguishable from its modern counterpart (Figures 5.11a and 5.11c). In the North Pacific for the tidal force ~620 Myr ago (Figures 5.11e and 5.11g), the tidal phases shift towards positive torques (Appendix D.1 and Figure D.1b). This shift is accompanied by a weakening of the region with negative torques in the eastern North Pacific and an increase of the region with positive torques in the western North Pacific. A zonally integrated positive torque is evident. On a global scale, this phenomenon is counterbalanced by a stronger negative torque in the Arabian Sea, attributable to higher tidal amplitudes. The zonally integrated torques per water column are observed to exhibit an increase in strength.

5.4.2.2. Land-water distribution ~750 Myr ago

In accordance with the tidal oscillation systems (Section 5.1.3.2), the spatial distribution pattern of the time-averaged global polar tidal torques per water column remains largely unchanged, irrespective of the selected tidal force and day length (Figures 5.11b, 5.11d, 5.11f and 5.11h). The higher tidal amplitudes and stronger tidal dynamics, combined with tidal phase shiftings for the tidal force ~620 Myr ago, amplify the torques per water column relatively moderately. In particular regions, the direction of torques undergoes a change, a phenomenon evident north of the substantial western island of Rodinia around the equator. The zonally integrated torques balance each other to such an extent that there are negligible differences between the time-averaged global polar tidal torques for the tidal force and day length in modern times and ~620 Myr ago.

5.4.2.3. Land-water distribution ~630 Myr and ~600 Myr ago

The global distribution patterns of the time-averaged global polar tidal torques per water column are analogous for tidal force and day length in modern times and ~620 Myr ago (Figure 5.12). This is based on similar spatial and temporal distribution patterns exhibited by the tides (Section 5.1.3.3), to which the torques develop in a consistent manner. In accordance with the nominal tidal phases (Figure 5.8b.2), the phases of the predominant tidal propagation as Kelvin waves exhibit relatively minimal shifts for tidal force and day length ~620 Myr ago.

The decline in resonance of the tides for the tidal force ~620 Myr ago (Section 5.1.3.3) is associated with a general decrease in both strength and extent of regions with pronounced torques (Figures 5.12e to 5.12h). In the Northern Hemisphere, the strength of the predominantly negative zonally integrated torques per water column experiences a moderate decrease. The shifts in the regions with relatively weak positive and negative torques have virtually no effect. Within the Southern Hemisphere, the strength of the negative zonally integrated torques per water column undergoes also a moderate decline. The positive zonally integrated torques per water column at the southern end remain relatively constant. On the other hand, the tidal amplitudes of the circumferential Kelvin waves in the eastern basin increase, leading to significant increase in positive torques per water column.

Summarized, the aforementioned results in a moderately weaker time-averaged global polar tidal torque for tidal force and day length ~620 Myr ago.

5.4.3. Summary

The global and zonally integrated distributions of the time-averaged polar tidal torques per water column of the M_2 and K_1 tides has been discussed for the tidal force and day length in modern times and ~620 Myr ago for the modern and paleo land-water distributions. The torques are composed of the harmonic and non-linear components of the tides. Under all conditions, the torque distributions of all land-water distributions reflect the spatial distribution of the zonal tidal force. The overlay of the torques with the harmonic tidal component serves to confirm the relationship between them that is derived in Appendix D.1. The direction of the torques is determined by the phase of the harmonic tides. The strength of the torques exhibits a correlation with the amplitudes of the harmonic tides, depending on the tidal phase. Consequently, the torques are predominantly influenced by the harmonic component of the tides.

With respect to the modern land-water distribution, the torques of the M_2 and, most notable, the K_1 tides respond relatively stable to the tidal force and day length ~620 Myr ago. The decisive factor is the predominant tidal propagation as non-dispersive Kelvin waves. The increased occurrence of Poincaré waves in the Pacific Ocean under the M_2 tidal force ~620 Myr ago is the critical factor in the significant weakening of the time-averaged global polar tidal torque.

The paleo land-water distributions demonstrate substantially greater dynamics in torques in response to tidal force and day length ~620 Myr ago. In the nearly hemispherically open paleo-oceans, tides propagate primarily as dispersive Poincaré waves. A potential augmentation in torques can occur for the day length ~620 Myr ago at the same tidal force. Locally, these distributions can exhibit stronger positive and negative torques than the modern land-water distribution. Positive torques occur more frequently. Even in their zonally integrated distribution, the paleo land-water distributions can exhibit significantly stronger positive and negative torques. The torques in both direction are balanced, resulting in negative global torques that are generally weaker than for the modern land-water distribution. In all conditions, negative global torques result, which are generally about one-third to two-third weaker than for the modern land-water distribution. However, the strongest global torque for the M_2 tides results from the tidal force ~620 Myr ago for the land-water distribution ~750 Myr ago.

For the propagation of the diurnal K_1 tides, the Poincaré waves are constrained to the equatorial waveguides. In consideration of the zonal tidal force in this region, the occurrence of significant torques in the nearly hemispherically open paleo-oceans is significantly dampened. The tidal propagation as Kelvin waves under all conditions along the significantly shorter coastline of the supercontinent Rodinia relative to the modern land-water distribution is associated with up to about 50 % of the global torques for the modern land-water distribution. As is the case for the modern land-water distribution, the torques demonstrate minimal variations in relation to tidal force and day length in modern times and ~620 Myr ago.

6. Conclusion and future work

The primary focus of this study is to reduce the substantial demand for research into the differentiated reconstruction of Earth's history, particularly the tides of the early oceans and the associated tidal friction between Earth and Moon. To this end, a series of numerical simulations were conducted to estimate the spatial and temporal characteristics of ocean tides in the Late Neoproterozoic era ~620 Myr ago (Sections 5.1 and 5.2). The Elatina and Reynella tidal rhythmites in South Australia provide observational data on the tidal spectrum during that period (Section 3.1.3). As indicated in the analysis by G. E. Williams (2000), there has been an documented increase in both day length and lunar distance (Table 2.2). In light of the inherent uncertainties concerning the Late Neoproterozoic context, the findings of this study should not be regarded as absolute or definitive. Nonetheless, they constitute an estimate of the tidal environment ~620 Myr ago.

In order to assess the impact of land-water distributions and tidal robustness, three current paleogeographic reconstructions by Scotese (2017) and Scotese and Wright (2018) were considered for the different time periods of the Late Neoproterozoic: ~750 Myr, ~630 Myr, and ~600 Myr ago (Section 4.2.2). The unknown ocean depths were mapped using two representative depths: 160 m for the shelf seas and 3480 m for the open ocean. These depths ensured that the volume of the paleo-oceans aligns with the ocean volume in modern times. In contrast to the reconstructions employed by Green et al. (2020) for tidal simulations, subduction zones and mid-ocean ridges were not considered in the reconstruction.

The foundation of the study was the data-unconstrained tide model TiME, which was developed by Weis (2006) (Sections 4.3.1 to 4.3.3, 4.4.2, 4.4.3 and 4.5). Given the two-depth distribution and the uncertainties regarding the land-water distributions in the Late Neoproterozoic, a resolution of 1° was chosen. The Elatina and Reynella tidal rhythmites indicate the presence of strong tides in shallow waters along the continental edge and the absence of global oceans covered by ice (G. E. Williams, 2023). In contrast to the simulations conducted by Green et al. (2020), the hypothesis of a Snowball Earth scenario was excluded in accordance with G. E. Williams (2023) (Section 3.2.2.2). The parameterizations and conditions for modern times were included in the simulations for the period ~620 Myr ago.

Estimates of the lunisolar tidal potential ~620 Myr ago (Section 4.2.1) were derived from the configuration of the Earth-Moon-Sun system corresponding to the recorded tidal spectrum (G. E. Williams, 2000), including a shorter day length of 21.9 h (Table 2.2). The semi-diurnal lunar M_2 and solar S_2 as well as the diurnal lunisolar K_1 and solar O_1 tidal constituents were selected for examination (Table 4.1). The lunar tidal constituents ~620 Myr ago were about 10 % stronger, while the semi-diurnal periods were shortened by about 1 h and the diurnal periods by about 2 h. The results presented of paleotides (Chapter 5) focused on simulations of M_2 and K_1 tides. For S_2 tides, the results were analogous to those for M_2, and for O_1, the results were analogous to those for K_1 tides.

A notable correlation has been identified between the regions exhibiting high and low

tidal heights in the detailed modern bathymetry and those in the two-depth distribution derived from the detailed bathymetry (Section 4.5.2.1). The amphidromic systems evolved in a comparable manner in terms of their spatial distribution and direction of rotation (Figures 4.5 and 4.7). However, there was a notable decrease in tidal amplitudes, alongside the occurrence of significant phase shifts. In contrast to the Atlantic Ocean, the Indian Ocean, and the South Pacific Ocean, the North Pacific Ocean demonstrated distinctive and substantial alterations in the spatial and temporal characteristics of the individual tides (Sections 4.5.2.1 and 4.5.2.2 and Figures 4.5, 4.7 and 4.8). The same applied for the energy supply and polar tidal torque per water column as temporal averages of the individual tidal constituents (Section 4.5.2.4 and Figures 4.11 and 4.12). Even the simulations with the comparatively coarse resolution of 1° of the detailed bathymetry were inadequate for representing the individual tides characteristic of this region (Section 4.5.1.2 and Figure 4.6), which features steep deep-sea trenches, adjacent ocean ridges and extensive island realms such as Indonesia and the Philippines (Figure 2.2). Such a region should not be able to exist over a long geological period, nor should it be able to have a significant influence on Earth's history. In the context of the tidal oscillation systems for the paleo land-water distribution, these systems could be regarded as robust with respect to more realistic depth distribution.

For the purposes of the study, the tidal oscillation system of all four tidal constituents could be simulated adequately for modern times using the implemented model version TiME(1°) (Section 4.5.1.1). An initial investigation into the influence of the tides on the sedimentation patterns of the Elatina rhythmites (Section 3.1.3) was conducted, taking into consideration the various tidal regime types (Section 5.2). In the context of a shelf of limited width with a rapid transition to deep water, as assumed for the deposition of the Elatina rhythmites (Figure 4.2), TiME(1°) demonstrated its capacity to adequately simulate the ratio of diurnal to semi-diurnal tides and the tidal regime type locally (Section 4.5.2.3 and Figure 4.10). The same was true for simulations using the two-depth distribution. Given the inherent uncertainties, the simulated tidal regimes for the region of the Elatina Formation ~620 Myr ago had the potential to generate the sedimentation pattern characteristic of the Elatina rhythmites (Section 5.2 and Figure 5.7). The observations made by G. E. Williams (2000) of the tidal spectrum (Section 3.1.3) could be confirmed. This phenomenon is particularly noteworthy when considering the robustness of the analogous tidal oscillation systems for the land-water distributions ~630 Myr and ~600 Myr ago (Sections 5.1.2.3 and 5.1.3.3). The resolution of the simulations in conjunction with the two-depth distribution, as outlined in their evaluation (Section 4.5.2.3), did not allow any conclusions to be drawn about the sedimentation potential of the tidal regime based on the tidal range. However, Green et al. (2020) were able to identify a sufficient tidal range for sedimentation using tidal simulations.

The implementation of the non-linear shallow-water equations in TiME facilitated the investigation of the tidal friction through the utilization of the time-averaged tidal torque. According to Brosche and Sündermann (1971) (Section 2.3), the process of tidal friction in the simulations was consistently and adequately accounted for by angular momentum transfer between Earth and Moon through the tides of the oceans (Section 5.4), in contrast to the prevailing method of energy dissipation (Section 3.2.2). The simulation of individual tidal constituents ensured stable time-averaged global tidal torques.

The geodetic module of TiME (Section 4.3.3), which was previously integrated in a tight manner, was replaced by a low-level module coupled to the model via a freely programmable

interface. Utilizing this interface enables users to specify the quantities to be calculated and their respective outputs. This approach facilitates flexible and economical adaptation to the specific requirements of each investigation. The model underwent a fundamental revise. It has been subdivided into functional procedures and modules. Consequently, this approach provided structured and consistent access to the required quantities.

The modern global balance quantities, encompassing energy supply and dissipation as well as the polar tidal torque as time averages, exhibited values that exceed the established reference values (Section 4.5.1.3). As is the case with all data-unconstrained models, the amplitudes were overestimated (Section 4.5.1.4). Additionally, the phases exhibited a delay in their progression. The two-depth distribution resulted in approximately half the polar tidal torques and energy supplies as global time averages (Section 4.5.2). This was attributed to nominal tides, which were about 30 % lower and advanced by about 10° to 15° (Figure 4.13). For the O_1 tides there was only a reduction of about 20 %. The O_1 had only a 4 % lower nominal amplitude.

The study made a mean transfer of angular momentum between the Earth and the Moon via the harmonic component of the tides evident, depending on the tidal phase (Appendix D.1 and Sections 4.5.2.4, 5.3.4 and 5.4). In each simulation, the harmonic component of the tides (Equation (2.41)) resulting from the linear terms of the underlying shallow-water equations (Equations (2.43) to (2.45) and Section 4.3.1) had a predominant influence on the time-averaged polar tidal torque per water column. A noteworthy aspect of all simulations was the global alternating sequence of regions where the Earth's rotation rate decelerates and accelerates in response to the negative and positive time-averaged polar tidal torques per water column, respectively (Figures 4.11 and 5.9 to 5.12). In accordance with Appendix D.1, it was found that the phase of the harmonic tidal component was decisive for the direction of the torques. Along with the zonal tidal force and the tidal amplitudes, the tidal phase was crucial for the strength of the torques. Thus, not all regions with high tides, such as the Gulf of Alaska and the Weddell Sea for the modern M_2 tides, exhibited extreme torques (Figures 4.5a and 4.11a). Another example was the land-water distribution ~750 Myr ago for the conditions in modern times and ~620 Myr ago. Both tidal oscillation systems of the M_2 tide (Figures 5.1b and 5.1h) exhibited nearly identical tidal amplitudes in the region surrounding the equator and at 30° E. Under modern conditions, moderate negative torques occurred (Figure 5.9b). However, under the conditions ~620 Myr ago, the modified tidal phases resulted in relatively strong positive tidal torques (Figure 5.9h). While the tidal amplitudes were also comparable on a global scale, a 72 % stronger negative global torque was determined to depend on the modified tidal phases. The occurrence of maxima and minima of zonal tidal gradients in regions with high tidal ranges favored the occurrence of high tidal torques, depending on tidal phases. These findings underscored the limitations of energy dissipation as a metric for detecting variations in Earth's rotation rate (Brosche & Sündermann, 1971).

With regard to the strength and direction of the time-averaged polar tidal torques per water column, the non-linear component of the simulated tides resulting from advection and frictional forces in the shallow-water equations (Equations (2.43) to (2.45) and Section 4.3.1) played a minor role. In subsequent studies, purely harmonic tides could be simulated using linearized shallow-water equations or the linear Laplace's tidal equations to further investigate their time-averaged polar tidal torque. This would also allow the influence of

purely harmonic tides to be quantified and distinguished from that of non-linear terms. Furthermore, the equivalent energetic description of the time-averaged angular momentum exchange by purely harmonic tides remains the subject of further inverstigations.

The response of the individual land-water distributions to the stronger tidal force, shorter tidal periods, and shorter day length ~620 Myr ago varied greatly and even ran counter each other (Figure 5.8). In all conditions, negative time-averaged global polar tidal torques were found, with these torques being, for the most part, one-third to two-thirds weaker for the paleo land-water distributions than that for the modern land-water distribution (Figure 5.8a.5 and Figure 5.8b.5), thus slowing down the Earth's rotation rate. The torques exerted by the K_1 tides (Figure 5.8b.5) were, in general, one order of magnitude weaker than those of the M_2 tides (Figure 5.8a.5). For the land-water distributions in modern times and ~630 Myr and ~600 Myr ago a decline in the M_2 (Figures 5.1a, 5.1g, 5.2a, 5.2b, 5.2g and 5.2h) and K_1 tides (Figures 5.3a, 5.3g, 5.4a, 5.4b, 5.4g and 5.4h) was observed, exhibiting a range of intensity. Concurrently, the torques of the M_2 (Figure 5.8a.5) and K_1 tides (Figure 5.8b.5) underwent a reduction in strength. In the context of the modern land-water distribution, a decline of about 28 % and a negligible decline of about 4 % respectively were found. For the land-water distributions ~630 Myr and ~600 Myr ago, the decline was disproportionately high, falling by about 66 % and 40 % for the M_2 tides, respectively. This was roughly in line with the magnitude of the torques for the diurnal tides. The weakening for the K_1 tides was found to be about 27 %. The M_2 (Figures 5.1b and 5.1h) and K_1 tides (Figures 5.3b and 5.3h) remained relatively stable with respect to land-water distribution ~750 Myr ago. However, a substantial, disproportionate increase in the strength of the torque of the M_2 tides of about 72 % was observed, accompanied by a transition from the weakest to the strongest level (Figure 5.8a.5). This was closely followed by the torque for the modern land-water distribution. Conversely, the torque of the K_1 tides exhibited a moderate weakening of about 15 % (Figure 5.8b.5).

The relatively weak time-averaged global polar tidal torques for land-water distributions ~630 Myr and ~600 Myr ago, in terms of tidal force and day length ~620 Myr ago, correlate very strongly with the observational data on evolution of day length in Earth's history presented in Deines and Williams (2016) and Figure 1.1. A notable inflection point in the rate of change of days per year occurred ~620 Myr ago, accompanied by relatively weak rates of change in its vicinity. Notwithstanding the tectonic activity between the land-water distributions ~630 Myr and ~600 Myr ago, their tides and tidal torques exhibited remarkable congruence (Figure 5.8). This finding suggests relatively weak torques during the given period. However, the relatively strong torque of the M_2 tides for land-water distribution ~750 Myr ago indicates that this distribution is not congruent with tidal force and day length ~620 Myr ago. It aligns more closely with the substantial rates of change observed between ~850 Myr and ~620 Myr ago. Furthermore, as discussed in Appendix D.1 and Section 5.4, the decrease in day length following the inflection point ~620 Myr ago in the observed data (Figure 1.1) could not be ruled out.

Numerical tidal simulation have the potential to enhance our understanding of the geological time scale, a fundamental prerequisite for unraveling the evolution of the Earth. The application of geological data in constraining astronomical solutions for the evolution of the Earth's orbit and that of all planets in the solar system over a large part of the

geological time scale has already been initiated, as evidenced by the ongoing *AstroGeo*[a] project. Tidal solutions merit consideration as an element of subsequent investigations.

A salient feature was the response of the M_2 tides for the paleo land-water distributions to the day length at the same tidal force (Figures 5.1b, 5.1d, 5.1f, 5.1h, 5.2 and 5.8a), which was almost nonexistent in the tides for the modern land-water distribution (Figures 5.1a, 5.1c, 5.1e, 5.1g and 5.8a). The relatively extensive modern coastline, in conjunction with the relatively substantial ocean basins, facilitated the propagation of semi-diurnal and diurnal tides by Kelvin waves and their interference across all latitudes (Figures 5.1a, 5.1c, 5.1e and 5.1g and Figures 5.3a, 5.3c, 5.3e and 5.3g, respectively). Non-dispersive Kelvin waves (Section 2.2.4.3) propagate independently of the Earth rotation rate. Therefore, they cannot respond to changes in the day length. Along the coastlines of the widely dispersed continents, extensive regions with relatively high semi-diurnal and diurnal tides developed in all conditions. These regions had the ability to extend considerably into the open ocean, thereby occupying a significant part of the ocean that exhibited relatively high time-averaged polar tidal torques per water column (Figures 5.9a, 5.9c, 5.9e, 5.9g, 5.11a, 5.11c, 5.11e and 5.11g).

In the Atlantic and Indian Oceans, the semi-diurnal and diurnal tides exhibited minimal response to tidal force and day length ~620 Myr ago (Figures 5.1a, 5.1c, 5.1e and 5.1g and Figures 5.3a, 5.3c, 5.3e and 5.3g, respectively). A phenomenon that was also observed in the diurnal tides of the Pacific. The increased occurrence of Poincaré waves in the Pacific under the M_2 tidal force ~620 Myr ago (Figures 5.1e and 5.1g) was the decisive factor for the significant weakening of the time-averaged global polar tidal torque by 28 % in conjunction with the day length ~620 Myr ago (Figures 5.9e and 5.9g). The relatively strong and predominantly strongest time-averaged global polar tidal torques in all conditions (Figure 5.8a.5) could be partially attributed to tidal amplitudes (Figure 5.8a.1). The more favorable tidal phases (Figure 5.8a.2) were found to be decisive. The K_1 tidal torques demonstrated relative stability, exhibiting only a negligible decrease in strength of 4 % for the tidal force and day length ~620 Myr ago (Figure 5.8b.5). However, the (nominal) tides underwent a moderate decrease in both height and phase (Figure 5.8b.1 and Figure 5.8b.2, respectively).

Along the much shorter coastline of the supercontinent Rodinia, the propagation of semi-diurnal and diurnal tides was less strongly influenced by Kelvin waves (Figures 5.1b, 5.1d, 5.1f, 5.1h and 5.2 and Figures 5.3b, 5.3d, 5.3f, 5.3h and 5.4, respectively). The propagation of Kelvin waves necessitates the presence of vertical boundaries (Section 2.2.4.3). The positioning of Rodinia around the South Pole in the land-water distributions ~630 Myr and ~600 Myr ago (Figure 4.1d and Figure 4.1c, respectively)—in contrast to its position around the equator in the land-water distribution ~750 Myr ago (Figure 4.1e)—fostered the occurrence of Kelvin waves and their interference with relatively high semi-diurnal and diurnal tides in the two extensive ocean basins in the mid-to-high southern latitudes.

In the nearly hemispherically open oceans, Poincaré waves exhibited a predominant role in tidal propagation. Given that dispersive Poincaré waves propagate depending on both the tidal period and Earth's rotation rate, they have the capacity to respond to changes in the day length (Section 2.2.4.3). A total of four waveguides were identified for the semi-diurnal

[a] https://www.astrogeo.eu, 09/03/2025

tides (Figures 5.1b, 5.1d, 5.1f, 5.1h and 5.2). Initially, the two equatorial waveguides were clearly visible, extending from 0° to about 30° S and 30° N, respectively. Adjacent to this, additional waveguides were formed by the critical latitude of the Poincaré waves for semi-diurnal tides at about 75° S and 75° N, respectively (Section 2.2.4.3). Depending on the extent of interference, the semi-diurnal tides could develop a distribution pattern of stringed cells with relatively high tidal amplitudes (Figures 5.1f and 5.2c). The diurnal tides were primarily confined to the equatorial waveguides with moderat amplitudes (Figures 5.3b, 5.3d, 5.3f, 5.3h and 5.4), as Poincaré waves cannot develop for diurnal tides at higher latitudes (Section 2.2.4.3).

For the modern M_2 tidal force, significant interference occurred in the land-water distributions ~630 Myr and ~600 Myr ago (Figures 5.2a to 5.2d). Consequently, these relatively high tides—which exceeded the tides for the modern land-water distribution—gave rise to the most pronounced nominal tidal amplitudes (Figure 5.8a.1). However, the nominal tidal phases were approximately 160° in conjunction with the modern day length (Figure 5.8a.2), resulting in a time-averaged global polar tidal torque that was significantly below the maximum torque observed for the modern land-water distribution (Figure 5.8a.5). This was despite the substantially smaller nominal tidal amplitude (Figure 5.8a.1) due to the smaller nominal tidal phase of about 20° (Figure 5.8a.2). The present finding underscored the significance of tidal phases for relativ high tidal torques, as detailed in Appendix D.1. Additionally, it demonstrated the capacity of the paleo land-water distributions to generate relatively high time-averaged global polar tidal torques. The decreasing resonance at the tidal force ~620 Myr ago yielded significantly smaller semi-diurnal tidal amplitudes across the entire open ocean, while tidal phases increased relatively moderately (Figures 5.2e to 5.2h). Evidence of this was clearly demonstrated in the nominal tides (Figure 5.8a.1 and Figure 5.8a.2), resulting in a pronounced decrease in the time-averaged global polar tidal torques of about 66 % and 40 % (Figure 5.8a.5 and Figures 5.10e to 5.10h).

For the land-water distribution ~750 Myr ago, significant interference patterns occurred in all four waveguides across the entire open ocean for the M_2 tidal force ~620 Myr ago and the modern day length (Figure 5.1f). In contrast to the tidal amplitudes, the nominal tidal amplitude demonstrated a decline (Figure 5.8a.1). Conversely, the decrease in tidal phases was evident in the nominal tidal phase in the second quadrant (Figure 5.8a.2). The resonance resulted in a notable pattern in the distribution of the time-averaged polar tidal torques per water column. The outer waveguides exhibited predominantly negative torques (Figure 5.9f). In the equatorial waveguides, however, the torques were predominantly positive. The torques as they occurred in the modern land-water distribution, have been attained and surpassed. In conjunction with the day length ~620 Myr ago, the interference had already diminished considerably (Figure 5.1h). The synergistic effect of nominal tide resulted in a substantial stronger time-averaged global polar tidal torque of approximately 72 %, accompanied by a transition from the weakest to the strongest level (Figure 5.8a.5).

The K_1 tides for the land-water distribution ~750 Myr ago (Figures 5.3b, 5.3d, 5.3f and 5.3h) illustrated the limited propagation potential with such a land-water distribution, which is accompanied by time-averaged global polar tidal torques at the weakest level (Figure 5.8b.5 and Figures 5.11b, 5.11d, 5.11f and 5.11h). The relatively short coastline and the absence of ocean basins resulted in a negligible tidal propagation by Kelvin waves. Even in the presence of interference from Poincaré waves in the equatorial wave guides, the

development of relatively high tidal torques is significantly limited. The zonal tidal forces would be deficient in this regard. The location of the supercontinent Rodinia around the South Pole, with two ocean basins in the land-water distributions ~630 Myr and ~600 Myr ago, enabled a much more pronounced propagation of K_1 tides through Kelvin waves. The development of the K_1 tides (Figure 5.4) and the quantities derived therefrom (Figures 5.8b and 5.12) with regard to tidal force and day length ~620 Myr ago was comparable to that of the semi-diurnal tides (Figures 5.2, 5.8a and 5.10). However, the nominal tidal phases deviated from this pattern (Figure 5.8b.5 and Figure 5.8a.5). When considered as a whole, this phenomenon could be attributed to the contribution of Kelvin waves to tidal propagation.

In the local context, the paleo land-water distributions could exhibit stronger time-averaged polar torques of the semi-diurnal and diurnal tides per water column relative to the modern torques (Figures 5.9f, 5.10a to 5.10d and 5.12a to 5.12d). Positive torques, which accelerate the Earth's rotation rate, occurred with greater frequency, particularly in the case of semi-diurnal tides. Even in their zonally integrated distributions, the paleo land-water distributions showed significantly stronger positive and negative torques. However, the net effect was that they largely canceled each other out. This indicates that paleo land-water distributions may be subject to stronger tidal torques compared to modern land-water distribution. Furthermore, given the extremely high opposing tidal torques per water column, particularly for the land-water distribution ~750 Myr ago with respect to M_2 tidal force ~620 Myr ago in conjunction with modern day length (Figure 5.9f), the question arises as to the extent to which tectonic activities could be triggered by these forces.

A striking similarity between the semi-diurnal and diurnal tides and the quantities derived therefrom for the similar land-water distributions ~630 Myr and ~600 Myr ago was found (Figures 5.2, 5.4, 5.8, 5.10 and 5.12). Additionally, the manner in which their nominal tides and their time-averaged global polar tidal torques responded to tidal force and day length ~620 Myr ago demonstrated a strong similarity to the response for the modern land-water distribution (Figure 5.8). One potential relationship to consider is the contribution of Kelvin waves to tidal propagation in the ocean basins due to Rodinia's location around the South Pole. In the context of the land-water distribution ~750 Myr ago, the response of semi-diurnal and diurnal nominal tides and time-averaged global polar tidal torques differed significantly (Figure 5.8). In all conditions, the lowest nominal tidal amplitudes were achieved with minimal fluctuations (Figure 5.8a.1 and Figure 5.8b.1) and nominal tidal phases with substantial variations (Figure 5.8a.2 and Figure 5.8b.2). The tidal propagation, which was predominantly characterized by Poincaré waves and, to a minor extent, by Kelvin waves due to Rodinia's equatorial location, suggests a potential correlation.

The Kelvin waves demonstrated a greater capacity to respond with interference in the various ocean basins of the modern land-water distribution, exhibiting greater stability in relation to tidal force and day length ~620 Myr ago compared with tidal propagation driven by Poincaré waves in the paleo land-water distributions. Consequently, a comparatively robust time-averaged global polar tidal torque was observed in all conditions. During a tectonically inactive period, torques of approximately equal magnitude could thus act. Given the variation in resonance conditions across various ocean basins, it is improbable that all basins would be affected simultaneously by a significant change in tides due to a change in the tidal (excitation) period and the day length. The phenomenon was particularly evident

in a nearly hemispherically open ocean, as evidenced by the paleo land-water distributions. However, a broader range was ascertained for the paleo land-water distributions.

A reliable example had been obtained by the effect of the single supercontinent Rodinia, which existed during most of the Neoproterozoic, on tidal friction. Further research could yield insights into the manner in which different land-water distributions and the nature of tidal propagation, predominantly influenced by these distributions, affect the secular changes in day length. This is of particular significance when considering the Earth's more distant past, which was marked by a predominant land distribution in the form of a single supercontinent.

Appendices

A.

A.1. Orbital elements

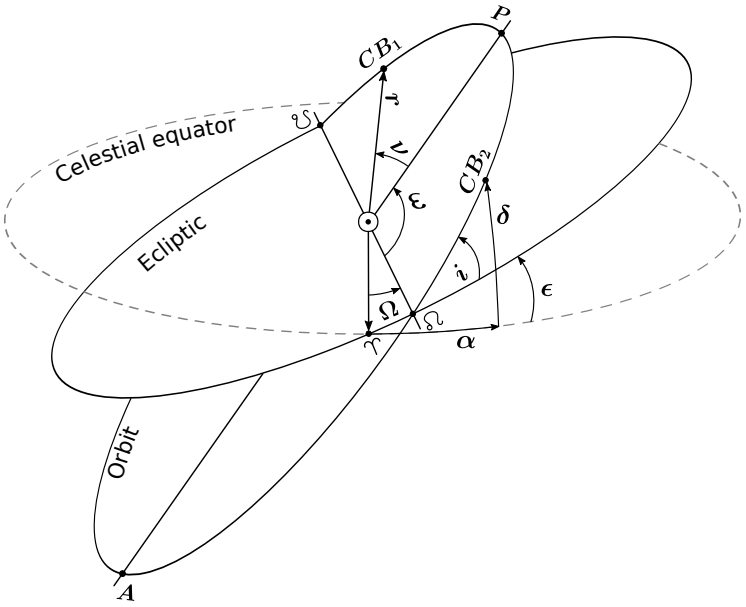

Figure A.1.: Orbital elements of the elliptical orbit of a celestial body (CB) around a central body.

The orbital elements of the elliptical orbit of a celestial body CB around a central body are shown in Figure A.1. The reference plane is the ecliptic in the case of the Sun ($\odot$) as the central body, as shown in the figure, and the equatorial plane in the case of the Earth. Where the celestial equator is the projection of the Earth's equator to the apparent *celestial sphere*. The angle at which the ecliptic plane and the equatorial plane are inclined is called the obliquity of the ecliptic ϵ. The two points of intersection of the Earth's orbit with the equatorial plane are called the vernal equinox Υ and *autumn equinox*, respectively. At the vernal equinox Υ, the Earth's orbit intersects the ecliptic from south to north. At the autumn equinox, the Earth's orbit intersects the ecliptic from north to south. The intersection points of the orbit of the celestial body with the reference plane are called nodes. At the ascending node ☊, the orbit intersects the reference plane from south to north. At the descending node ☋, the orbit intersects the reference plane from north to south. The intersection is called the *line of nodes*. The vertex of the orbital ellipse with the greatest distance to the central body is called *apoapsis* A and the one with the least is called *periapsis* P; both together are called apsides, their interconnecting line is called *apsidal line*. In the case of an orbit around the Sun, perihelion denotes the point closest to

the Sun and *aphelion* the point farthest from the Sun. In an orbit around the Earth, perigee is the point closest to the Earth and apogee is the point farthest from the Earth. The orbit is specified by the two orbital elements of the length of the major semi-major axis a and the numerical eccentricity e of the orbital ellipse, which are not shown in the figure. In addition, there are the four elements of orbital inclination i as the vertical inclination of the ellipse with respect to the reference plane measured at the ascending node, the longitude of the ascending node Ω as the horizontal orientation of the ascending node of the ellipse to the vernal equinox of the reference frame, the *argument of periapsis* ω as the angle measured from the ascending node to the periapsis defining the orientation of the ellipse in the orbital plane, and the *true anomaly* ν as the current angle of the celestial body to the periapsis measured at the center of gravity of the system. In the rotating equatorial coordinate system, the declination δ and *right ascension* α, measured from the vernal equinox, specify the position of the celestial body. The hour angle τ (not shown) is used in place of right ascension α in the fixed equatorial coordinate system. Where the hour angle τ is the angular distance of the celestial body from the meridian of the observer on the extended Earth and changes by about 2π per 24 h due to the Earth's rotation.

B.

B.1. Equilibrium tide

The surfaces with constant gravity potential $\Phi^{gravity} = const.$ are referred to as *equipotential surfaces* of gravity. Whereby the gravity $\Phi^{gravity}$ is related to the gravity acceleration by

$$\vec{\boldsymbol{g}} = \vec{\boldsymbol{\nabla}}\Phi^{gravity}.$$

Thus, the difference of gravity potential in the direction of an infinitesimal displacement $\mathrm{d}\vec{\mathbf{s}}$ is equal to the component of gravity acceleration along that direction:

$$\mathrm{d}\Phi^{gravity} = \vec{\boldsymbol{g}} \cdot \mathrm{d}\vec{\mathbf{s}} = g\,\mathrm{d}s\cos(\vec{\boldsymbol{g}}, \mathrm{d}\vec{\mathbf{s}}).$$

Since only the projection of $\mathrm{d}\vec{\mathbf{s}}$ onto the direction of gravity acceleration enters into the potential difference $\mathrm{d}\Phi^{gravity}$, it is independent of the path. As a result, a displacement along an equipotential surface $\Phi^{gravity} = const.$ does not require any work; the equipotential surfaces are equilibrium surfaces.

Based on the potential difference $\mathrm{d}\Phi^{gravity} = 0$ for a displacement $\mathrm{d}\vec{\mathbf{s}}$ along an equipotential surface, it follows that the projection of the displacement $\mathrm{d}\vec{\mathbf{s}}$ onto the direction of gravity acceleration $\cos(\vec{\boldsymbol{g}}, \mathrm{d}\vec{\mathbf{s}}) = \cos(90°) = 0$ vanishes and that gravity is normal to the equipotential surfaces. From a displacement $\mathrm{d}\vec{\mathbf{s}}$ along the outer surface normal $\vec{\mathbf{n}}$ follows with $\cos(\vec{\boldsymbol{g}}, \mathrm{d}\vec{\mathbf{n}}) = \cos(180°) = -1$ the relation of the difference of the gravity potential $\mathrm{d}\Phi^{gravity}$ with the difference in height of neighboring equipotential surfaces

$$\mathrm{d}\Phi^{gravity} = -g\,\mathrm{d}n \tag{B.1}$$

respectively the relation of a physical quantity with a geometrical quantity.

An equipotential surface of the gravity potential is superimposed by the astronomical tidal potential to

$$\Phi^{gravity} + \Phi^{t} = \Phi \tag{B.2}$$

and lifted by the height $\overline{\zeta}$. The lifted equilibrium surface is also called equilibrium tide. With Equation (B.1) is in good approximation (Bartels, 1957)

$$\Phi^{gravity} = \Phi + \overline{\zeta} \cdot \frac{\mathrm{d}\Phi^{gravity}}{\mathrm{d}n} = \Phi + \overline{\zeta} \cdot g.$$

Inserting into Equation (B.2) yields the height of the equilibrium tide

$$\overline{\zeta} = \frac{\Phi^t}{g}. \tag{B.3}$$

C.

C.1. Spherical expansion of tidal heights

An expansion of tidal amplitude ζ_σ^0 and tidal phase ϕ_σ (Equation (2.41)) in spherical surface functions

$$\zeta_\sigma^0 \cos\phi_\sigma = \sum_{s=1}^{\infty}\sum_{t=0}^{s}(a'_{st}\cos(t\lambda) + b'_{st}\sin(t\lambda))P_s^t(\sin\varphi) \tag{C.1}$$

$$\zeta_\sigma^0 \sin\phi_\sigma = \sum_{s=1}^{\infty}\sum_{t=0}^{s}(a''_{st}\cos(t\lambda) + b''_{st}\sin(t\lambda))P_s^t(\sin\varphi) \tag{C.2}$$

with the boundary condition $\zeta_\sigma = 0$ for the continents, allows the tidal oscillation system to be represented by spherical harmonics:

$$\zeta_\sigma = \sum_{s=1}^{\infty}\sum_{t=0}^{s}\sum_{-}^{+}\zeta_{st}^{\pm}\cos\Big(\sigma t \pm t\lambda - \epsilon_{st}^{\pm}\Big)P_s^t(\sin\varphi) \tag{C.3}$$

with the harmonic coefficients

$$\zeta_{st}^{\pm}\cos\epsilon_{st}^{\pm} = \frac{1}{2}(a'_{st} \mp b''_{st}) \tag{C.4}$$

$$\zeta_{st}^{\pm}\sin\epsilon_{st}^{\pm} = \frac{1}{2}(a''_{st} \pm b'_{st}). \tag{C.5}$$

The $P_s^t(\sin\varphi)$ are unnormalized associated Legendre function of degree s and order t. The summation $\sum_{-}^{+}$ stands for $\zeta_{st}^{-}\cos\Big(\sigma t - t\lambda - \epsilon_{st}^{-}\Big) + \zeta_{st}^{+}\cos\Big(\sigma t + t\lambda - \epsilon_{st}^{+}\Big)$; the first term yields an eastward (retrograde) propagating and the second term a westward (prograde) propagating component of the tidal wave. The prograde harmonic $\zeta_{\sigma,lm}^{+}, \epsilon_{\sigma,lm}^{+}$ of the same degree $s = l$ and order $t = m$ as that of the exciting tidal constituent of the astronomical tidal potential (Equations (2.24) and (2.27)) gives the nominal ocean tide.

D.

D.1. Polar tidal torque of harmonic tides

The interaction of a harmonic partial tide (Equation (2.27)) with the harmonic component of the ocean tides (Equation (2.41)) has the potential to exert a polar torque on the Earth's rotation rate (Equation (2.6)). When integrating over one tidal period T_σ, the global polar tidal torque for barotropic tides becomes

$$\langle \overline{M_{t,z}} \rangle = \varrho \int_V \int_{T_\sigma} \frac{\partial \Phi_\sigma^t}{\partial \lambda} \, \mathrm{d}t \, \mathrm{d}V, \tag{D.1}$$

where ϱ is the mean density of sea water. The ocean's volume elements are given by

$$\mathrm{d}V = H(\varphi, \lambda) \mathrm{d}S, \tag{D.2}$$

the ocean's surface elements are given by

$$\mathrm{d}S = \cos\varphi \, \mathrm{d}\lambda \, \mathrm{d}\varphi, \tag{D.3}$$

the tidally disturbed height of the water column is given by

$$H(\varphi, \lambda) = D(\varphi, \lambda) + \zeta_\sigma(\varphi, \lambda, t), \tag{D.4}$$

with the undisturbed depth D, and the harmonic tidal elevation (Equation (2.41)) employing the addition theorem for cosines

$$\zeta_\sigma(\varphi, \lambda, t) = \zeta_\sigma^0(\varphi, \lambda) \Big(\cos(\sigma_\sigma t) \cos(\phi_\sigma(\varphi, \lambda)) + \sin(\sigma_\sigma t) \sin(\phi_\sigma(\varphi, \lambda)) \Big). \tag{D.5}$$

According to the addition theorem for cosines, the partial tide (Equation (2.27)) is expressed as

$$\Phi_\sigma^t = c_\sigma \, G_A(\varphi) \Big(\cos(\sigma_\sigma t) \cos(A\lambda) - \sin(\sigma_\sigma t) \sin(A\lambda) \Big), \tag{D.6}$$

and its zonal partial derivative is defined as

$$\frac{\partial \Phi_\sigma^t}{\partial \lambda} = c_\sigma \, G_A(\varphi) A \Big(- \cos(\sigma_\sigma t) \sin(A\lambda) - \sin(\sigma_\sigma t) \cos(A\lambda) \Big). \tag{D.7}$$

For the sake of convenience, t is used to denote the mean solar time along the Greenwich meridian. In conjunction with the aforementioned quantities, the time-averaged global polar tidal torque comprises two distinct components: one stemming from the undisturbed ocean depth and another stemming from the tides.

The contribution from the individual undisturbed water columns

$$\langle\overline{M_{t,z,D}}\rangle = \varrho\, c_\sigma A \int_S D(\varphi,\lambda)\, G_A(\varphi) \times \int_{T_\sigma} \Big(-\cos(\sigma_\sigma t_0)\sin(A\lambda) - \sin(\sigma_\sigma t_0)\cos(A\lambda)\Big)\mathrm{d}t\cos\varphi\,\mathrm{d}\lambda\,\mathrm{d}\varphi, \tag{D.8}$$

when integrated across the tidal period

$$\langle\overline{M_{t,z,D}}\rangle = \varrho\, c_\sigma A \int_S D(\varphi,\lambda)\, G_A(\varphi) \times \Big(\big(-\sin(2\pi)+\sin(0)\big)\sin(A\lambda) + \big(\cos(2\pi)-\cos(0)\big)\cos(A\lambda)\Big) \tag{D.9}$$

$$\times \cos\varphi\,\mathrm{d}\lambda\,\mathrm{d}\varphi \tag{D.10}$$

$$\langle\overline{M_{t,z,D}}\rangle = 0\cdot\varrho\, c_\sigma A \int_S D(\varphi,\lambda)\, G_A(\varphi)\,\cos\varphi\,\mathrm{d}\lambda\,\mathrm{d}\varphi \tag{D.11}$$

is equal to zero. Consequently, the integration across the ocean surface

$$\langle\overline{M_{t,z,D}}\rangle = 0 \tag{D.12}$$

also vanishes.

The contribution from the individual disturbed water columns

$$\langle\overline{M_{t,z,\zeta}}\rangle = \varrho\, c_\sigma A \int_S \zeta_\sigma^0(\varphi,\lambda)\, G_A(\varphi) \int_{T_\sigma} \Big(\cos(\sigma_\sigma t)\cos(\phi_\sigma(\varphi,\lambda)) + \sin(\sigma_\sigma t)\sin(\phi_\sigma(\varphi,\lambda))\Big) \times \Big(-\cos(\sigma_\sigma t_0)\sin(A\lambda) - \sin(\sigma_\sigma t_0)\cos(A\lambda)\Big)\mathrm{d}t\cos\varphi\,\mathrm{d}\lambda\,\mathrm{d}\varphi, \tag{D.13}$$

when integrated across the tidal period results in

$$\begin{aligned}\langle\overline{M_{t,z,\zeta}}\rangle = {}& \varrho\, c_\sigma A \int_S \zeta_\sigma^0(\varphi,\lambda)\, G_A(\varphi) \\ & \times \Big(-\Big(\frac{1}{2}\cdot 2\pi - \frac{1}{2}\cdot 0 + \frac{1}{4}\sin(2\cdot 2\pi) - \frac{1}{4}\sin(2\cdot 0)\Big)\cos(\phi_\sigma(\varphi,\lambda))\sin(A\lambda) \\ & - \Big(\frac{1}{2}\sin^2(2\pi) - \frac{1}{2}\sin^2(0)\Big)\cos(\phi_\sigma(\varphi,\lambda))\cos(A\lambda) \\ & - \Big(\frac{1}{2}\sin^2(2\pi) - \frac{1}{2}\sin^2(0)\Big)\sin(\phi_\sigma(\varphi,\lambda))\sin(A\lambda) \\ & - \Big(\frac{1}{2}\cdot 2\pi - \frac{1}{2}\cdot 0 - \frac{1}{4}\sin(2\cdot 2\pi) + \frac{1}{4}\sin(2\cdot 0)\Big)\sin(\phi_\sigma(\varphi,\lambda))\cos(A\lambda)\Big) \\ & \times \cos\varphi\,\mathrm{d}\lambda\,\mathrm{d}\varphi \end{aligned} \tag{D.14}$$

$$\langle\overline{M_{t,z,\zeta}}\rangle = \varrho\, c_\sigma A \int_S \zeta_\sigma^0(\varphi,\lambda)\, G_A(\varphi) \times \Big(-\pi\left(\cos(\phi_\sigma(\varphi,\lambda))\sin(A\lambda) + \sin(\phi_\sigma(\varphi,\lambda))\cos(A\lambda)\right)\Big)\cos\varphi\,\mathrm{d}\lambda\,\mathrm{d}\varphi, \tag{D.15}$$

and applying the addition theorem for cosines yields

$$\langle\overline{M_{t,z,\zeta}}\rangle = -\pi\varrho\, c_\sigma A \int_S \zeta_\sigma^0(\varphi,\lambda)\, G_A(\varphi)\sin(\phi_\sigma(\varphi,\lambda) + A\lambda)\cos\varphi\,\mathrm{d}\lambda\,\mathrm{d}\varphi. \tag{D.16}$$

Figure D.1 illustrates the tidal torques normalized to 1 of a water column disturbed by harmonic tides, i. e., the contribution form the tidal phase ϕ_σ and the partial tide phase $A\lambda$ (Equation (D.16)) The contribution vanishes whenever the tidal phase

$$0 \leq \phi_\sigma(\varphi, \lambda) = n\pi - A\lambda < 2\pi, \quad \text{where} \quad n = 1, 2, \ldots. \tag{D.17}$$

is equal to an integer multiple of π minus the partial tide phase $A\lambda$. The longitude ranges from $0 \leq \lambda < 2\pi$. This occurrence is precisely evidenced on two separate instance. There is one occurrence for the first n, for which the tidal phase ϕ_σ becomes positive, and subsequently for this first $n + 1$. That is to say, when the high tide or the low tide of the water column is aligned with the tide-generating body. The intervals

$$0 \leq \qquad 2n\pi - A\lambda < \phi_\sigma(\varphi, \lambda) < (2n + 1)\pi - A\lambda < 2\pi \tag{D.18}$$

and

$$0 \leq (2n - 1)\pi - A\lambda < \phi_\sigma(\varphi, \lambda) < \qquad 2n\pi - A\lambda < 2\pi, \tag{D.19}$$

in conjunction with the associated geodetic function $G_A(\varphi)$ of the partial tide (Equation (2.27) and Table 2.3), i. e. depending on the latitude φ, establish the direction of the tidal torque (Equation (D.16)). Table D.1 presents the tidal phases with negative and positive tidal torque for both diurnal ($A = 1$) and semi-diurnal ($A = 2$) tides. In the event, at the time when the maximum partial tide acts on the water column, the high tide of the water column is behind the partial tide, a negative tidal torque occurs. In circumstances where the high tide is ahead the partial tide, the resultant tidal torque is positive.

Table D.1.: Tidal phases ϕ_σ with negative and positive time-averaged polar tidal torque $\overline{M_{t,z,\zeta}}$ per water column for diurnal ($A = 1$) and semi-diurnal tides ($A = 2$).

ϕ_σ	$A = 1$		$A = 2$
	$-90° \leq \varphi < 0°$	$0° < \varphi \leq 90°$	$-90° \leq \varphi \leq 90°$
Equation (D.18)	$\overline{M_{t,z,\zeta}} > 0$	$\overline{M_{t,z,\zeta}} < 0$	$\overline{M_{t,z,\zeta}} < 0$
Equation (D.19)	$\overline{M_{t,z,\zeta}} < 0$	$\overline{M_{t,z,\zeta}} > 0$	$\overline{M_{t,z,\zeta}} > 0$

Tidal phase Φ (°) \ Longitude λ (°)	0	15	30	45	60	75	90	105	120	135	150	165	180	195	210	225	240	255	270	285	300	315	330	345	360
0	0.000	0.500	0.866	1.000	0.866	0.500	0.000	-0.500	-0.866	-1.000	-0.866	-0.500	0.000	0.500	0.866	1.000	0.866	0.500	0.000	-0.500	-0.866	-1.000	-0.866	-0.500	0.000
15	0.259	0.707	0.966	0.966	0.707	0.259	-0.259	-0.707	-0.966	-0.966	-0.707	-0.259	0.259	0.707	0.966	0.966	0.707	0.259	-0.259	-0.707	-0.966	-0.966	-0.707	-0.259	0.259
30	0.500	0.866	1.000	0.866	0.500	0.000	-0.500	-0.866	-1.000	-0.866	-0.500	0.000	0.500	0.866	1.000	0.866	0.500	0.000	-0.500	-0.866	-1.000	-0.866	-0.500	0.000	0.500
45	0.707	0.966	0.966	0.707	0.259	-0.259	-0.707	-0.966	-0.966	-0.707	-0.259	0.259	0.707	0.966	0.966	0.707	0.259	-0.259	-0.707	-0.966	-0.966	-0.707	-0.259	0.259	0.707
60	0.866	1.000	0.866	0.500	0.000	-0.500	-0.866	-1.000	-0.866	-0.500	0.000	0.500	0.866	1.000	0.866	0.500	0.000	-0.500	-0.866	-1.000	-0.866	-0.500	0.000	0.500	0.866
75	0.966	0.966	0.707	0.259	-0.259	-0.707	-0.966	-0.966	-0.707	-0.259	0.259	0.707	0.966	0.966	0.707	0.259	-0.259	-0.707	-0.966	-0.966	-0.707	-0.259	0.259	0.707	0.966
90	1.000	0.866	0.500	0.000	-0.500	-0.866	-1.000	-0.866	-0.500	0.000	0.500	0.866	1.000	0.866	0.500	0.000	-0.500	-0.866	-1.000	-0.866	-0.500	0.000	0.500	0.866	1.000
105	0.966	0.707	0.259	-0.259	-0.707	-0.966	-0.966	-0.707	-0.259	0.259	0.707	0.966	0.966	0.707	0.259	-0.259	-0.707	-0.966	-0.966	-0.707	-0.259	0.259	0.707	0.966	0.966
120	0.866	0.500	0.000	-0.500	-0.866	-1.000	-0.866	-0.500	0.000	0.500	0.866	1.000	0.866	0.500	0.000	-0.500	-0.866	-1.000	-0.866	-0.500	0.000	0.500	0.866	1.000	0.866
135	0.707	0.259	-0.259	-0.707	-0.966	-0.966	-0.707	-0.259	0.259	0.707	0.966	0.966	0.707	0.259	-0.259	-0.707	-0.966	-0.966	-0.707	-0.259	0.259	0.707	0.966	0.966	0.707
150	0.500	0.000	-0.500	-0.866	-1.000	-0.866	-0.500	0.000	0.500	0.866	1.000	0.866	0.500	0.000	-0.500	-0.866	-1.000	-0.866	-0.500	0.000	0.500	0.866	1.000	0.866	0.500
165	0.259	-0.259	-0.707	-0.966	-0.966	-0.707	-0.259	0.259	0.707	0.966	0.966	0.707	0.259	-0.259	-0.707	-0.966	-0.966	-0.707	-0.259	0.259	0.707	0.966	0.966	0.707	0.259
180	0.000	-0.500	-0.866	-1.000	-0.866	-0.500	0.000	0.500	0.866	1.000	0.866	0.500	0.000	-0.500	-0.866	-1.000	-0.866	-0.500	0.000	0.500	0.866	1.000	0.866	0.500	0.000
195	-0.259	-0.707	-0.966	-0.966	-0.707	-0.259	0.259	0.707	0.966	0.966	0.707	0.259	-0.259	-0.707	-0.966	-0.966	-0.707	-0.259	0.259	0.707	0.966	0.966	0.707	0.259	-0.259
210	-0.500	-0.866	-1.000	-0.866	-0.500	0.000	0.500	0.866	1.000	0.866	0.500	0.000	-0.500	-0.866	-1.000	-0.866	-0.500	0.000	0.500	0.866	1.000	0.866	0.500	0.000	-0.500
225	-0.707	-0.966	-0.966	-0.707	-0.259	0.259	0.707	0.966	0.966	0.707	0.259	-0.259	-0.707	-0.966	-0.966	-0.707	-0.259	0.259	0.707	0.966	0.966	0.707	0.259	-0.259	-0.707
240	-0.866	-1.000	-0.866	-0.500	0.000	0.500	0.866	1.000	0.866	0.500	0.000	-0.500	-0.866	-1.000	-0.866	-0.500	0.000	0.500	0.866	1.000	0.866	0.500	0.000	-0.500	-0.866
255	-0.966	-0.966	-0.707	-0.259	0.259	0.707	0.966	0.966	0.707	0.259	-0.259	-0.707	-0.966	-0.966	-0.707	-0.259	0.259	0.707	0.966	0.966	0.707	0.259	-0.259	-0.707	-0.966
270	-1.000	-0.866	-0.500	0.000	0.500	0.866	1.000	0.866	0.500	0.000	-0.500	-0.866	-1.000	-0.866	-0.500	0.000	0.500	0.866	1.000	0.866	0.500	0.000	-0.500	-0.866	-1.000
285	-0.966	-0.707	-0.259	0.259	0.707	0.966	0.966	0.707	0.259	-0.259	-0.707	-0.966	-0.966	-0.707	-0.259	0.259	0.707	0.966	0.966	0.707	0.259	-0.259	-0.707	-0.966	-0.966
300	-0.866	-0.500	0.000	0.500	0.866	1.000	0.866	0.500	0.000	-0.500	-0.866	-1.000	-0.866	-0.500	0.000	0.500	0.866	1.000	0.866	0.500	0.000	-0.500	-0.866	-1.000	-0.866
315	-0.707	-0.259	0.259	0.707	0.966	0.966	0.707	0.259	-0.259	-0.707	-0.966	-0.966	-0.707	-0.259	0.259	0.707	0.966	0.966	0.707	0.259	-0.259	-0.707	-0.966	-0.966	-0.707
330	-0.500	0.000	0.500	0.866	1.000	0.866	0.500	0.000	-0.500	-0.866	-1.000	-0.866	-0.500	0.000	0.500	0.866	1.000	0.866	0.500	0.000	-0.500	-0.866	-1.000	-0.866	-0.500
345	-0.259	0.259	0.707	0.966	0.966	0.707	0.259	-0.259	-0.707	-0.966	-0.966	-0.707	-0.259	0.259	0.707	0.966	0.966	0.707	0.259	-0.259	-0.707	-0.966	-0.966	-0.707	-0.259
360	0.000	0.500	0.866	1.000	0.866	0.500	0.000	-0.500	-0.866	-1.000	-0.866	-0.500	0.000	0.500	0.866	1.000	0.866	0.500	0.000	-0.500	-0.866	-1.000	-0.866	-0.500	0.000

(a) $A = 2$, semi-diurnal tides for $-90° \leq \varphi \leq 90°$.

Tidal phase Φ (°) \ Longitude λ (°)	0	15	30	45	60	75	90	105	120	135	150	165	180	195	210	225	240	255	270	285	300	315	330	345	360
0	0.000	0.259	0.500	0.707	0.866	0.966	1.000	0.966	0.866	0.707	0.500	0.259	0.000	-0.259	-0.500	-0.707	-0.866	-0.966	-1.000	-0.966	-0.866	-0.707	-0.500	-0.259	0.000
15	0.259	0.500	0.707	0.866	0.966	1.000	0.966	0.866	0.707	0.500	0.259	0.000	-0.259	-0.500	-0.707	-0.866	-0.966	-1.000	-0.966	-0.866	-0.707	-0.500	-0.259	0.000	0.259
30	0.500	0.707	0.866	0.966	1.000	0.966	0.866	0.707	0.500	0.259	0.000	-0.259	-0.500	-0.707	-0.866	-0.966	-1.000	-0.966	-0.866	-0.707	-0.500	-0.259	0.000	0.259	0.500
45	0.707	0.866	0.966	1.000	0.966	0.866	0.707	0.500	0.259	0.000	-0.259	-0.500	-0.707	-0.866	-0.966	-1.000	-0.966	-0.866	-0.707	-0.500	-0.259	0.000	0.259	0.500	0.707
60	0.866	0.966	1.000	0.966	0.866	0.707	0.500	0.259	0.000	-0.259	-0.500	-0.707	-0.866	-0.966	-1.000	-0.966	-0.866	-0.707	-0.500	-0.259	0.000	0.259	0.500	0.707	0.866
75	0.966	1.000	0.966	0.866	0.707	0.500	0.259	0.000	-0.259	-0.500	-0.707	-0.866	-0.966	-1.000	-0.966	-0.866	-0.707	-0.500	-0.259	0.000	0.259	0.500	0.707	0.866	0.966
90	1.000	0.966	0.866	0.707	0.500	0.259	0.000	-0.259	-0.500	-0.707	-0.866	-0.966	-1.000	-0.966	-0.866	-0.707	-0.500	-0.259	0.000	0.259	0.500	0.707	0.866	0.966	1.000
105	0.966	0.866	0.707	0.500	0.259	0.000	-0.259	-0.500	-0.707	-0.866	-0.966	-1.000	-0.966	-0.866	-0.707	-0.500	-0.259	0.000	0.259	0.500	0.707	0.866	0.966	1.000	0.966
120	0.866	0.707	0.500	0.259	0.000	-0.259	-0.500	-0.707	-0.866	-0.966	-1.000	-0.966	-0.866	-0.707	-0.500	-0.259	0.000	0.259	0.500	0.707	0.866	0.966	1.000	0.966	0.866
135	0.707	0.500	0.259	0.000	-0.259	-0.500	-0.707	-0.866	-0.966	-1.000	-0.966	-0.866	-0.707	-0.500	-0.259	0.000	0.259	0.500	0.707	0.866	0.966	1.000	0.966	0.866	0.707
150	0.500	0.259	0.000	-0.259	-0.500	-0.707	-0.866	-0.966	-1.000	-0.966	-0.866	-0.707	-0.500	-0.259	0.000	0.259	0.500	0.707	0.866	0.966	1.000	0.966	0.866	0.707	0.500
165	0.259	0.000	-0.259	-0.500	-0.707	-0.866	-0.966	-1.000	-0.966	-0.866	-0.707	-0.500	-0.259	0.000	0.259	0.500	0.707	0.866	0.966	1.000	0.966	0.866	0.707	0.500	0.259
180	0.000	-0.259	-0.500	-0.707	-0.866	-0.966	-1.000	-0.966	-0.866	-0.707	-0.500	-0.259	0.000	0.259	0.500	0.707	0.866	0.966	1.000	0.966	0.866	0.707	0.500	0.259	0.000
195	-0.259	-0.500	-0.707	-0.866	-0.966	-1.000	-0.966	-0.866	-0.707	-0.500	-0.259	0.000	0.259	0.500	0.707	0.866	0.966	1.000	0.966	0.866	0.707	0.500	0.259	0.000	-0.259
210	-0.500	-0.707	-0.866	-0.966	-1.000	-0.966	-0.866	-0.707	-0.500	-0.259	0.000	0.259	0.500	0.707	0.866	0.966	1.000	0.966	0.866	0.707	0.500	0.259	0.000	-0.259	-0.500
225	-0.707	-0.866	-0.966	-1.000	-0.966	-0.866	-0.707	-0.500	-0.259	0.000	0.259	0.500	0.707	0.866	0.966	1.000	0.966	0.866	0.707	0.500	0.259	0.000	-0.259	-0.500	-0.707
240	-0.866	-0.966	-1.000	-0.966	-0.866	-0.707	-0.500	-0.259	0.000	0.259	0.500	0.707	0.866	0.966	1.000	0.966	0.866	0.707	0.500	0.259	0.000	-0.259	-0.500	-0.707	-0.866
255	-0.966	-1.000	-0.966	-0.866	-0.707	-0.500	-0.259	0.000	0.259	0.500	0.707	0.866	0.966	1.000	0.966	0.866	0.707	0.500	0.259	0.000	-0.259	-0.500	-0.707	-0.866	-0.966
270	-1.000	-0.966	-0.866	-0.707	-0.500	-0.259	0.000	0.259	0.500	0.707	0.866	0.966	1.000	0.966	0.866	0.707	0.500	0.259	0.000	-0.259	-0.500	-0.707	-0.866	-0.966	-1.000
285	-0.966	-0.866	-0.707	-0.500	-0.259	0.000	0.259	0.500	0.707	0.866	0.966	1.000	0.966	0.866	0.707	0.500	0.259	0.000	-0.259	-0.500	-0.707	-0.866	-0.966	-1.000	-0.966
300	-0.866	-0.707	-0.500	-0.259	0.000	0.259	0.500	0.707	0.866	0.966	1.000	0.966	0.866	0.707	0.500	0.259	0.000	-0.259	-0.500	-0.707	-0.866	-0.966	-1.000	-0.966	-0.866
315	-0.707	-0.500	-0.259	0.000	0.259	0.500	0.707	0.866	0.966	1.000	0.966	0.866	0.707	0.500	0.259	0.000	-0.259	-0.500	-0.707	-0.866	-0.966	-1.000	-0.966	-0.866	-0.707
330	-0.500	-0.259	0.000	0.259	0.500	0.707	0.866	0.966	1.000	0.966	0.866	0.707	0.500	0.259	0.000	-0.259	-0.500	-0.707	-0.866	-0.966	-1.000	-0.966	-0.866	-0.707	-0.500
345	-0.259	0.000	0.259	0.500	0.707	0.866	0.966	1.000	0.966	0.866	0.707	0.500	0.259	0.000	-0.259	-0.500	-0.707	-0.866	-0.966	-1.000	-0.966	-0.866	-0.707	-0.500	-0.259
360	0.000	0.259	0.500	0.707	0.866	0.966	1.000	0.966	0.866	0.707	0.500	0.259	0.000	-0.259	-0.500	-0.707	-0.866	-0.966	-1.000	-0.966	-0.866	-0.707	-0.500	-0.259	0.000

(b) $A = 1$, diurnal tides for $0° < \varphi \leq 90°$.

Tidal phase Φ (°) \ Longitude λ (°)	0	15	30	45	60	75	90	105	120	135	150	165	180	195	210	225	240	255	270	285	300	315	330	345	360
0	0.000	-0.259	-0.500	-0.707	-0.866	-0.966	-1.000	-0.966	-0.866	-0.707	-0.500	-0.259	0.000	0.259	0.500	0.707	0.866	0.966	1.000	0.966	0.866	0.707	0.500	0.259	0.000
15	-0.259	-0.500	-0.707	-0.866	-0.966	-1.000	-0.966	-0.866	-0.707	-0.500	-0.259	0.000	0.259	0.500	0.707	0.866	0.966	1.000	0.966	0.866	0.707	0.500	0.259	0.000	-0.259
30	-0.500	-0.707	-0.866	-0.966	-1.000	-0.966	-0.866	-0.707	-0.500	-0.259	0.000	0.259	0.500	0.707	0.866	0.966	1.000	0.966	0.866	0.707	0.500	0.259	0.000	-0.259	-0.500
45	-0.707	-0.866	-0.966	-1.000	-0.966	-0.866	-0.707	-0.500	-0.259	0.000	0.259	0.500	0.707	0.866	0.966	1.000	0.966	0.866	0.707	0.500	0.259	0.000	-0.259	-0.500	-0.707
60	-0.866	-0.966	-1.000	-0.966	-0.866	-0.707	-0.500	-0.259	0.000	0.259	0.500	0.707	0.866	0.966	1.000	0.966	0.866	0.707	0.500	0.259	0.000	-0.259	-0.500	-0.707	-0.866
75	-0.966	-1.000	-0.966	-0.866	-0.707	-0.500	-0.259	0.000	0.259	0.500	0.707	0.866	0.966	1.000	0.966	0.866	0.707	0.500	0.259	0.000	-0.259	-0.500	-0.707	-0.866	-0.966
90	-1.000	-0.966	-0.866	-0.707	-0.500	-0.259	0.000	0.259	0.500	0.707	0.866	0.966	1.000	0.966	0.866	0.707	0.500	0.259	0.000	-0.259	-0.500	-0.707	-0.866	-0.966	-1.000
105	-0.966	-0.866	-0.707	-0.500	-0.259	0.000	0.259	0.500	0.707	0.866	0.966	1.000	0.966	0.866	0.707	0.500	0.259	0.000	-0.259	-0.500	-0.707	-0.866	-0.966	-1.000	-0.966
120	-0.866	-0.707	-0.500	-0.259	0.000	0.259	0.500	0.707	0.866	0.966	1.000	0.966	0.866	0.707	0.500	0.259	0.000	-0.259	-0.500	-0.707	-0.866	-0.966	-1.000	-0.966	-0.866
135	-0.707	-0.500	-0.259	0.000	0.259	0.500	0.707	0.866	0.966	1.000	0.966	0.866	0.707	0.500	0.259	0.000	-0.259	-0.500	-0.707	-0.866	-0.966	-1.000	-0.966	-0.866	-0.707
150	-0.500	-0.259	0.000	0.259	0.500	0.707	0.866	0.966	1.000	0.966	0.866	0.707	0.500	0.259	0.000	-0.259	-0.500	-0.707	-0.866	-0.966	-1.000	-0.966	-0.866	-0.707	-0.500
165	-0.259	0.000	0.259	0.500	0.707	0.866	0.966	1.000	0.966	0.866	0.707	0.500	0.259	0.000	-0.259	-0.500	-0.707	-0.866	-0.966	-1.000	-0.966	-0.866	-0.707	-0.500	-0.259
180	0.000	0.259	0.500	0.707	0.866	0.966	1.000	0.966	0.866	0.707	0.500	0.259	0.000	-0.259	-0.500	-0.707	-0.866	-0.966	-1.000	-0.966	-0.866	-0.707	-0.500	-0.259	0.000
195	0.259	0.500	0.707	0.866	0.966	1.000	0.966	0.866	0.707	0.500	0.259	0.000	-0.259	-0.500	-0.707	-0.866	-0.966	-1.000	-0.966	-0.866	-0.707	-0.500	-0.259	0.000	0.259
210	0.500	0.707	0.866	0.966	1.000	0.966	0.866	0.707	0.500	0.259	0.000	-0.259	-0.500	-0.707	-0.866	-0.966	-1.000	-0.966	-0.866	-0.707	-0.500	-0.259	0.000	0.259	0.500
225	0.707	0.866	0.966	1.000	0.966	0.866	0.707	0.500	0.259	0.000	-0.259	-0.500	-0.707	-0.866	-0.966	-1.000	-0.966	-0.866	-0.707	-0.500	-0.259	0.000	0.259	0.500	0.707
240	0.866	0.966	1.000	0.966	0.866	0.707	0.500	0.259	0.000	-0.259	-0.500	-0.707	-0.866	-0.966	-1.000	-0.966	-0.866	-0.707	-0.500	-0.259	0.000	0.259	0.500	0.707	0.866
255	0.966	1.000	0.966	0.866	0.707	0.500	0.259	0.000	-0.259	-0.500	-0.707	-0.866	-0.966	-1.000	-0.966	-0.866	-0.707	-0.500	-0.259	0.000	0.259	0.500	0.707	0.866	0.966
270	1.000	0.966	0.866	0.707	0.500	0.259	0.000	-0.259	-0.500	-0.707	-0.866	-0.966	-1.000	-0.966	-0.866	-0.707	-0.500	-0.259	0.000	0.259	0.500	0.707	0.866	0.966	1.000
285	0.966	0.866	0.707	0.500	0.259	0.000	-0.259	-0.500	-0.707	-0.866	-0.966	-1.000	-0.966	-0.866	-0.707	-0.500	-0.259	0.000	0.259	0.500	0.707	0.866	0.966	1.000	0.966
300	0.866	0.707	0.500	0.259	0.000	-0.259	-0.500	-0.707	-0.866	-0.966	-1.000	-0.966	-0.866	-0.707	-0.500	-0.259	0.000	0.259	0.500	0.707	0.866	0.966	1.000	0.966	0.866
315	0.707	0.500	0.259	0.000	-0.259	-0.500	-0.707	-0.866	-0.966	-1.000	-0.966	-0.866	-0.707	-0.500	-0.259	0.000	0.259	0.500	0.707	0.866	0.966	1.000	0.966	0.866	0.707
330	0.500	0.259	0.000	-0.259	-0.500	-0.707	-0.866	-0.966	-1.000	-0.966	-0.866	-0.707	-0.500	-0.259	0.000	0.259	0.500	0.707	0.866	0.966	1.000	0.966	0.866	0.707	0.500
345	0.259	0.000	-0.259	-0.500	-0.707	-0.866	-0.966	-1.000	-0.966	-0.866	-0.707	-0.500	-0.259	0.000	0.259	0.500	0.707	0.866	0.966	1.000	0.966	0.866	0.707	0.500	0.259
360	0.000	-0.259	-0.500	-0.707	-0.866	-0.966	-1.000	-0.966	-0.866	-0.707	-0.500	-0.259	0.000	0.259	0.500	0.707	0.866	0.966	1.000	0.966	0.866	0.707	0.500	0.259	0.000

(c) $A = 1$, diurnal tides for $-90° \leq \varphi < 0°$.

Figure D.1.: Tidal torque of a water column disturbed by harmonic tides (Equation (D.16)), normalized to 1 ($\sin(\phi_\sigma(\varphi, \lambda) + A\lambda)$). Negative tidal torques are shown in orange, positive tidal torques in green, and vanishing tidal torques in yellow.

Glossary

anomalistic month The time it takes the *see* mean Moon to revolve once in its orbit around the Earth relative to the *see* perigee. Its current value is 27.55 d. Due to the *see apsidal precessing* of the Moon's orbit with a period currently of about 8.85 yr, the perigee moves in the same direction as the Moon in its orbit around Earth. Thus, the anomalistic month is currently longer than the *see* sidereal month.

anomalistic year The time it takes the *see mean Earth* to revolve once in its orbit around the Sun relative to the *see* perihelion. Its current value is 365.2596 d. Due to the *see* apsidal precessing of the Earth's orbit with a period currently of about 112 000 yr, the perihelion moves in the same direction as the Earth in its orbit around the Sun. Thus, the anomalistic year is currently 4 min and 40 s longer than the *see* sidereal year.

aphelion The *see* apoapsis in the case of the Sun as the central body of the orbital ellipse.

apoapsis The vertex of the orbital ellipse with the greatest distance to the central body.

apogee The apoapsis in the case of the Earth as the central body of the orbital ellipse.

apsidal line The line joining the *see* apoapsis and *see* periapsis.

apsidal precessing The precession of the *see* apsidal line.

Archean The second of four *see* Eons in Earth's history, representing the time from ~4000 Myr to 2500 Myr ago.

argument of periapsis The angle measured from the *see* ascending node to the *see* periapsis defining the orientation of the orbit in the orbital plane.

ascending node The elliptical orbit intersects the reference plane in the ascending node from south to north.

autumn equinox The Earth's orbit intersects the *see* ecliptic at the autumn equinox from north to south. Due to *see* Earth's lunisolar precession and *see* nutation, the autumn equinox is precessing in the opposition to the Earth's and Moon's orbital direction.

celestial equator The projection of Earth's equator to the apparent *see* celestial sphere.

celestial pole The projection of Earth's own poles to the apparent *see* celestial sphere.

celestial sphere An imaginary sphere centered on Earth of infinite radius on which the stars seem to be fixed.

day *see* mean solar day.

declination The angular distance of a point above the Earth north or south of the *see* celestial equator measured along a *see hour circle* passing through the point in question. Declination is the south-north coordinate that locate a point on the *see* celestial sphere in the *see equatorial coordinate system*.

descending node The elliptical orbit intersects the reference plane in the descending node from north to south.

Earth axis The rotation axis of the Earth.

Earth's lunisolar precession The *see* Earth axis is inclined by about 23.5° and the Moon's orbit about 5.1° relative to the *see* ecliptic. Thus, the gravitational forces of the Sun and the Moon act with a torque on the equatorial bulge of the Earth, which tries to upright the Earth axis. Along with the Earth's moment of inertia, which tries to dodge the uplifting pull perpendicularly, the precession of the Earth axis around the *see* ecliptic poles against the Earth's rotation with a current period of about 25 800 yr results. The displacement of the Earth axis is only about 50″ per year, but can add up to considerable size over longer periods of time. Superimposed on this is the *see* nutation.

ecliptic The plane of the Earth's orbit around the Sun.

ecliptic pole One of the two points of intersection of the *see* celestial sphere with a straight line passing through the center of the Earth and perpendicular to the *see* ecliptic.

Eon The name for the highest-ranking unit in the subdivision of the Earth's history. Eons always cover several hundred million to far more than one billion years. Four eons are distinguished: Hadean (~4600 Myr to 4000 Myr ago), *see* Archean (~4000 Myr to 2500 Myr ago), *see* Proterozoic (~2500 Myr to 539 Myr ago), *see* Phanerozoic (~539 Myr to 0 Myr ago). The first three eons together are also called *see* Precambrian.

equatorial bulge The shape and size of the Earth can be represented geometrically by an ellipsoid with an equatorial bulge and a flattening at the poles. The difference between the equatorial radius and the polar radius is 21 km, and the flattening is about $^1/_{300}$, with the mean Earth radius being 6371 km (Moritz, 2000).

equatorial coordinate system The rotating and the fixed geocentric coordinate systems on the *see* celestial sphere. With reference to the *see* celestial equator and *see celestial pole*s two angular coordinates specify the location. In the rotating system these are the *see* declination and the *see* right ascension and in the fixed system these are the *see* declination and the *see* hour angle.

equilibrium tide The total lift of the *see* equipotential surface of *see gravity* by the astronomical tidal potential.

equipotential surface The surface of constant potential.

Era The name for the second highest-ranking unit in the subdivision of the Earth's history and further subdivides the Eons. It usually covers periods of several hundred million years.

Gerstenkorn event The event that the Moon would be so critically close to the Earth that devastating tidal waves would pass around the Earth, while still being outside the Earth's *see* Roche limit, from where the tidal forces would tear the Moon apart.

gravity The gravity acceleration $\vec{g}$ is the resultant of the combined effect of gravitation of the mass distribution within the Earth and centrifugal force from Earth's rotation.

hour circle Any great circle on the *see* celestial sphere that passes through the *see* celestial poles, i. e. perpendicular to the *see* celestial equator.

hour angle The angular distance of the *see* hour circle of a point above the Earth east of the observer's meridian measured along the *see* celestial equator. Hour angle is the east-west coordinate that locate a point on the *see* celestial sphere in the fixed *see* equatorial coordinate system and changes by about 2π per 24 h due to the Earth 's rotation.

inclination The vertical inclination of the orbit of a celestial body with respect to the reference plane measured at the *see* ascending node.

intertidal The intertidal zone is the area between extreme low tide and extreme high tide. It is above water level at low tide and below water level at high tide.

lamina In geology, the term lamina is used to characterize sedimentary structures composed of several layers. Laminae are individual layers less than 1 cm thick, bus usually much thinner (between 0.1 mm to 1 mm).

line of nodes The intersection of the plane of the elliptical orbit with the reference plane interconnects the *see* ascending node with the *see* descending node.

longitude of the ascending node The horizontal orientation of the *see* ascending node of the orbit to the *see* vernal equinox first.

lunar apsidal precessing The lunar *see* apsidal precessing, with a period currently of about 8.85 yr. The perigee moves in the same direction as the Moon in its orbit around Earth.

lunar orbital precession The lunar orbital plane, and thus the lunar *see* line of nodes, is precessing in the opposition to the lunar orbital direction with a current period of 18.6 yr in the ecliptic. Thus, the *see* declination of the lunar orbit changes constantly, because once the *see* inclination of the lunar orbit is added to the *see* obliquity of the *see* ecliptic and then subtracted, when the lunar nodes have further moved by half the period.

mean Earth An imaginary Earth moving with the same mean period as the real Earth but unlike the real Earth with constant angular velocity.

mean lunar day The time it takes the Earth to rotate once on its axis relative to the *see* mean Moon. Since the mean Moon moves further along its orbit, it will not appear at the same place in the sky after one rotation of the Earth relative to the *see* mean vernal equinox (*see* mean sidereal day). The Earth currently has to rotate for another 54 min to face the Moon again; about 24 h 50 min 28 s last a lunar day in *see* mean solar time.

mean lunar time Time measured by Earth's rotation relative to the *see* mean Moon rather than to the Sun, *see* mean lunar day.

mean Moon An imaginary Moon moving with the same mean period as the real Moon but unlike the real Moon with constant angular velocity.

mean sidereal day The time it takes the Earth to rotate once on its axis relative to the *see* mean vernal equinox.

mean sidereal time Time measured by Earth's rotation relative to the *see* mean vernal equinox rather than to the mean Sun, *see* mean sidereal day.

mean solar day The time it takes the Earth to rotate once on its axis relative to the *see* mean Sun. Since the Earth moves further along its orbit, the mean Sun will not appear at the same place in the sky after one rotation of the Earth relative to the *see* mean vernal equinox (*see* mean sidereal day). The Earth currently has to rotate for about another four minutes to face the mean Sun again. Generally referred to as a day, given by 24 (solar) hours.

mean solar time Time measured by Earth's rotation relative to the *see* mean Sun, *see* mean solar day.

mean solar year *see* tropical year.

mean Sun An imaginary Sun moving with the same mean period as the real Sun but unlike the real Sun with constant angular velocity.

mean vernal equinox It is the mean position of the *see* vernal equinox that changes only with the *see* Earth's lunisolar precession component and not with the *see* nutation component of its precession motion (*see* vernal equinox precession).

month *see* synodic month.

neap-spring tidal cycle At full and new Moon, the Moon and Sun are aligned with the Earth and their tidal forces reinforce each other to form a spring tide. At crescent moon, the Moon and Sun are at 90° to each other as seen from Earth, and their tidal forces attenuate each other to a neap tide. Hence, the neap-spring cycle correlates to the half *see* synodic month.

neap tide At crescent moon, the Moon and Sun are at 90° to each other as seen from Earth, and their tidal forces attenuate each other to a neap tide.

Neoproterozoic The last *see Era* of the *see* Proterozoic Eon and is succeeded by the current *see* Phanerozoic Eon and the *see* Paleozoic Era, spanning the time from ~1000 Myr to 539 Myr ago.

nutation The superpostion of the *see* Earth's lunisolar precession with short-period oscillations with small amplitudes up to 15″. Precession rate and angle of the *see* Earth axis vary with the non-constant torque on the axis, which results primarily from the *see* lunar orbital precession.

obliquity The inclination of the equatorial plane of currently 23.5 against the *see* ecliptic.

Paleozoic The earliest of three *see* Eras of the current *see* Phanerozoic Eon; it is the longest of the Phanerozoic Eras, lasting from ~539 Myr to 252 Myr ago.

periapsis The vertex of the orbital ellipse with the least distance to the central body is called periapsis.

perigee The *see* periapsis in the case of the Earth as the central body of the orbital ellipse.

perihelion The *see* periapsis in the case of the Sun as the central body of the orbital ellipse.

Period The name for the third highest-ranking unit in the subdivision of the Earth's history and further subdivides the Eras. It usually covers periods of millions of years to tens of million of years.

Phanerozoic The current *see* Eon since when there is an abundance of animals and plants. It covers ~539 Myr ago to the current time.

Precambrian The earliest part of Earth's history comprises the first three *see* Eons Hadean (~4600 Myr to 4000 Myr ago), *see* Archean (~4000 Myr to 2500 Myr ago), *see* Proterozoic (~2500 Myr to 539 Myr ago), and precedes the current *see* Phanerozoic (~539 Myr ago to the current time); accounting for 88 % of the Earth's history.

Proterozoic The third of four *see* Eons of Earth history, spanning the time from ~2500 Myr to 539 Myr ago. It is subdivided into three *see* Eras (from oldest to youngest): the Paleoproterozoic, Mesoproterozoic, and *see* Neoproterozoic.

right ascension The angular distance of the *see* hour circle of a point above the Earth east of the *see* vernal equinox measured along the *see* celestial equator. It is the east-west coordinate that locate a point on the *see* celestial sphere in the rotating *see* equatorial coordinate system. Thus, the value range from 0° to 360° is equivalent to the sidereal day of 24 sidereal hours.

Roche limit The distance from a celestial body within which a second celestial body orbiting it, held together only by its own gravity, fractures because the tidal forces of the first body exceed the second body's self-attraction.

secular In astronoy, the term secular is used to describe minor but long-term alterations in the motion (orbital elements, rotation) of celestial bodies.

sidereal month The time it takes the *see* mean Moon to revolve once in its orbit around the Earth relative to the *see* mean vernal equinox. Its current value is 27.32 d.

sidereal year The time it takes the *see* mean Earth to revolve once in its orbit around the Sun relative to the *see* mean vernal equinox. Its current value is 365.2564 d.

Snowball Earth A geoscientific hypothesis about several global glaciations that began about 717 Myr ago in the Cryogenian and whose last phase ended about 580 Myr ago in the Ediacaran. During these glaciations, continental ice advanced to very low latitudes near the equator. The oceans were largely covered with ice, as was most of the Earth's surface.

spring tide At full and new Moon, the Moon and Sun are aligned with the Earth and their tidal forces reinforce each other to form a spring tide.

subinertial Waves with frequencies below the Coriolis parameter $|\omega| < |f|$ are referred to as subinertial.

subtidal The deep ocean zone from the lower limit of the *intertidal* zone to the shelf edge at about 200 m.

superinertial Waves with frequencies beyond the Coriolis parameter $|\omega| > |f|$ are referred to as superinertial.

synodic month The time it takes the *see* mean Moon to revolve once in its orbit around the Earth relative to the line joining the Sun and the Earth, or to the lunar phases. Its current value is 29.53 d.

tidal range The difference in water level between successive high and low tide (twice the tidal amplitude).

tidal year The mean period of the monthly spring tide inequality.

tropical month The time it takes the *see* mean Moon to revolve once in its orbit around the Earth relative to the *see* mean vernal equinox. Its current value is 27.32 d. Due to *see* vernal equinox precession the period is currently 7 s shorten than the *see* sidereal month.

tropical year The time it takes the *see* mean Earth to revolve once in its orbit around the Sun relative to the *see* mean vernal equinox. By more precise definition, it is the time during which the mean ecliptical longitude of the Sun increases by 360°. Whereby the mean ecliptical longitude of the Sun refers to the mean vernal equinox. It currently has 365.2422 d and is about 20 min shorter than a *see* sidereal year due to the precession of the mean vernal equinox toward the Earth.

true anomaly The current angle of the celestial body on its orbit to the *see* periapsis, measured at the center of gravity of the system, and thus the time reference for the true orbit of the celestial body.

vernal equinox precession At the *see* vernal equinox, the *see* celestial equator intersects the *see* ecliptic with the *see* obliquity of the ecliptic. Perpendicular to the plane of the celestial equator is the *see* Earth axis. Hence, along with the *see* Earth's lunisolar precession, the plane of the celestial equator and the vernal equinox are precessing in the same direction and with the same period in the ecliptic. Superimposed on this is the *see* nutation.

vernal equinox The Earth's orbit intersects the *see* ecliptic at the vernal equinox from south to north. The *see* vernal equinox precession causes it to move opposite to the orbital direction of the Earth.

year *see mean solar year*.

zenith distance Geocentric angle between celestial object and observer.

Bibliography

Accad, Y., & Pekeris, C. L. (1978). Solution of the tidal equations for the M_2 and S_2 tides in the world oceans from a knowlegde of the tidal potential alone. *Philosophical Transactions of the Royal Society of London. Series A, Mathematical and Physical Sciences*, *290*(1368), 235–266. http://www.jstor.org/stable/75153

Allen, J. R. L. (1970). *Physical Processes of Sedimentation* (J. Sutton & J. V. Watson, Eds.). George Allen & Unwin.

Allen, J. R. L. (1981). Palaeotidal speeds and ranges estimated from cross-bedding sets with mud drapes. *Nature*, *293*, 394–396. https://doi.org/10.1038/293394a0

Allen, J. R. L. (2000). Morphodynamics of Holocene salt marshes: a review sketch from the Atlantic and Southern North Sea coasts of Europe. *Quaternary Science Reviews*, *19*(12), 1155–1231. https://doi.org/10.1016/S0277-3791(99)00034-7

Arbic, B. K., Garner, S. T., Hallberg, R. W., & Simmons, H. L. (2004). The accuracy of surface elevations in forward global barotropic and baroclinic tide models. *Deep Sea Research Part II: Topical Studies in Oceanography*, *51*(25), 3069–3101. https://doi.org/10.1016/j.dsr2.2004.09.014

Arbic, B. K., Karsten, R. H., & Garrett, C. (2009). On tidal resonance in the global ocean and the back-effect of coastal tides upon open-ocean tides. *Atmosphere-Ocean*, *47*(4), 239–266. https://doi.org/10.3137/OC311.2009

Arbic, B. K., Mitrovica, J. X., MacAyeal, D. R., & Milne, G. A. (2008). On the factors behind large Labrador Sea tides during the last glacial cycle and the potential implications for Heinrich events. *Paleoceanography*, *23*(3). https://doi.org/10.1029/2007PA001573

Arbic, B. K., Richman, J. G., Shriver, J. F., Timko, P. G., Metzger, E. J., & Wallcraft, A. J. (2012). Global Modeling of Internal Tides Within an Eddying Ocean General Circulation Model. *Oceanography*, *25*. https://doi.org/10.5670/oceanog.2012.38

Arbic, B. K., Wallcraft, A. J., & Metzger, E. J. (2010). Concurrent simulation of the eddying general circulation and tides in a global ocean model [The magic of modelling: A special volume commemorating the contributions of Peter D. Killworth – Part 2]. *Ocean Modelling*, *32*(3), 175–187. https://doi.org/10.1016/j.ocemod.2010.01.007

Archer, A. W. (1991). Modeling of tidal rhythmites using modern tidal periodicities and implications for shortterm sedimentation rates. In E. K. Franseen, W. L. Watney, C. G. S. C. Kendall, & W. C. Ross (Eds.), *Sedimentary modeling; computer simulations and methods for improved parameter definition* (185–189). Kansas Geological Survey, Bulletin.

Archer, A. W. (1998). Hierarchy of Controls on Cyclic Rhythmite Deposition: Carboniferous Basins of Eastern and Mid-Continental U.S.A. In *Tidalites: Processes and Products*. SEPM Society for Sedimentary Geology. https://doi.org/10.2110/pec.98.61.0059

Archer, A. W. (1996a). Panthalassa: paleotidal resonance and a global paleocean seiche. *Paleoceanography*, *11*(5), 625–632. https://doi.org/10.1029/96PA01739

Archer, A. W. (1996b). Reliability of lunar orbital periods extracted from ancient cyclic tidal rhythmites. *Earth and Planetary Science Letters*, *141*(1), 1–10. https://doi.org/10.1016/0012-821X(96)00063-5

Archer, A. W., & Johnson, T. W. (1997). Modelling of cyclic tidal rhythmites (Carboniferous of Indiana and Kansas, Precambrian of Utah, USA) as a basis for reconstruction of intertidal positioning and palaeotidal regimes. *Sedimentology*, *44*(6), 991–1010. https://doi.org/10.1111/j.1365-3091.1997.tb02174.x

Archer, A. W., Kuecher, G. J., & Kvale, E. P. (1995). The role of tidal-velocity asymmetries in the deposition of silty tidal rhythmites (Carboniferous, eastern Interior Coal Basin, U.S.A.) *Journal of Sedimentary Research*, *65*(2a), 408–416. https://doi.org/10.1306/D42680D6-2B26-11D7-8648000102C1865D

Archer, A. W., Kvale, E. P., & Johnson, H. (1991). Analysis of modern equatorial tidal periodicities as a test of information encoded in ancient tidal rhythmites. In D. Smith, G. Reinson, B. A. Zaitlin, & R. A. Rahmani (Eds.), *Clastic Tidal Sedimentology*.

Australian Hydrographic Office. (2024). AusTides (AHP 114) [Access on 10/09, 2024]. https://hydro.gov.au/prodserv/publications/ausTides/tides.htm

Baader, H.-R. (1982). Balance Problems in Tidal Computations. In P. Brosche & J. Sündermann (Eds.), *Tidal Friction and the Earth's Rotation II* (122–164). Springer Verlag.

Backhaus, J. O. (1985). A three-dimensional model for the simulation of shelf sea dynamics. *Deutsche hydrographische Zeitung*, *38*(H.4), 167–262.

Backhaus, J. O. (1983). A semi-implicit scheme for the shallow water equations for application to shelf sea modelling. *Continental Shelf Research*, *2*(4), 243–254. https://doi.org/10.1016/0278-4343(82)90020-6

Baenas, T., Escapa, A., & Ferrándiz, J. M. (2021). Secular changes in length of day: Effect of the mass redistribution. *Astronomy & Astrophysics*, *648*. https://doi.org/10.1051/0004-6361/202140356

Barboni, M., Boehnke, P., Keller, B., Kohl, I. E., Schoene, B., Young, E. D., & McKeegan, K. D. (2017). Early formation of the Moon 4.51 billion years ago. *Science Advances*, *3*(1). https://doi.org/10.1126/sciadv.1602365

Bartels, J. (1957). Gezeitenkräfte. In J. Bartels (Ed.), *Geophysik II / Geophysics II* (pp. 734–774). Springer Berlin Heidelberg. https://doi.org/10.1007/978-3-642-45881-1_13

Battat, J. B. R., Adelberger, E., Colmenares, N. R., Farrah, M., Gonzales, D. P., Hoyle, C. D., McMillan, R. J., Murphy, T. W., Sabhlok, S., & Stubbs, C. W. (2023). Fifteen Years of Millimeter Accuracy Lunar Laser Ranging with APOLLO: Data Set Characterization. *Publications of the Astronomical Society of the Pacific*, *135*(1052). https://doi.org/10.1088/1538-3873/aceb2f

Bennett, A. F., & McIntosh, P. C. (1982). Open Ocean Modeling as an Inverse Problem: Tidal Theory. *Journal of Physical Oceanography*, *12*(10), 1004–1018. https://doi.org/10.1175/1520-0485(1982)012<1004:OOMAAI>2.0.CO;2

Berger, A., Loutre, M. F., & Dehant, V. (1989). Influence of the changing lunar orbit on the astronomical frequencies of pre-quaternary insolation patterns. *Paleoceanography*, *4*(5), 555–564. https://doi.org/10.1029/PA004i005p00555

Bills, B. G., & Ray, R. D. (1999). Lunar orbital evolution: A synthesis of recent results. *Geophysical Research Letters*, *26*(19), 3045–3048.

Blackledge, B. W., Green, J. A. M., Barnes, R., & Way, M. J. (2020). Tides on Other Earths: Implications for Exoplanet and Palaeo-Tidal Simulations. *Geophysical Research Letters*, *47*(12). https://doi.org/10.1029/2019GL085746

Boothroyd, J. C. (1985). Tidal Inlets and Tidal Deltas. In R. A. Davis (Ed.), *Coastal Sedimentary Environments* (pp. 445–532). Springer New York. https://doi.org/10.1007/978-1-4612-5078-4_7

Borg, L. E., Connelly, J. N., Boyet, M., & Carlson, R. W. (2011). Chronological evidence that the Moon is either young or did not have a global magma ocean. *Nature*, *477*, 70–72. https://doi.org/10.1038/nature10328

Boulila, S., Laskar, J., Haq, B. U., Galbrun, B., & Hara, N. (2018). Long-term cyclicities in Phanerozoic sea-level sedimentary record and their potential drivers. *Global and Planetary Change*, *165*, 128–136. https://doi.org/10.1016/j.gloplacha.2018.03.004

Bridge, J., & Demicco, R. (2008). *Earth Surface Processes, Landforms and Sediment Deposits*. Cambridge University Press. https://doi.org/10.1017/CBO9780511805516

Brosche, P., & Hövel, W. (1982). Tidal friction for times around the presence. In P. Brosche & J. Sündermann (Eds.), *Tidal Friction and the Earth's Rotation II* (pp. 175–188). Springer-Verlag.

Brosche, P., & Sündermann, J. (1971). Die Gezeiten des Meeres und die Rotation der Erde. *Pure Applied Geophysics*, *86*(3), 95–117.

Brosche, P., & Sündermann, J. (Eds.). (1978). *Tidal Friction and the Earth's Rotation* [September 1977, Bielefeld, West Germany]. Springer-Verlag.

Brosche, P., & Sündermann, J. (Eds.). (1982). *Tidal Friction and the Earth's Rotation II. Proceedings of a Workshop* [28 September-3 October 1981, Bielefeld, West Germany]. Springer-Verlag.

Brosche, P., & Sündermann, J. (1984). 2.5.3 Tidal friction and dynamics of the earth-moon-system. In K. Fuchs & H. Soffel (Eds.), *Geophysics of the Solid Earth, the Moon and the Planets*. Springer-Verlag Berlin Heidelberg. https://doi.org/10.1007/10201917_84

Brosche, P., & Sündermann, J. (Eds.). (1990). *Earth's Rotation from Eons to Days. Proceedings of a Workshop* [26-30 September 1988, Bielefeld, West Germany]. Springer-Verlag.

Brosche, P., & Sündermann, J. (2011). Ozeanschwingungen und Gezeitenreibung - Zur Bewertung von Renonanzkurven. *Mitteilungen der Deutschen Geophysikalischen Gesellschaft*, *1*, 43–50.

Brown, E. H. (1905). Theory of the Motion of the Moon. *Memoirs of the Royal Astronomical Society*, *57*, 51–145.

Brown, M. A., Archer, A. W., & Kvale, E. P. (1990). Neap-spring tidal cyclicity in laminated carbonate channel-fill deposits and its implications; Salem Limestone (Mississippian), south-central Indiana, U.S.A. *Journal of Sedimentary Research*, *60*(1), 152–159. https://doi.org/10.1306/212F9133-2B24-11D7-8648000102C1865D

Brown, M., Johnson, T., & Gardiner, N. J. (2020). Plate tectonics and the archean earth. *Annual Review of Earth and Planetary Sciences*, *48*(1), 291–320. https://doi.org/10.1146/annurev-earth-081619-052705

Buijsman, M. C., Arbic, B. K., Green, J. A. M., Helber, R. W., Richman, J. G., Shriver, J. F., Timko, P. G., & Wallcraft, A. (2015). Optimizing internal wave drag in a forward barotropic model with semidiurnal tides. *Ocean Modelling*, *85*, 42–55. https://doi.org/10.1016/j.ocemod.2014.11.003

Caldwell, P. C., Merrifield, M. A., & Thompson, P. R. (2015). Sea level measured by tide gauges from global oceans–the Joint Archive for Sea Level holdings (NCEI Accession 0019568), Version 5.5., Record Id 401, 1001, 8221 [Accessed 01.01.2023]. *NOAA National Centers for Environmental Information, Dataset*. https://doi.org/doi:10.7289/V5V40S7W.

Carless, S. J., Green, J. M., Pelling, H. E., & Wilmes, S.-B. (2016). Effects of future sea-level rise on tidal processes on the Patagonian Shelf. *Journal of Marine Systems*, *163*, 113–124. https://doi.org/10.1016/j.jmarsys.2016.07.007

Carlson, R. W. (2005). *The Mantle and Core: Treatise on Geochemistry*. Elsevier Science.

Carrère, L., Lyard, F., Cancet, M., Allain, D., Dabat, M.-L., Fouchet, E., Sahuc, E., Faugere, Y., Dibarboure, G., & Picot, N. (2022). A new barotropic tide model for global ocean: FES2022. *2022 Ocean Surface Topography Science Team Meeting*. https://doi.org/10.24400/527896/a03-2022.3287

Cartwright, D. E., & Ray, R. D. (1990). Oceanic tides from Geosat altimetry. *Journal of Geophysical Research: Oceans*, *95*(C3), 3069–3090. https://doi.org/10.1029/JC095iC03p03069

Cartwright, D. E., & Ray, R. D. (1991). Energetics of global ocean tides from Geosat altimetry. *Journal of Geophysical Research: Oceans*, *96*(C9), 16897–16912. https://doi.org/10.1029/91JC01059

Chan, M. A., Kvale, E. P., Archer, A. W., & Sonett, C. P. (1994). Oldest direct evidence of lunar-solar tidal forcing encoded in sedimentary rhythmites, Proterozoic Big Cottonwood Formation, central Utah. *Geology*, *22*(9), 791–794. https://doi.org/10.1130/0091-7613(1994)022<0791:ODEOLS>2.3.CO;2

Cheng, M., Tapley, B. D., & Ries, J. C. (2013). Deceleration in the earth's oblateness. *Journal of Geophysical Research: Solid Earth*, *118*(2), 740–747. https://doi.org/10.1002/jgrb.50058

Christodoulidis, D. C., Smith, D. E., Williamson, R. G., & Klosko, S. M. (1988). Observed tidal braking in the Earth/Moon/Sun system. *Journal of Geophysical Research: Solid Earth*, *93*(B6), 6216–6236. https://doi.org/10.1029/JB093iB06p06216

CNES. (2024). „The FES2022 Tide product was funded by CNES, produced by LEGOS, NOVELTIS and CLS and made freely available by Aviso". CNES, 2024. FES2022 (Finite Element Solution) Ocean Tide (Version 2022) [Data set]. https://doi.org/10.24400/527896/a01-2024.004

Coats, R. P., & Preiss, W. V. (1987). Stratigraphy of the Umberatana Group. In W. V. Preiss (Ed.), *The Adelaide Geosyncline* (pp. 125–209). Department of Mines; Energy of South Australia.

Collins, D. S., Avdis, A., Allison, P. A., Johnson, H. D., Hill, J., & Piggott, M. D. (2018). Controls on tidal sedimentation and preservation: Insights from numerical tidal modelling in the Late Oligocene–Miocene South China Sea, Southeast Asia. *Sedimentology*, *0*(0). https://doi.org/10.1111/sed.12474

Collins, D. S., Avdis, A., Wells, M. R., Dean, C. D., Mitchell, A. J., Allison, P. A., Johnson, H. D., Hampson, G. J., Hill, J., & Piggott, M. D. (2021). Prediction of shoreline–shelf depositional process regime guided by palaeotidal modelling. *Earth-Science Reviews*, *223*. https://doi.org/10.1016/j.earscirev.2021.103827

Colmenares, N. R., Battat, J. B. R., Gonzales, D. P., Murphy, T. W., & Sabhlok, S. (2023). Fifteen Years of Millimeter Accuracy Lunar Laser Ranging with APOLLO: Data Reduction and Calibration. *Publications of the Astronomical Society of the Pacific*, *135*(1052). https://doi.org/10.1088/1538-3873/acf787

Coughenour, C. L., Archer, A. W., & Lacovara, K. J. (2009). Tides, tidalites, and secular changes in the Earth-Moon system. *Earth-Science Reviews*, *97*(1-4), 59–79. https://doi.org/{10.1016/j.earscirev.2009.09.002}

Coughenour, C. L., Archer, A. W., & Lacovara, K. J. (2013). Calculating Earth–Moon system parameters from sub-yearly tidal deposit records: An example from the carboniferous tradewater formation. *Sedimentary Geology*, *295*, 67–76. https://doi.org/10.1016/j.sedgeo.2013.08.001

Daher, H., Arbic, B. K., Williams, J. G., Ansong, J. K., Boggs, D. H., Müller, M., Schindelegger, M., Austermann, J., Cornuelle, B. D., Crawford, E. B., Fringer, O. B., Lau, H. C., Lock, S. J., Maloof, A. C., Menemenlis, D., Mitrovica, J. X., Green, J. M., & Huber, M. (2021). Long-term Earth-Moon evolution with high-level orbit and ocean tide models. *Journal of Geophysical Research: Planets*. https://doi.org/10.1029/2021JE006875

Dalrymple, R. W., Knight, R. J., Zaitlin, B. A., & Middelton, G. V. (1990). Dynamics and facies model of a macrotidal sand-bar complex, Cobequid Bay—Salmon River Estuary (Bay of Fundy). *Sedimentology*, *37*(4), 577–612. https://doi.org/10.1111/j.1365-3091.1990.tb00624.x

Dalrymple, R. W., Makino, Y., & Zaitlin, B. A. (1991). Temporal and spatial patterns of rhythmite deposition on mud-flats in the macrotidal, Cobequid Bay-Salmon River estuary, Bay of Fundy, Canada. In D. Smith, G. Reinson, B. A. Zaitlin, & R. A. Rahmani (Eds.), *Clastic Tidal Sedimentology*.

Dalrymple, R. W. (2010). 9. tidal depositional systems. In N. P. James & R. W. Dalrymple (Eds.), *Facies models 4* (pp. 201–231). Geological Association of Canada. https://doi.org/10.1007/978-94-007-0123-6

Darwin, G. H. (1891). XI. On the harmonic analysis of tidal observations of high and low water. *Proceedings of the Royal Society of London*, *48*(292-295), 278–340. https://doi.org/10.1098/rspl.1890.0041

Darwin, G. H. (1883–1886). Reports of a committee for the harmonic analysis of tides. *British Association for the Advancement of Science*.

De Azarevich, V. L. L., & Azarevich, M. B. (2017). Lunar recession encoded in tidal rhythmites: a selective overview with examples from Argentina. *Geo-Marine Letters*, *37*, 333–344. https://doi.org/10.1007/s00367-017-0500-z

De Boer, P. L., Oost, A. P., & Visser, M. J. (1989). The diurnal inequality of the tide as a parameter for recognizing tidal influences. *Journal of Sedimentary Research*, *59*(6), 912–921. https://doi.org/10.1306/212F90B1-2B24-11D7-8648000102C1865D

De Boer, P. L., & Alexandre, J. T. (2012). Orbitally forced sedimentary rhythms in the stratigraphic record: Is there room for tidal forcing? *Sedimentology*, *59*(2), 379–392. https://doi.org/10.1111/j.1365-3091.2011.01255.x

Defant, A. (1961). *Physical oceanography*. Macmillan.

Deines, S. D., & Williams, C. A. (2016). EARTH's ROTATIONAL DECELERATION: DETERMINATION OF TIDAL FRICTION INDEPENDENT OF TIMESCALES.

The Astronomical Journal, *151*(4), 103. https://doi.org/10.3847/0004-6256/151/4/103

Denis, C., Schreider, A., Varga, P., & Závoti, J. (2002). Despinning of the earth rotation in the geological past and geomagnetic paleointensities. *Journal of Geodynamics*, *34*(5), 667–685. https://doi.org/10.1016/S0264-3707(02)00049-2

Dickey, J. O., Marcus, S. L., Steppe, J. A., & Hide, R. (1992). The Earth's Angular Momentum Budget on Subseasonal Time Scales. *Science*, *255*(5042), 321–324. https://doi.org/10.1126/science.255.5042.321

Dietz, R. S., & Holden, J. C. (1970). Reconstruction of Pangaea - Breakup and Dispersion of Continents, Permian to Present. *Journal of Geophysical Research*, *75*(26), 4939–4956.

Doodson, A. T. (1921). The Harmonic Development of the Tide-Generating Potential. *Proceedings of the Royal Society of London Series A*, *100*, 305–329. https://doi.org/10.1098/rspa.1921.0088

Dumberry, M., & Bloxham, J. (2006). Azimuthal flows in the Earth's core and changes in length of day at millennial timescales. *Geophysical Journal International*, *165*(1), 32–46. https://doi.org/10.1111/j.1365-246X.2006.02903.x

Egbert, G. D., & Ray, R. D. (2000). Significant dissipation of tidal energy in the deep ocean inferred from satellite altimeter data. *Nature*, *405*. https://doi.org/10.1038/35015531

Egbert, G. D., Bennett, A. F., & Foreman, M. G. G. (1994). TOPEX/POSEIDON tides estimated using a global inverse model. *Journal of Geophysical Research: Oceans*, *99*(C12), 24821–24852. https://doi.org/10.1029/94JC01894

Egbert, G. D., & Erofeeva, S. Y. (2002). Efficient Inverse Modeling of Barotropic Ocean Tides. *Journal of Atmospheric and Oceanic Technology*, *19*(2), 183–204. https://doi.org/10.1175/1520-0426(2002)019<0183:EIMOBO>2.0.CO;2

Egbert, G. D., Ray, R. D., & Bills, B. (2004). Numerical modeling of the global semidiurnal tide in the present day and in the last glacial maximum. *Journal of Geophysical Research*, *109*.

Egbert, G. D., & Ray, R. D. (2001). Estimates of M2 tidal energy dissipation from TOPEX/-Poseidon altimeter data. *Journal of Geophysical Research: Oceans*, *106*(C10), 22475–22502. https://doi.org/10.1029/2000JC000699

Egbert, G. D., & Ray, R. D. (2003). Semi-diurnal and diurnal tidal dissipation from TOPEX/Poseidon altimetry. *Geophysical Research Letters*, *30*(17). https://doi.org/10.1029/2003GL017676

Egbert, G. D., & Ray, R. D. (2017). Tidal prediction. *Journal of Marine Research*, *75*(3), 189–237. https://doi.org/doi:10.1357/002224017821836761

Eriksson, K. A. (1977). Tidal deposits from the Archaean Moodies Group, Barberton Mountain Land, South Africa. *Sedimentary Geology*, *18*(1), 257–281. https://doi.org/10.1016/0037-0738(77)90015-X

Eriksson, K. A., & Simpson, E. L. (2000). Quantifying the oldest tidal record: The 3.2 Ga Moodies Group, Barberton Greenstone Belt, South Africa. *Geology*, *28*(9), 831–834. https://doi.org/10.1130/0091-7613(2000)28<831:QTOTRT>2.0.CO;2

Eriksson, P. G., Banerjee, S., Catuneanu, O., Corcoran, P. L., Eriksson, K. A., Hiatt, E. E., Laflamme, M., Lenhardt, N., Long, D. G., Miall, A. D., Mints, M. V., Pufahl, P. K., Sarkar, S., Simpson, E. L., & Williams, G. E. (2013). Secular changes in

sedimentation systems and sequence stratigraphy. *Gondwana Research*, *24*(2), 468–489. https://doi.org/10.1016/j.gr.2012.09.008

Eubanks, T. M. (2013). Variations in the Orientation of the Earth. In *Contributions of Space Geodesy to Geodynamics: Earth Dynamics* (pp. 1–54). American Geophysical Union (AGU). https://doi.org/10.1029/GD024p0001

Evans, D. A. (2013). Reconstructing pre-Pangean supercontinents. *GSA Bulletin*, *125*, 1735–1751.

Farhat, M., Auclair-Desrotour, P., Boué, G., & Laskar, J. (2022). The resonant tidal evolution of the Earth-Moon distance. *A&A*, *665*. https://doi.org/10.1051/0004-6361/202243445

FitzGerald, D. M. (1977). *Hydraulics, Morphology and Sediment Transport at Price Inlet, South Carolina* (Doctoral dissertation). University of South Carolina.

FitzGerald, D. M., & Nummedal, D. (1983). Response characteristics of an ebb-dominated tidal inlet channel. *Journal of Sedimentary Research*, *53*(3), 833–845. https://doi.org/10.1306/212F82CE-2B24-11D7-8648000102C1865D

Flick, R. E., Murray, J. F., & Ewing, L. C. (2003). Trends in United States Tidal Datum Statistics and Tide Range. *Journal of Waterway, Port, Coastal and Ocean Engineering*, *129*(4), 155–164. https://escholarship.org/uc/item/5846m8hm

Fok, H. S. (2012). *Ocean Tides Modeling using Satellite Altimetry* (Doctoral dissertation). Geodetic Science, The Ohio State University. Columbus, Ohio 43210.

Gaviño, J. H. (1984). *On The Calculation Of Resonance Oscillations Of A World Ocean's Finite Difference Model By Means Of The Lanczos Method* (Doctoral dissertation). Universität Hamburg. Inst. für Meereskunde d. Univ. Hamburg.

Gerkema, T. (2019). *An Introduction to Tides*. Cambridge University Press. https://doi.org/10.1017/9781316998793

Gerstenkorn, H. (1955). Über Gezeitenreibung beim Zweikörperproblem. *Zeitschrift für Astrophysik*, *36*, 245–274.

Gordeev, R. G., Kagan, B. A., & Polyakov, E. V. (1977). The Effects of Loading and Self-Attraction on Global Ocean Tides: The Model and the Results of a Numerical Experiment. *Journal of Physical Oceanography*, *7*(2), 161–170. https://doi.org/10.1175/1520-0485(1977)007<0161:TEOLAS>2.0.CO;2

Götze, H.-J., Mertmann, D., Riller, U., & Arndt, J. (2015). *Einführung in die Geowissenschaften* (2., vollständig überarbeitete und erweiterte Auflage). Verlag Eugen Ulmer.

Green, J. A. M. (2010). Ocean tides and resonance. *Ocean Dynamics*, *60*(5), 1243–1253. https://doi.org/10.1007/s10236-010-0331-1

Green, J. A. M., & Huber, M. (2013). Tidal dissipation in the early Eocene and implications for ocean mixing. *Geophysical Research Letters*, *40*(11), 2707–2713. https://doi.org/10.1002/grl.50510

Green, J. A. M., Huber, M., Waltham, D., Buzan, J., & Wells, M. (2017). Explicitly modelled deep-time tidal dissipation and its implication for Lunar history. *Earth and Planetary Science Letters*, *461*, 46–53. https://doi.org/10.1016/j.epsl.2016.12.038

Green, J. A. M., Molloy, J. L., Davies, H. S., & Duarte, J. C. (2018). Is There a Tectonically Driven Supertidal Cycle? *Geophysical Research Letters*, *45*(8), 3568–3576. https://doi.org/10.1002/2017GL076695

Green, J. A. M., Duarte, J. C., Creveling, J. R., & Scotese, C. R. (2020). Weak tides during Cryogenian glaciations. *Nature Communications*, *11*(6227). https://doi.org/10.1038/s41467-020-20008-3

Green, J. A. M., & Nycander, J. (2013). A Comparison of Tidal Conversion Parameterizations for Tidal Models. *Journal of Physical Oceanography*, *43*(1), 104–119. https://doi.org/10.1175/JPO-D-12-023.1

Griffiths, S. D., & Peltier, W. R. (2008). Megatides in the arctic ocean under glacial conditions. *Geophysical Research Letters*, *35*(8). https://doi.org/10.1029/2008GL033263

Griffiths, S. D., & Peltier, W. R. (2009). Modeling of Polar Ocean Tides at the Last Glacial Maximum: Amplification, Sensitivity, and Climatological Implications. *Journal of Climate*, *22*(11), 2905–2924. https://doi.org/10.1175/2008JCLI2540.1

Gross, R. S. (2007). 3.09 - Earth Rotation Variations – Long Period. In G. Schubert (Ed.), *Treatise on Geophysics* (pp. 239–294). Elsevier. https://doi.org/https://doi.org/10.1016/B978-044452748-6.00057-2

Groves, G. W., & Reynolds, R. W. (1975). An orthogonalized convolution method of tide prediction. *Journal of Geophysical Research*, *80*(30), 4131–4138. https://doi.org/10.1029/JC080i030p04131

Guthmann, A. (2000). *Einführung in die Himmelsmechanik und Ephemeridenrechnung* (2nd ed.). Spektrum Akademischer Verlag.

Haigh, I. D., Marcos, M., Talke, S. A., Woodworth, P. L., Hunter, J. R., Hague, B. S., Arns, A., Bradshaw, E., & Thompson, P. (2022). GESLA Version 3: A major update to the global higher-frequency sea-level dataset. *Geoscience Data Journal*, *10*(3), 293–314. https://doi.org/10.1002/gdj3.174

Hallberg, R., & Rhines, P. (1996). Buoyancy-Driven Circulation in an Ocean Basin with Isopycnals Intersecting the Sloping Boundary. *Journal of Physical Oceanography*, *26*(6), 913–940. https://doi.org/10.1175/1520-0485(1996)026<0913:BDCIAO>2.0.CO;2

Halley, E. (1695). Some account of the ancient state of the city of Palmyra, with short remarks upon the inscriptions found there. *Philosophical Transactions of the Royal Society*, *19*, 160–175.

Hansen, K. S. (1982). Secular effects of oceanic tidal dissipation of the moon's orbit and the earth's rotation. *Reviews of Geophysics and Space Physics*, *20*, 457–480. https://doi.org/10.1029/RG020i003p00457

Harris, P. T., Pattiaratchi, C. B., Collins, M. B., & Dalrymple, R. W. (1995). What is a bedload parting? In B. W. Flemming and A. Bartholoma (Ed.), *Tidal signatures in modern and ancient sediments* (3–18). Blackwell.

Hart-Davis, M. G., Dettmering, D., & Seitz, F. (2022). TICON-3: Tidal Constants based on GESLA-3 sea-level records from globally distributed tide gauges including gauge type information (data). https://doi.org/10.1594/PANGAEA.951610

Hart-Davis, M. G., Piccioni, G., Dettmering, D., Schwatke, C., Passaro, M., & Seitz, F. (2021a). EOT20: a global ocean tide model from multi-mission satellite altimetry. *Earth System Science Data*, *13*(8), 3869–3884. https://doi.org/10.5194/essd-13-3869-2021

Hart-Davis, M. G., Sulzbach, R., Dettmering, D., Thomas, M., & Seitz, F. (2022). TICON-td: Third-degree tidal constants based on GESLA sea-level records from globally distributed tide gauges (data). https://doi.org/10.1594/PANGAEA.943444

Hart-Davis, M. G., Piccioni, G., Dettmering, D., Schwatke, C., Passaro, M., & Seitz, F. (2021b). EOT20 - A global Empirical Ocean Tide model from multi-mission satellite altimetry [SEANOE]. https://doi.org/10.17882/79489

Hartmann, T., & Wenzel, H.-G. (1995). Catalogue HW95 of the tide generating potential. *Bulletin d'Information des Marées Terrestres*, *123*.

Hayden, A.-M., Wilmes, S.-B., Gomez, N., Green, J. A. M., Pan, L., Han, H., & Golledge, N. R. (2020). Multi-Century Impacts of Ice Sheet Retreat on Sea Level and Ocean Tides in Hudson Bay. *Journal of Geophysical Research: Oceans*, *125*(11). https://doi.org/10.1029/2019JC015104

Herold, N., Buzan, J., Seton, M., Goldner, A., Green, J. A. M., Müller, R. D., Markwick, P., & Huber, M. (2014). A suite of early Eocene (~55 Ma) climate model boundary conditions. *Geoscientific Model Development*, *7*(5), 2077–2090. https://doi.org/10.5194/gmd-7-2077-2014

Hide, R., & Dickey, J. O. (1991). Earth's Variable Rotation. *Science*, *253*(5020), 629–637. https://doi.org/10.1126/science.253.5020.629

Hoffman, P. F., Abbot, D. S., Ashkenazy, Y., Benn, D. I., Brocks, J. J., Cohen, P. A., Cox, G. M., Creveling, J. R., Donnadieu, Y., Erwin, D. H., Fairchild, I. J., Ferreira, D., Goodman, J. C., Halverson, G. P., Jansen, M. F., Hir, G. L., Love, G. D., Macdonald, F. A., Maloof, A. C., ... Warren, S. G. (2017). Snowball Earth climate dynamics and Cryogenian geology-geobiology. *Science Advances*, *3*(11). https://doi.org/10.1126/sciadv.1600983

Hoffman, P. F., Kaufman, A. J., Halverson, G. P., & Schrag, D. P. (1998). A neoproterozoic snowball earth. *Science*, *281*(5381), 1342–1346. https://doi.org/10.1126/science.281.5381.1342

Holme, R. (1998). Electromagnetic core—mantle coupling—I. Explaining decadal changes in the length of day. *Geophysical Journal International*, *132*(1), 167–180. https://doi.org/10.1046/j.1365-246x.1998.00424.x

Hufschmidt, A. (1995). *Berechnung des Auflast- und Eigenanziehungspotentials in einem globalen Gezeitenmodell und Auswirkungen auf die Energiebilanz* (Master's thesis). Institut für Meereskunde, Universität Hamburg, Germany.

Hufschmidt, A. (2025) [private communication].

Jeffreys, H. (1920). Tidal Friction in Shallow Seas. *Philosophical Transactions of the Royal Society of London. Series A, Containing Papers of a Mathematical or Physical Character*, *221*, 239–264. http://www.jstor.org/stable/91194

Johnson, M. A., Kenyon, N. H., Belderson, R. H., & Stride, A. H. (1982). Sand transport. In Stride, A. H. (Ed.), *Offshore Tidal Sands* (58–94). Chapman and Hall.

Jungclaus, J. H., Keenlyside, N., Botzet, M., Haak, H., Luo, J. .-., Latif, M., Marotzke, J., Mikolajewicz, U., & Roeckner, E. (2006). Ocean circulation and tropical variability in the coupled model ECHAM5/MPI-OM. *Journal of Climate*, *19*(16), 3952–3972.

Kagan, B. A., & Maslova, N. B. (1994). A stochastic model of the Earth-Moon tidal evolution accounting for cyclic variations of resonant properties of the ocean: an asymptotic solution. *Earth, Moon, and Planets*, *66*, 173–188.

Kagan, B. A. (1997). Earth—Moon tidal evolution: model results and observational evidence [Tidal Science In Honour of David E. Cartwright]. *Progress in Oceanography*, *40*(1), 109–124. https://doi.org/10.1016/S0079-6611(97)00027-X

Kagan, B. A., & Sündermann, J. (1996). Dissipation of Tidal Energy, Paleotides, and Evolution of the Earth–Moon System. In R. Dmowska & B. Saltzman (Eds.), *Advances in Geophysics* (pp. 179–266). Elsevier. https://doi.org/10.1016/S0065-2687(08)60021-7

Kant, I. (1754). Untersuchung der Frage, ob die Erde in ihrer Umdrehung um die Achse, wodurch sie die Abwechselung des Tages und der Nacht hervorbringt, einige Veränderung seit den ersten Zeiten ihres Ursprungs erlitten habe und woraus man sich ihrer versichern könne, welche von der Königl. Akademie der Wissenschaften zu Berlin zum Preise für das jetzt laufende Jahr aufgegeben worden. In *Kant's Werke* (pp. 183–191). http://www.korpora.org/Kant/aa01/Inhalt1.html.

Kaula, W. M. (1966). *Introduction to Satellite Geodesy*. Blaisdell.

Kodaira, T., Thompson, K. R., & Bernier, N. B. (2016). Prediction of M2 tidal surface currents by a global baroclinic ocean model and evaluation using observed drifter trajectories. *Journal of Geophysical Research: Oceans*, *121*(8), 6159–6183. https://doi.org/10.1002/2015JC011549

Komar, P. D., & Enfield, D. B. (1987). Short-Term Sea-Level Changes and Coastal Erosion. In *Sea-Level Fluctuation and Coastal Evolution*. SEPM Society for Sedimentary Geology. https://doi.org/10.2110/pec.87.41.0017

Krohn, J., & Sündermann, J. (1982). Paleotides before the Permian. In Brosche, P. and Sündermann, J. (Ed.), *Tidal Friction and the Earth's Rotation II* (pp. 190–207). Springer Verlag.

Krohn, J., Brosche, P., & Sündermann, J. (1981). Paläogezeiten und Erdrotation. *Geologische Rundschau*, *70*(1), 64–77. https://doi.org/10.1007/BF01764315

Kvale, E. P. (2003). Tides and tidal rhytmites. In G. V. Middleton, M. J. Church, M. Coniglio, L. A. Hardie, & F. J. Longstaffe (Eds.), *Encyclopedia of Sediments and Sedimentary Rocks* (741–744). Springer Netherlands. https://doi.org/10.1007/978-1-4020-3609-5_238

Kvale, E. P., & Archer, A. W. (1990). Tidal deposits associated with low-sulfur coals, Brazil Fm. (Lower Pennsylvanian), Indiana. *Journal of Sedimentary Research*, *60*(4), 563–574. https://doi.org/10.1306/212F91E7-2B24-11D7-8648000102C1865D

Kvale, E. P., & Archer, A. W. (1991). Characteristics of Two, Pennsylvanian-Age, Semidiurnal Tidal Deposits in the Illinois Basin, U.S.A. In D. Smith, G. Reinson, B. A. Zaitlin, & R. A. Rahmani (Eds.), *Clastic Tidal Sedimentology*.

Kvale, E. P., Cutright, J., BIlodeau, D., Archer, A., Johnson, H. R., & Pickett, B. (1995). Analysis of modern tides and implications for ancient tidalites. *Continental Shelf Research*, *15*(15), 1921–1943. https://doi.org/10.1016/0278-4343(95)00001-H

Kvale, E. P., Fraser, G. S., Archer, A. W., Zawistoski, A., Kemp, N., & McGough, P. (1994). Evidence of seasonal precipitation in Pennsylvanian sediments of the Illinois basin. *Geology*, *22*(4), 331–334. https://doi.org/10.1130/0091-7613(1994)022<0331:EOSPIP>2.3.CO;2

Kvale, E. P., Johnson, H. W., Sonett, C. P., Archer, A. W., & Zawistoski, A. (1999). Calculating lunar retreat rates using tidal rhythmites. *Journal of Sedimentary Research*, *69*(6), 1154–1168. https://doi.org/10.2110/jsr.69.1154

Lambeck, K. (1975). Effects of tidal dissipation in the oceans on the Moon's orbit and the Earth's Rotation. *Journal of Geophysical Research (1896-1977)*, *80*(20), 2917–2925. https://doi.org/10.1029/JB080i020p02917

Lambeck, K. (1977). Tidal dissipation in the oceans: Astronomical, geophysical and oceanographic consequences. *Philosophical Transactions of the Royal Society of London. Series A, Mathematical and Physical Sciences*, *287*(1347), 545–594. https://doi.org/10.1098/rsta.1977.0159

Lambeck, K. (1980a). Changes in length-of-day and atmospheric circulation. *Nature*, *286*, 104–105. https://doi.org/10.1038/286104a0

Lambeck, K. (1980b). *The Earth's Variable Rotation: Geophysical Causes and Consequences*. Cambridge University Press. https://doi.org/10.1017/CBO9780511569579

Lambeck, K., & Cazenave, A. (1977). The Earth's Variable Rate of Rotation: A Discussion of Some Meteorological and Oceanic Causes and Consequences. *Philosophical Transactions of the Royal Society of London. Series A, Mathematical and Physical Sciences*, *284*(1326), 495–506. http://www.jstor.org/stable/74779

Lambeck, K., Cazenave, A., & Balmino, G. (1974). Solid earth and ocean tides estimated from satellite orbit analyses. *Reviews of Geophysics*, *12*(3), 421–434. https://doi.org/10.1029/RG012i003p00421

Laskar, J., Correia, A. C. M., Gastineau, M., Joutel, F., Levrard, B., & Robutel, P. (2004). A long term evolution and chaotic diffusion of the insolation quantities of Mars. *Icarus*, *170*(2), 343–364. https://doi.org/10.1016/j.icarus.2004.04.005

Laskar, J., Fienga, A., Gastineau, M., & Manche, H. (2011). La2010: a new orbital solution for the long-term motion of the Earth. *Astronomy & Astrophysics*, *532*, 15p. https://doi.org/{10.1051/0004-6361/201116836}

Laskar, J., Joutel, F., & Boudin, F. (1993). Orbital, precessional, and insolation quantities for the earth from -20 Myr to +10 Myr. *Astronomy & Astrophysics*, *270*(1-2), 522–533.

Le Provost, C. (2001). Ocean Tides. In L.-L. Fu & A. Cazenave (Eds.), *Satellite Altimetry and Earth Sciences: A Handbook of Techniques and Applications* (pp. 267–304). Academic Press, San Diego, CA.

Le Provost, C., Genco, M. L., Lyard, F., Vincent, P., & Canceil, P. (1994). Spectroscopy of the world ocean tides from a finite element hydrodynamic model. *Journal of Geophysical Research: Oceans*, *99*(C12), 24777–24797. https://doi.org/10.1029/94JC01381

LeBlond, P., & Mysak, L. (1978). *Waves in the ocean*. Elsevier Scientific Publishing Company.

Lemoine, F. G., Kenyon, S. C., Factor, J. K., Trimmer, R., Pavlis, N. K., Chinn, D. S., Cox, C. M., Klosko, S. M., Luthcke, S. B., Torrence, M. H., Wang, Y. M., Williamson, R. G., Pavlis, E. C., Rapp, R. H., & Olson, T. R. (1998). *The Development of the Joint NASA GSFC and NIMA Geopotential Model EGM96* (tech. rep.). NASA Goddard Space Flight Center.

Lemon, N. M., & Gostin, V. A. (1990). The Evolution of a late Precambrian-early Palaeozoic rift complex : the Adelaide geosyncline. In J. B. Jago & P. S. Moore (Eds.), *Glacigenic sediments of the late Proterozoic ElatinaFormation and equivalents, Adelaide Geosyncline, South Australia* (149–163). Geological Society of Australia.

Li, Z. X., Bogdanova, S. V., Collins, A. S., Davidson, A., De Waele, B., Ernst, R. E., Fitzsimons, I. C. W., Fuck, R. A., Gladkochub, D. P., Jacobs, J., Karlstrom, K. E., Lu,

S., Natapov, L. M., Pease, V., Pisarevsky, S. A., Thrane, K., & Vernikovsky, V. (2008). Assembly, configuration, and break-up history of Rodinia: A synthesis. *Precambrian Research*, *160*(1-2), 179–210. https://doi.org/{10.1016/j.precamres.2007.04.021}

Lionel, M. T., Florent, L., Loren, C., Mathilde, C., Damien, A., Ergane, F., Mei-ling, D., Ramiro, F., Yannice, F., Gerald, D., & Nicolas, P. (2023). The new FES2022 tidal atlas. *EGU General Assembly 2023, Vienna, Austria, 23–28 Apr 2023*. https://doi.org/10.5194/egusphere-egu23-9008

Lisitzin, E. (1974). *Sea-level Changes*. Elsevier Scientific Publishing Company.

Longhitano, S. G., Mellere, D., Steel, R. J., & Ainsworth, R. B. (2012). Tidal depositional systems in the rock record: A review and new insights. *Sedimentary Geology*, *279*, 2–22. https://doi.org/10.1016/j.sedgeo.2012.03.024

Lourens, L. J., Antonarakou, A., Hilgen, F. J., VanHoof, A. A. M., Vergnaud-Grazzini, C., & Zachariasse, W. J. (1996). Evaluation of the Plio-Pleistocene astronomical timescale. *Paleoceanography*, *11*(4), 391–413.

Lourens, L. J., Wehausen, R., & Brumsack, H. J. (2001). Geological constraints on tidal dissipation and dynamical ellipticity of the Earth over the past three million years. *Nature*, *409*(22), 1029–1033. https://doi.org/10.1038/35059062

Lyard, F. H., Allain, D. J., Cancet, M., Carrère, L., & Picot, N. (2021). Fes2014 global ocean tide atlas: Design and performance. *Ocean Science*, *17*(3), 615–649. https://doi.org/10.5194/os-17-615-2021

Lyard, F. H., Lefevre, F., Letellier, T., & Francis, O. (2006). Modelling the global ocean tides: modern insights from FES2004. *Ocean Dynamics*, *56*, 394–415.

Macdonald, F. A., Schmitz, M. D., Crowley, J. L., Roots, C. F., Jones, D. S., Maloof, A. C., Strauss, J. V., Cohen, P. A., Johnston, D. T., & Schrag, D. P. (2010). Calibrating the cryogenian. *Science*, *327*(5970), 1241–1243. https://doi.org/10.1126/science.1183325

Maddock Jr., T. (1969). *The Behavior of Straight Open Channels With Movable Beds* (tech. rep.).

Marchenko, A. N., & Lopushanskyi, A. N. (2018). Change in the Zonal Harmonic Coefficient C20, Earth's Polar Flattening, and DynamicalEllipticity from SLR Data. *Geodynamics*, *2*(2 (25)), 5–14.

Marsh, R., & van Sebille, E. (2021). Chapter 1 - the restless ocean. In R. Marsh & E. van Sebille (Eds.), *Ocean currents* (pp. 1–24). Elsevier. https://doi.org/10.1016/B978-0-12-816059-6.00005-X

Marsland, S. J., Haak, H., Jungclaus, J. H., Latif, M., & Roske, F. (2003). The Max-Planck-Institute global ocean/sea ice model with orthogonal curvilinear coordinates. *Ocean Modelling*, *5*(2), 91–127.

Maurice, M., Tosi, N., Schwinger, S., Breuer, D., & Kleine, T. (2020). A long-lived magma ocean on a young moon. *Science Advances*, *6*(28). https://doi.org/10.1126/sciadv.aba8949

Mawson, D. (1949). The elatina glaciation. *Trans. R. Soc. S. Aust*, *73*, 117–121.

Mazumder, R., & Arima, M. (2005). Tidal rhythmites and their implications. *Earth-Science Reviews*, *69*(1), 79–95. https://doi.org/10.1016/j.earscirev.2004.07.004

McIntosh, P. C., & Bennett, A. F. (1984). Open Ocean Modeling as an Inverse Problem: M2 Tides in Bass Strait. *Journal of Physical Oceanography*, *14*(3), 601–614. https://doi.org/10.1175/1520-0485(1984)014<0601:OOMAAI>2.0.CO;2

Melchior, P. J. (1983). *The tides of the planet earth* (2nd). Oxford [Oxfordshire]: Pergamon Press.

Merdith, A. S., Williams, S. E., Collins, A. S., Tetley, M. G., Mulder, J. A., Blades, M. L., Young, A., Armistead, S. E., Cannon, J., Zahirovic, S., & Müller, R. D. (2021). Extending full-plate tectonic models into deep time: Linking the Neoproterozoic and the Phanerozoic. *Earth-Science Reviews*, *214*. https://doi.org/10.1016/j.earscirev.2020.103477

Miller, D. J., & Eriksson, K. A. (1997). Late Mississippian prodeltaic rhythmites in the Appalachian Basin; a hierarchical record of tidal and climatic periodicities. *Journal of Sedimentary Research*, *67*(4), 653–660. https://doi.org/10.1306/D4268608-2B26-11D7-8648000102C1865D

Mitrovica, J. X., & Forte, A. M. (1997). Radial profile of mantle viscosity: Results from the joint inversion of convection and postglacial rebound observables. *Journal of Geophysical Research: Solid Earth*, *102*(B2), 2751–2769. https://doi.org/10.1029/96JB03175

Mitrovica, J. X., Hay, C. C., Morrow, E., Kopp, R. E., Dumberry, M., & Stanley, S. (2015). Reconciling past changes in Earth's rotation with 20th century global sea-level rise: Resolving Munk's enigma. *Science Advances*, *1*(11). https://doi.org/10.1126/sciadv.1500679

Moritz, H. (2000). Geodetic Reference System 1980. *Journal of Geodesy*, *74*(1), 128–133. https://doi.org/10.1007/s001900050278

Morrison, L. V., & Stephenson, F. R. (2001). Historical eclipses and the variability of the earth's rotation. *Journal of Geodynamics*, *32*(1), 247–265. https://doi.org/10.1016/S0264-3707(01)00024-2

Morrison, L. V., Stephenson, F. R., Hohenkerk, C. Y., & Zawilski, M. (2021). Addendum 2020 to 'Measurement of the Earth's rotation: 720 BC to AD 2015'. *Proceedings of the Royal Society A: Mathematical, Physical and Engineering Sciences*, *477*(2246). https://doi.org/10.1098/rspa.2020.0776

Müller, M. (2009). *A large spectrum of free oscillations of the world ocean including the full ocean loading and selfattraction effects*. Springer Verlag.

Müller, M., Haak, H., Jungclaus, J. H., Suendermann, J., & Thomas, M. (2010). The effect of ocean tides on a climate model simulation. *Ocean Modelling*, *35*(4), 304–313. https://doi.org/{10.1016/j.ocemod.2010.09.001}

Müller, R. D., Sdrolias, M., Gaina, C., & Roest, W. R. (2008). Age, spreading rates, and spreading asymmetry of the world's ocean crust. *Geochemistry, Geophysics, Geosystems*, *9*(4). https://doi.org/10.1029/2007GC001743

Müller, R. D., Seton, M., Zahirovic, S., Williams, S. E., Matthews, K. J., Wright, N. M., Shephard, G. E., Maloney, K. T., Barnett-Moore, N., Hosseinpour, M., Bower, D. J., & Cannon, J. (2016). Ocean basin evolution and global-scale plate reorganization events since Pangea breakup. *Annual Review of Earth and Planetary Sciences*, *44*(1), 107–138. https://doi.org/10.1146/annurev-earth-060115-012211

Munk, W. H. (1997). Once again: Once again - tidal friction [Conference on Tidal Science, London, England, Oct 21-22, 1996]. *Progress in Oceanography*, *40*(1-4), 7–35.

Munk, W. H., & Cartwright, D. E. (1966). Tidal Spectroscopy and Prediction. *Philosophical Transactions of the Royal Society of London. Series A, Mathematical and Physical*

Sciences, *259*(1105), 533–581. Retrieved October 27, 2023, from http://www.jstor.org/stable/73232

Munk, W. H., & McDonald, G. J. F. (1960). *The Rotation of the Earth*. Cambridge University Press.

Murphy, T. W., Adelberger, E. G., Battat, J. B. R., Hoyle, C. D., Johnson, N. H., McMillan, R. J., Stubbs, C. W., & Swanson, H. E. (2012). APOLLO: millimeter lunar laser ranging. *Classical and Quantum Gravity*, *29*(18). https://doi.org/10.1088/0264-9381/29/18/184005

Nance, R. D., & Murphy, J. B. (2013). Origins of the supercontinent cycle. *Geoscience Frontiers*, *4*(4), 439–448. https://doi.org/10.1016/j.gsf.2012.12.007

Nerge, P. (1998). *Resonanzeigenschaften der globalen Ozeangezeiten für Topographien der Gegenwart und des Proterozoikums - Gezeitendrehmoment und die Entwicklung des Systems Erde-Mond während der Erdgeschichte* (Master's thesis). Institut für Meereskunde, Universität Hamburg, Germany.

Néron de Surgy, O., & Laskar, J. (1997). On the long term evolution of the spin of the Earth. *Astronomy & Astrophysics*, *318*(3), 975–989.

Ngodock, H. E., Souopgui, I., Wallcraft, A. J., Richman, J. G., Shriver, J. F., & Arbic, B. K. (2016). On improving the accuracy of the M_2 barotropic tides embedded in a high-resolution global ocean circulation model. *Ocean Modelling*, *97*, 16–26. https://doi.org/10.1016/j.ocemod.2015.10.011

Nietzsche, F. (1885). *Also sprach Zarathustra. Ein Buch für Alle und Keinen.* [Vierter und letzter Teil].

Nycander, J. (2005). Generation of internal waves in the deep ocean by tides. *Journal of Geophysical Research: Oceans*, *110*(C10). https://doi.org/10.1029/2004JC002487

Ooe, M. (1989). EFFECTS OF CONFIGURATION AND BATHYMETRY OF THE OCEANS ON THE TIDAL DISSIPATION OF THE EARTH'S ROTATION. *Journal of Physics of the Earth*, *37*(5), 345–355. https://doi.org/10.4294/jpe1952.37.345

Oost, A., de Haas, H., Ijnsen, F., van den Boogert, J., & de Boer, P. (1993). The 18.6 yr nodal cycle and its impact on tidal sedimentation. *Sedimentary Geology*, *87*(1), 1–11. https://doi.org/10.1016/0037-0738(93)90032-Z

Özsoy, E. (1986). Ebb-tidal jets: A model of suspended sediment and mass transport at tidal inlets. *Estuarine, Coastal and Shelf Science*, *22*(1), 45–62. https://doi.org/10.1016/0272-7714(86)90023-5

Pannella, G. (1975). Palaeontological clocks and the history of the Earth's rotation. In G. D. Rosenberg & S. K. Runcorn (Eds.), *Growth rhythms and the history of the Earth's rotation* (pp. 253–284). Wiley.

Pannella, G. (1976). Chapter 12.1 Geophysical Inferences from Stromatolite Lamination. In M. R. Walter (Ed.), *Stromatolites* (pp. 673–685). Elsevier. https://doi.org/10.1016/S0070-4571(08)71166-X

Pattullo, J. G. (1966). Mean sea level. In R. W. Fairbridge (Ed.), *The Encyclopedia of Oceanography* (475–479). Reinhold, New York.

Pekeris, C. L., & Accad, Y. (1969). Solution of Laplace's Equations for the M2 Tide in the World Oceans. *Philosophical Transactions of the Royal Society of London. Series A, Mathematical and Physical Sciences*, *265*(1165), 413–436. Retrieved October 17, 2023, from http://www.jstor.org/stable/73773

Petit, G., & Luzum, B. (2010). *IERS Convention (2010)* (IERS Technical Note No. 36). International Earth Rotation and Reference Systems Service (IERS).

Piccioni, G., Dettmering, D., Bosch, W., & Seitz, F. (2018). TICON: Tidal Constants based on GESLA sea-level records from globally distributed tide gauges (data) [Supplement to: Piccioni, G et al. (2019): TICON: TIdal CONstants based on GESLA sea-level records from globally located tide gauges. Geoscience Data Journal, 6(2), 97-104, https://doi.org/10.1002/gdj3.72]. https://doi.org/10.1594/PANGAEA.896587

Piccioni, G., Dettmering, D., Bosch, W., & Seitz, F. (2019). TICON: TIdal CONstants based on GESLA sea-level records from globally located tide gauges. *Geoscience Data Journal*, *6*(2), 97–104. https://doi.org/10.1002/gdj3.72

Pickering, M. D., Horsburgh, K. J., Blundell, J. R., Hirschi, J. J.-M., Nicholls, R. J., Verlaan, M., & Wells, N. C. (2017). The impact of future sea-level rise on the global tides. *Continental Shelf Research*, *142*, 50–68. https://doi.org/10.1016/j.csr.2017.02.004

Piper, J. D. A. (1982a). Movements of the continental crust und lithosphere-aesthnosphere systems in Precambrian times. In P. Brosche & J. Sündermann (Eds.), *Tidal Friction and the Earth's Rotation II* (253–321). Springer Verlag.

Piper, J. D. A. (1982b). The Precambrian palaeomagnetic record: the case for the Proterozoic supercontinent. *Earth and Planetary Science Letters*, *59*(1), 61–89.

Piper, J. D. A. (1990). Continental configurations and mantle references frames. In Brosche, P. and Sündermann, J. (Ed.), *Earth's Rotation from Eons to Days* (197–239). Springer Verlag.

Piper, J. (2018). Dominant lid tectonics behaviour of continental lithosphere in precambrian times: Palaeomagnetism confirms prolonged quasi-integrity and absence of supercontinent cycles. *Geoscience Frontiers*, *9*(1), 61–89. https://doi.org/10.1016/j.gsf.2017.07.009

Platzman, G. W., Curtis, G. A., Hansen, K. S., & Slater, R. D. (1981). Normal modes of the world ocean. Part II: Description of modes in the period range 8 to 80 hours. *Journal of Physical Oceanography*, *11*(5), 579–603.

Platzman, G. W. (1984). Planetary energy balance for tidal dissipation. *Reviews of Geophysics*, *22*(1), 73–84. https://doi.org/10.1029/RG022i001p00073

Platzman, G. W. (1991). An observational study of energy balance in the atmospheric lunar tide. *Pure and Applied Geophysics*, *137*(1-2), 1–33. https://doi.org/10.1007/BF00876887

Poliakow, E. (2004). Numerical modelling of the paleotidal evolution of the Earth-Moon System. *Proceedings of the International Astronomical Union*, *2004*(IAUC197), 445–452. https://doi.org/10.1017/S174392130400897X

Ponchaut, F., Lyard, F., & Provost, C. L. (2001). An Analysis of the Tidal Signal in the WOCE Sea Level Dataset. *Journal of Atmospheric and Oceanic Technology*, *18*(1), 77–91. https://doi.org/10.1175/1520-0426(2001)018<0077:AAOTTS>2.0.CO;2

Poulain, P.-M., & Centurioni, L. (2015). Direct measurements of World Ocean tidal currents with surface drifters. *Journal of Geophysical Research: Oceans*, *120*(10), 6986–7003. https://doi.org/10.1002/2015JC010818

Preiss, W. V. (Ed.). (1987). *The Adelaine Geosyncline. Late Proterozoic Stratigraphy, Sedimentation, Palaeontology and Tectonics* (Vol. Bulletin 53). Department of Mines; Energy of South Australia.

Preiss, W. V. (1993). Neoproterozoic. In J. F. Drexel, W. V. Preiss, & A. J. Parker (Eds.), *The Geology of South Australia* (pp. 171–203). Mines; Energy, South Australia, Geological Survey of South Australia.

Pugh, D. T. (1981). Tidal amphidrome movement and energy dissipation in the Irish Sea. *Geophysical Journal International*, *67*(2), 515–527. https://doi.org/10.1111/j.1365-246X.1981.tb02763.x

Quinn, T. R., Tremaine, S., & Duncan, M. (1991). A three million year integration of the Earth's orbit. *Astronomical Journal*, *101*(6), 2287–2305.

Ray, R. D. (1998). Ocean self-attraction and loading in numerical tidal models. *Marine Geodesy*, *21*(3), 181–192. https://doi.org/10.1080/01490419809388134

Ray, R. D. (2013). Precise comparisons of bottom-pressure and altimetric ocean tides. *Journal of Geophysical Research: Oceans*, *118*(9), 4570–4584. https://doi.org/10.1002/jgrc.20336

Ray, R. D., Eanes, R. J., & Chao, B. F. (1996). Detection of tidal dissipation in the solid Earth by satellite tracking and altimetry. *Nature*, *381*(6583), 595–597. https://doi.org/10.1038/381595a0

Ray, R. D., Egbert, G. D., & Erofeeva, S. Y. (2011). Tide Predictions in Shelf and Coastal Waters: Status and Prospects. In S. Vignudelli, A. G. Kostianoy, P. Cipollini, & J. Benveniste (Eds.), *Coastal altimetry* (pp. 191–216). Springer Berlin Heidelberg. https://doi.org/10.1007/978-3-642-12796-0_8

Ray, R. D., Loomis, B. D., Luthcke, S. B., & Rachlin, K. E. (2019). Tests of ocean-tide models by analysis of satellite-to-satellite range measurements: an update. *Geophysical Journal International*, *217*(2), 1174–1178. https://doi.org/10.1093/gji/ggz062

Ray, R. D. (1999). *A Global Ocean Tide Model From TOPEX/POSEIDON Altimetry: GOT99.2* (NASA/TM-1999-209478 NASA/TM-1999-209478). NASA Goddard Space Flight Center Greenbelt, MD United States.

Ray, R. D. (2020). First global observations of third-degree ocean tides. *Science Advances*, *6*(48). https://doi.org/10.1126/sciadv.abd4744

Ray, R. D., Bills, B. G., & Chao, B. F. (1999). Lunar and solar torques on the oceanic tides. *Journal of Geophysical Research: Solid Earth*, *104*(B8), 17653–17659. https://doi.org/10.1029/1999JB900165

Ray, R. D., Eanes, R. J., & Lemoine, F. G. (2001). Constraints on energy dissipation in the Earth's body tide from satellite tracking and altimetry. *Geophysical Journal International*, *144*(2), 471–480. https://doi.org/10.1046/j.1365-246x.2001.00356.x

Reading, H. G. (1978). *Sedimentary Environments and Facies* (H. G. Reading, Ed.). Blackwell Scientific.

Reineck, H.-E., & Singh, I. B. (1973). *Depositional Sedimentary Environments*. Springer Berlin Heidelberg. https://doi.org/10.1007/978-3-642-96291-2

Rooney, A. D., Strauss, J. V., Brandon, A. D., & Macdonald, F. A. (2015). A Cryogenian chronology: Two long-lasting synchronous Neoproterozoic glaciations. *Geology*, *43*(5), 459–462. https://doi.org/10.1130/G36511.1

Rosen, R. D. (1993). The axial momentum balance of Earth and its fluid envelope. *Surveys in Geophysics*, *14*, 1–29. https://doi.org/10.1007/BF01044076

Rosen, R. D., Salstein, D. A., & Wood, T. M. (1990). Discrepancies in the Earth-atmosphere angular momentum budget. *Journal of Geophysical Research: Solid Earth*, *95*(B1), 265–279. https://doi.org/10.1029/JB095iB01p00265

Rosenberg, G. D. (1997). How long was the day of the Dinosaur? And why does it matter? In D. L. Wolberg & E. Stump (Eds.), *Dinofest International, Proceedings of a Symposium Sponsored by Arizona State University* (pp. 493–512). The Academy of Science.

Rosenberg, G. D., & Runcorn, S. K. (Eds.). (1975). *Proceedings of the Interdisciplinary Winter Conference on Biological Clocks and Changes in the Earth's Rotation: Geophysical and Astronomical Consequences, University of Newcastle-upon-Tyne, Newcastle-upon-Tyne, England, January 8-10, 1974*. Wiley.

Russell, R. C. H., & MacMillan, D. H. (1970). *Waves and tides*. Greenwood Press.

Salstein, D. A., Kolaczek, B., & Gambis, D. (Eds.). (1999). *The impact of El Niño and other low-frequency signals on Earth rotation and global Earth system parameters* (Vol. IERS Technical Note).

Salstein, D. A., & Rosen, R. D. (1994). Topographic Forcing of the Atmosphere and a Rapid Change in the Length of Day. *Science*, *264*(5157), 407–409. https://doi.org/10.1126/science.264.5157.407

Samain, E., Mangin, J. F., Veillet, C., Torre, J. M., Fridelance, P., Chabaudie, J. E., Féraudy, D., Glentzlin, M., Pham Van, J., Furia, M., Journet, A., & Vigouroux, G. (1998). Millimetric Lunar Laser Ranging at OCA (Observatoire de la Côte d'Azur). *Astron. Astrophys. Suppl. Ser.*, *130*(2), 235–244. https://doi.org/10.1051/aas:1998227

Savcenko, R., & Bosch, W. (2008). *EOT08a - empirical ocean tide model from multi-mission satellite altimetry* (tech. rep. Report No. 81). Deutsches Geodätisches Forschungsinstitut (DGFI), München.

Savcenko, R., & Bosch, W. (2012). *EOT11a - empirical ocean tide model from multi-mission satellite altimetry* (tech. rep. Report No. 89). Deutsches Geodätisches Forschungsinstitut (DGFI), München.

Schmidt, P. W., Williams, G. E., & McWilliams, M. O. (2009). Palaeomagnetism and magnetic anisotropy of late Neoproterozoic strata, South Australia: Implications for the palaeolatitude of late Cryogenian glaciation, cap carbonate and the Ediacaran System. *Precambrian Research*, *174*(1-2), 35–52. https://doi.org/10.1016/j.precamres.2009.06.002

Schmittner, A., Green, J. A. M., & Wilmes, S.-B. (2015). Glacial ocean overturning intensified by tidal mixing in a global circulation model. *Geophysical Research Letters*, *42*(10), 4014–4022. https://doi.org/10.1002/2015GL063561

Schrama, E. J. O., & Ray, R. D. (1994). A preliminary tidal analysis of TOPEX/POSEIDON altimetry. *Journal of Geophysical Research: Oceans*, *99*(C12), 24799–24808. https://doi.org/10.1029/94JC01432

Schuh, H., Dill, R., Greiner-Mai, H., Kutterer, H., Müller, J., Nothnagel, A., Richter, B., Rothacher, M., Schreiber, U., & Soffel, M. (2003). *Erdrotation und globale dynamische Prozesse*. Verlag des Bundesamts für Kartographie und Geodäsie.

Schwiderski, E. W. (1980). Ocean tides, part ii: A hydrodynamical interpolation model. *Marine Geodesy*, *3*(1-4), 219–255. https://doi.org/10.1080/01490418009387998

Scotese, C. R. (2009). Late Proterozoic plate tectonics and palaeogeography: a tale of two supercontinents, Rodinia and Pannotia. *Geological Society, London, Special Publications*, *326*(1), 67–83. https://doi.org/10.1144/SP326.4

Scotese, C. R. (2017). *Atlas of Ancient Oceans & Continents: 1.5 billion years - Today* (tech. rep. PALEOMAP Project Report 112171A). Department of Earth and Planetary Sciences, Northwestern University, Evanston, United States.

Scotese, C. R. (2020) [private communication].

Scotese, C. R., & Wright, N. (2018). *PALEOMAP Paleodigital Elevation Models (PaleoDEMS) for the Phanerozoic PALEOMAP Project* (tech. rep. PALEOMAP Project Report 112171A). Department of Earth and Planetary Sciences, Northwestern University, Evanston, United States. https://www.earthbyte.org/paleodem-resource-%20scotese-and-wright-2018/

Scrutton, E. W. (1978). Periodic growth features in fossil organisms and the length of the day and month. In Brosche, P. and Sündermann, J. (Ed.), *Tidal Friction and the Earth's Rotation* (pp. 154–196). Springer Verlag.

Seiler, U. (1989). *An Investigation to the Tides of the World Ocean and their Instantaneous Angular Momentum Budgets* (Doctoral dissertation). Universität Hamburg. Inst. für Meereskunde d. Univ. Hamburg.

Seiler, U. (1991). Periodic changes of the angular momentum budget due to the tides of the World Ocean. *Journal of Geophysical Research: Solid Earth*, *96*(B6), 10287–10300. https://doi.org/10.1029/91JB00219

Seitz, F., & Müller, J. (2016). Erdrotation. In W. Freeden & R. Rummel (Eds.), *Handbuch der Geodäsie: 5 Bände* (pp. 1–29). Springer Berlin Heidelberg. https://doi.org/10.1007/978-3-662-46900-2_12-1

Seitz, F., & Schuh, H. (2010). Earth Rotation. In G. Xu (Ed.), *Sciences of Geodesy - I: Advances and Future Directions* (pp. 185–227). Springer Berlin Heidelberg. https://doi.org/10.1007/978-3-642-11741-1_6

Seton, M., Müller, R. D., Zahirovic, S., Gaina, C., Torsvik, T., Shephard, G., Talsma, A., Gurnis, M., Turner, M., Maus, S., & Chandler, M. (2012). Global continental and ocean basin reconstructions since 200Ma. *Earth-Science Reviews*, *113*(3), 212–270. https://doi.org/10.1016/j.earscirev.2012.03.002

Shriver, J. F., Arbic, B. K., Richman, J. G., Ray, R. D., Metzger, E. J., Wallcraft, A. J., & Timko, P. G. (2012). An evaluation of the barotropic and internal tides in a high-resolution global ocean circulation model. *Journal of Geophysical Research: Oceans*, *117*(C10). https://doi.org/10.1029/2012JC008170

Shriver, J. F., Richman, J. G., & Arbic, B. K. (2014). How stationary are the internal tides in a high-resolution global ocean circulation model? *Journal of Geophysical Research: Oceans*, *119*(5), 2769–2787. https://doi.org/10.1002/2013JC009423

Shum, C. K., Woodworth, P. L., Andersen, O. B., Egbert, G. D., Francis, O., King, C., Klosko, S. M., Le Provost, C., Li, X., Molines, J.-M., Parke, M. E., Ray, R. D., Schlax, M. G., Stammer, D., Tierney, C. C., Vincent, P., & Wunsch, C. I. (1997). Accuracy assessment of recent ocean tide models. *Journal of Geophysical Research: Oceans*, *102*(C11), 25173–25194. https://doi.org/10.1029/97JC00445

Simmons, H. L., Hallberg, R. W., & Arbic, B. K. (2004). Internal wave generation in a global baroclinic tide model [Small and mesoscale processes and their impact on the

large scale]. *Deep Sea Research Part II: Topical Studies in Oceanography*, *51*(25), 3043–3068. https://doi.org/10.1016/j.dsr2.2004.09.015

Simon, J. L., Bretagnon, P., Chapront, J., Chapront-Touze, M., Francou, G., & Laskar, J. (1994). Numerical expressions for precession formulae and mean elements for the Moon and the planets. *Astron. Astrophys.*, *282*, 663.

Skiba, A. W., Zeng, L., Arbic, B. K., Müller, M., & Godwin, W. J. (2013). On the resonance and shelf/open-ocean coupling of the global diurnal tides. *Journal of Physical Oceanography*, *43*(7), 1301–1324. https://doi.org/{10.1175/JPO-D-12-054.1.}

Smith, N. D., Phillips, A. C., & Powell, R. D. (1990). Tidal drawdown: A mechanism for producing cyclic sediment laminations in glaciomarine deltas. *Geology*, *18*(1), 10–13. https://doi.org/10.1130/0091-7613(1990)018<0010:TDAMFP>2.3.CO;2

Sonett, C. P., & Chan, M. A. (1998). Neoproterozoic Earth-Moon dynamics: Rework of the 900 Ma Big Cottonwood Canyon tidal laminae. *Geophysical Research Letters*, *25*(4), 539–542. https://doi.org/10.1029/98GL00048

Sonett, C. P., Kvale, E. P., Zakharian, A., Chan, M. A., & Demko, T. M. (1996). Late Proterozoic and Paleozoic Tides, Retreat of the Moon, and Rotation of the Earth. *Science*, *273*(5271), 100–104. https://doi.org/10.1126/science.273.5271.100

Spencer, R., & Vassie, J. (1997). The evolution of deep ocean pressure measurements in the UK [Tidal Science In Honour of David E. Cartwright]. *Progress in Oceanography*, *40*(1), 423–435. https://doi.org/10.1016/S0079-6611(98)00011-1

Stammer, D., Ray, R. D., Andersen, O. B., Arbic, B. K., Bosch, W., Carrère, L., Cheng, Y., Chinn, D. S., Dushaw, B. D., Egbert, G. D., Erofeeva, S. Y., Fok, H. S., Green, J. A. M., Griffiths, S., King, M. A., Lapin, V., Lemoine, F. G., Luthcke, S. B., Lyard, F., … Yi, Y. (2014). Accuracy assessment of global barotropic ocean tide models. *Reviews of Geophysics*, *52*(3), 243–282. https://doi.org/10.1002/2014RG000450

Stein, C. A., & Stein, S. (1992). A model for the global variation in oceanic depth and heat flow with lithospheric age. *Nature*, *359*, 123–129. https://doi.org/10.1038/359123a0

Stephenson, F. R., Morrison, L. V., & Hohenkerk, C. Y. (2016). Measurement of the Earth's rotation: 720 BC to AD 2015. *Proceedings of the Royal Society A: Mathematical, Physical and Engineering Sciences*, *472*(2196). https://doi.org/10.1098/rspa.2016.0404

Stephenson, F. R., Morrison, L. V., & Smith, F. T. (1995). Long-term fluctuations in the Earth's rotation: 700 BC to AD 1990. *Philosophical Transactions of the Royal Society of London. Series A: Physical and Engineering Sciences*, *351*(1695), 165–202. https://doi.org/10.1098/rsta.1995.0028

Strahler, A. H., & Strahler, A. N. (1999). *Physische Geographie*. Ulmer.

Stumpf, R. ., & Haines, J. W. (1998). Variations in Tidal Level in the Gulf of Mexico and Implications for Tidal Wetlands. *Estuarine, Coastal and Shelf Science*, *46*(2), 165–173. https://doi.org/10.1006/ecss.1997.0276

Sulzbach, R., Dobslaw, H., & Thomas, M. (2021). High-resolution numerical modeling of barotropic global ocean tides for satellite gravimetry. *Journal of Geophysical Research: Oceans*, *126*(5). https://doi.org/10.1029/2020JC017097

Sulzbach, R., Klemann, V., Knorr, G., Dobslaw, H., Dümpelmann, H., Lohmann, G., & Thomas, M. (2023). Evolution of Global Ocean Tide Levels Since the Last Glacial

Maximum. *Paleoceanography and Paleoclimatology*, *38*(5). https://doi.org/10.1029/2022PA004556

Sulzbach, R., Wziontek, H., Hart-Davis, M., Dobslaw, H., Scherneck, H.-G., Van Camp, M., Omang, O. C. D., Antokoletz, E. D., Voigt, C., Dettmering, D., & Thomas, M. (2022). Modeling gravimetric signatures of third-degree ocean tides and their detection in superconducting gravimeter records. *Journal of Geodesy*, *96*, 1432–1394. https://doi.org/10.1007/s00190-022-01609-w

Sündermann, J., & Brosche, P. (1978). The numerical computation of tidal friction for present and ancient oceans. In P. Brosche & J. Sündermann (Eds.), *Tidal Friction and the Earth's Rotation* (pp. 125–144). Springer-Verlag.

Taguchi, E., Stammer, D., & Zahel, W. (2014). Inferring deep ocean tidal energy dissipation from the global high-resolution data-assimilative HAMTIDE model. *Journal of Geophysical Research: Oceans*, *119*(7), 4573–4592. https://doi.org/10.1002/2013JC009766

Taylor, G. I. (1919). Tidal Friction in the Irish Sea. *Philosophical Transactions of the Royal Society of London. Series A, Containing Papers of a Mathematical or Physical Character*, *220*, 1–33. http://www.jstor.org/stable/91129

Taylor, G. I. (1922). Tidal Oscillations in Gulfs and Rectangular Basins. *Proceedings of the London Mathematical Society*, *s2-20*(1), 148–181. https://doi.org/10.1112/plms/s2-20.1.148

Tessier, B. (1993). Upper intertidal rhythmites in the Mont-Saint-Michel Bay (NW France): Perspectives for paleoreconstruction. *Marine Geology*, *110*(3), 355–367. https://doi.org/10.1016/0025-3227(93)90093-B

Thomas, M. (2002). *Ozeanisch induzierte Erdrotationsschwankungen - Ergebnisse eines Simultanmodells für Zirkulation und ephemeridische Gezeiten im Weltozeans* (Doctoral dissertation). Universität Hamburg.

Thomas, M., & Sündermann, J. (1999). Tides and tidal torques of the world ocean since the last glacial maximum. *Journal of Geophysical Research*, *104*(C2), 3159–3183.

Thomas, M., Sündermann, J., & Maier-Reimer, E. (2001). Consideration of ocean tides in an OGCM and impacts on subseasonal to decadal polar motion excitation. *Geophysical Research Letters*, *28*(12), 2457–2460.

Thomas, M. (1996). *Gezeiten und Drehimpuls im Ozean während der letzten 21000 Jahre* (Master's thesis) [Diplomarbeit]. Diplomarbeit, Institut für Meereskunde, Universität Hamburg, Germany.

Torge, W. (2001). *Geodesy* (3rd ed.). de Gruyter.

Tyler, R. H. (2021). On the Tidal History and Future of the Earth–Moon Orbital System. *The Planetary Science Journal*, *2*(2), 70. https://doi.org/10.3847/psj/abe53f

Uehara, K., Scourse, J. D., Horsburgh, K. J., Lambeck, K., & Purcell, A. P. (2006). Tidal evolution of the northwest European shelf seas from the Last Glacial Maximum to the present. *Journal of Geophysical Research: Oceans*, *111*(C9). https://doi.org/10.1029/2006JC003531

van Rijn, L. C. (1993). *Principles of sediment transport in rivers, estuaries and coastal seas*. Aqua Publications.

Vanyo, J. P., & Awramik, S. M. (1985). Stromatolites and earth—sun—moon dynamics [Proceedings of International Symposium Late Precambrian Geology]. *Precambrian Research*, *29*(1), 121–142. https://doi.org/10.1016/0301-9268(85)90064-6

Varga, P., Denis, C., & Varga, T. (1998). Tidal friction and its consequences in palaeogeodesy, in the gravity field variations and in tectonics. *Journal of Geodynamics*, *25*(1), 61–84. https://doi.org/10.1016/S0264-3707(97)00007-0

Visser, M. J. (1980). Neap-spring cycles reflected in Holocene subtidal large-scale bedform deposits: A preliminary note. *Geology*, *8*(11), 543–546. https://doi.org/10.1130/0091-7613(1980)8<543:NCRIHS>2.0.CO;2

von Brunn, V., & Mason, T. (1977). Siliciclastic—carbonate tidal deposits from the 3000 M.Y. Pongola Supergroup, South Africa. *Sedimentary Geology*, *18*(1), 245–255. https://doi.org/10.1016/0037-0738(77)90014-8

von Storch, J.-S., Hertwig, E., Lüschow, V., Brüggemann, N., Haak, H., Korn, P., & Singh, V. (2023). Open-ocean tides simulated by ICON-O, version icon-2.6.6. *Geoscientific Model Development*, *16*(17), 5179–5196. https://doi.org/10.5194/gmd-16-5179-2023

Wang, P. (2012). Principles of Sediment Transport Applicable in Tidal Environments. In R. A. Davis Jr. & R. W. Dalrymple (Eds.), *Principles of Tidal Sedimentology* (pp. 19–34). Springer Netherlands. https://doi.org/10.1007/978-94-007-0123-6_1

Wang, R. (1995). Theorie der Erdgezeiten. In *DGG-Seminar Gezeiten* (Oberwolfach/Schwarzwald, 17.-21.10.1994. Sonderband II/1995). Deutsche Geophysikalische Gesellschaft.

Watchorn, M. (1980). Fluvial and tidal sedimentation in the 3000 Ma Mozaan basin, South Africa. *Precambrian Research*, *13*(1), 27–42. https://doi.org/10.1016/0301-9268(80)90057-1

Webb, D. J. (1980). Tides and tidal friction in a hemispherical ocean centred at the equator. *Geophysical Journal International*, *61*(3), 573–600. https://doi.org/10.1111/j.1365-246X.1980.tb04833.x

Webb, D. J. (1982a). On the reduction in tidal dissipation produced by increases in the earth's rotation rate and it's effect on the long-term history of the moon's orbit. In P. Brosche & J. Sündermann (Eds.), *Tidal Friction and the Earth's Rotation II* (pp. 190–207). Springer Verlag.

Webb, D. J. (1982b). Tides and the Evolution of the Earth-Moon system. *Geophysical Journal of Royal Astronomical Society*, *70*(1), 261–271.

Weis, P. (2006). *Ocean tides and the Earth's rotation - Results of a high-resolving ocean model forced by the lunisolar tidal potential* (Doctoral dissertation). Universität Hamburg. https://doi.org/10.17617/2.994758

Weis, P., Thomas, M., & Sündermann, J. (2008). Broad frequency tidal dynamics simulated by a high-resolution global ocean tide model forced by ephemerides. *Journal of Geophysical Research*, *113*(C10), 15p. https://doi.org/{10.1029/2007JC004556}

Wells, J. W. (1963). Coral growth and geochronometry. *Nature*, *197*(487), 948–950.

Wells, M. R., Allison, P. A., Piggott, M. D., Hampson, G. J., Pain, C. C., & Gorman, G. J. (2010). Tidal modeling of an ancient tide-dominated seaway, Part 1: Model validation and application to global Early Cretaceous (Aptian) Tides. *Journal of Sedimentary Research*, *80*(5), 393. https://doi.org/10.2110/jsr.2010.044

Wenzel, H.-G. (1997). Tide-generating potential for the earth. In H. Wilhelm, W. Zürn, & H.-G. Wenzel (Eds.), *Tidal Phenomena* (pp. 9–26). Springer Berlin / Heidelberg. https://doi.org/10.1007/BFb0011455

Williams, G. E. (1988). Cyclicity in the late Precambrian Elatina Formation, South Australia: Solar or tidal signature? *Climatic Change*, *13*, 117–128. https://doi.org/10.1007/BF00140565

Williams, G. E. (1989a). Late Precambrian tidal rhythmites in South Australia and the history of the Earth's rotation. *Journal of the Geological Society*, *146*(1), 97–111. https://doi.org/10.1144/gsjgs.146.1.0097

Williams, G. E. (1989b). Tidal rhythmites: Geochronometers for the ancient Earth-Moon system. *Episodes*, *12*(3), 162–171.

Williams, G. E. (1991). Upper Proterozoic Tidal Rhythmites, South Australia: Sedimentary Features, Deposition, and Implications for the Earth's Paleorotation. *Clastic Tidal Sedimentology*.

Williams, G. E. (1998a). Late neoproterozoic periglacial aeolian sand sheet, stuart shelf, south australia. *Australian Journal of Earth Sciences*, *45*(5), 733–741. https://doi.org/10.1080/08120099808728429

Williams, G. E. (2000). Geological constraints on the Precambrian history of earth's rotation and the moon's orbit. *Reviews of Geophysics*, *38*(1), 37–59.

Williams, G. E. (2004). The paradox of Proterozoic glaciomarine deposition, open seas and strong seasonality near the palaeoequator: global implications. In P. G. Eriksson, W. Altermann, D. R. Nelson, W. U. Mueller, O. Catuneanu, & O. Catuneanu (Eds.), *The Precambrian Earth: Tempos and Events* (448–459). Elsevier Science.

Williams, G. E. (2023). Strong tides during cryogenian glaciations: Tidal rhythmites from early and late cryogenian glacial successions and interglacial beds, south australia. *Australian Journal of Earth Sciences*, *70*(6), 751–762. https://doi.org/10.1080/08120099.2023.2222795

Williams, G. E., Gostin, V. A., McKirdy, D. A., & Preiss, W. V. (2008). The Elatina glaciation, Late Cryogenian (Marinoan Epoch), South Australia: Sedimentary facies and palaeoenvironments. *Precambrian Research*, *163*(3-4), 307–331. https://doi.org/{10.1016/j.precamres.2007.12.001}

Williams, G. E., & Tonkin, D. G. (1985). Periglacial structures and palaeoclimatic significance of a late precambrian block field in the cattle grid copper mine, mount gunson, south australia. *Australian Journal of Earth Sciences*, *32*(3), 287–300. https://doi.org/10.1080/08120098508729331

Williams, G. E. (1989c). Precambrian tidal sedimentary cycles and Earth's paleorotation. *Eos, Transactions American Geophysical Union*, *70*(3), 33–41. https://doi.org/10.1029/89EO00012

Williams, G. E. (1990). Tidal Rhythmites: Key to the History of the Earth's Rotation and the Lunar Orbit. *Journal of Physics of the Earth*, *38*(6), 475–491. https://doi.org/10.4294/jpe1952.38.475

Williams, G. E. (1997). Precambrian length of day and the validity of tidal rhythmite paleotidal values. *Geophysical Research Letters*, *24*(4), 421–424. https://doi.org/10.1029/97GL00234

Williams, G. E. (1998b). Precambrian tidal and glacial clastic deposits: implications for Precambrian Earth–Moon dynamics and palaeoclimate. *Sedimentary Geology*, *120*(1), 55–74. https://doi.org/10.1016/S0037-0738(98)00027-X

Williams, G. E., & Gostin, V. A. (2019). Late cryogenian glaciation in south australia: Fluctuating ice margin and no extreme or rapid post-glacial sea-level rise. *Geoscience Frontiers*, *10*(4), 1397–1408. https://doi.org/10.1016/j.gsf.2019.02.002

Williams, G. E., Gostin, V. A., Mckirdy, D. M., Preiss, W. V., & Schmidt, P. W. (2011). The Elatina glaciation (late Cryogenian), South Australia. In E. Arnaud, G. P. Halverson, & G. Shields-Zhou (Eds.), *The Geological Record of Neoproterozoic Glaciations*. Geological Society of London. https://doi.org/10.1144/M36.70

Williams, G. E., & Schmidt, P. W. (2004). Neoproterozoic glaciation: Reconciling low paleolatitudes and the geologic record. In G. S. Jenkins, M. McMenamin, L. E. Sohl, & C. P. McKay (Eds.), *The extreme proterozoic: Geology, geochemistry, and climate* (pp. 145–159). American Geophysical Union (AGU). https://doi.org/10.1029/146GM12

Williams, G. E., Schmidt, P. W., & Young, G. M. (2016). Strongly seasonal proterozoic glacial climate in low palaeolatitudes: Radically different climate system on the pre-ediacaran earth. *Geoscience Frontiers*, *7*(4), 555–571. https://doi.org/10.1016/j.gsf.2016.01.005

Williams, J. G., & Boggs, D. H. (2016). Secular tidal changes in lunar orbit and Earth rotation. *Celestial Mechanics and Dynamical Astronomy*, *126*(1), 89–129. https://doi.org/10.1007/s10569-016-9702-3

Williams, J. G., Turyshev, S. G., Boggs, D. H., & Ratcliff, J. T. (2006). Lunar laser ranging science: Gravitational physics and lunar interior and geodesy. *Advances in Space Research*, *37*(1), 67–71. https://doi.org/10.1016/j.asr.2005.05.013

Willis, B. J. (2005). Deposits of Tide-Influenced River Deltas. In *River Deltas–Concepts, Models, and Examples*. SEPM Society for Sedimentary Geology. https://doi.org/10.2110/pec.05.83.0087

Wilmes, S.-B., & Green, J. A. M. (2014). The evolution of tides and tidal dissipation over the past 21,000 years. *Journal of Geophysical Research: Oceans*, *119*(7), 4083–4100. https://doi.org/10.1002/2013JC009605

Wilmes, S.-B., Pedersen, V. K., Schindelegger, M., & Green, J. A. M. (2023). Late pleistocene evolution of tides and tidal dissipation. *Paleoceanography and Paleoclimatology*, *38*(11). https://doi.org/10.1029/2023PA004727

Wilmes, S.-B., Schmittner, A., & Green, J. A. M. (2019). Glacial Ice Sheet Extent Effects on Modeled Tidal Mixing and the Global Overturning Circulation. *Paleoceanography and Paleoclimatology*, *34*(8), 1437–1454. https://doi.org/10.1029/2019PA003644

Wilmes, S.-B., Green, J. A. M., Gomez, N., Rippeth, T. P., & Lau, H. (2017). Global Tidal Impacts of Large-Scale Ice Sheet Collapses. *Journal of Geophysical Research: Oceans*, *122*(11), 8354–8370. https://doi.org/10.1002/2017JC013109

Woodworth, P. L., Hunter, J. R., Marcos, M., Caldwell, P., Menéndez, M., & Haigh, I. (2017). Towards a global higher-frequency sea level dataset. *Geoscience Data Journal*, *3*(2), 50–59. https://doi.org/10.1002/gdj3.42

Woodworth, P. L. (1999). High waters at Liverpool since 1768: the UK's longest sea level record. *Geophysical Research Letters*, *26*(11), 1589–1592. https://doi.org/10.1029/1999GL900323

Wöppelmann, G., Pouvreau, N., & Simon, B. (2006). Brest sea level record: A time series construction back to the early eighteenth century. *Ocean Dynamics*, *56*, 487–497. https://doi.org/10.1007/s10236-005-0044-z

Wunsch, C. (1972). Bermuda sea level in relation to tides, weather, and baroclinic fluctuations. *Reviews of Geophysics*, *10*(1), 1–49. https://doi.org/10.1029/RG010i001p00001

Wunsch, C. (2016). Tides of global ice-covered oceans. *Icarus*, *274*, 122–130. https://doi.org/10.1016/j.icarus.2016.03.026

Yang, C.-S., & Nio, S.-D. (1985). The estimation of palaeohydrodynamic processes from subtidal deposits using time series analysis methods. *Sedimentology*, *32*(1), 41–57. https://doi.org/10.1111/j.1365-3091.1985.tb00491.x

Yang, C.-S., & Nio, S.-D. (1989). An ebb-tide delta depositional model—a comparison between the modern Eastern Scheldt tidal basin (southwest Netherlands) and the Lower Eocene Roda Sandstone in the southern Pyrenees (Spain). *Sedimentary Geology*, *64*(1), 175–196. https://doi.org/10.1016/0037-0738(89)90091-2

Zaffos, A., Finnegan, S., & Peters, S. E. (2017). Plate tectonic regulation of global marine animal diversity. *Proceedings of the National Academy of Sciences*, *114*(22), 5653–5658. https://doi.org/10.1073/pnas.1702297114

Zahel, W. (1978). The Influence of Solid Earth Deformations on Semidiurnal and Diurnal Oceanic Tides. In P. Brosche & J. Sündermann (Eds.), *Tidal Friction and the Earth's Rotation* (pp. 98–124). Springer-Verlag.

Zahel, W. (1995). Assimilating ocean tide determined data into global tidal models [Data Assimilation in Manine Science]. *Journal of Marine Systems*, *6*(1), 3–13. https://doi.org/10.1016/0924-7963(94)00014-3

Zahel, W., Gaviño, J. H., & Seiler, U. (2000). Balances De Energía Y Momento Angular De Un Modela Global De Mareas Con Asimilación De Datos. *GEOS*, *20*(4), 400–413.

Zahel, W. (1970). *Die Reproduktion gezeitenbedingter Bewegungsvorgänge im Weltozean mittels des hydrodynamisch-numerischen Verfahrens* (Doctoral dissertation). Universität Hamburg. Inst. für Meereskunde d. Univ. Hamburg.

Zahel, W. (1977). A global hydrodynamic-numerical 1°-model of the ocean tides; the oscillation system of the M_2-tide and its distribution of energy dissipation. *Ann. Geophys.*, *33*(1/2), 31–40.

Zahel, W. (1991). Modeling ocean tides with and without assimilating data. *Journal of Geophysical Research: Solid Earth*, *96*(B12), 20379–20391. https://doi.org/10.1029/91JB00424

Zaron, E. D., & Elipot, S. (2021). An Assessment of Global Ocean Barotropic Tide Models Using Geodetic Mission Altimetry and Surface Drifters. *Journal of Physical Oceanography*, *51*(1), 63–82. https://doi.org/10.1175/JPO-D-20-0089.1

Zaron, E. D., & Ray, R. D. (2017). Using an altimeter-derived internal tide model to remove tides from in situ data. *Geophysical Research Letters*, *44*(9), 4241–4245. https://doi.org/10.1002/2017GL072950

Zeebe, R. E., & Lourens, L. J. (2022). A Deep-Time Dating Tool for Paleo-Applications Utilizing Obliquity and Precession Cycles: The Role of Dynamical Ellipticity and Tidal Dissipation. *Paleoceanography and Paleoclimatology*, *37*(2). https://doi.org/10.1029/2021PA004349

Zschau, J. (1978). Tidal friction in the solid earth: Loading tides versus body tides. In Brosche, P. and Sündermann, J. (Ed.), *Tidal Friction and the Earth's Rotation* (62–94). Springer Verlag.

Zürn, W., & Wilhelm, H. (1984). 2.5.2 Tides of the solid earth. In K. Fuchs & H. Soffel (Eds.), *Geophysics of the Solid Earth, the Moon and the Planets*. Springer-Verlag Berlin Heidelberg. https://doi.org/10.1007/10201917_77

List of Figures

List of Tables

Eidesstattliche Versicherung

Hiermit erkläre ich an Eides statt, dass ich die vorliegende Dissertationsschrift selbst verfasst und keine anderen als die angegebenen Quellen und Hilfsmittel benutzt habe. Sofern im Zuge der Erstellung der vorliegenden Dissertationsschrift generative Künstliche Intelligenz (gKI) basierte elektronische Hilfsmittel verwendet wurden, versichere ich, dass meine eigene Leistung im Vordergrund stand und dass eine vollständige Dokumentation aller verwendeten Hilfsmittel gemäß der Guten wissenschaftlichen Praxis vorliegt. Ich trage die Verantwortung für eventuell durch die gKI generierte fehlerhafte oder verzerrte Inhalte, fehlerhafte Referenzen, Verstöße gegen das Datenschutz- und Urheberrecht oder Plagiate. Alle Stellen, die wörtlich oder sinngemäß aus Veröffentlichungen entnommen wurden, sind als solche kenntlich gemacht. Ich versichere weiterhin, dass dieses gebundene Exemplar der Dissertation und das in elektronischer Form eingereichte Dissertationsexemplar und das bei der Fakultät zur Archivierung eingereichte gebundene Exemplar der Dissertationsschrift identisch sind.

Ich bin mit einer Einstellung in den Bestand der Bibliothek des Fachbereiches einverstanden.

Hamburg, 01.09.2025	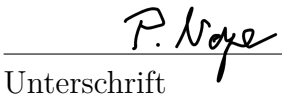
Ort, Datum	Unterschrift